

High-order harmonic generation in topological Haldanite systems

Kumulative Dissertation

zur Erlangung des Akademischen Grades

Doctor rerum naturalium (Dr. rer. nat.)

der Mathematisch-Naturwissenschaftlichen Fakultät

der Universität Rostock

Vorgelegt von:

Hannah Jürß

Geboren am:

05.08.1995 in Rostock

Abgabedatum:

15.09.2023

Betreuer:

Prof. Dr. Dieter Bauer

https://doi.org/10.18453/rosdok_id00004558

GutachterInnen

Prof. Dr. Dieter Bauer, Universität Rostock, Institut für Physik

Prof. Dr. Mette Gaarde, Louisiana State University, Department of Physics & Astronomy

Datum der Verteidigung

19.01.2024

Abstract

High-order harmonic generation (HHG) is a mechanism of strong field attosecond physics in which laser light is converted to high harmonic frequencies of the incoming laser frequency. While this process was first observed and explained for atoms, ions, and molecules in the gas phase, HHG from solid-state targets has been the subject of many studies in recent years.

A special kind of solid is the topological insulator. It is insulating in its center (referred to as bulk) but the surface or edge can host states that allow an electron transport along the boundary of the topological insulator. To turn a trivial insulator into a topological one, a topological phase transition is needed. For this, the band gap between the valence and conduction band has to be closed before it can open again, leaving behind the edge or surface states in between those two bands. These edge or surface states are responsible for the edge current and are topologically protected. Another phase transition is required to erase them. Hence, they are very robust against perturbations like disorder and impurities.

Studies of HHG in topological insulators give insight into the dynamical processes of those systems. Many of the initial studies investigate the harmonic generation from the bulk system, assuming periodic boundary conditions. However, this neglects the contributions from the conducting edge, which can also have a huge influence on the emitted harmonic spectra. This study focuses mainly on finite systems, taking the edge states into account.

The two-dimensional, topological insulator called Haldanite (Haldane model) is studied in this work. Haldanite is a model system, named after Duncan Haldane, which is formulated using the tight-binding description. It has a honeycomb structure like graphene. A broken time-reversal symmetry by introducing a complex next-nearest neighbor hopping turns Haldanite into a topological insulator.

Haldanite nanoribbons are one major focus of this work. It appears that the helicity of the emitted photons from this system can change in two different ways. One process involves the edge states and the other one the properties of the bulk states and the band structure.

In a system that is more extended in both spatial directions than ribbons, an edge current is observed. The edge current is excited by the laser pulse and results in two bright peaks in the emitted spectrum. These peaks shift towards smaller energies in the spectrum when the size of the system is increased. The results of this work show how important edge states can be in the HHG process.

Kurzzusammenfassung

Die Erzeugung hoher, harmonischer Strahlung (HHG) ist ein Mechanismus der Starkfeld-, Attosekundenphysik, bei der die Frequenz des Lichtes eines Laserstrahls in höhere, harmonische Frequenzen umgewandelt wird. Die erste Beobachtung und Erklärung dieses Prozesses fand für Atome, Ionen und Moleküle in der Gasphase statt. In den letzten Jahren fokussiert sich die Forschung aber immer mehr auf HHG in Festkörpern.

Eine besondere Art von Festkörpern stellen topologische Isolatoren dar. Dieses Material ist isolierend im Inneren, dem Bulk, aber am Rand oder an der Oberfläche gibt es Zustände, die einen Elektronentransport entlang des Randes des topologischen Isolators erlauben. Um einen trivialen Isolator in einen topologischen zu konvertieren, wird ein topologischer Phasenübergang benötigt. Dafür muss die Bandlücke zwischen dem Valenz- und dem Leitungsband zunächst geschlossen werden, bevor sich die Bandlücke erneut öffnen kann um Randzustände in der neuen Bandlücke zu erzeugen. Diese Randzustände sind verantwortlich für die Randströme, welche topologisch geschützt sind. In sie zu zerstören ist ein weiterer Phasenübergang erforderlich. Dadurch sind diese Zustände sehr robust gegen Störungen am System wie zum Beispiel Unordnung und Unreinheiten.

Die Erforschung von HHG in topologischen Isolatoren ergab einen Einblick in die dynamischen Prozesse dieser Materialien. Viele der ersten Veröffentlichungen untersuchten dabei die HHG des Bulk-Systems unter Annahme periodischer Randbedingungen. Allerdings werden dabei die Beiträge des leitenden Randes vernachlässigt. Dieser kann aber einen großen Einfluss auf das Emissionsspektrum haben. Diese Arbeit fokussiert sich überwiegend auf endliche Systeme und zieht dafür die Randzustände mit ein.

In dieser Arbeit wird der zweidimensionale topologische Isolator namens Haldanite untersucht. Haldanite ist ein nach Duncan Haldane benanntes Modell-System, welches die tight-binding Beschreibung verwendet. Der Festkörper besitzt eine Honigwaben-Struktur wie Graphen. Eine gebrochene Zeitumkehr-Symmetrie durch die Einführung eines komplexwertigen Tunnelparameters zwischen übernächsten Nachbaratomen, macht Haldanite zu einem topologischen Isolator.

Ein Fokus dieser Arbeit sind Nano-Bänder aus Haldanite. Es stellt sich heraus, dass sich die Helizität der emittierten Photonen aus diesem System durch zwei verschiedene Prozesse ändern kann. Bei einem Prozess sind die Randzustände involviert, bei dem anderen Prozess spielen die Bulk-Zustände und die Bandstruktur eine wichtige Rolle.

Für ein System, welches mehr in beiden räumlichen Richtungen ausgedehnt ist als die Haldanite Nano-Bänder, wurde ein Randstrom, der durch die Wechselwirkung mit dem externen Laserfeld angeregt wird, beobachtet. Der Randstrom tritt als zwei intensive Peaks im Emissionsspektrum in Erscheinung. Diese Peaks verschieben sich für größere System zu kleineren Energien. Die Ergebnisse dieser Arbeit zeigen die Wichtigkeit der Randzustände für den HHG-Prozess auf.

Contents

Abstract	ii
Kurzzusammenfassung	iii
Abbreviations	vi
List of publications	vi
1 Introduction	1
1.1 High-order harmonic generation	2
1.1.1 High-order harmonic generation from targets in the gas phase	2
1.1.2 High-order harmonic generation in solids	3
1.2 Topological insulators	5
1.2.1 Basics of topological insulators	5
1.2.2 Berry connection and Berry curvature	7
1.2.3 The Haldane model	8
1.2.4 Graphene and Haldanite nanoribbons	11
1.3 HHG in topological insulators	12
1.3.1 One-dimensional topological insulators	12
1.3.2 Two-dimensional topological insulators	12
1.3.3 Three-dimensional topological insulators	13
1.3.4 Concluding remarks	13
2 Theory and Methods	14
2.1 Methods for the bulk of Haldanite	14
2.1.1 Static system	14
2.1.2 Coupling to an external field	17
2.2 Methods for finite Haldanite systems	18
2.2.1 Coupling to an external field	19
2.2.2 Numerical implementation	20
2.2.3 Calculation of the current	22
2.3 Calculation of the emission spectrum	23
3 Results	25
3.1 Paper: Intense-laser-driven electron dynamics and high-order harmonic generation in solids including topological effects	25
3.2 Paper: High-order harmonic generation in hexagonal nanoribbons	25
3.3 Changing the helicity of the emitted photons	26
3.3.1 Paper: Edge-state influence on high-order harmonic generation in topological nanoribbons	27
3.3.2 Paper: Helicity flip of high-order harmonic photons in Haldane nanoribbons	27

3.4	Paper: Topological edge-state contributions to high-order harmonic generation in finite flakes	28
3.4.1	Results from the publication	28
3.4.2	Edge and bulk contributions	29
4	Summary and Outlook	31
5	Publications	33
5.1	Publications relevant for this thesis	33
5.1.1	Helicity flip of high-order harmonic photons in Haldane nanoribbons . . .	33
5.1.2	Intense-laser-driven electron dynamics and high-order harmonic generation in solids including topological effects	44
5.1.3	High-order harmonic generation in hexagonal nanoribbons	58
5.1.4	Edge-state influence on high-order harmonic generation in topological nanoribbons	68
5.1.5	Topological edge-state contributions to high-order harmonic generation in finite flakes	77
5.2	Additional publication during my Ph.D. studies	88
5.3	List of conference contributions	88
6	Bibliography	89
	Danksagung	96
	Eidesstattliche Versicherung	97

Abbreviations

BZ	Brillouin zone
c.c.	complex conjugate
DC	direct current
FFT	fast Fourier transformation
h-BN	hexagonal boron nitride
h.c.	hermitian conjugate
HHG	high-order harmonic generation
SSH chain/model	Su-Schrieffer-Heeger chain/model
TDSE	time-dependent Schrödinger equation
TISE	time-independent Schrödinger equation
TDDFT	time-dependent density functional theory
UV	ultraviolet

List of publications

The following publications are part of this cumulative thesis:

- [1]: H. Jürß and D. Bauer: *Helicity flip of high-order harmonic photons in Haldane nanoribbons*, Physical Review A **102**, 043105 (2020), DOI: [10.1103/PhysRevA.102.043105](https://doi.org/10.1103/PhysRevA.102.043105)
- [2]: D. Moos, H. Jürß, and D. Bauer: *Intense-laser-driven electron dynamics and high-order harmonic generation in solids including topological effects*, Physical Review A **102**, 053112 (2020), DOI: [10.1103/PhysRevA.102.053112](https://doi.org/10.1103/PhysRevA.102.053112)
- [3]: H. Jürß and D. Bauer: *High-order harmonic generation in hexagonal nanoribbons*, Eur. Phys. J. Spec. Top. **230**, 4081–4089 (2021), DOI: [10.1140/epjs/s11734-021-00106-z](https://doi.org/10.1140/epjs/s11734-021-00106-z)
- [4]: H. Jürß and D. Bauer: *Edge-state influence on high-order harmonic generation in topological nanoribbons*, Eur. Phys. J. D **75**, 190 (2021), DOI: [10.1140/epjd/s10053-021-00201-9](https://doi.org/10.1140/epjd/s10053-021-00201-9)
- [5]: H. Jürß and D. Bauer: *Topological edge-state contributions to high-order harmonic generation in finite flakes*, Physical Review B **106**, 054303 (2022), DOI: [10.1103/PhysRevB.106.054303](https://doi.org/10.1103/PhysRevB.106.054303)

1 Introduction

The invention of the laser in 1960 [6] revolutionized many fields in physics. Suddenly, a light source was available that could reach intensities far beyond the intensities from conventional sources. With those high intensities, the nonlinear regime could be reached. For low intensities, the polarization inside a medium induced by light is proportional to the electric field E . For nonlinear processes, however, the polarization also contains higher orders $n > 1$ ($n \in \mathbb{N}$) of the electric field: E^n , which leads to new physical phenomena.

One interesting nonlinear effect is the high-order harmonic generation (HHG): a medium is illuminated by an intense, monochromatic light pulse. The system then emits photons with higher frequencies. In particular, integer multiples $n\omega_0$ ($n \in \mathbb{N}$, $n \geq 1$), the so-called harmonics, of the laser frequency ω_0 are emitted [7–9]. The incoming light is usually in the infrared region, generating light that can reach energies up into the UV and even the soft x-ray regime [10–12].

High-harmonics can be generated in any type of material, ranging from gases (e.g. [7, 10–12]) over liquids (e.g. [13]) to solids (e.g. [14–16]). One particularly interesting group of solids are topological insulators. Those materials are an insulator in their interior (their bulk) but conducting at their boundaries. This unique behavior will also affect the harmonic spectra of those materials. While signatures of the topology can be found in the spectra from the bulk system (system with periodic boundary conditions, no edge) too [17, 18], the conducting edge is arguably the interesting part of a topological insulator and can have a huge influence on the harmonic spectra [19–26]. This work focuses mainly on HHG in finite systems, where edges are present.

The model system used in this study is the Haldane model [27], which is based on graphene but includes topological effects. The Haldane model is illuminated by an intense laser field. The emitted harmonic spectra are simulated by solving the Schrödinger equation using the tight-binding approximation.

This thesis is structured as follows: in the rest of this chapter, the fundamental concepts of this work are introduced. This includes the concept of HHG in Sec. 1.1, topological insulators in Sec. 1.2, and finally both fields combined: HHG in topological insulators in Sec. 1.3. An extended overview of the used methods and theory can be found in chapter 2 before the results of this thesis are presented in chapter 3. Chapter 4 summarizes this thesis and gives an outlook to studies that might follow. The papers that are part of this cumulative thesis are integrated into chapter 5.

Atomic units ($\hbar = |e| = m_e = 4\pi\epsilon_0 = 1$) are used throughout this work unless stated otherwise.

1.1 High-order harmonic generation

1.1.1 High-order harmonic generation from targets in the gas phase

While the process of generating low-order harmonics like second or third harmonics of the laser frequency has been observed already in 1961 [28], probably the first publication on high-order harmonic generation from rare gases appeared in 1987 [7]. That work reports experimental observation up to harmonic order seventeen. In the following years, many studies on HHG from rare gases followed.

A typical high-harmonic spectrum from gases is sketched in Fig. 1a. The intensities of the first few harmonics decrease exponentially. For higher energies, the intensity of the harmonics stays almost the same. This is referred to as a plateau. For energies above a cutoff at the end of the plateau, the intensities of the harmonics decrease rapidly until no more radiation is detected.

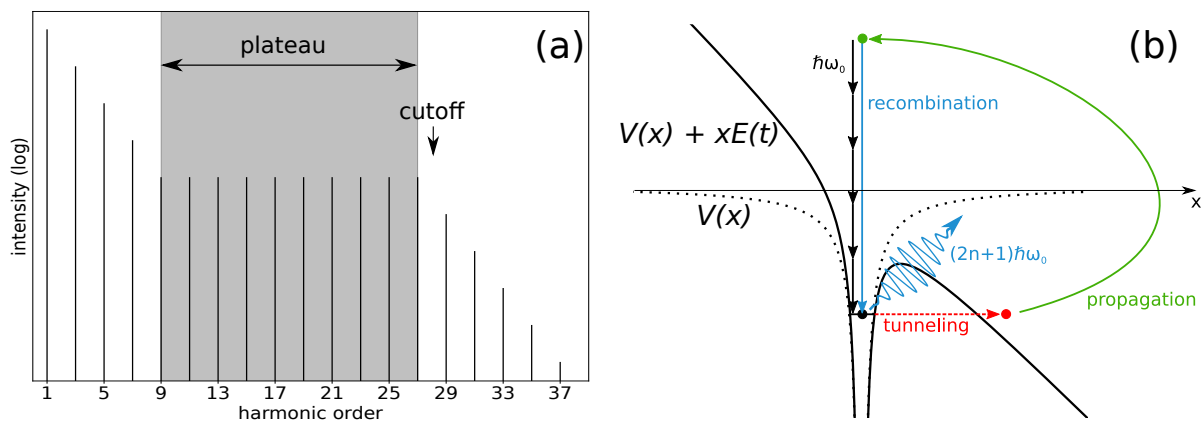


Figure 1: (a) Sketch of a typical high-harmonic spectrum from a gas-target. (b) Sketch of the three-step model that describes the HHG in a gas target as proposed in [29].

As the name suggests, high-harmonic spectra usually show peaks at integer multiples of the fundamental frequency. For atoms illuminated by a linearly polarized laser pulse, only odd harmonics are observed. This can be shown using Floquet theory [9, 30, 31].

The harmonic spectra can differ from the selection rule for which only odd harmonics are observed. Breaking this selection rule is often related to breaking the symmetry of the material (molecules or solid) and/or the symmetry of the laser field itself [31–36]. Disorders and imperfections of the material can also have an influence on the selection rules for HHG [37, 38].

In 1994, Paul B. Corkum developed a simple semi-classical three-step model that is able to predict the properties of the high-harmonic spectra from gases observed in the experiments [29]. This model, also referred to as simple man’s theory, is sketched in Fig. 1b. It considers a single active electron that does not interact with other electrons and its motion is restricted to one dimension x . Initially, the electron is bound to the ion via a Coulomb-potential $V(x)$. The strong, electric field of the linearly polarized laser pulse $E(t)$ bends the potential such that it becomes $V(x) + xE(t)$. If the electric field is strong enough, the electron has a finite probability of tunneling out into the vacuum. This is the first step of the three-step model. In the second step, the now free electron is accelerated away from the ion by the electric field. When the sign of the field changes, the electron is decelerated and might even move towards the ion again.

When the electron eventually returns to the ion, both ion and electron might recombine and a photon is emitted whose energy is given by the ionization potential I_p plus the kinetic energy of the electron at the time of the recombination.

The kinetic energy the electron acquired when returning to the ion or whether the electron is actually able to return to the ion at all, is determined by the phase of the electric field at the time of ionization. This simple model is able to determine the kinetic energy at the time of return and predicts the highest possible energy of the harmonic spectra at an energy of [29]

$$E_{\max} = I_p + 3.17 U_p, \quad (1)$$

in which

$$U_p = E_0^2 / (4 \omega_0^2) \quad (2)$$

is the ponderomotive energy, the mean quiver energy of the free electron in the laser field. The amplitude of the electric field is given by E_0 . In a full quantum mechanical description of the process, Lewenstein et al. [39] found the cutoff energy at

$$E_{\max} = 1.32 I_p + 3.17 U_p, \quad (3)$$

for $I_p \ll U_p$. This expression is similar to the one derived from the semiclassical calculation, eq. (1).

1.1.2 High-order harmonic generation in solids

In 2010, HHG from a solid (ZnO) was observed in the experiment [14]. The harmonic spectra from solids show a similar structure as the spectra from gas targets: the intensities of the first few harmonics decrease exponentially followed by a plateau at which the intensity is similar for certain harmonic orders, followed by a cutoff. One difference, however, is the existence of multiple plateaus [40, 41].

A semiclassical model, similar to the one for gas-phase HHG, exists for solid-state HHG as well [42]. This model is described in momentum (\mathbf{k}) space, as depicted in Fig. 2: the solid is considered to have a fully occupied valence band and an empty conduction band. Both bands are usually separated by a non-zero energy gap, hence the material is an insulator or semiconductor. The photon energy is usually much smaller than the band gap so the process of exciting electrons from the valence to the conduction band requires multiple photons and hence is a nonlinear process, which needs high laser intensities. This is exactly what happens in step 1: at time t_0 , the laser excites an electron at lattice momentum \mathbf{k}_0 from the valence band into the conduction band, which creates a hole in the valence band. The excitation occurs mainly around the minimal band gap as the tunneling probability between bands is larger for a smaller energy difference [42]. In step 2, the electron moves inside the conduction band and the hole moves inside the valence band. The movement is determined by the vector-potential $\mathbf{A}(t)$ that moves the electron and hole from the initial momentum \mathbf{k}_0 to $\mathbf{k}_0 + \mathbf{A}(t) - \mathbf{A}(t_0)$. The slope of the band structure determines the group velocity of the electron (“+” for the conduction band)

and hole (“−” for the valence band) at momentum \mathbf{k}

$$\mathbf{v}_{\pm}(\mathbf{k}) = \nabla_{\mathbf{k}} E_{\pm}(\mathbf{k}). \quad (4)$$

Here, $E_{\pm}(\mathbf{k})$ is the energy of the valence “−” or conduction “+” band as function of the lattice momentum \mathbf{k} and $\mathbf{v}_{\pm}(\mathbf{k})$ is the group velocity to the respective band. When the electron and hole recombine at time t_r (step 3), a photon is emitted with the energy given by the energy difference between the valence and conduction band at momentum $\mathbf{k}_0 + \mathbf{A}(t_r) - \mathbf{A}(t_0)$.

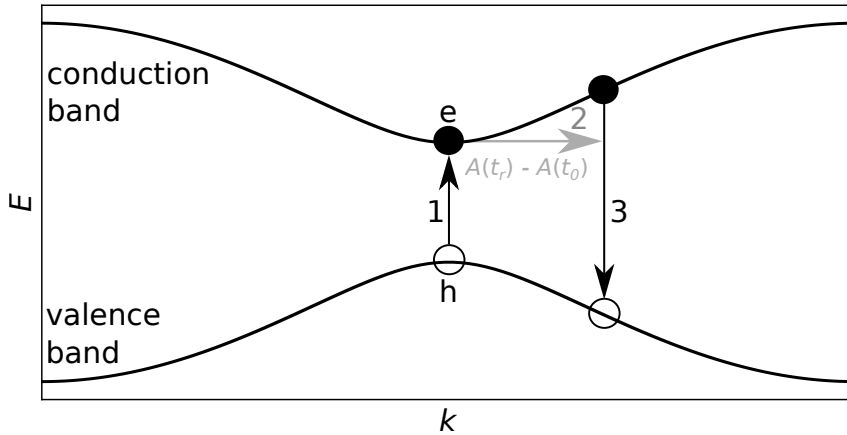


Figure 2: Sketch of the three-step model in solid-state physics, after [42]. The electron (e) is indicated by a filled circle, and the hole (h) by an unfilled circle.

Similar to gas-phase HHG, one might assume that the electron and hole recollide (at time t_r) when their positions, given by the integration over the group velocities, are identical [43]

$$\int_{t_0}^{t_r} \mathbf{v}_-(\mathbf{k}(t)) dt = \int_{t_0}^{t_r} \mathbf{v}_+(\mathbf{k}(t)) dt \text{ for } t_r > t_0. \quad (5)$$

However, Ref. [44] showed that the recollision does not necessarily need to be perfect for electron and hole to recombine. Nevertheless, eq. (5) leads to a good prediction of the cutoff law for HHG in solids. Differently to HHG from gas-phase targets where the cutoff shifts with E_0^2 , the HHG-cutoff from solid targets scales in good approximation with E_0 [43, 45–48]. However, if the field intensity becomes too strong, the cutoff energy is given by the maximal energy difference between the valence and conduction band.

Further, solids usually have more than two bands. When considering more conduction bands, there is a chance that the electrons that are excited from the valence band to the first conduction band might be excited to higher-lying bands. However, this process requires another tunneling process through an energy barrier, making this process less likely to occur. In the high-harmonic spectrum, the transitions between a higher conduction band and the valence band can be observed, but their intensity is smaller than the intensity of the plateau corresponding to transitions between the valence and the first conduction band [40, 41]. In this work, a tight-binding model is used, for which the number of bands is determined by the number of sites within the unit cell. This is described in more detail later in this chapter and in chapter 2.

One major problem in simulating high-harmonic spectra from solid targets is that no clean harmonics are observed at energies around the plateau. However, experiments show clean harmonics, e.g., [15, 40]. There are different approaches to solve this problem. One commonly used

approach is to consider relaxation or dephasing that originates from interaction with phonons or the environment, for example. Dephasing is usually achieved by adding dephasing times manually, which damps the off-diagonal terms in the density matrix (the coherences) over time, e.g., [42, 49–51]. Another possibility to obtain clean harmonic spectra is by placing a spatial filter in the far field [52]. The simulated spectrum shows clean harmonics. However, as the authors of that publication note, experiments show clean harmonics even without such a spatial filter.

In this work, no manual adjustments to the spectra are performed. Therefore the harmonic spectra around the plateau region do not show clean harmonics. This work wants to study the effects that originate from solving the Schrödinger equation before adding relaxation times manually. However, dephasing effects were briefly investigated towards the end of the Ph.D. studies but results are only preliminary and will hence not be analyzed in this thesis.

Reviews on HHG in solid-state materials can be found in [53] and with a more theoretical focus, in [54].

1.2 Topological insulators

Topological materials have gained a lot of interest in recent years. Their importance has been recognized by the Nobel committee when awarding the Nobel prize to David J. Thouless, F. Duncan M. Haldane, and J. Michael Kosterlitz “for theoretical discoveries of topological phase transitions and topological phases of matter” in 2016 [55]. Topology treats the global properties of objects. A famous example is the number of holes that an object has. The object can be formed into different shapes while preserving the number of holes. In this example, the number of holes is the topological invariant. The topological invariant can only be changed when a discontinuous operation is performed. In the previous example, the number of holes can only be changed when the object is cut or glued together.

However, topology is not restricted to geometrical properties in position space alone. Topology and the topological invariant can also be defined in more abstract spaces, for example, the momentum space. One example are topological insulator, which will be covered in detail in the next section. A detailed introduction and summary for topological insulators can be found in [56, 57].

1.2.1 Basics of topological insulators

A topological insulator is a special type of material. The inner part of the material, the bulk, is insulating, the edge¹ however, can conduct electric currents. Topological insulators are related to the quantum Hall effect, first observed by Klaus von Klitzing et al. in 1980 [58]. To understand the principle of topological insulators, a finite, two-dimensional semiconductor in a strong external magnetic field perpendicular to the material is considered. This scenario is depicted in Fig. 3a. The electrons moving in the bulk/center of the system are forced onto cyclotron orbits. Averaged over time, these orbits result in a net current of zero: the bulk is insulating. Along the edges however, the electrons hit the edge, which causes them to skip half of the cyclotron orbit, resulting in a directed transport along the surface. In this example, the edge current is directed in an anti-clockwise motion along the edge of the solid.

¹Two-dimensional materials are studied in this work, hence the word “edge” is used to refer to the boundary of the solid. For three dimensions one should rather use the word “surface” instead of “edge”.

In an actual (two-dimensional) topological insulator, the magnetic field originates from spin-orbit coupling, leading to the quantum spin Hall effect [56, 59]. In the quantum spin Hall effect, spin-orbit coupling causes a quantized Hall conductivity, leading to currents along the edge with their direction dependent on the spin [59]. In the example shown in Fig. 3a, the different spins would lead to two edge currents, one moving along the edge in a clockwise and the other one in an anti-clockwise motion.

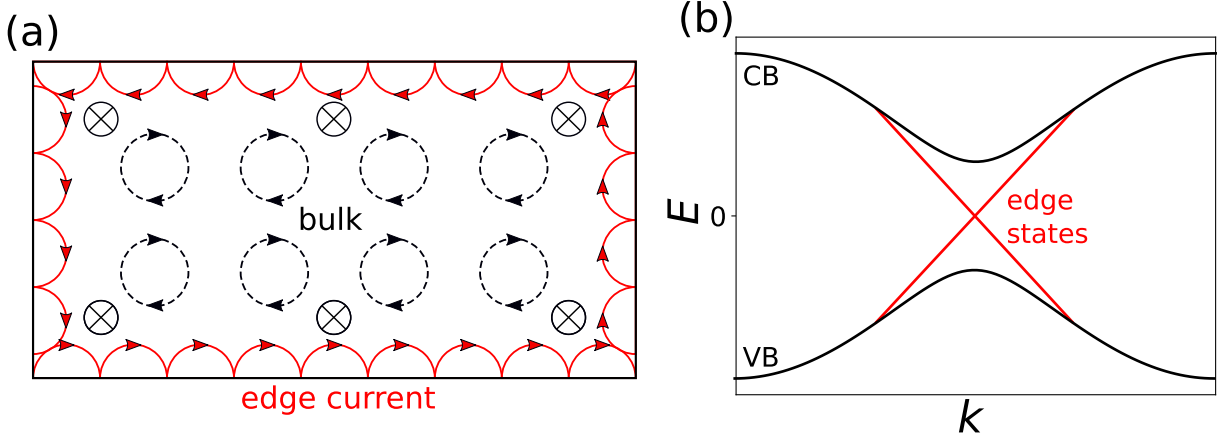


Figure 3: (a) Sketch of an induced edge current by an external magnetic field. The magnetic field is directed into the plane, indicated by the symbol \otimes (b) Typical band structure of a two-dimensional topological insulator: separated conduction (CB) and valence band (VB), connected by edge states

The band structure of a typical two-dimensional topological insulator is illustrated in Fig. 3b. Only two bands are shown here: the valence (VB) and the conduction (CB) band. Those two bands are well separated by a band gap as for a conventional insulator. In addition, the edge states connect those two bands by two straight lines with a constant slope. As shown in eq. (4), the slope of the band structure determines the group velocity of the electrons in position space. Hence, those two lines correspond to the two different edge modes moving in opposite directions.

One essential property of topology in general is the protection against perturbations. For topological insulators, the edge states are protected from perturbations like impurities, defects, and disorder [56, 57, 59, 60]. Only a topological phase transition would destroy the edge states. Further, the edge currents do not scatter into the bulk but stay located along the edge.

In Fig. 4, the robustness of edge currents is demonstrated. The electron probability density is shown for three different times ($T_1 < T_2 < T_3$). The material is Haldanite² with a significant defect of three missing lattice sites on the bottom of the material. The system is excited with an external laser pulse. The snapshots of the probability density are taken after the laser pulse. At time T_1 , the electron probability density is largest on the right edge of the material. A few moments later the probability density moved towards the bottom of the material (T_2) before moving further to the left edge (T_3). This clockwise motion along the edge will continue and the probability density stays located along the edge and does not scatter further into the system, despite the defect.

²The model will be introduced later on in section 1.2.3 and in the methods section 2. Parameters for this example are $t_1 = -0.1$, $t_2 = -0.025$, $M = -0.01$, $A_0 = 0.05$, $\omega_0 = 0.0075$, $n_{\text{cyc}} = 5$

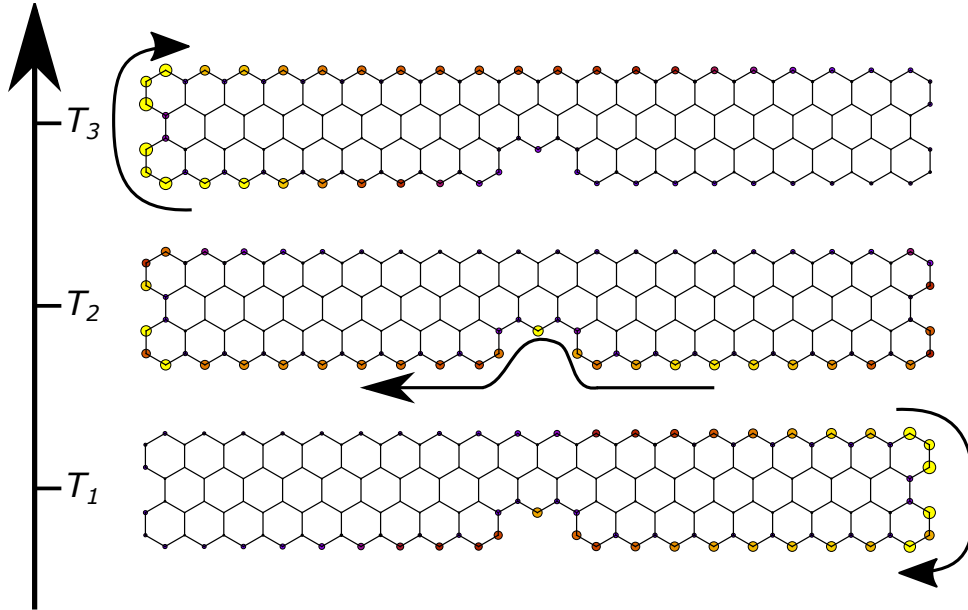


Figure 4: Electronic probability density for a topological insulator (Haldanite) for different times $T_1 < T_2 < T_3$. The probability density is encoded in the color and size of the circles: bigger circles and brighter colors correspond to a higher probability density. The arrows indicate the movement of the electron density.

Edge states are only present for finite topological insulators but absent for infinite ones, i.e., for the bulk. However, describing the bulk system is mathematically easier because a Bloch ansatz can be made for periodic systems, which simplifies the equations. The Bloch ansatz will be demonstrated later in this thesis in section 2.1. Still, the bulk-boundary-correspondence states that the existence of edge states in the finite system can be determined by the corresponding bulk system [56]. The topological invariant, which is usually calculated for the bulk system, can be used to obtain the topological phase the solid is in, which determines whether edge states are present for the corresponding finite system.

1.2.2 Berry connection and Berry curvature

As previously shown, the band structure plays an important role in the dynamical processes within a solid, compare eq. (4). However, another physical quantity is responsible for the dynamical process in solids: the Berry curvature. While the Berry curvature is particularly important for topological insulators because a topological phase transition will usually affect the Berry curvature, the Berry curvature is important for conventional solids as well. In order to calculate the Berry curvature, the Berry connection must be defined first, which reads [57]

$$\mathcal{A}_n(\mathbf{k}) = i \langle \psi_n(\mathbf{k}) | \nabla_{\mathbf{k}} \psi_n(\mathbf{k}) \rangle. \quad (6)$$

Here, $|\psi_n(\mathbf{k})\rangle$ is a wavefunction for band n dependent on the parameter \mathbf{k} . The parameter \mathbf{k} might be any parameter the wavefunction depends on. In this work, \mathbf{k} is the lattice momentum.

From the Berry connection, the Berry curvature (of band n) can be defined by

$$\Omega_n(\mathbf{k}) = \nabla_{\mathbf{k}} \times \mathcal{A}_n(\mathbf{k}). \quad (7)$$

For two-dimensional materials that are oriented in the x - y -plane, the Berry curvature becomes [57]

$$\boldsymbol{\Omega}_n(\mathbf{k}) = (\partial_{k_x} \mathcal{A}_{n,y}(\mathbf{k}) - \partial_{k_y} \mathcal{A}_{n,x}(\mathbf{k})) \mathbf{e}_z \quad (8)$$

where $\mathcal{A}_{n,i}$ and k_i ($i = x, y$) are the x - or y -components of those vectors and \mathbf{e}_z is the unity vector in z -direction.

The velocities of the electrons are given in the semiclassical approximation by [61, 62]

$$\dot{\mathbf{r}}(t) = \nabla_{\mathbf{k}} E_n(\mathbf{k}(t)) + \mathbf{E}(t) \times \boldsymbol{\Omega}_n(\mathbf{k}(t)). \quad (9)$$

The first term on the right-hand side, $\nabla_{\mathbf{k}} E_n(\mathbf{k}(t))$, is the group velocity of the electron at $\mathbf{k}(t) = \mathbf{k}_0 + \mathbf{A}(t)$. Here, $\mathbf{A}(t)$ is the vector potential and not the Berry connection $\mathcal{A}_n(\mathbf{k})$. The second term on the right-hand side, $\mathbf{E}(t) \times \boldsymbol{\Omega}_n(\mathbf{k}(t))$, describes the influence of the Berry curvature on the motion of the electron. It is called anomalous velocity. Here, $\mathbf{E}(t)$ is the electric field. Note that the term with the Berry curvature results in a motion perpendicular to the electric field.

The publication [63] makes use of eq. (9) in order to estimate the Berry curvature $\boldsymbol{\Omega}(\mathbf{k})$ in a (non-topological) solid using the experimentally obtained high-harmonic spectra.

1.2.3 The Haldane model

In 1988, a paper by Duncan Haldane was published proposing a model based on graphene that would describe the quantum Hall effect by using a periodic local magnetic field that breaks the time-reversal symmetry [27]. Kane and Mele pointed out that the Haldane model describes in fact spin-orbit interactions and hence describes the quantum spin Hall effect, i.e., a topological insulator [59]. While the Haldane model was first proposed as a toy model, it was later realized in cold atoms [64]. Additionally, it was proposed and shown that topological insulators can also be implemented using photonic waveguide systems [65–68]. Another publication showed that a Haldane-like system can theoretically be realized from the interaction of a solid (with a similar lattice structure as the Haldane model) with a tailored light field [69]. However, an actual material that displays the properties of the Haldane model (for which HHG might be observed) has not been realized in the laboratory so far. Still, the simplicity of this model system makes it a popular candidate for theoretical studies on topological insulators. In the following, the material described by the Haldane model is referred to as Haldanite.

To understand Haldanite, graphene has to be introduced first. Graphene is a two-dimensional material which is known for its honeycomb lattice structure, shown in Fig. 5a: the lattice sites are indicated by the dots. The dashed box indicates one unit cell. The arrows \mathbf{a}_1 and \mathbf{a}_2 are the lattice vectors.

The system is described using the tight-binding approximation, which uses basis functions that are strongly localized at the lattice sites. The single electron wavefunction localized at site m is denoted by $|m\rangle$. The electrons are then allowed to jump or tunnel with a defined probability between the different sites. This probability is also referred to as hopping parameter or hopping

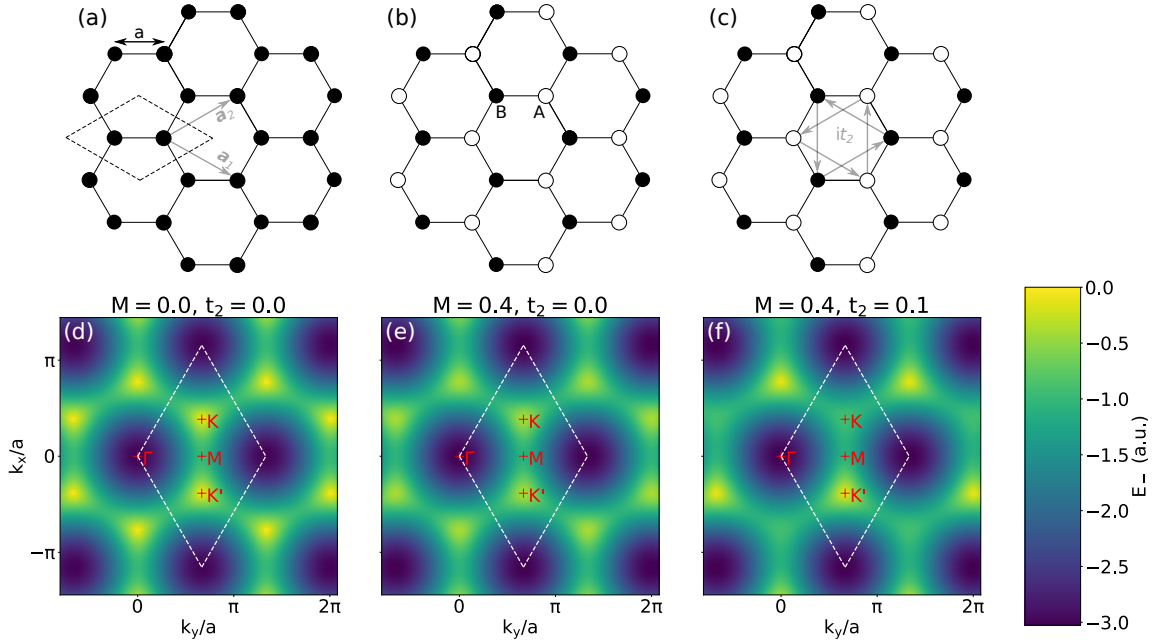


Figure 5: (a) Sketch of the lattice structure of graphene, dots indicate atomic sites, hopping is allowed between neighboring sites (distance a) only. The possible hoppings are indicated by solid lines. The dashed box indicates one unit cell. Vectors \mathbf{a}_1 and \mathbf{a}_2 are the lattice vectors. (d) Energy of the valence band $E_-(\mathbf{k})$ of the system in (a), indicating its band structure. (b) Lattice structure of the system in (a) but with two different atomic elements indicated by unfilled (A) and filled (B) circles. (e) Energy of the valence band $E_-(\mathbf{k})$ of the system in (b), indicating its band structure. (c) Lattice structure as in (b) with an additional complex next-nearest neighbor hopping. The arrows indicate hopping with amplitude it_2 , while the hopping element is $-it_2$ in the opposite direction of the arrows. (f) Energy of the valence band $E_-(\mathbf{k})$ of the system shown in (c), indicating its band structure. The dashed box in (d-f) highlights the first BZ. Important points (Γ -, K -, K' - and M -point) within the first BZ are indicated. The colorbar is the same for all plots (d-f). The energy of the conduction band is given by $E_+(\mathbf{k}) = -E_-(\mathbf{k})$ for all cases (d-f).

probability. A general tight-binding wavefunction reads

$$|\psi\rangle = \sum_m c_m |m\rangle, \quad (10)$$

where m runs over all sites. The values of $|c_m|^2$ are the probabilities to find the electron in state $|m\rangle$, i.e., localized around site m . All states $|m\rangle$ are assumed to be orthonormal

$$\langle m | n \rangle = \delta_{m,n}, \quad (11)$$

where $\delta_{m,n}$ is the Kronecker-delta.

For graphene, only the hopping probability between nearest neighbors is considered and denoted as $t_1 \in \mathbb{R}$. In Fig. 5a, the possible hoppings (between nearest neighbors) are indicated by the solid lines. Nearest neighbors are separated by distance a . Figure 5d shows the energy of the valence band $E_-(\mathbf{k})$ as a colorplot. The energy of the conduction band $E_+(\mathbf{k})$ is just the negative of the valence band energy. Figure 5d indicates also the lattice in reciprocal (lattice momentum, \mathbf{k}) space. The first Brillouin zone (BZ) is indicated by the dashed box. The most important points in reciprocal space for graphene are marked. They are the Γ -, K -, K' -, and M -points. Mathematical equations for the system are given in the methods section 2.1 later on.

Graphene has no band gap, so it is a conductor. The valence and conduction band touch at the K- and K'-points. Around those points, the dispersion relation is linear, which allows to draw the analogy to ultra-relativistic systems [56]. The M-point is a saddle point while the maximal energy gap between the valence and conduction band is at the Γ -point.

In order to open a band gap, an alternating on-site potential $\pm M$ is introduced. This is achieved by including two different atomic elements on the two sublattice sites within the unit cell, as depicted in Fig. 5b by the unfilled (sublattice site A, potential M) and filled (sublattice site B, potential $-M$) circles. There are materials that have a honeycomb (hexagonal) lattice structure which are made out of two elements, e.g., h-BN. The alternating on-site potential opens a band gap around the K- and K'-points (see Fig. 5e), so the material becomes an insulator or semiconductor. The band gaps at both the K- and the K'-point are identical.

To make this material topological, the time-reversal symmetry has to be broken. This is achieved by including a complex next-nearest neighbor hopping. The arrows in Fig. 5c indicate the complex hopping between next-nearest neighbors. The hopping is it_2 ($t_2 \in \mathbb{R}$) in the direction of the arrows and $-it_2$ in the opposite direction. This results in an asymmetry between the K and K' points, see Fig. 5f. In this example, the band gap at the K-point increases when t_2 becomes bigger, while the band gap at the K'-point decreases until the band gap vanishes at $t_2 = |M|/(3\sqrt{3})$. The closure of the band gap marks the topological phase transition. The band gap increases if t_2 is increased further but now the system is topological. If the system was finite, edge states would connect the valence and conduction band if the system is in its topological phase.

In order to obtain the band structures discussed here, the bulk system should be considered. To obtain the bulk Hamiltonian, a Bloch ansatz can be performed for the finite system with periodic boundary conditions. This will be presented in Sec. 2.1.

The Hamiltonian of the finite system can be written down in a very general way and can then be constructed for each individual finite system. In practice, this is done by considering a specific system with N sites numbered with $m, n = 1, 2, 3, \dots, N$. The general Hamiltonian reads [4, 5]

$$\begin{aligned} \hat{H}_0 = & t_1 \underbrace{\sum_{\langle m,n \rangle} \left(|m\rangle \langle n| + |n\rangle \langle m| \right)}_{\text{nearest neighbor hopping}} + M \underbrace{\left(\sum_{m \in A} |m\rangle \langle m| - \sum_{m \in B} |m\rangle \langle m| \right)}_{\text{on-site potential}} \\ & + \underbrace{\sum_{\langle\langle m,n \rangle\rangle} \left(t_2^{mn} |m\rangle \langle n| + (t_2^{mn})^* |n\rangle \langle m| \right)}_{\text{next-nearest neighbor hopping}}. \end{aligned} \quad (12)$$

Where the first sum runs over all nearest neighbors, $\langle m, n \rangle$ and the third term only considers next-nearest neighbors $\langle\langle m, n \rangle\rangle$. In the second term, $m \in A$ ($m \in B$) indicates that only sites from sublattice A (B) are summed over. In the above equation (12), the elements t_2^{mn} govern the hopping between next-nearest neighbors. The arrows sketched in Fig. 5c indicate the direction of the next-nearest neighbor hopping (only shown for one hexagon). Their values are [5]

$$t_2^{mn} = \begin{cases} it_2 & \text{for hopping along the arrows} \\ -it_2 & \text{for hopping against the arrows} \end{cases}. \quad (13)$$

Note that often the next-nearest neighbor hopping is given by $t_2 e^{i\phi}$, with an additional parameter ϕ that determines the complex phase. This is more general than the approach used here where the next-nearest neighbor hopping is just it_2 (i.e., $\phi = \pi/2$). Further, in the derivation by Haldane, it was shown that the phase ϕ actually corresponds to the magnetic flux through certain parts of the unit cell [27] and hence, has a physical meaning. However, the real part in the next-nearest neighbor hopping only amounts to an energy shift of both bands (equation (B8) in [2], sec. 5.1.2), which does not yield any new physics for the HHG later on. For this more general model, the system is in its topological phase if [27]

$$\left| \frac{M}{3\sqrt{3}} \right| < |t_2 \sin \phi|. \quad (14)$$

Hence, for $\phi = \pm\pi/2$ the phase transition to the topological phase can be observed for the smallest value of $|t_2|$ (for fixed M). The absolute value of $t_2 e^{i\phi}$ should be rather small compared to $|t_1|$ because the tunneling probability between next-nearest neighbors should be less likely than between nearest neighbors.

1.2.4 Graphene and Haldanite nanoribbons

Haldanite is a two-dimensional material but it can of course be arranged in a ribbon shape such that the system is much longer along one coordinate than along the other. Hence, the system is almost one-dimensional. The honeycomb structure for Haldanite can have different edge configurations, e.g., the zig-zag and the armchair edge. Another possibility is for example the cove edge [70], but this one will not be considered in this work. Figure 6 displays the nanoribbon with armchair edges (Fig. 6a) and the one with zig-zag edges (Fig. 6b). The dotted boxes outline the unit cells. The number of unit cells within one nanoribbon is given by N_{hex} . The focus of this thesis is on ribbons as displayed in Fig. 6. However, our publications [1, 4] consider longer chains than the ones sketched here, i.e., N_{hex} is bigger.

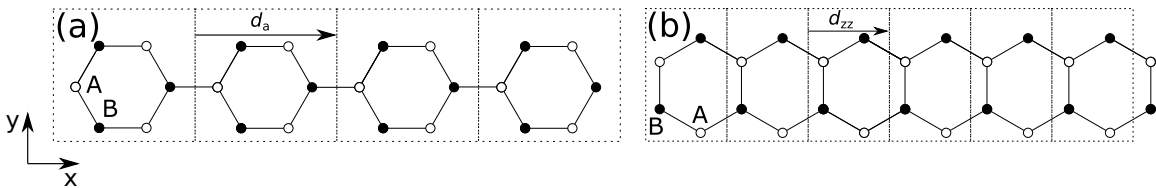


Figure 6: (a) Nanoribbon with armchair edges containing $N_{\text{hex}} = 4$ hexagons. (b) Nanoribbon with zig-zag edges containing $N_{\text{hex}} = 6$ hexagons. (a) and (b): The dotted boxes indicate the unit cells. The values of d_a and d_{zz} determine the width of the unit cells. Adapted from publication [3].

One could also make the ribbons wider by stacking nanoribbons together along in the y -direction. Interestingly, graphene nanoribbons (without on-site potential and complex next-nearest neighbor hopping $M = t_2 = 0$) can host topological interface states dependent on, for example, the width of the ribbons and the edge configuration [71, 72]. A complex next-nearest neighbor hopping is not needed for that. However, this is not part of this work. Here, only topological effects due to the complex next-nearest neighbor hopping are investigated.

The number of bands in the tight-binding model is determined by the number of sites within the unit cell. The bulk of graphene has two bands (valence and conduction band) because the

unit cell contains two sites (compare Fig. 5a). The nanoribbons here have more sites within the unit cell (see Fig. 6): six for the ribbon with armchair edges and four for the one with a zig-zag edge, leading to six and four bands, respectively. However, for graphene nanoribbons ($M = t_2 = 0$), only transitions between certain bands are allowed [73, 74].

1.3 HHG in topological insulators

1.3.1 One-dimensional topological insulators

Illuminating topological materials with intense laser light in order to generate high harmonics is quite new. The first theoretical result for HHG in a topological insulator was published in 2018 [19]. The studied model was the Su-Schrieffer-Heeger (SSH) chain, a linear, one-dimensional model solid originally introduced to describe polyacetylene [75]. Nowadays, the SSH chain is mainly used as a toy-model to study topological effects that can, to a certain extent, even be analyzed analytically. In its topological phase, the SSH model has two edge states. Using a time-dependent density functional theory approach (TDDFT), it was reported in Ref. [19] that the intensity of low-order harmonics are up to $\simeq 14$ orders of magnitude higher for the topological phase than for the trivial phase. This originates from the edge states that are located in the band gap between the valence and the conduction band. Usually, the emitted harmonics from a fully occupied band vanish. However, only one edge state is occupied so that the edge states act as an additional, partially filled band which produces harmonics more efficiently in the topological phase compared to the trivial phase without edge states. The robustness of this effect to various perturbations was confirmed in Ref. [20]. Later on, the effect was also observed when using a tight-binding approach [21] instead of the TDDFT calculation. Similar results were obtained for an extended SSH model with next-nearest neighbor hopping, resulting in more edge states between the valence and conduction band [76].

However, in a later publication, it was shown that adding a finite dephasing time to the simulation can destroy the huge difference between both topological phases [77].

1.3.2 Two-dimensional topological insulators

While HHG in topologically trivial materials with honeycomb lattices like graphene or h-BN have been studied both theoretically (e.g. [3, 78–84]) and experimentally (e.g. [85–87]), the studies on HHG in the topological Haldanite material is limited to theoretical works so far.

However, those theoretical works on HHG in Haldanite revealed some effects originating from the topology. For the two-dimensional Haldanite, a Berry curvature $\mathbf{\Omega}(\mathbf{k})$ can be defined. The Berry curvature leads to an anomalous velocity perpendicular to the external field, eq. (9). In Ref. [17], a change in the helicity (handedness) of the emitted photons for certain odd harmonics (especially the third and ninth harmonic) was reported when a topological phase transition occurred. The authors explain this by a change in the Berry curvature, which changes the direction of the component of the current perpendicular to the linearly polarized laser field. This then leads to a change in the helicity of the emitted photons [17].

Another theoretical work investigated the harmonic spectra from Haldanite illuminated by circularly polarized laser fields [18]. Their results showed that the harmonic spectrum depends

on the helicity of the incoming laser light and the topology of the system, i.e., a circular dichroism imprints the topological phase of the system.

Even though Haldanite shows unique signatures in the high-harmonic spectrum dependent on the topological phase, those signatures cannot be generalized for other topological insulators, as shown in Ref. [88]. The authors of that reference state that the contributions from the band structure, lattice symmetry, and chemical nature of the orbitals are probably more dominant than effects from the topology itself. Consequently, topological effects differ in different topological systems and have to be studied for each material individually.

1.3.3 Three-dimensional topological insulators

Instead of the one-dimensional edge states present for two-dimensional topological insulators, three-dimensional topological insulators have two-dimensional surface states. This higher dimensionality results in more degrees of freedom in the dynamical processes. Further, three-dimensional topological insulators are accessible for experimental studies:

In Ref. [22], measured harmonic spectra from surface states and the bulk in bismuth telluride (Bi_2Te_3) are compared. The authors find that the harmonics originating from the surface can be shifted in frequency by the carrier-envelope phase of the driving laser pulse, leading to non-integer harmonics. However, the harmonics from the bulk are unaffected by the carrier-envelope phase. The surface states have a Dirac-cone-like dispersion relation, which the authors identify as the cause of the dependence on the carrier-envelope phase. The signatures of surface states on the HHG in BiSbTeSe_2 are also investigated in Ref. [23]. Their results indicate that even-order harmonics from that material originate mainly from the surface states.

The papers [24, 25] investigate the HHG in bismuth selenide (Bi_2Se_3) theoretically and experimentally. The dependence of bulk and surface harmonics on the ellipticity and orientation of the laser field is studied, showing a difference between bulk and surface harmonics. In Ref. [26], it is shown that bismuth selenide can undergo a topological phase transition into the trivial phase by doping the system with indium. The authors report a difference in the dependence on the ellipticity and orientation of the laser field between the trivial phase and topologically non-trivial phase.

1.3.4 Concluding remarks

The results reported in the previous section show the importance of surface states on HHG in three-dimensional topological insulators. Many theoretical results, especially on Haldanite, focus on the bulk while the edge effects are neglected. The topological edge states might arguably be the most important part of a topological insulator. However, some of the effects observed in HHG from topological insulators are caused by the Berry curvature, a property that is defined for the bulk, and can only be approximated for finite systems. To understand the influence of the Berry curvature, bulk simulations are hence more suitable. This thesis focuses mainly on finite systems and compares the results to the ones from the respective bulk system when needed. The main goal of this work is to further understand the role of topological edge states in the interaction with intense, ultrashort laser fields.

2 Theory and Methods

In the following, the theoretical equations used to simulate the system are presented. The important equations from our published papers are summarized, and additional details and derivations are given. The bulk is extensively studied in [2] for a general system and Haldanite in detail. The references [1, 3–5] cover (mainly) finite systems. While the methods in those publications are similar, some details are different. I developed a code to perform simulations, this code was improved and adjusted continuously over the course of my Ph.D. study.

2.1 Methods for the bulk of Haldanite

The bulk system describes the interior of a solid with the assumption that the solid has periodic boundary conditions. Using a Bloch ansatz, the Hamiltonian of the periodic system breaks down to a matrix with the dimension given by the number of sites within the unit cell [2].

2.1.1 Static system

In the paper [2], the 2×2 Bloch Hamiltonian of the Haldanite system is obtained. However, the derivation of that Bloch Hamiltonian itself is not explained in detail in that publication. Therefore, this derivation is sketched in the following.

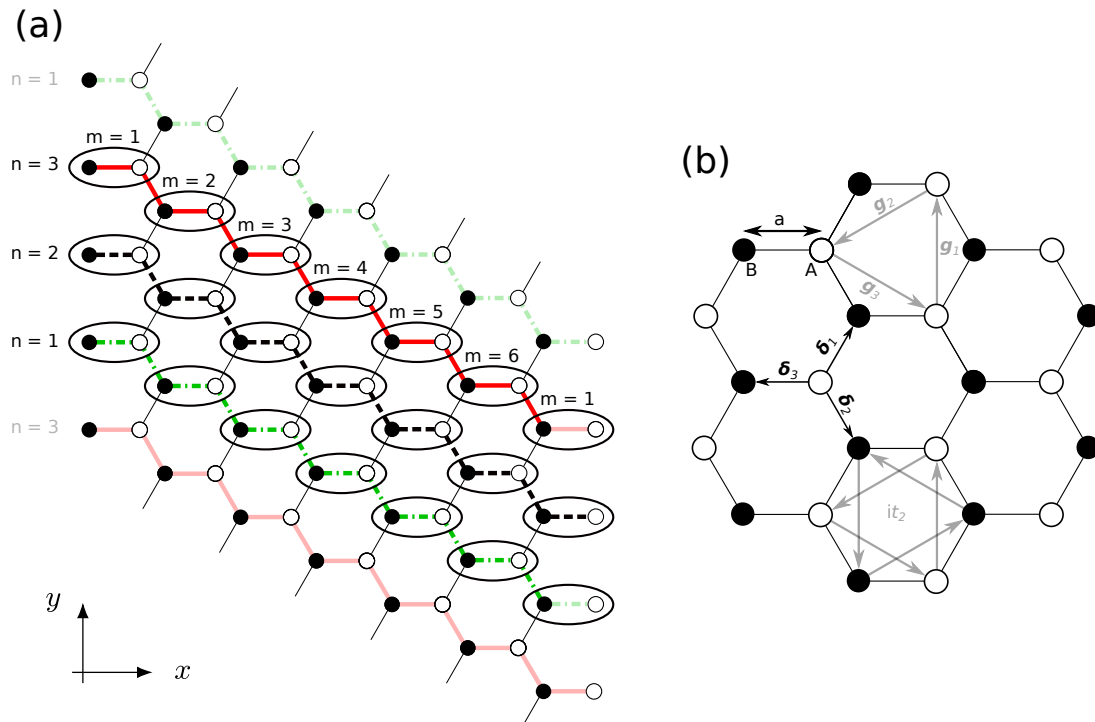


Figure 7: (a) Sketch of the periodic Haldanite system. The unit cells (illustrated by ellipses) are organized in chains $n = 1, 2, 3$, where the unit cells within a chain are numerated by $m = 1, 2, 3, 4, 5, 6$. Sites with the same parameter n are connected by lines with same color and drawing style. The pattern is repeated periodically in both directions. Sublattice sites A (B) are indicated by unfilled (filled) circles. (b) Part of the Haldanite system, introducing the vectors describing the shift between nearest neighbors δ_i and next-nearest neighbors g_i ($i = 1, 2, 3$). The distance between nearest neighbors is a . The next-nearest neighbor hopping is indicated as well. The value of the next-nearest neighbor hopping is it_2 in the direction of the gray arrows and $-it_2$ in the opposite direction. (b) is adapted from [2].

A Haldanite system with periodic boundary conditions is shown in Fig 7a. One unit cell contains two sublattice sites: A and B . The sublattice site A (B) has an on-site potential of M ($-M$). The unit cells can be organized in a two-dimensional grid using the indices m and n . For a better visualization, lattice sites with the same n are connected by lines with the same color (and the same drawing style). Unit cells with the same m lie on top of each other (have the same x -value). The indices can have the values $m = 1, 2, \dots, M'$ and $n = 1, 2, \dots, N'$, in Fig. 7a, $M' = 6$ and $N' = 3$ is chosen³. An electron orbital strongly localized at sublattice site α ($\alpha = A, B$) in unit cell (m, n) is given by $|m, n, \alpha\rangle$. The periodic boundary condition is implemented by setting $|M' + 1, n, \alpha\rangle = |1, n, \alpha\rangle$ and $|m, N' + 1, \alpha\rangle = |m, 1, \alpha\rangle$. The states are orthonormal $\langle m', n', \alpha' | m, n, \alpha\rangle = \delta_{m',m} \delta_{n',n} \delta_{\alpha',\alpha}$.

The Hamiltonian reads

$$\begin{aligned} \hat{H}_0 = & \sum_{m=1}^{M'} \sum_{n=1}^{N'} \left[t_1 \left(|m, n, B\rangle \langle m, n, A| + |m+1, n, B\rangle \langle m, n, A| + |m+1, n+1, B\rangle \langle m, n, A| \right) \right. \\ & + it_2 \left(|m, n+1, A\rangle \langle m, n, A| + |m-1, n-1, A\rangle \langle m, n, A| + |m+1, n, A\rangle \langle m, n, A| \right. \\ & \left. \left. + |m-1, n, B\rangle \langle m, n, B| + |m, n-1, B\rangle \langle m, n, B| + |m+1, n+1, B\rangle \langle m, n, B| \right) \right] + \text{h.c.} \\ & + M \sum_{m=1}^{M'} \sum_{n=1}^{N'} |m, n, A\rangle \langle m, n, A| - |m, n, B\rangle \langle m, n, B| \end{aligned} \quad (15)$$

Here, h.c. is the hermitian conjugate of all the terms before. Note that t_1 and t_2 are real values. The Bloch ansatz to obtain the Bloch Hamiltonian for this system is

$$|\pm, \mathbf{k}\rangle = \frac{1}{\sqrt{M'N'}} \sum_{m=1}^{M'} \sum_{n=1}^{N'} e^{i\mathbf{k}\cdot(m\mathbf{g}_3+n\mathbf{g}_1)} |m, n\rangle \otimes \left(C_{\pm}^A(\mathbf{k}) |A\rangle + C_{\pm}^B(\mathbf{k}) e^{i\mathbf{k}\cdot\delta_3} |B\rangle \right). \quad (16)$$

Here, the \pm indicates the different bands, ‘-’ for the valence and ‘+’ for the conduction band. Note that this ansatz is slightly different from the one in Ref. [2]. This is due to the different numbering of the unit cells in this work, which will make the calculation a bit less cumbersome. The Bloch ansatz requires several vectors that describe the shift between the different sites. Those vectors are introduced in Fig. 7b. The vectors describing the shift between nearest neighbors are given by [2]

$$\boldsymbol{\delta}_1 = \frac{a}{2} \begin{pmatrix} 1 \\ \sqrt{3} \end{pmatrix}, \quad \boldsymbol{\delta} = \frac{a}{2} \begin{pmatrix} 1 \\ -\sqrt{3} \end{pmatrix}, \quad \text{and} \quad \boldsymbol{\delta}_3 = -a \begin{pmatrix} 1 \\ 0 \end{pmatrix} \quad (17)$$

and for the next-nearest neighbors, they are

$$\mathbf{g}_1 = a \begin{pmatrix} 0 \\ \sqrt{3} \end{pmatrix}, \quad \mathbf{g}_2 = -\frac{a}{2} \begin{pmatrix} 3 \\ \sqrt{3} \end{pmatrix}, \quad \text{and} \quad \mathbf{g}_3 = \frac{a}{2} \begin{pmatrix} 3 \\ -\sqrt{3} \end{pmatrix}. \quad (18)$$

³Note that M is the on-site potential and M' the number of unit cells in one particular spatial direction.

With the Bloch ansatz (16), the time-independent Schrödinger equation (TISE)

$$\hat{H}_0 |\pm, \mathbf{k}\rangle = E_\pm |\pm, \mathbf{k}\rangle \quad (19)$$

can be solved. By inserting the Hamiltonian and the Bloch ansatz, the expression becomes quite lengthy. It can be simplified by multiplying with $\sqrt{M'N'} \langle m', n' | e^{-i\mathbf{k}\cdot(m'\mathbf{g}_3+n'\mathbf{g}_1)}$ from the left of eq. (19):

$$\begin{aligned} & t_1 \left[C_\pm^B e^{i\mathbf{k}\cdot\delta_3} |A\rangle \left(1 + e^{i\mathbf{k}\cdot\mathbf{g}_3} + e^{i\mathbf{k}\cdot(\mathbf{g}_3+\mathbf{g}_1)} \right) + C_\pm^A |B\rangle \left(1 + e^{-i\mathbf{k}\cdot\mathbf{g}_3} + e^{-i\mathbf{k}\cdot(\mathbf{g}_3+\mathbf{g}_1)} \right) \right] \\ & + it_2 \left[C_\pm^A |A\rangle \left(e^{-i\mathbf{k}\cdot\mathbf{g}_1} + e^{i\mathbf{k}\cdot(\mathbf{g}_3+\mathbf{g}_1)} + e^{-i\mathbf{k}\cdot\mathbf{g}_3} \right) + C_\pm^B e^{i\mathbf{k}\cdot\delta_3} |B\rangle \left(e^{i\mathbf{k}\cdot\mathbf{g}_3} + e^{i\mathbf{k}\cdot\mathbf{g}_1} + e^{-i\mathbf{k}\cdot(\mathbf{g}_3+\mathbf{g}_1)} \right) \right] \\ & - it_2 \left[C_\pm^A |A\rangle \left(e^{i\mathbf{k}\cdot\mathbf{g}_1} + e^{-i\mathbf{k}\cdot(\mathbf{g}_3+\mathbf{g}_1)} + e^{i\mathbf{k}\cdot\mathbf{g}_3} \right) + C_\pm^B e^{i\mathbf{k}\cdot\delta_3} |B\rangle \left(e^{-i\mathbf{k}\cdot\mathbf{g}_3} + e^{-i\mathbf{k}\cdot\mathbf{g}_1} + e^{i\mathbf{k}\cdot(\mathbf{g}_3+\mathbf{g}_1)} \right) \right] \\ & + M \left(C_\pm^A |A\rangle - C_\pm^B e^{i\mathbf{k}\cdot\delta_3} |B\rangle \right) = E_\pm \left(C_\pm^A |A\rangle + C_\pm^B e^{i\mathbf{k}\cdot\delta_3} |B\rangle \right). \end{aligned} \quad (20)$$

This expression can be simplified by using the vector relations

$$\mathbf{g}_3 + \delta_3 = \delta_2 \quad \text{and} \quad \delta_3 - \mathbf{g}_2 = \delta_1 \quad \text{and} \quad \mathbf{g}_1 + \mathbf{g}_3 = -\mathbf{g}_2. \quad (21)$$

Further, eq. (20) comprises two independent equations that can be uncoupled by multiplying with $\langle A |$ or $\langle B |$ from the left

$$\langle A | : \quad t_1 C_\pm^B \sum_{i=1}^3 e^{i\mathbf{k}\cdot\delta_i} + C_\pm^A \left[it_2 \sum_{i=1}^3 \left(e^{-i\mathbf{k}\cdot\mathbf{g}_i} - e^{i\mathbf{k}\cdot\mathbf{g}_i} \right) + M \right] = E_\pm C_\pm^A \quad (22)$$

$$\langle B | : \quad t_1 C_\pm^A \sum_{i=1}^3 e^{-i\mathbf{k}\cdot\delta_i} + C_\pm^B \left[it_2 \sum_{i=1}^3 \left(e^{i\mathbf{k}\cdot\mathbf{g}_i} - e^{-i\mathbf{k}\cdot\mathbf{g}_i} \right) - M \right] = E_\pm C_\pm^B. \quad (23)$$

This can be written in a matrix-format

$$\mathbf{H}(\mathbf{k}) \mathbf{C}_\pm(\mathbf{k}) = E_\pm(\mathbf{k}) \mathbf{C}_\pm(\mathbf{k}) \quad (24)$$

in which $\mathbf{C}_\pm(\mathbf{k}) = \begin{pmatrix} C_\pm^A \\ C_\pm^B \end{pmatrix}$. The 2×2 Bloch Hamiltonian is defined as

$$\mathbf{H}(\mathbf{k}) = \begin{pmatrix} \sigma(\mathbf{k}) & \tau(\mathbf{k}) \\ \tau^*(\mathbf{k}) & -\sigma(\mathbf{k}) \end{pmatrix}, \quad (25)$$

where

$$\tau(\mathbf{k}) = t_1 \sum_{n=1}^3 e^{i\delta_n \cdot \mathbf{k}} \quad \text{and} \quad \sigma(\mathbf{k}) = M + 2t_2 \sum_{n=1}^3 \sin(\mathbf{g}_n \cdot \mathbf{k}). \quad (26)$$

Equation (24) has two solutions. The energies of those are

$$E_{\pm}(\mathbf{k}) = \pm \sqrt{|\tau(\mathbf{k})|^2 + \sigma^2(\mathbf{k})} \quad (27)$$

The solution with the smaller energy corresponds to the valence band ('-') while the solution with the larger energy corresponds to the conduction band ('+').

The results of this derivation are given in [2]. The exception is: in this work here, the next-nearest neighbor hopping is given by it_2 and purely imaginary, while in that reference it can also have a real part. As discussed earlier, the real part in the next-nearest neighbor hopping only leads to an energy shift of the band structure and is hence set to zero in this work.

2.1.2 Coupling to an external field

The coupling of a tight-binding model to an external field is derived in [89]. Two different gauges are commonly used for coupling to an external field: the velocity gauge and the length gauge. Usually, the choice of the gauge can have a huge influence on the convergence behaviour and the computational time, shown in Ref. [90] using semiconductor Bloch equations.

Using length gauge and dipole approximation, only the diagonal elements of the tight-binding Hamiltonian are affected when coupling to the laser field

$$\langle m, n, \alpha | \hat{H}(t) | m, n, \alpha \rangle = \langle m, n, \alpha | \hat{H}_0 | m, n, \alpha \rangle + \mathbf{E}(t) \cdot \mathbf{r}_{m,n,\alpha}. \quad (28)$$

Here, $\mathbf{r}_{m,n,\alpha}$ is the position of the atom in unit cell (m, n) at sublattice site α and $\mathbf{E}(t)$ the external electric field.

A different gauge, known as the Peierls substitution [91], is gauge invariant to the length gauge, as shown for the SSH model explicitly in Ref. [21]. In this gauge, the hopping elements of the time-dependent Hamiltonian $\hat{H}(t)$ gain a phase factor compared to the time-independent Hamiltonian \hat{H}_0

$$\langle m', n', \alpha' | \hat{H}(t) | m, n, \alpha \rangle = e^{-i(\mathbf{r}_{m',n',\alpha'} - \mathbf{r}_{m,n,\alpha}) \cdot \mathbf{A}(t)} \langle m', n', \alpha' | \hat{H}_0 | m, n, \alpha \rangle. \quad (29)$$

Here, $\mathbf{A}(t)$ is the vector potential ($\mathbf{E}(t) = -\partial_t \mathbf{A}(t)$). Note that only the shifts between the sites are needed. For non-vanishing hopping elements, possible shifts are determined by the vectors $\boldsymbol{\delta}_i$ and \mathbf{g}_i ($i = 1, 2, 3$), eqs. (17) and (18). In our publications, we refer to this gauge, eq. (29), as velocity gauge but it is different from the commonly known velocity gauge for the general Schrödinger equation (without tight-binding approximation).

To solve the time-dependent Schrödinger equation (TDSE)

$$i \frac{\partial}{\partial t} |\mathbf{k}, t\rangle = \hat{H}_t |\mathbf{k}, t\rangle, \quad (30)$$

a Bloch ansatz similar to eq. (16) can be made

$$|\mathbf{k}, t\rangle = \frac{1}{\sqrt{M'N'}} \sum_{m=1}^{M'} \sum_{n=1}^{N'} e^{i\mathbf{k} \cdot (m\mathbf{g}_3 + n\mathbf{g}_1)} |m, n\rangle \otimes \left(C^A(\mathbf{k}, t) |A\rangle + C^B(\mathbf{k}, t) e^{i\mathbf{k} \cdot \boldsymbol{\delta}_3} |B\rangle \right). \quad (31)$$

With a similar calculation as performed for the time-independent case, one ends up with a TDSE

that reads

$$i\dot{\mathbf{C}}(\mathbf{k}, t) = \mathbf{H}(\mathbf{k}(t))\mathbf{C}(\mathbf{k}, t). \quad (32)$$

where $\mathbf{C}(\mathbf{k}, t) = \begin{pmatrix} C^A(\mathbf{k}, t) \\ C^B(\mathbf{k}, t) \end{pmatrix}$. The time-dependent Hamiltonian $\mathbf{H}(\mathbf{k}(t))$ is the same as the time-independent Hamiltonian (eq. (25)) but evaluated at $\mathbf{k}(t) = \mathbf{k} + \mathbf{A}(t)$.

Initially, the system is assumed to be in its ground state, hence the valence band is completely occupied while the conduction band is unoccupied. This leads to the initial condition $\mathbf{C}(\mathbf{k}, t = 0) = \mathbf{C}_-(\mathbf{k})$ before the laser pulse is turned on, where $\mathbf{C}_-(\mathbf{k})$ is the solution of the TISE (24) with the smaller energy. The propagation has to be repeated for sufficiently many values of \mathbf{k} within the first BZ to assure convergence of the calculated high-harmonic spectra later on.

The velocity is used as observable to obtain the high-harmonic spectra. The velocity operator is given by the gradient of the Hamiltonian with respect to \mathbf{k} . The velocity follows as [2]

$$\mathbf{v}(\mathbf{k}, t) = \mathbf{C}^\dagger(\mathbf{k}, t) [\nabla_{\mathbf{k}} \mathbf{H}(\mathbf{k}(t))] \mathbf{C}(\mathbf{k}, t), \quad (33)$$

with the velocity vector $\mathbf{v}(\mathbf{k}, t) = (v_x(\mathbf{k}, t), v_y(\mathbf{k}, t))^\top$.

The total current is given by the integration of the current over the first BZ [2]

$$\mathbf{v}(t) = \frac{V_{\text{cell}}}{(2\pi)^2} \int_{\text{BZ}} d^2k \mathbf{v}(\mathbf{k}, t). \quad (34)$$

The prefactor will be dropped, as the absolute values are not important for the discussion and comparison of harmonic spectra later on, Sec. 2.3.

2.2 Methods for finite Haldanite systems

The general Hamiltonian of the finite system was introduced previously in eq. (12). This Hamiltonian matrix has the same dimension as the number of atoms N in the system. This is fundamentally different from the bulk system in which the Hamiltonian is always a 2×2 -matrix, which however, has to be solved for several \mathbf{k} -values in order to achieve converged spectra. In the finite system, only one $N \times N$ -matrix for the Hamiltonian has to be considered. Consequently, the time-independent Schrödinger-equation

$$\hat{H}_0 |\psi_i\rangle = E_i |\psi_i\rangle \quad (35)$$

has N solution ($i = 0, 1, 2, \dots, N-1$). The energies are numbered such that they are in ascending order: $E_0 \leq E_1 \leq E_2 \leq \dots \leq E_{N-1}$, their respective states are occupied according to the Pauli principle. Interactions between electrons are neglected.

In the previous section, the tight-binding orbitals of the periodic Haldanite system were given by $|m, n, \alpha\rangle$, where m and n determine the unit cell and $\alpha = A, B$ the sublattice site within the unit cell. For the finite system with an arbitrary shape, it is much more convenient to numerate all the sites by one index $m = 1, 2, 3, \dots, N$ and denote their respective orbitals as $|m\rangle$, as it was done in eq. (12).

2.2.1 Coupling to an external field

A laser field is now coupled to the system. The external field can be put into an operator $\hat{V}(t)$ in a way that the time-dependent Hamiltonian reads $\hat{H}(t) = \hat{H}_0 + \hat{V}(t)$. Hence, the TDSE becomes

$$i\partial_t |\Psi(t)\rangle = \hat{H}(t) |\Psi(t)\rangle = \left(\hat{H}_0 + \hat{V}(t) \right) |\Psi(t)\rangle. \quad (36)$$

The explicit form of the potential $\hat{V}(t)$ will be determined later.

The time-dependent wavefunction $|\Psi(t)\rangle$ can be expanded in the basis of the unperturbed system [1]

$$|\Psi(t)\rangle = \sum_{i=0}^{N-1} c_i(t) e^{-iE_i t} |\psi_i\rangle, \quad (37)$$

where $c_i(t)$ are complex amplitudes of the corresponding eigenfunction $|\psi_i\rangle$ of the unperturbed Hamiltonian \hat{H}_0 . Plugging this ansatz into equation (36) gives

$$\begin{aligned} i \sum_{i=0}^{N-1} (\dot{c}_i(t) - iE_i c_i(t)) |\psi_i\rangle e^{-iE_i t} &= \sum_{i=0}^{N-1} c_i(t) e^{-iE_i t} \left(E_i + \hat{V}(t) \right) |\psi_i\rangle \\ \Leftrightarrow \sum_{i=0}^{N-1} \dot{c}_i(t) e^{-iE_i t} |\psi_i\rangle &= -i \sum_{i=0}^{N-1} c_i(t) e^{-iE_i t} \hat{V}(t) |\psi_i\rangle, \end{aligned} \quad (38)$$

where the TISE (35) was used. Multiplying with $\langle \psi_j | e^{iE_j t}$ from the left of this equation yields

$$\dot{c}_j(t) = -i \sum_{i=0}^{N-1} c_i(t) e^{-i(E_i - E_j)t} \langle \psi_j | \hat{V}(t) |\psi_i\rangle \quad (39)$$

because the orbitals are orthonormal $\langle \psi_j | \psi_i \rangle = \delta_{j,i}$.

Equation (38) can be written in a compact form: by defining

$$V_{j,i}(t) := e^{-i(E_i - E_j)t} \langle \psi_j | \hat{V}(t) |\psi_i\rangle, \quad (40)$$

one gets [1]

$$\dot{c}_j(t) = -i \sum_{i=0}^{N-1} V_{j,i}(t) c_i(t). \quad (41)$$

Further, this becomes

$$\dot{\mathbf{c}}(t) = -i \mathbf{V}(t) \mathbf{c}(t), \quad (42)$$

by using a vector that contains all coefficients $\mathbf{c}(t) = (c_1(t), c_2(t), c_3(t), \dots, c_N(t))^T$ and defining a matrix $\mathbf{V}(t)$ out of the elements $V_{j,i}(t)$.

The considered systems in this work are assumed to contain several valence electrons. Hence, the TDSE (36) has to be solved for different single electron wave functions $|\Psi^k(t)\rangle$, with $k = 0, 1, 2, \dots, K - 1$. Here, K is the total number of electrons that are propagated. Therefore, the coefficients $c_i^k(t)$ acquire an upper index k that indicates which electron is considered. All coefficients can then be put in a matrix of the form $\mathbf{C}(t) = (\mathbf{c}^0(t), \mathbf{c}^1(t), \mathbf{c}^2(t), \dots, \mathbf{c}^{K-1}(t))$, which

leads to

$$\dot{\mathbf{C}}(t) = -i\mathbf{V}(t)\mathbf{C}(t). \quad (43)$$

It is assumed that each atom has one active valence electron. Considering spin-degeneracy, half of all the states (the ones with the lowest energy) are occupied initially. This means $K = N/2$ and that the initial conditions are given by $|\Psi^k(t=0)\rangle = |\psi_k\rangle$ ($k = 0, 1, 2, \dots, N/2 - 1$). Here, $|\psi_k\rangle$ is the k th eigenstate of the unperturbed system (35). This implies further: $c_i^k(t=0) = \delta_{k,i}$.

2.2.2 Numerical implementation

The choice of the gauge was discussed in Sec. 2.1.2. To keep the code general so that periodic systems (like periodic nanoribbons) can be considered, the Peierls substitution is used to couple the system to an external field.

While equation (43) might look simple, solving it for the Haldanite case using Peierls substitution is not. In order to make this equation manageable in the code, certain steps need to be done.

The modification of the entries in the Hamiltonian when coupling to an external field using Peierls substitution is identical to eq. (29) used for the derivation of the bulk. With the notation of the finite system, this reads

$$\langle m' | \hat{H}(t) | m \rangle = \langle m' | \hat{H}_0 | m \rangle e^{-i(\mathbf{r}_{m'} - \mathbf{r}_m) \cdot \mathbf{A}(t)}. \quad (44)$$

The orbital $|m\rangle$ is the basis function of an electron strongly localized around the atom at position \mathbf{r}_m . However, for the differential equation, the time-dependent part is needed

$$\hat{V}(t) = \hat{H}(t) - \hat{H}_0. \quad (45)$$

The elements of the matrix $\hat{V}(t)$ are

$$\begin{aligned} \langle m' | \hat{V}(t) | m \rangle &= \langle m' | \hat{H}(t) | m \rangle - \langle m' | \hat{H}_0 | m \rangle = \langle m' | \hat{H}_0 | m \rangle e^{-i(\mathbf{r}_{m'} - \mathbf{r}_m) \cdot \mathbf{A}(t)} - \langle m' | \hat{H}_0 | m \rangle \\ &= \langle m' | \hat{H}_0 | m \rangle \left(e^{-i(\mathbf{r}_{m'} - \mathbf{r}_m) \cdot \mathbf{A}(t)} - 1 \right). \end{aligned} \quad (46)$$

The operator $\hat{V}(t)$ can be written in the following way in order to simulate the system more efficiently

$$\begin{aligned} \hat{V}(t) &= \sum_{m,m'=1}^N |m'\rangle \langle m' | \hat{V}(t) | m \rangle \langle m| = \sum_{m,m'=1}^N |m'\rangle \langle m' | \hat{H}_0 | m \rangle \langle m| \left(e^{-i(\mathbf{r}_{m'} - \mathbf{r}_m) \cdot \mathbf{A}(t)} - 1 \right) \\ &= \sum_{\Delta\mathbf{r}} \left(e^{-i\Delta\mathbf{r} \cdot \mathbf{A}(t)} - 1 \right) \sum_{m,m'=\Delta\mathbf{r}} |m'\rangle \langle m' | \hat{H}_0 | m \rangle \langle m|. \end{aligned} \quad (47)$$

Here, the notation $\sum_{m,m'=1}^N = \sum_{m=1}^N \sum_{m'=1}^N$ is used. Further, the sum $\sum_{\Delta\mathbf{r}}$ runs over all the possible shifts (vectors) between two atoms $\Delta\mathbf{r} = \mathbf{r}_{m'} - \mathbf{r}_m$ for which the hopping element is non-vanishing. Those possible vectors are given in eqs. (17) and (18) (and the negative of those vectors). The sum $\sum_{m,m'=\Delta\mathbf{r}}$ only runs over those atoms m and m' that are separated by a

given vector $\Delta\mathbf{r} = \mathbf{r}_{m'} - \mathbf{r}_m$. In practice, this splits up the Hamiltonian matrix into several matrices, which only include hopping elements between atoms that are separated by the same vector. Hence, the potential can be written as

$$\hat{V}(t) = \sum_{\Delta\mathbf{r}} f_{\Delta\mathbf{r}}(t) \hat{A}_{\Delta\mathbf{r}} \quad (48)$$

with $f_{\Delta\mathbf{r}}(t) = e^{-i\Delta\mathbf{r} \cdot \mathbf{A}(t)} - 1$ and $\hat{A}_{\Delta\mathbf{r}} = \sum_{m,m'=\Delta\mathbf{r}} |m'\rangle \langle m'| \hat{H}_0 |m\rangle \langle m|$. Note that the matrix $\hat{A}_{\Delta\mathbf{r}}$ is time-independent.

The following relations are fulfilled

$$f_{-\Delta\mathbf{r}}(t) = f_{\Delta\mathbf{r}}^*(t), \quad (49)$$

$$\begin{aligned} \hat{A}_{-\Delta\mathbf{r}} &= \hat{A}_{-(\mathbf{r}_{m'} - \mathbf{r}_m)} = \sum_{m,m'=-\Delta\mathbf{r}} |m'\rangle \langle m'| \hat{H}_0 |m\rangle \langle m| \\ &= \sum_{m,m'=\Delta\mathbf{r}} |m\rangle \langle m| \hat{H}_0 |m'\rangle \langle m'| = \sum_{m,m'=\Delta\mathbf{r}} |m'\rangle \langle m'| \hat{H}_0^\dagger |m\rangle \langle m| = \hat{A}_{\Delta\mathbf{r}}^\dagger. \end{aligned} \quad (50)$$

The last relation, eq. (50), holds because $-\Delta\mathbf{r}$ refers to hopping in the opposite direction compared to $\Delta\mathbf{r}$. Due to the hermitian Hamiltonian, hopping in the opposite direction is given by the complex conjugate of that hopping element.

For the time-propagation, the elements $\langle \psi_i | \hat{V}(t) | \psi_j \rangle$ are needed (39), where the states $|\psi_i\rangle$ and $|\psi_j\rangle$ are eigenstates of \hat{H}_0 . Using eq. (48), one gets

$$\langle \psi_i | \hat{V}(t) | \psi_j \rangle = \sum_{\Delta\mathbf{r}} f_{\Delta\mathbf{r}}(t) \langle \psi_i | \hat{A}_{\Delta\mathbf{r}} | \psi_j \rangle. \quad (51)$$

If hopping between atoms m' and m is possible and their distance is given by $\Delta\mathbf{r} = \mathbf{r}(m') - \mathbf{r}(m)$, then also the hopping in the opposite direction is possible with the distance $-\Delta\mathbf{r}$. Hence, instead of summing over all possible $\Delta\mathbf{r}$, one can also sum over all $\Delta\mathbf{r}$ excluding $-\Delta\mathbf{r}$. It follows

$$\langle \psi_i | \hat{V}(t) | \psi_j \rangle = \sum_{\Delta\mathbf{r} \neq -\Delta\mathbf{r}} f_{\Delta\mathbf{r}}(t) \langle \psi_i | \hat{A}_{\Delta\mathbf{r}} | \psi_j \rangle + f_{-\Delta\mathbf{r}}(t) \langle \psi_i | \hat{A}_{-\Delta\mathbf{r}} | \psi_j \rangle. \quad (52)$$

Using equations (49) and (50), one gets

$$\begin{aligned} \langle \psi_i | \hat{V}(t) | \psi_j \rangle &= \sum_{\Delta\mathbf{r} \neq -\Delta\mathbf{r}} f_{\Delta\mathbf{r}}(t) \langle \psi_i | \hat{A}_{\Delta\mathbf{r}} | \psi_j \rangle + f_{\Delta\mathbf{r}}^*(t) \langle \psi_i | \hat{A}_{\Delta\mathbf{r}}^\dagger | \psi_j \rangle \\ &= \sum_{\Delta\mathbf{r} \neq -\Delta\mathbf{r}} \underbrace{f_{\Delta\mathbf{r}}(t) \langle \psi_i | \hat{A}_{\Delta\mathbf{r}} | \psi_j \rangle}_{\text{I}} + \underbrace{f_{\Delta\mathbf{r}}^*(t) \left(\langle \psi_j | \hat{A}_{\Delta\mathbf{r}} | \psi_i \rangle \right)^*}_{\text{II}}. \end{aligned} \quad (53)$$

Note that the second term (II) is not the complex conjugate of the first one (I) because $\hat{A}_{\Delta\mathbf{r}}$ is not hermitian. The operators $\hat{A}_{\Delta\mathbf{r}}$ are time-independent. Hence, the values $\langle \psi_i | \hat{A}_{\Delta\mathbf{r}} | \psi_j \rangle$ need to be calculated only once, at the beginning of the propagation. The alternative, calculating $\langle \psi_i | \hat{V}(t) | \psi_j \rangle$ at each time-step, would increase the simulation time dramatically. However, it was checked explicitly, that the simulations from both methods give the same results.

2.2.3 Calculation of the current

Calculation of the total current

The current operator is given by [92]

$$\hat{\mathbf{j}}(t) = -i \sum_{m,m'=1}^N (\mathbf{r}_{m'} - \mathbf{r}_m) |m'\rangle \langle m'| \hat{H}(t) |m\rangle \langle m|. \quad (54)$$

Inserting the Peierls substitution, eq. (44), one gets

$$\begin{aligned} \hat{\mathbf{j}}(t) &= -i \sum_{m,m'=1}^N (\mathbf{r}_{m'} - \mathbf{r}_m) |m'\rangle \langle m'| \hat{H}_0 |m\rangle \langle m| e^{-i(\mathbf{r}_{m'} - \mathbf{r}_m) \cdot \mathbf{A}(t)} \\ &= -i \sum_{\Delta \mathbf{r}} \Delta \mathbf{r} e^{-i\Delta \mathbf{r} \cdot \mathbf{A}(t)} \sum_{m,m'=\Delta \mathbf{r}} |m'\rangle \langle m'| \hat{H}_0 |m\rangle \langle m| = -i \sum_{\Delta \mathbf{r}} \Delta \mathbf{r} (f_{\Delta \mathbf{r}}(t) + 1) \hat{A}_{\Delta \mathbf{r}}. \end{aligned} \quad (55)$$

In the last two step, calculations similar to the ones in eqs. (47) and (48) were performed.

The total current is obtained by summing over the currents originating from all the states $|\Psi^k(t)\rangle$ that are propagated

$$\mathbf{J}(t) = \sum_{k=0}^{K-1} \langle \Psi^k(t) | \hat{\mathbf{j}}(t) | \Psi^k(t) \rangle. \quad (56)$$

The expansion of $|\Psi^k(t)\rangle$ in the eigenstates $|\psi_i\rangle$ of the time-independent Hamiltonian \hat{H}_0 is given in eq. (37) by

$$|\Psi^k(t)\rangle = \sum_i c_i^k(t) e^{-iE_i t} |\psi_i\rangle. \quad (57)$$

This expansion can be inserted into eq. (56). By using eq. (55), this results in

$$\begin{aligned} \mathbf{J}(t) &= \sum_{i,j=0}^{N-1} e^{-i(E_j - E_i)t} \left[\sum_{k=0}^{K-1} \left(c_i^k(t) \right)^* c_j^k(t) \right] \langle \psi_i | \hat{\mathbf{j}}(t) | \psi_j \rangle \\ &= -i \sum_{i,j=0}^{N-1} e^{-i(E_j - E_i)t} \left[\sum_{k=0}^{K-1} \left(c_i^k(t) \right)^* c_j^k(t) \right] \sum_{\Delta \mathbf{r}} \Delta \mathbf{r} (f_{\Delta \mathbf{r}}(t) + 1) \langle \psi_i | \hat{A}_{\Delta \mathbf{r}} | \psi_j \rangle. \end{aligned} \quad (58)$$

The last sum can further be written down similar to eq. (53). The result is

$$\begin{aligned} &\sum_{\Delta \mathbf{r}} \Delta \mathbf{r} (f_{\Delta \mathbf{r}}(t) + 1) \langle \psi_i | \hat{A}_{\Delta \mathbf{r}} | \psi_j \rangle \\ &= \sum_{\Delta \mathbf{r} \neq -\Delta \mathbf{r}} \Delta \mathbf{r} \left[(f_{\Delta \mathbf{r}}(t) + 1) \langle \psi_i | \hat{A}_{\Delta \mathbf{r}} | \psi_j \rangle - (f_{-\Delta \mathbf{r}}^*(t) + 1) \left(\langle \psi_j | \hat{A}_{\Delta \mathbf{r}} | \psi_i \rangle \right)^* \right]. \end{aligned} \quad (59)$$

The matrix elements $\langle \psi_i | \hat{A}_{\Delta \mathbf{r}} | \psi_j \rangle$ only need to be calculated once and can even be reused from the time propagation.

Calculation of the current between two sites

From eq. (54), one can define the operator

$$\begin{aligned}\hat{\mathbf{j}}_{m',m}(t) &= |m'\rangle \langle m'| \hat{\mathbf{j}}(t) |m\rangle \langle m| + |m\rangle \langle m| \hat{\mathbf{j}}(t) |m'\rangle \langle m'| \\ &= -i(\mathbf{r}_{m'} - \mathbf{r}_m) \left(|m'\rangle \langle m'| \hat{H}(t) |m\rangle \langle m| - |m\rangle \langle m| \hat{H}(t) |m'\rangle \langle m'| \right).\end{aligned}\quad (60)$$

The current that flows between sites m' and m is given by

$$\mathbf{J}_{m',m}(t) = \sum_{k=0}^{K-1} \langle \Psi^k(t) | \hat{\mathbf{j}}_{m',m}(t) | \Psi^k(t) \rangle. \quad (61)$$

Those individual currents can be used to calculate spatially resolved spectra. The total current can be calculated by summing up all individual currents. However, it is computationally more efficient to use eq. (58) instead.

2.3 Calculation of the emission spectrum

A laser pulse of the form

$$\mathbf{A}(t) = A_0 \sin^2 \left(\frac{\omega_0 t}{2 n_{\text{cyc}}} \right) \sin(\omega_0 t) \mathbf{e} \quad (62)$$

is used in all relevant publications of this work. The vector potential is set to zero for $t < 0$ and for $t > 2\pi n_{\text{cyc}}/\omega_0$. Here, A_0 is the amplitude of the vector potential, ω_0 is the angular frequency of the driving pulse, and n_{cyc} is the number of cycles in the pulse. The pulse is linearly polarized in the direction of the normalized vector \mathbf{e} . The laser parameters differ in the different publications of this thesis.

For calculating the harmonic spectra, either the dipole moment, velocity, or acceleration has to be Fourier-transformed [93–95]. For sufficiently long pulses, the only difference is a prefactor, given by $1/\omega^2$ or $1/\omega^4$ for the velocity and the dipole compared to the acceleration, respectively. In the publications, we either use the current, which turns out to be proportional to the expectation value of a properly defined velocity operator [2], or its first derivative, which is proportional to the acceleration. Using the derivative of the current has the advantage that a constant offset in the current will vanish after performing the derivative. Hence, the derivative of the current usually shows a cleaner Fourier transformation without DC component.

In the rest of this section, the derivative of the current $\dot{\mathbf{J}}(t)$ is used, but it can always be replaced by the velocity $\mathbf{v}(t)$ or the current $\mathbf{J}(t)$ itself. The difference in the spectra will only be a simple frequency-dependent prefactor. As only relative values of the harmonic intensities are compared, those prefactors are not important for this study.

The system is two-dimensional, hence, the current also has two dimensions. Instead of dividing the current into x - and y -components, it is divided into the components parallel ($J_{\parallel}(t)$) and perpendicular ($J_{\perp}(t)$) to the incoming field. With the Fourier transformation, the following

quantity is defined [5]

$$P_{\parallel,\perp}(\omega) = |P_{\parallel,\perp}(\omega)| e^{i\varphi_{\parallel,\perp}(\omega)} = \int_{-\infty}^{+\infty} \dot{J}_{\parallel,\perp}(t) e^{-i\omega t} dt. \quad (63)$$

The emission spectrum is proportional to $|P_{\parallel,\perp}(\omega)|^2$ and the phase difference between both components

$$\Delta\varphi(\omega) = \varphi_{\parallel}(\omega) - \varphi_{\perp}(\omega) \quad (64)$$

indicates the polarization of the emitted photons. For $\Delta\varphi(\omega) = 0$ or $\Delta\varphi(\omega) = \pm\pi$, the emitted light (with frequency ω) is linearly polarized while for other values of $\Delta\varphi(\omega)$, the emitted photons are elliptically polarized in general (circular if $\Delta\varphi(\omega) = \pm\pi/2$ and in addition $|P_{\parallel}(\omega)| = |P_{\perp}(\omega)|$). Further, the sign of $\Delta\varphi(\omega)$ indicates the helicity, i.e., the handedness, of the emitted light.

3 Results

This chapter briefly summarizes the results of the published papers during my Ph.D. studies. In addition, the papers are set in context to each other. The papers themselves are integrated into chapter 5.

3.1 Paper: Intense-laser-driven electron dynamics and high-order harmonic generation in solids including topological effects

This publication [2] can be found in section 5.1.2.

This paper is a rather analytical work. For the bulk of a solid with two sites within the unit cell, an analytical equation of the electron velocity for the bulk system is derived. With this equation, the emission spectra of any bulk system (with two sites within its unit cell) can be calculated. Besides the tight-binding approximation, the only assumption is that the depletion of the valence band is negligible, which appears to be a good approximation. This is similar to the results of the famous Lewenstein et al. paper on HHG in the gas phase [39], which shows that the depletion of the ground state can be neglected for the considered process as well. Further, the obtained equation for the velocity from interband transitions has the same structure as the equation derived in the paper by Lewenstein et al. for gas targets [39]. The equation derived in our publication is a full quantum mechanical alternative to the widely used semiclassical equation (9).

Further, in publication [2], the derived equations are verified for two different materials: the bulk of the SSH chain and the bulk of Haldanite. For the bulk of the SSH model, the results are in agreement with the results from [19–21], even though those papers consider finite SSH chains. For the Haldanite case, a helicity change similar to the one reported in Ref. [17] can be captured by our formalism.

3.2 Paper: High-order harmonic generation in hexagonal nanoribbons

This publication [3] can be found in section 5.1.3

In the publication [3], graphene-like nanoribbons are investigated. Hence, no complex next-nearest neighbor hopping is included. The main purpose of this work is the verification of the tight-binding approximation used in further works. The publication compares the tight-binding results to simulations without the tight-binding approximation, published by colleagues in Ref. [80]. The simulations without tight-binding approximation are much more accurate than the simulations with that approximation. However, the tight-binding method is three orders of magnitude faster than the simulations from Ref. [80]. The simulations in that paper and in our paper were performed on similar machines, allowing us to maximize the comparability.

Both papers [3, 80] study the high-harmonic spectra in nanoribbons with zig-zag and armchair edges as function of the alternating on-site potential M . The results for both methods agree well with each other. However, the chains are chosen to be very small. The ribbon with armchair edges contains only $N_{\text{hex}} = 4$ hexagons and the one with zig-zag edges $N_{\text{hex}} = 6$

hexagons (see Fig. 6). This restriction comes from the simulations without tight-binding approximation, for which the simulation time is too high for longer chains. The simulation time for the tight-binding approximation is much faster, and bigger systems can be considered in future works. The results from paper [3] show that the tight-binding approximation captures the main features of the harmonic spectrum and can hence be used for further studies.

One drawback is that the tight-binding approximation here only captures a finite number of bands. Therefore, the results from simulations without the tight-binding approximation also show harmonics above the cutoff found in the tight-binding simulations. However, the most interesting features in the spectra are observed for low-order harmonics, so for our studies, this restriction of the tight-binding model is acceptable. Though the papers [3] and [80] were published later than the first publication of this Ph.D. study [1], the results were internally known much earlier within our work-group to assure the tight-binding approximation was valid for this system.

Additionally, in Fig. 7 of Ref. [3] (Sec. 5.1.3), a drop for low-order harmonics is observed for a longer ribbon ($N_{\text{hex}} = 15$) with zig-zag edges and without on-site potential, i.e., $M = 0$. The drop indicates a band gap between the highest occupied and lowest unoccupied state, similar to the findings in [19]. The ribbon with zig-zag edges has four bands without a band gap between the highest occupied and lowest unoccupied band. However, for $M = 0$, transitions are only allowed between certain bands [73, 74], creating an effective band gap between occupied and unoccupied bands, which explains the drop in the harmonic yield. The selection rule is due to the symmetry of the system, which is destroyed when a finite on-site potential is included. Hence, for a non-zero on-site potential M , transitions between all bands are possible. Indeed, for a small on-site potential of $M = 0.001$, the drop in the harmonic yield is filled up. Hence, this tight-binding model is able to capture the accepted selection rules in graphene nanoribbons.

3.3 Changing the helicity of the emitted photons

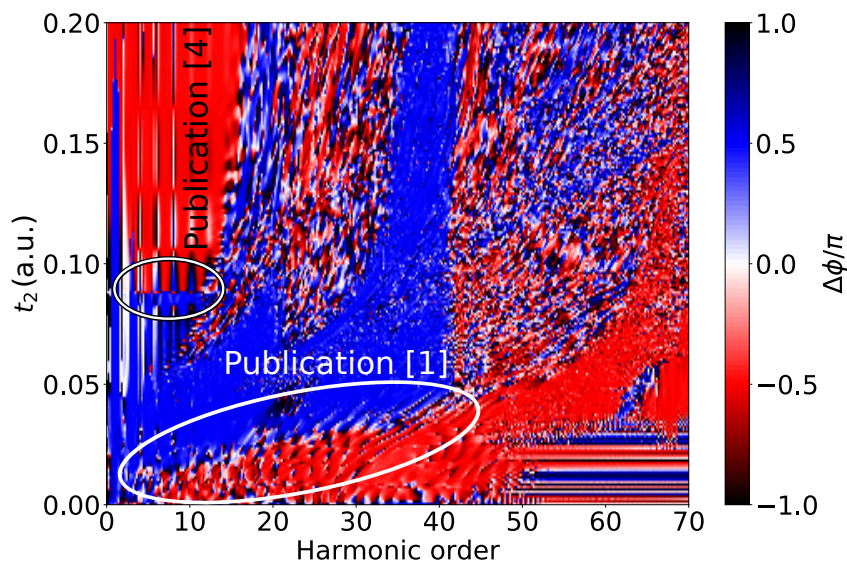


Figure 8: Phase difference of the Fourier components $\Delta\phi$ indicating the helicity of the emitted light from a finite ($N_{\text{hex}} = 30$) nanoribbon with $M = 0.01$. The two different effects that were observed in publications [1] and [4] are indicated. Adapted from publication [1].

One major finding in the Haldanite bulk is that the helicity of the emitted photon spectrum encodes the topological phase of Haldanite [17]. For finite Haldanite nanoribbons, we found that actually two different mechanisms can change the helicity. Both mechanisms are somewhat different from the one observed in the bulk.

In Fig. 8, the phase difference $\Delta\varphi(\omega)$, introduced in eq. (64), is shown. This plot indicates the helicity of the emitted photons: bluish colors stand for one helicity and reddish colors for the opposite helicity. The effect that leads to the helicity flip discussed in publication [4] is due to the edge states and will be discussed in section 3.3.1. The second effect originates from changes in the states and is reported in publication [1]. This one will be discussed in section 3.3.2. Both of these effects are highlighted in Fig. 8.

3.3.1 Paper: Edge-state influence on high-order harmonic generation in topological nanoribbons

This publication [4] can be found in section 5.1.4.

In this paper, nanoribbons with zig-zag edges of size $N_{\text{hex}} = 30$ are considered. In the energy gap between the occupied and unoccupied states, two edge states appear when the amplitude of the next-nearest neighbor hopping t_2 is large enough. Those edge states have similar, but not identical energies. In fact, the energies of the edge states cross several times as a function of t_2 (for $M = 0$) or an avoided crossing can be observed ($M \neq 0$). In the high-harmonic spectrum, the helicity of certain low-order harmonics changes when a crossing or an avoided crossing takes place. The helicity flip is highlighted in Fig. 8, labeled by publication [4]. The edge state with a smaller energy is occupied, the other one unoccupied.

This effect is somewhat different than the helicity-flip reported in [17] for the bulk. A topological phase transition requires a band gap to close. In the finite case, the edge states do not exist for $t_2 = 0$. The band gap between the valence and conduction band closes for a certain t_2 , and starts to open again if t_2 is increased further. At least this happens for $M \neq 0$, for $M = 0$ the band gap is already closed for $t_2 = 0$.

When the band gap closes, a topological phase transition is expected. The edge states appear in the middle of the band gap after it reopens. However, the crossings or avoided crossings of the edge state energies are observed for much larger t_2 than the point of the band gap closure. Hence, for this finite system, a helicity flip does not occur when the band gap closes (as observed in the bulk [17]), but it is rather related to the energy gap between the edge states.

3.3.2 Paper: Helicity flip of high-order harmonic photons in Haldane nanoribbons

This publication [1] can be found in section 5.1.1.

In the previous section, it was reported that the helicity changes for low-order harmonics when the system parameter t_2 is varied and edge states cross or have an avoided crossing. An entirely different process that also has an influence on the helicity was reported in our paper [1]. There, the helicity can change for a fixed value of t_2 : photons with an energy below a certain value have one helicity and photons with higher energies will have the opposite helicity. In addition, the energy at which this helicity flip occurs shifts towards higher energies as t_2 increases (compare Fig. 8). For this investigation, nanoribbons of size $N_{\text{hex}} = 30$ with and

without periodic boundary conditions in the direction along the ribbon (along the x -direction of Fig. 6b) are investigated. Interestingly, the effect can be observed for both a ribbon with a periodic boundary condition and without it.

The band structure and the eigenstates of the bulk system are able to explain this effect. This nanoribbon has four bands, the lowest two are occupied. It appears that band two (highest occupied band) and band three (lowest unoccupied band) are the important bands here. Without a complex next-nearest neighbor hopping, i.e., $t_2 = 0$, the periodic part of the Bloch states obey the common node rule: zero nodes for states from the lowest band up to three nodes for states from the highest band. For a non-zero next-nearest neighbor hopping amplitude t_2 , this node rule is only observed around the center of the first BZ (around $k = 0$). At the boundaries of the first BZ, the bands appear to be exchanged because the number of nodes is now different. For example, states from the third band now only have one node instead of two nodes. However, states from the second band have two nodes instead of one. So it appears like the properties of the states from those two bands are exchanged. As mentioned, this exchange only occurs for certain k -values within the first BZ. For those points, an energy difference between band two and band three can be determined. It turns out that the helicity flip occurs for those energies. The intensity of the emitted photons, however, is almost unaffected by this.

The interesting part about this finding is that the helicity flip occurs for a fixed t_2 at a certain energy. In real systems, the parameter t_2 might not be easily changed, still this effect might be observed in such systems. The effect discussed previously, Ref. [4], requires a change of t_2 to be observed. Hence, for a system with fixed t_2 it is impossible to see that effect.

3.4 Paper: Topological edge-state contributions to high-order harmonic generation in finite flakes

This publication [5] can be found in section 5.1.5.

3.4.1 Results from the publication

In this work, Haldanite flakes expanded (almost) equally in both spatial directions, instead of the almost one-dimensional nanoribbons, are investigated. A flake that resembles a hexagon is chosen. The system is sketched in Fig. 9 but its size is varied. The flake shown here has a size of $N = 4$. Zig-zag edges are present along the whole boundary of the material. In the study, we found that for energies above the band gap, the spectra from the bulk and sufficiently big finite flakes are similar. For energies below the band gap, two peaks appear in the finite system that are absent for the bulk. Those peaks shift towards smaller harmonic orders as the size of the flake increases. It was shown that those peaks are due to edge currents. Their velocity is determined by the slope of the edge states in momentum space, eq. (4). The velocity is independent on the size of the flake so the electrons need longer to move along the whole edge for a larger system. Hence, the peaks corresponding to that edge current shift to smaller energies for bigger systems.

The experimental results from Ref. [22], briefly discussed in section 1.3.3, show that the carrier-envelope phase can shift harmonic peaks from the surface states in energy. However, this is a different process that requires two-dimensional surface states instead of the one-dimensional edge states in our Haldanite system. Hence, that effect is unrelated to the shifting peaks observed

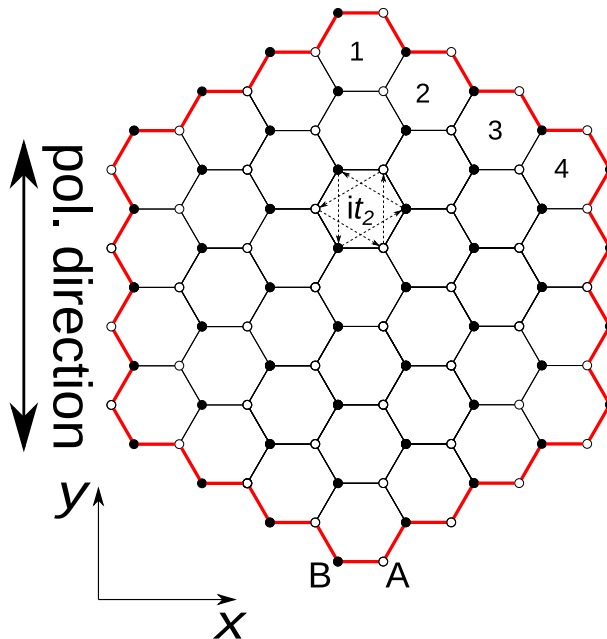


Figure 9: Sketch of a flake used in the simulation. The number N (here $N = 4$) determines the number of small hexagons along one edge of the flake. The polarization direction of the linear polarized laser-field is indicated. From publication [5], copyright © by American Physical Society.

in Haldanite when changing the size of the system.

3.4.2 Edge and bulk contributions

In the simulations, the current between every pair of two sites is calculated, eq. (61). The harmonic spectrum from each of those individual currents is calculated in order to obtain a spatial intensity distribution of the harmonic spectrum. The intensities of the individual spectra at a certain frequency ω_i ($i = a, b, c$) are plotted in Figs. 10a-c for a flake with size $N = 7$. In those figures, two sites with a non-vanishing hopping parameter between them, are connected by colored lines. Brighter colors indicate a higher harmonic yield at frequency ω_i for that individual current compared to darker colors. For better comparison, the individual intensities in Figs. 10a-c are normalized to the maximum for each ω_i . Figure 10d shows the corresponding total harmonic spectrum of that flake. The vertical lines in indicate the frequencies ω_i .

The peak at frequency ω_a is a peak that shifts to smaller energies as the size of the flake increases. The main contribution to this peak originates from the edge, while the contribution from the center of the flake is about 10 orders of magnitude smaller. This finding is important for the results in the paper [5] because this peak originates from an edge current.

The second plot, Fig. 10b, shows the spatial intensity distribution at $\omega_b = 22.0\omega_0$. The main contribution comes from the edge of the flake as well, while the center of this flake does not contribute much to this frequency. However, compared to the previous peak at ω_a , the intensity decreases more gradually towards the center of the flake. The frequency of this peak here is smaller than the band gap $\omega_{\text{band}} \simeq 26.8\omega_0$. Further, note that this frequency is within a plateau that is located between harmonic orders $\simeq 15$ and $\simeq 27$, so ranging roughly from half the band gap energy to the energy of the band gap. A plateau at energies below the band gap is not present in the spectra of the bulk system at all [5]. However, in the finite topological insulator considered here, edge states in between the valence and conduction band are present.

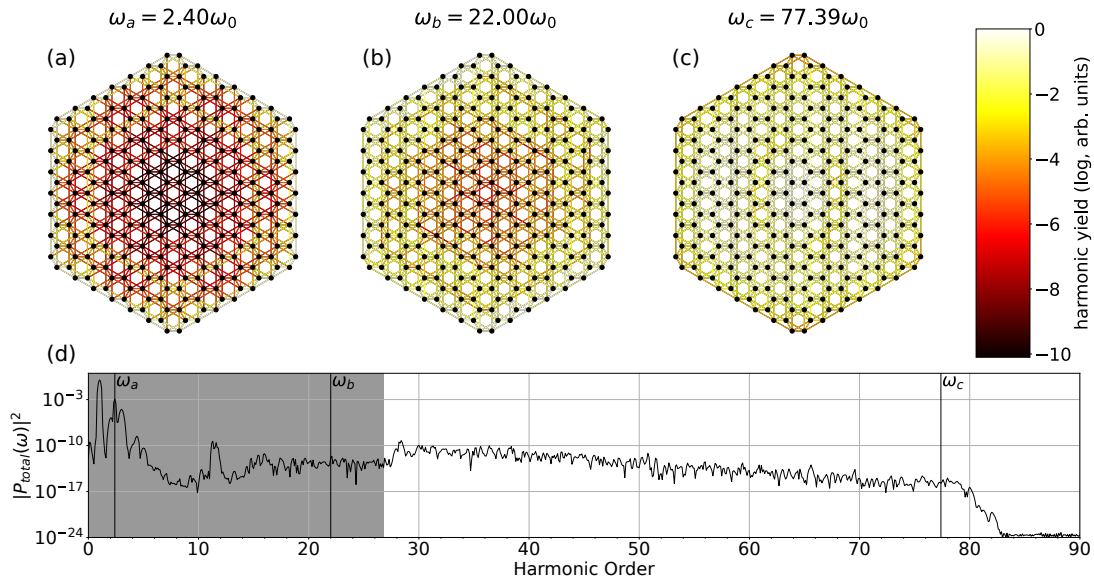


Figure 10: (a-c) Spatial intensity distribution for a fixed harmonic order ω_i ($i = a, b, c$). The maximum intensity of each plot is set to 1. (d) Total harmonic spectrum of the same system as in (a-c). The gray shaded area indicates energies below the band gap of the corresponding bulk system. The vertical lines indicate the frequencies displayed in (a-c).

Transitions from either the valence or conduction band to the edge states would emit photons within this energy range of the below-band-gap plateau. The spatial intensity distribution at this particular harmonic order ω_b indicates that edge states are involved in the generation of this frequency. However, as the intensity towards the center of the flake is larger than for the peak at ω_a (which was identified as a contribution from the edge current) it indicates that other states, which are more delocalized over the flake, are involved too.

The spatial intensity distributions for the other frequencies were also checked. For frequencies below the band gap, the highest intensity is located at the edge of the flake and then decreases towards the center, similar to ω_a and ω_b . For the size-dependent peak at ω_a , the intensity drops faster towards the center of the bulk compared to other frequencies. One exception is the peak at $11.3\omega_0$ where the intensity drops also very fast towards the center. Both these peaks (at ω_a and $11.3\omega_0$) are, as discussed in Ref. [5], due to the edge current. So it is no surprise that the intensity for these peaks decreases faster towards the edge than for other frequencies.

The last frequency considered here is far above the band gap at $\omega_c = 77.39\omega_0$, which is actually close to the cutoff. The intensity is distributed quite equally over the whole flake, Fig. 10c. Note that the same colorbar, with the same maximal and minimal value, is used for all three plots. If one uses separate colorbars, the intensity distribution for ω_c is more structured. This structure originates from the structure of the states involved in the transition process that generates this harmonic order. However, this structure is not so interesting as the intensity fluctuation over the flake is small compared to the other distributions at $\omega_{a,b}$. The results for other frequencies above the band gap of $26.8\omega_0$ were checked and similar results were found: the distribution is more equal over the whole flake than for the harmonics below the band gap. In the results of paper [5], we found that the spectra above the band gap are similar for the bulk and (sufficiently big) finite flakes. Hence, an almost equal intensity distribution over the whole flake could be expected.

4 Summary and Outlook

The work presented in this thesis focuses on HHG in the topological Haldanite system. It was found that the tight-binding approximation is sufficient to simulate those systems. Hence, bigger systems could be considered that would have been almost impossible to solve in reasonable times using methods without the tight-binding approximation.

This work focuses mainly on finite systems and compares to results from the bulk or systems with periodic boundary conditions if needed. The publications show that edge states can have significant influences on the emitted harmonic spectra. In particular, the edge states can be linked to a change in the helicity of the emitted photons. Additionally, edge currents can produce peaks in the spectra that depend on the size of the considered medium.

It was found that the helicity of the emitted photons can be influenced by the complex next-nearest neighbor hopping in two different ways. The first mechanism flips the helicity at a certain photon energy. The energy for which this flip occurs shifts to a larger energy when the amplitude of the complex next-nearest neighbor hopping is increased. The next-nearest neighbor hopping can influence the properties of the states corresponding to a certain band in a way that two states basically exchange their properties. The corresponding transition energies explain the energy at which the helicity changes.

A second possibility to influence the helicity comes from the edge states in the finite system, i.e., a system without periodic boundary conditions. The two edge states appear to cross or show an avoided crossing dependent on the next-nearest neighbor hopping. When a (avoided) crossing occurs, the helicity of the emitted photons changes.

This work underlines the importance of taking edge states into account when simulating HHG in topological insulators. The possibilities to manipulate the spectra of Haldanite with the complex next-nearest neighbor hopping are demonstrated.

One major problem when simulating high-harmonic spectra in solid-state systems is the lack of clean peaks in the plateau region, which are observed in the experiment. One way to resolve this problem is by including interaction with phonons. This is usually done by adding a relaxation or dephasing time manually. However, it would be more accurate if the interaction with the phonons could be implemented directly into the Schrödinger equation. It remains unclear how this would affect the results of this work. Nevertheless, topological edge states and edge currents are robust against perturbations so it can be assumed that the interaction with phonons might not have too much of an influence on the major results presented here.

One other effect that is neglected in this simulations, is electron-electron interactions and considering the different spins the electrons can have. This adds more complexity to the equations and the simulations. It has been shown that the used tight-binding approximation, without interactions between electrons, gives reasonable results. However, studies investigating how those interactions affect the harmonic spectra are needed for comparison.

At the beginning of this Ph.D. study, only a few theoretical papers on HHG in topological insulators existed. Over the years, the number of publications about this topic increased. Nowadays, experimental results focusing on three-dimensional topological insulators exist. It was shown experimentally that the edge states or a topological phase transition can have significant influences on the high-harmonic spectrum. In the future, theoretical studies on HHG in

topological insulators might focus more on three-dimensional systems to predict and explain the effects observed in the experiment. Further, the robust edge currents and their interaction with laser light might be used for developing and advancing new technologies, for example, quantum computing and lightwave electronics.

5 Publications

5.1 Publications relevant for this thesis

5.1.1 Helicity flip of high-order harmonic photons in Haldane nanoribbons

by Hannah Jürß and Dieter Bauer

Physical Review A **102**, 043105 (2020)

DOI: [10.1103/PhysRevA.102.043105](https://doi.org/10.1103/PhysRevA.102.043105)

Reference: [1]



Author Contributions

Hannah Jürß	performing the numerical simulations (deriving the necessary equations for the simulations, writing the code and running it), analyzing the results, writing the manuscript
-------------	-----------------------------------------------------------------------------------------------------------------------------------------------------------------------------

Dieter Bauer	providing critical feedback, supporting the analysis of the results, improving the manuscript, supervision
--------------	------------------------------------------------------------------------------------------------------------

Copyright © of this paper by the American Physical Society.

Helicity flip of high-order harmonic photons in Haldane nanoribbons

Hannah Jürß  and Dieter Bauer 

Institute of Physics, University of Rostock, 18051 Rostock, Germany



(Received 29 June 2020; accepted 9 September 2020; published 13 October 2020)

Recent studies in high-harmonic spectroscopy of condensed matter mainly focused on the bulk of the system under consideration. In this work we investigate the response of thin, hexagonal nanoribbons to an intense laser pulse that is linearly polarized along the ribbon. Such nanoribbons are prime examples of two-dimensional systems that are bulklike in one direction and finite in the other direction. Despite the atomically thin scale in the direction perpendicular to the linearly polarized driving laser field, the emitted harmonics are elliptically polarized if an alternating onsite potential and Haldane hopping is taken into account. For given hoppings, we find a sudden change of the helicity for a certain harmonic order. The origin of this flip is traced back to phase differences between the components of Bloch states.

DOI: [10.1103/PhysRevA.102.043105](https://doi.org/10.1103/PhysRevA.102.043105)

I. INTRODUCTION

High-harmonic generation (HHG) in condensed matter is a relatively new though meanwhile intensely investigated topic in strong-field, attosecond physics [1–7]. The mechanism of HHG in solids is similar to the paradigmatic three-step process known from atomic and molecular-gas-phase HHG [8,9]. In solids, HHG can be used to probe static [10,11] and dynamical [12,13] properties. HHG in amorphous solids [14], magnetic materials [15], and in the presence of an additional static field [16] has been investigated.

Topological insulators [17–19] are an especially interesting kind of condensed matter because they can host edge currents that are immune to scattering thanks to their “topological protection.” The steering of these ballistic edge currents by light may pave the way towards ultrafast electronics [20]. Recently, the study of attosecond processes in topological condensed matter started both theoretically [21–26] and experimentally [20]. Berry phases and curvatures are key to determining the topological phase of a system. Reference [27] shows an experimental way to obtain the Berry phase in solids using HHG.

In two dimensions, graphene is one of the most investigated condensed-matter systems. HHG in graphene [28] and MoS₂ [29,30], a quasi-two-dimensional material, was observed experimentally. Haldane introduced a toy model [31] to make graphene topological by adding (i) an alternating onsite potential to open a band gap, and (ii) a complex next-nearest-neighbor hopping (which has an effect similar to a magnetic field). The system was implemented experimentally using, e.g., cold atoms [32]. HHG in the bulk of “Haldanite” coupled to a laser field was studied recently. It was found that the topological phase of the system determines the helicity of the emitted photons [23] and that the topological phase can be measured through circular dichroism [24]. Besides graphene bulk, the electronic structure and topological properties of graphene nanoribbons were studied as well, see, e.g., [33,34].

The ribbons are finite and hence edge effects become important.

In this work we investigate “zigzag” graphenelike (i.e., with Haldane hopping) nanoribbons in laser fields linearly polarized along the ribbon. The structure and notation is introduced in Fig. 1. The electrons can hop in two spatial dimensions x and y , but as the ribbons are much longer (in x) than wide (in y), the system is almost one dimensional. One unit cell n contains four sublattice sites $\alpha = 1, 2, 3, 4$, as shown in Fig. 1(a). Finite-sized ribbons with periodic boundary conditions in the x direction are investigated in tight-binding approximation. Hence the rightmost unit cell $n = N$ is connected with the leftmost one $n = 1$. In addition to the usual real-valued hopping amplitude between neighboring atoms, an additional, alternating onsite potential and a complex next-nearest-neighbor hopping as in the Haldane model are included. The system is topologically nontrivial for a sufficiently large next-nearest-neighbor hopping.

In the following Sec. II, the tight-binding modeling is introduced, including the coupling to an external field in II B and the properties of the bulk system (with respect to the x direction) in II C. The results for the bulk system are used to explain the features observed in the HHG spectra in Sec. III B. The results are compared to the respective system without periodic boundary conditions in Sec. IV. We conclude in Sec. V. Details on the calculation of the current and its dependence on phase differences between Bloch-state components are given in the Appendix. Atomic units (a.u.; $\hbar = |e| = m_e = 4\pi\epsilon_0 = 1$) are used throughout the paper if not stated otherwise.

II. THEORY

A. System without external field

Hexagonal ribbons with zigzag edges as sketched in Fig. 1 are investigated. The circles in Fig. 1(a) indicate the atomic

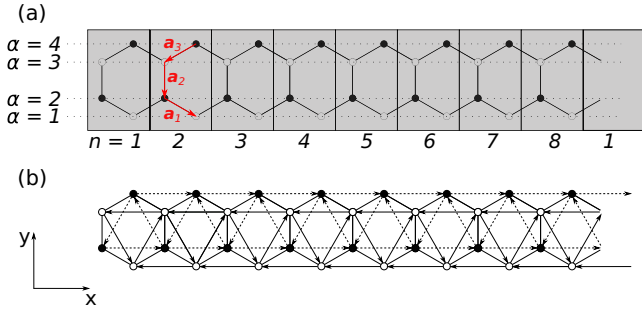


FIG. 1. (a) Sketch of the hexagonal ribbon in zigzag configuration. Sites with onsite potential M ($-M$) are indicated by open (filled) circles. Solid lines show nearest-neighbor hoppings with amplitude $t_1 \in \mathbb{R}$ between adjacent sites. The unit cells are numbered by $n = 1, 2, \dots, N$ (here $N = 8$). The unit cell N is connected with unit cell $n = 1$, implying periodic boundary conditions. The sublattice sites are denoted by α . (b) Hexagonal ribbon with an additional next-nearest-neighbor hopping of strength $t_2 e^{i\phi}$ along the arrows and $t_2 e^{-i\phi}$ in the opposite direction ($t_2 \in \mathbb{R}$).

positions, and the vectors \mathbf{a}_i ($i = 1, 2, 3$),

$$\begin{aligned} \mathbf{a}_1 &= a/2(\sqrt{3}, -1)^\top, \\ \mathbf{a}_2 &= a(0, -1)^\top, \\ \mathbf{a}_3 &= a/2(-\sqrt{3}, -1)^\top, \end{aligned} \quad (1)$$

connect neighboring sites. A tight-binding approach is used. The hopping amplitude between nearest neighbors is given by t_1 and sketched by solid lines in Figs. 1(a) and 1(b). With only nearest-neighbor hopping, this system describes a graphene ribbon. Bulk graphene is a conductor and has a vanishing band gap. If an alternating onsite potential ($\pm M$) is introduced, a band gap between valence and conduction band opens, and the system becomes an insulator. This can be realized by using two different elements instead of carbon only in the case of graphene, for instance, boron and nitrogen in hexagonal boron nitride (h-BN). The sites with an onsite potential of M ($-M$) are denoted as sublattice sites A (B) and are indicated by open (filled) circles in Figs. 1(a) and 1(b).

Haldane proposed a way to make such a system topologically nontrivial [31]. He introduced a complex hopping $t_2 e^{i\phi}$ between next-nearest neighbors. Here $t_2 \in \mathbb{R}$ is the hopping amplitude and ϕ is the phase of the hopping. This hopping is sketched in Fig. 1(b) with arrows. The orientation there denotes a hopping of $t_2 e^{i\phi}$; the hopping in the opposite direction is $t_2 e^{-i\phi}$. The unit cells are numbered by the index $n = 1, 2, 3, \dots, N$. Each cell contains four atomic sites, labeled by $\alpha = 1, 2, 3, 4$. Periodic boundary conditions are used. Hence to the right of hexagon $n = N$ follows the first hexagon $n = 1$ again.

An electronic wave function in tight-binding description has the form

$$|\Psi\rangle = \sum_{n=1}^N \sum_{\alpha=1}^4 g_{n,\alpha} |n, \alpha\rangle, \quad (2)$$

where $|N+1, \alpha\rangle = |1, \alpha\rangle$. The Hamiltonian reads

$$\hat{H}_0 = \hat{H}_{\text{nn}} + \hat{H}_M + \hat{H}_{\text{nnn}}, \quad (3)$$

where \hat{H}_{nn} , \hat{H}_M , and \hat{H}_{nnn} are the Hamiltonians describing the nearest-neighbor hopping, the onsite potential, and the next-nearest-neighbor hopping, respectively. The nearest-neighbor part reads

$$\begin{aligned} \hat{H}_{\text{nn}} = t_1 \sum_{n=1}^N \left(\left[\sum_{\alpha=1}^3 |n, \alpha\rangle \langle n, \alpha+1| \right] + |n+1, 3\rangle \langle n, 4| \right. \\ \left. + |n+1, 2\rangle \langle n, 1| \right) + \text{H.c.}, \end{aligned} \quad (4)$$

the onsite part reads

$$\hat{H}_M = M \sum_{n=1}^N \sum_{\alpha=1}^4 (-1)^{\alpha+1} |n, \alpha\rangle \langle n, \alpha|, \quad (5)$$

and the next-nearest-neighbor Hamiltonian is

$$\begin{aligned} \hat{H}_{\text{nnn}} = t_2 \sum_{n=1}^N \left(e^{i\phi} [|n, 2\rangle \langle n, 4| + |n, 1\rangle \langle n, 3| \right. \\ \left. + |n+1, 3\rangle \langle n, 1| + |n, 4\rangle \langle n+1, 2| \right] \\ \left. + \sum_{\alpha=1}^4 \exp\{(-1)^\alpha i\phi\} |n+1, \alpha\rangle \langle n, \alpha| \right) + \text{H.c.} \end{aligned} \quad (6)$$

The time-independent Schrödinger equation (TISE)

$$\hat{H}_0 |\psi_i\rangle = E_i |\psi_i\rangle \quad (7)$$

is solved to obtain the eigenstates of the system. Here, E_i is the eigenvalue of state $|\psi_i\rangle$. The ribbon contains $L = 4N$ sites, and hence the Hamiltonian has L orthogonal eigenstates.

B. Coupling to an external field

It is known that in a continuous description, i.e., before a tight-binding approximation is adopted, the velocity gauge may require many bands for the convergence of observables [35]. In the context of HHG and a continuous 1D periodic potential, this issue has been discussed in [36]. How to couple a given tight-binding model with a limited number of bands to an external field in a gauge-invariant manner is shown in [37]. In our case, where we apply the dipole approximation, the coupling is identical to the well-known Peierls substitution [38]. Further, we tested explicitly that for finite nanoribbons, length gauge and Peierls substitution give the same result. We thus have

$$\langle n, \alpha | \hat{H}(t) | n', \alpha' \rangle = \langle n, \alpha | \hat{H}_0 | n', \alpha' \rangle e^{-i(\mathbf{r}_{n,\alpha} - \mathbf{r}_{n',\alpha'}) \cdot \mathbf{A}(t)}, \quad (8)$$

where $\mathbf{r}_{n,\alpha}$ ($\mathbf{r}_{n',\alpha'}$) are the positions of the atoms at hexagon n (n') and site α (α'), and $\mathbf{A}(t)$ is the vector potential of the n_{cyc} -cycle laser pulse of frequency ω_0 and amplitude A_0 ,

$$\mathbf{A}(t) = [A(t), 0]^\top \text{ and } A(t) = A_0 \sin^2 \left(\frac{\omega_0 t}{2n_{\text{cyc}}} \right) \sin(\omega_0 t), \quad (9)$$

for $0 \leq t \leq 2\pi n_{\text{cyc}}/\omega_0$ and zero otherwise. The parameters used in the following are $A_0 = 0.05$ (corresponding to an intensity of $\simeq 5 \times 10^9 \text{ W cm}^{-2}$), $\omega_0 = 7.5 \times 10^{-3}$ (i.e., $\lambda = 6.1 \mu\text{m}$), and $n_{\text{cyc}} = 5$.

The system contains multiple electrons but we neglect electron-electron interaction. A single-electron wave function $|\Psi^i(t)\rangle$ can be expanded in the eigenstates from the TISE (7):

$$|\Psi^i(t)\rangle = \sum_{l=0}^{L-1} c_l^i(t) |\psi_l\rangle e^{-iE_l t}. \quad (10)$$

The initial conditions are chosen

$$|\Psi^i(t=0)\rangle = |\psi_i\rangle. \quad (11)$$

It is assumed that all eigenstates below the Fermi level ($E_i < 0$) are occupied before the laser hits the nanoribbon, i.e., the lower half of the states are occupied initially ($i = 0, 1, 2, \dots, L/2 - 1$).

The time-dependent Hamiltonian can be written in the form

$$\hat{H}(t) = \hat{H}_0 + \hat{V}(t). \quad (12)$$

The ansatz (10) is plugged into the time-dependent Schrödinger equation (TDSE),

$$i\partial_t |\Psi(t)\rangle = \hat{H}(t) |\Psi(t)\rangle = (\hat{H}_0 + \hat{V}(t)) |\Psi(t)\rangle. \quad (13)$$

After a few steps one arrives at a system of differential equations for the coefficients c_j^i :

$$\dot{c}_j^i(t) = -i \sum_{l=0}^{L-1} c_l^i(t) e^{-i(E_l - E_j)t} \langle \psi_j | \hat{V}(t) | \psi_l \rangle. \quad (14)$$

The current is required to calculate the harmonic spectra. The current operator reads [39]

$$\hat{J}(t) = -i \sum_{n,\alpha} \sum_{n',\alpha'} (\mathbf{r}_{n,\alpha} - \mathbf{r}_{n',\alpha'}) |n, \alpha\rangle H_{n,\alpha}^{n',\alpha'}(t) \langle n', \alpha'|, \quad (15)$$

with $H_{n,\alpha}^{n',\alpha'}(t) = \langle n, \alpha | \hat{H}(t) | n', \alpha' \rangle$. The expectation value of the current is calculated as

$$\mathbf{J}(t) = \sum_i \langle \Psi^i(t) | \hat{J}(t) | \Psi^i(t) \rangle, \quad (16)$$

where the sum runs over all propagated electrons in the states $|\Psi^i(t)\rangle$ (here $i = 0, 1, 2, \dots, L/2 - 1$). The current has two components, $\mathbf{J}(t) = [J_{\parallel}(t), J_{\perp}(t)]$. The vector potential is linearly polarized along the chain $\mathbf{A}(t) = [A(t), 0]^T$. The component J_{\parallel} (J_{\perp}) refers to the polarization component parallel (perpendicular) to the vector potential.

The HHG spectrum is calculated by Fourier transforming the current [40–42],

$$P_{\parallel,\perp}(\omega) = |P_{\parallel,\perp}(\omega)| e^{i\Phi_{\parallel,\perp}(\omega)} = \text{FFT}[J_{\parallel,\perp}(t)]. \quad (17)$$

The phase difference

$$\Delta\Phi = \Phi_{\parallel} - \Phi_{\perp} \quad (18)$$

indicates the polarization (i.e., helicity) of the emitted photons.

C. Nanoribbon bulk Hamiltonian

The Bloch ansatz

$$|\psi_i\rangle = \frac{1}{\sqrt{N}} \sum_{m=1}^N e^{imk_d} |m\rangle \otimes [u_1(k_i) e^{ik_id/2} |1\rangle + u_2(k_i) |2\rangle + u_3(k_i) |3\rangle + u_4(k_i) e^{ik_id/2} |4\rangle] \quad (19)$$

can be used to simplify the TISE (7). The phase factors $e^{ik_id/2}$ are included to take the shifts inside one unit cell into account. The function $u_{\alpha}(k_i)$ is the periodic part (at site α) of a Bloch state $|\psi_i\rangle$, and $d = \sqrt{3}a$ is the lattice constant. Inserting this Bloch ansatz into the TISE (7) yields, after a few standard calculation steps,

$$\hat{H}_{\text{bulk}}(k_i) \mathbf{u}(k_i) = E_i \mathbf{u}(k_i), \quad (20)$$

where

$$\hat{H}_{\text{bulk}}(k_i) = \begin{pmatrix} M_+(k_i) & T_1(k_i) & h_-(k_i) & 0 \\ T_1(k_i) & M_-(k_i) & t_1 & h_+(k_i) \\ h_-(k_i) & t_1 & M_+(k_i) & T_1(k_i) \\ 0 & h_+(k_i) & T_1(k_i) & M_-(k_i) \end{pmatrix} \quad (21)$$

with

$$\mathbf{u}(k_i) = [u_1(k_i), u_2(k_i), u_3(k_i), u_4(k_i)]^T, \quad (22)$$

$$T_1(k_i) = 2t_1 \cos(k_id/2), \quad (23)$$

$$M_{\pm}(k_i) = \pm M + 2t_2 \cos(\phi \pm k_id), \quad (24)$$

$$h_{\pm}(k_i) = 2t_2 \cos(\phi \pm k_id/2), \quad (25)$$

the bulk Bloch Hamiltonian for the nanoribbon.

The bulk Hamiltonian is a 4×4 matrix so that there are four solutions of the TISE for each k_i , i.e., four bands. The bands are indicated by $j = 1, 2, 3, 4$ with E_i^j and $\mathbf{u}^j(k_i) = [u_1^j(k_i), u_2^j(k_i), u_3^j(k_i), u_4^j(k_i)]^T$. The states are sorted so that the energies are in ascending order, $E_i^1 \leq E_i^2 \leq E_i^3 \leq E_i^4$. The eigenvector components can be written as $u_{\alpha}^j(k_i) = |u_{\alpha}^j(k_i)| e^{i\phi_{\alpha}^j(k_i)}$. The phases $\phi_{\alpha}^j(k_i)$ are random because the states $u_{\alpha}^j(k_i)$ are calculated for each k_i separately. In order to compare the phases, a certain structure gauge is applied:

$$\tilde{\mathbf{u}}^j(k_i) = \mathbf{u}^j(k_i) e^{-i\phi_1^j(k_i)}, \quad (26)$$

$$\tilde{u}_{\alpha}^j(k_i) = |u_{\alpha}^j(k_i)| e^{i[\phi_{\alpha}^j(k_i) - \phi_1^j(k_i)]} = |u_{\alpha}^j(k_i)| e^{i\phi'_{\alpha,j}(k_i)}. \quad (27)$$

By definition, the phases $\phi'_{1,j}(k_i)$ are zero in this gauge. Observables such as HHG spectra must be independent of the gauge. And indeed, for the generation of high harmonics, only phase differences between bands are important:

$$\Delta\phi'_{\alpha,\alpha'}^{j,j'} = \phi'_{\alpha,j} - \phi'_{\alpha',j'}. \quad (28)$$

Note that the Hamiltonian (21) is symmetric and real, which means that the $\tilde{u}_{\alpha}^j(k_i)$ are also real, and the phases $\Delta\phi'_{\alpha,\alpha'}^{j,j'}$ can only be 0 or π (we restrict the phases to $\Delta\phi'_{\alpha,\alpha'}^{j,j'} \in [0, 2\pi[$). As demonstrated in Sec. III C, states near the minimal band gap contribute most to the spectrum. Hence the phase difference between the bands around the band gap, $\Delta\phi'_{\alpha} \equiv \Delta\phi'_{\alpha,\alpha}^{3,2}$, is investigated in detail.

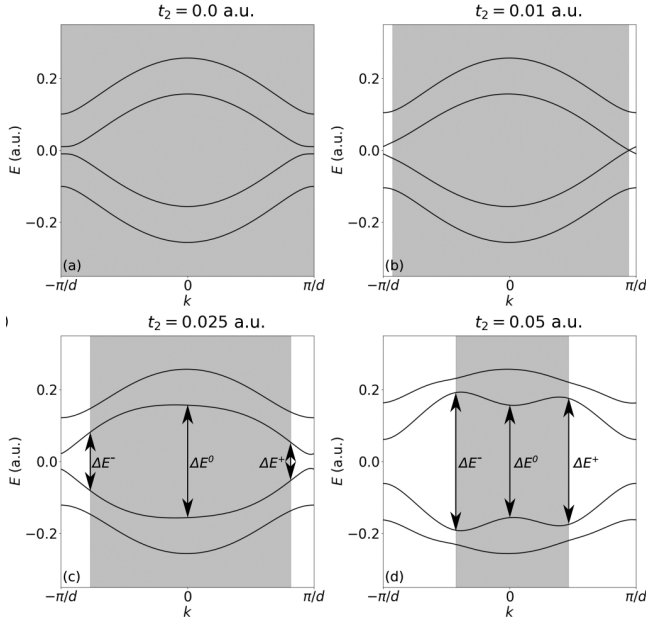


FIG. 2. Band structure of the nanoribbon with periodic boundary in x direction for different t_2 . The shaded areas are identical to those in Fig. 3.

III. RESULTS FOR THE PERIODIC SYSTEM

The system is initialized with the following parameters: the distance between adjacent atoms is $a = 2.68 \simeq 1.42 \text{ \AA}$, and the hopping between these atoms is set to $t_1 = -2.7 \text{ eV} \simeq -0.1 \text{ (a.u.)}$, which are the known parameters of graphene [43]. In the bulk, a topological phase transition occurs at $t_2 = \pm M / (3\sqrt{3} \sin \phi)$ [31]. This formula is not fulfilled exactly for these ribbons. But still, the onsite potential is chosen to be rather small, $M = 0.01$, to assure a topological phase transition for a small next-nearest-neighbor hopping. In particular, the transition should be observed for $|t_2| < |t_1|$ because hopping between next-nearest neighbors should be smaller than hopping between nearest ones. We set the next-nearest neighbor hopping to a purely imaginary number (i.e., $\phi = \pi/2$). The system contains $N = 30$ unit cells.

A. The bulk system

In Fig. 2, the bands are plotted for four different t_2 . There are four bands that are all well separated at every k for $t_2 = 0$. The minimal band gap between bands $j = 2$ and 3 is located at the boundaries of the first Brillouin zone ($k = \pm\pi/d$). This band gap is $\Delta E_{\text{gap}}(t_2 = 0) = 2|M| = 0.02$. For $t_2 \simeq 0.01$ the gap between bands $j = 2$ and 3 vanishes and the topological phase transition occurs. For larger t_2 , the band gap opens again. At the two boundaries of the gray-shaded areas in Fig. 2 phase differences $\Delta\phi'_\alpha \equiv \Delta\phi'_{\alpha,3,2}$ of the periodic part of the Bloch functions jump (at least for one α). The phase differences are plotted in Fig. 3. Due to the real, symmetric Hamiltonian, the phase differences can only be $\Delta\phi'_\alpha = 0$ (solid line) or $\Delta\phi'_\alpha = \pi$ (dotted line).

For vanishing next-nearest-neighbor hopping $t_2 = 0$, the phase differences $\Delta\phi'_\alpha$ are constant over the whole Brillouin zone, see Fig. 3(a). Their values are 0, π , 0, and π for sites

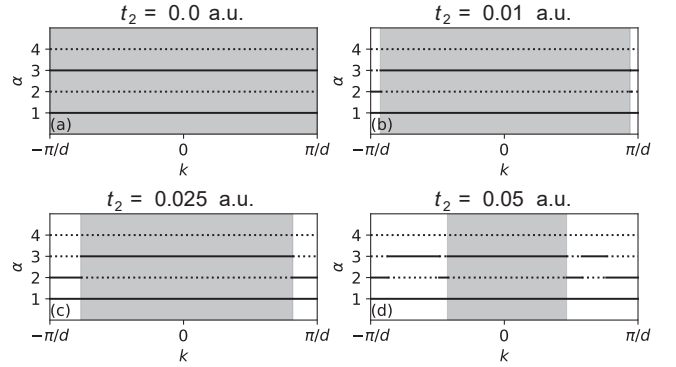


FIG. 3. Plots of $\Delta\phi'_\alpha$ as a function of k for various t_2 . This phase difference can assume two different values only. Solid lines denote $\Delta\phi'_\alpha = 0$, dotted lines $\Delta\phi'_\alpha = \pi$. The gray shaded areas indicate the region around $k = 0$ where the phase differences are identical to the $t_2 = 0$ case.

1, 2, 3, and 4, respectively. As t_2 increases, at least one value starts to differ around the boundaries of the Brillouin zone ($k = \pm\pi/d$) while around $k = 0$ they remain identical to the case $t_2 = 0$. The gray shaded areas in Fig. 3 indicate the regions of $t_2 = 0$ -like behavior around $k = 0$. The gray shaded areas shrink towards $k = 0$ with increasing t_2 . Note that $\Delta\phi'_2$ jumps at $t_2 = 0.01$ on the right edge of the shaded area from π to 0 and back to π at a slightly larger k .

Instead of phase differences, Fig. 4 shows the individual phases $\phi'_{\alpha,j}$ for $j = 2$ (a), (b) and $j = 3$ (c), (d) in a similar kind of plot. The shaded areas are identical to Fig. 3. A kind of node rule can be identified. In the $t_2 = 0$ -like region (shaded area), the values $\phi'_{\alpha,j=2}$ are 0 for sites $\alpha = 1, 2$ and π for $\alpha = 3, 4$. Hence the Bloch states $\tilde{u}_\alpha^{j=2}$ are positive for the first two sites and negative for the last two—the state has one “node.” For band $j = 3$, the Bloch state is positive for sites $\alpha = 1, 4$ and negative for $\alpha = 2, 3$, i.e., there are two “nodes.” For $t_2 = 0.025$ the values of $\phi'_{\alpha,j}$ change in the nonshaded area in such a way that band 2 has two nodes and band 3 only one, which is indicative of a band inversion. For $t_2 = 0.05$ one can see that

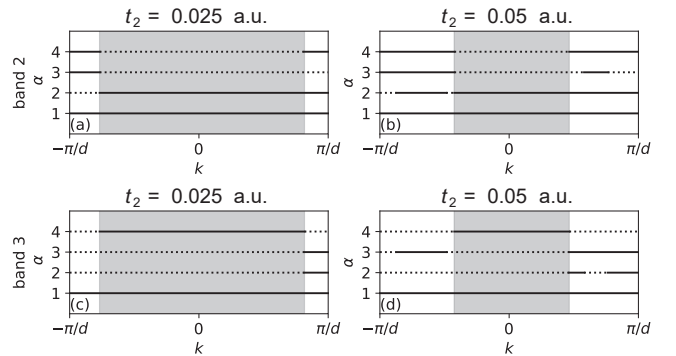


FIG. 4. Phases $\phi'_{\alpha,j}$ for band $j = 2$ (a), (b) and band $j = 3$ (c), (d) for different t_2 . Solid lines denote $\phi'_{\alpha,j} = 0$, dotted lines $\phi'_{\alpha,j} = \pi$. Gray shaded areas indicate regions where $\phi'_{\alpha,j}$ is identical to the case $t_2 = 0$ (not shown). These shaded areas are identical to those in Fig. 3.

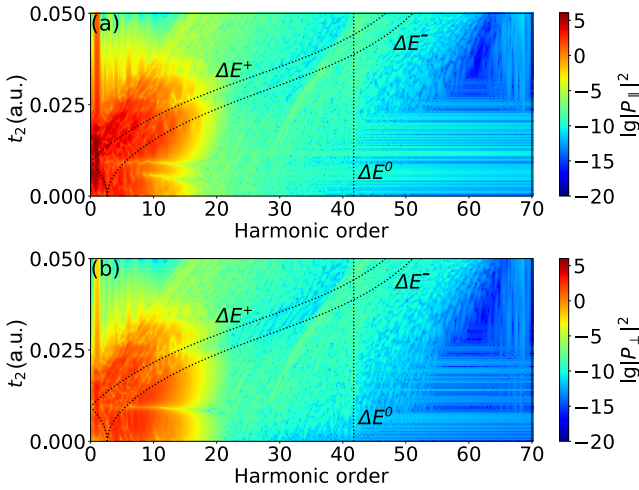


FIG. 5. Harmonic spectra $|P_{\parallel}(\omega)|^2$, $|P_{\perp}(\omega)|^2$ vs t_2 in parallel (a) and perpendicular polarization direction (b), respectively. The dotted lines indicate the energy differences defined before [see Figs. 2(c) and 2(d)].

a region appears where band 2 has no nodes and band 3 even four nodes.

The same gray-shaded areas are shown in the plots of the band structure, Fig. 2. The energy difference between band 2 and 3 at the boundaries of the gray shaded area are traced as a function of t_2 . They are labeled by ΔE^- (left boundary, negative k) and ΔE^+ (right boundary, positive k). The energy difference between these bands at $k = 0$ is called ΔE^0 . For better visibility, these energies are only indicated in Figs. 2(c) and 2(d). Further, the energy differences in the nonshaded areas are always smaller than the energy differences in the gray-shaded areas for $t_2 \lesssim 0.0387$. For $t_2 > 0.0387$, it appears that $\Delta E^0 < \Delta E^-$ and certain energy differences in the nonshaded area are larger than differences in the shaded area between bands $j = 2$ and 3, see Fig. 2(d).

B. Spectra

The harmonic spectra $|P_{\parallel}(\omega)|^2$, $|P_{\perp}(\omega)|^2$ for this system in parallel (a) and perpendicular polarization direction (b), respectively, are shown in Fig. 5 for $t_2 \in [0, 0.05]$. Note that clean harmonics are only observed for small energies. The fact that simulated HHG spectra on the time-dependent Schrödinger level show less clean, discrete harmonics than experimental spectra is well known, although its resolution is still under debate. It is known, though, that propagation of the emitted light in the medium [44] or to the detector [6] “purifies” the microscopic response towards cleaner harmonics due to phase-matching effects. Further, the assumption of a dephasing time in the semiconductor optical Bloch equations “helps” to obtain a clear harmonic structure that is closer to experiment [9]. However, for the purpose of the current paper there is no need to postprocess the microscopic response in such ways.

The highest yield is found at small harmonic orders and small t_2 when the band gap is small compared to the photon energy of the driving field. For larger t_2 , the band gap increases, and low-order harmonics are due to intraband

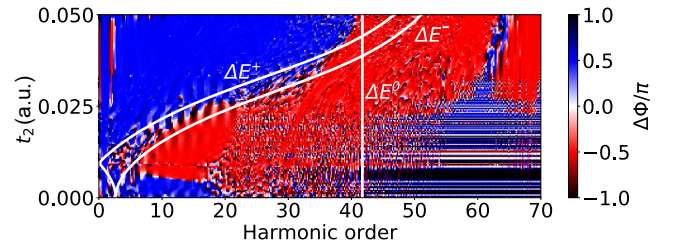


FIG. 6. Phase difference (helicity) between the spectra in the two polarization directions.

movement of electrons, which destructively interferes if the valence bands are fully occupied [22,45]. As the gap closes at $t_2 \simeq 0.01$, the harmonic yield decreases. This effect appears as a clearly visible horizontal cut in the region of high-harmonic yield. However, a system with a vanishing band gap is a metal. In metals, screening is important but not included in our tight-binding approach so that this sharp cut might be less pronounced in simulations with screening taken into account, e.g., using time-dependent density functional theory [22].

The three energies ΔE^{\pm} and ΔE^0 are indicated in these plots by dotted lines. The energies ΔE^{\pm} describe two curves that go through the region of the highest harmonic yield.

The emitted light has two polarization directions, and the phase difference between those two components can be obtained via Eq. (18). The phase difference determines the helicity of the emitted photons. The result is shown in Fig. 6. The phase difference is preferably $\Delta\Phi = \pm\pi/2$. The interesting fact, and the main result of this work, is that for a given, sufficiently large $t_2 > 0.006$ the phase changes from $+\pi/2$ to $-\pi/2$ at a certain harmonic order. This phase flip appears between the energies ΔE^{\pm} . To be precise, the phase difference is $-\pi/2$ for energies below ΔE^+ and it is $+\pi/2$ for energies larger than ΔE^- , at least as long as $\Delta E^0 > \Delta E^{\pm}$.

The case where $\Delta E^0 > \Delta E^{\pm}$ is examined. As shown previously, the phase difference of the periodic part of the Bloch states $\Delta\phi'_{\alpha} = \phi'_{\alpha,j} - \phi'_{\alpha',j'}$ has a symmetry which changes at certain points in k space for sufficiently large t_2 . To be more precise, the phases $\phi'_{\alpha,j=2}$ and $\phi'_{\alpha',j=3}$ change at these points in such a way that the properties of band $j = 2$ and $j = 3$ are inverted. If the energy difference between these states is smaller than ΔE^+ (nonshaded area in Fig. 2), then $\Delta\phi'_{\alpha}$ is different compared to points where this energy difference is larger than ΔE^- (gray-shaded area in Fig. 2). How $\Delta\phi'_{\alpha}$ affects the current, which finally determines the emitted harmonic radiation, is shown in the Appendix. The ΔE^{\pm} describe the change of the helicity quite well unless $\Delta E^0 < \Delta E^{\pm}$ (where ΔE^0 determines the change of the helicity).

C. Partially filled valence bands

Until now, all the states of the valence bands were occupied, i.e., all states with a negative energy. Now, only the ten highest states of the valence bands are occupied. These states belong to the second valence band $j = 2$. In this way we demonstrate that the electrons occupying the second valence band are responsible for the helicity change of the emitted photons. The result is shown in Fig. 7.

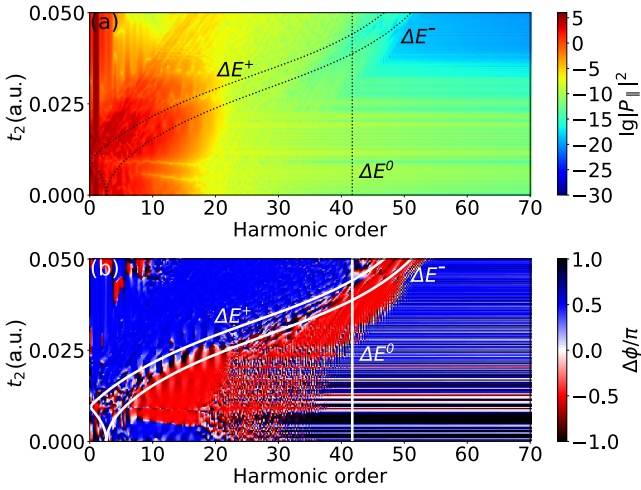


FIG. 7. Harmonic spectra $|P_{||}(\omega)|^2$ vs t_2 in parallel polarization direction (a) and helicity (b) calculated from only the ten highest states of the valence bands (i.e., band $j = 2$).

There are only minor differences between the spectra in Fig. 5(a) and Fig. 7(a). As far as the helicity of the emitted harmonic photons is concerned, one can notice differences between Fig. 6 and Fig. 7(b), but the phase flip for given t_2 still occurs at the same harmonic order as before.

IV. FINITE NANORIBBON WITH EDGES

In order to show that the helicity flip also occurs in finite nanoribbons despite the fact that the explanation for the flip is based on a bulk analysis, a finite system with edges as shown in Fig. 8 is investigated. For the ribbon with edges, hopping from the right to the left edge is not possible. The system contains two more atoms compared to the periodic system in order to complete the hexagon at the right edge. The cutoff of the plateau for small harmonic orders and small t_2 occurs at larger energies as for the periodic system, as seen in Fig. 9.

The phase flip discussed for the periodic system can be observed for the finite ribbon as well, see Fig. 10. We observe an additional phase flip at around $t_2 \approx 0.09$ for small odd harmonics (up to order 11), except for the fundamental (the same flip can be observed for the periodic system, not shown). This helicity flip might be similar to that for bulk Haldanite explained in [23]. The authors of [23] explain their observed phase flip with a topological phase transition in bulk Haldanite. However, there is no topological phase transition around $t_2 = 0.09$ in our nanoribbon. Instead, our finite system has two edge states, and the energy difference of these states is smallest at $t_2 \approx 0.09$, which coincides with the helicity change. The increasing energy difference of the edge states for $t_2 > 0.09$ might be caused by the large next-nearest-neighbor hopping

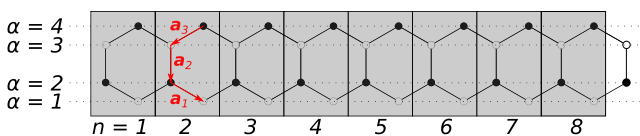


FIG. 8. Finite nanoribbon containing $L = 4N + 2$ atoms.

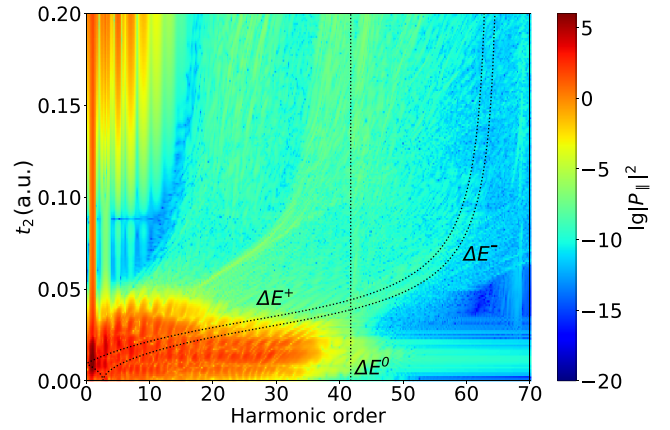


FIG. 9. Harmonic spectra $|P_{||}(\omega)|^2$ vs t_2 in parallel polarization direction for the finite system. The dotted lines indicate the energy differences defined by the bulk system, as described before.

compared to the nearest-neighbor hopping. Charge transfer between the edge states leads to an increased harmonic yield for small harmonic orders for $t_2 > 0.1$, similar to what was observed in [26] for finite Su-Schrieffer-Heeger chains. The regime of t_2 being comparable in magnitude to t_1 or even larger might be analyzed in more detail in the future but is beyond the scope of this work.

V. SUMMARY AND OUTLOOK

A helicity flip of the emitted photons in high-harmonic spectra from Haldane-like nanoribbons is observed. For a fixed next-nearest-neighbor hopping, the helicity of the emitted photons changes at a certain harmonic order. The photon energy where this helicity flip occurs can be predicted by examining the phase differences between the periodic parts of the Bloch states. In previous theoretical works [23], helicity flips of harmonics in bulk Haldanite were observed as a function of the next-nearest-neighbor hopping, mapping out the known topological phase transition of the Haldane model. The helicity flip discussed in this work might be observed in systems where the next-nearest-neighbor hopping

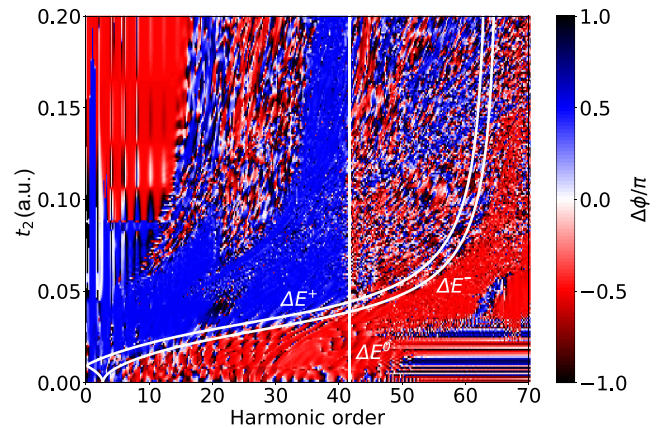


FIG. 10. Phase difference (helicity) between the spectra in both polarization directions for the finite ribbon.

cannot be easily changed. Moreover, the effect might allow one to manipulate the helicity of high-harmonic photons, e.g., by multicolor incident laser pulses. In future work, the robustness of this effect with respect to different laser polarizations and for different system sizes (e.g., more 2D-like) might be investigated.

ACKNOWLEDGMENT

H.J. acknowledges financial support by the doctoral fellowship program of the University of Rostock.

APPENDIX: CALCULATION OF THE CURRENT AND THE RELEVANCE OF THE PHASE DIFFERENCES $\Delta\phi_{\alpha,\alpha}^{j',j}(k_i)$

The current is calculated as the expectation value of the current operator

$$\mathbf{j}^i(t) = \langle \Psi^i(t) | \hat{\mathbf{j}}(t) | \Psi^i(t) \rangle \quad (\text{A1})$$

with the current operator (15). For the state $|\Psi^i(t)\rangle$, one can make a similar Bloch ansatz as before,

$$|\Psi^i(t)\rangle = \frac{1}{\sqrt{N}} \sum_{m=1}^N e^{imk_i d} |m\rangle \otimes [u_1(k_i, t) e^{ik_i d/2} |1\rangle + u_2(k_i, t) |2\rangle + u_3(k_i, t) |3\rangle + u_4(k_i, t) e^{ik_i d/2} |4\rangle], \quad (\text{A2})$$

but now with time-dependent coefficients $u_\alpha(k_i, t)$. Using this ansatz, one ends up with two 4×4 current operators, for the x and y direction. The corresponding currents are then calculated as

$$j^{x,y}(k_i, t) = \mathbf{u}^\dagger(k_i, t) \hat{\mathcal{J}}_{\text{bulk}}^{x,y}(k_i, t) \mathbf{u}(k_i, t). \quad (\text{A3})$$

For the x direction one obtains

$$\hat{\mathcal{J}}_{\text{bulk}}^x(k_i, t) = \begin{pmatrix} f_1(k_i, t) & f_2(k_i, t) & f_3(k_i, t) & 0 \\ f_2(k_i, t) & f_4(k_i, t) & 0 & f_5(k_i, t) \\ f_3(k_i, t) & 0 & f_1(k_i, t) & f_2(k_i, t) \\ 0 & f_5(k_i, t) & f_2(k_i, t) & f_4(k_i, t) \end{pmatrix} \quad (\text{A4})$$

with

$$f_1(k_i, t) = idt_2 e^{i\phi} e^{id(A(t)+k)} + \text{c.c.}, \quad (\text{A5})$$

$$f_2(k_i, t) = -dt_1 \sin[(k + A(t))d/2], \quad (\text{A6})$$

$$f_3(k_i, t) = i\frac{d}{2} t_2 e^{-i\phi} e^{id(A(t)+k)/2} + \text{c.c.}, \quad (\text{A7})$$

$$f_4(k_i, t) = -idt_2 e^{i\phi} e^{-id(A(t)+k)} + \text{c.c.}, \quad (\text{A8})$$

$$f_5(k_i, t) = i\frac{d}{2} t_2 e^{i\phi} e^{id(A(t)+k)/2} + \text{c.c.}, \quad (\text{A9})$$

and in y direction,

$$\hat{\mathcal{J}}_{\text{bulk}}^y(k_i, t) = \begin{pmatrix} 0 & g_1(k_i, t) & g_2(k_i, t) & 0 \\ -g_1(k_i, t) & 0 & g_3 & g_4(k_i, t) \\ -g_2(k_i, t) & -g_3 & 0 & g_1(k_i, t) \\ 0 & -g_4(k_i, t) & -g_1(k_i, t) & 0 \end{pmatrix} \quad (\text{A10})$$

with

$$g_1(k_i, t) = iat_1 \cos[(k + A(t))d/2], \quad (\text{A11})$$

$$g_2(k_i, t) = i\frac{3}{2} at_2 e^{-i\phi} e^{id(A(t)+k)/2} - \text{c.c.}, \quad (\text{A12})$$

$$g_3 = iat_1, \quad (\text{A13})$$

$$g_4(k_i, t) = i\frac{3}{2} at_2 e^{i\phi} e^{id(A(t)+k)/2} - \text{c.c.} \quad (\text{A14})$$

Note that all $f_l(k_i, t)$ ($l = 1, 2, 3, 4, 5$) are real and all $g_s(k_i, t)$ ($s = 1, 2, 3, 4$) are purely imaginary. In the following, the arguments of $f_l(k_i, t)$ and $g_s(k_i, t)$ are dropped. The argument k_i of $u_\alpha(k_i, t)$ is suppressed as well. The current in x direction reads

$$j^x(k_i, t) = f_1(|u_1(t)|^2 + |u_3(t)|^2) + f_4(|u_2(t)|^2 + |u_4(t)|^2) + f_2[u_1^*(t)u_2(t) + u_2^*(t)u_1(t) + u_3^*(t)u_4(t) + u_4^*(t)u_3(t)] \\ + f_3[u_1^*(t)u_3(t) + u_3^*(t)u_1(t)] + f_5[u_2^*(t)u_4(t) + u_4^*(t)u_2(t)], \quad (\text{A15})$$

and in y direction

$$j^y(k_i, t) = g_1[u_1^*(t)u_2(t) - u_2^*(t)u_1(t) + u_3^*(t)u_4(t) - u_4^*(t)u_3(t)] + g_2[u_1^*(t)u_3(t) - u_3^*(t)u_1(t)] \\ + g_3[u_2^*(t)u_3(t) - u_3^*(t)u_2(t)] + g_4[u_2^*(t)u_4(t) - u_4^*(t)u_2(t)]. \quad (\text{A16})$$

Note that for certain α and α' one has in x direction the terms $u_\alpha^*(t)u_{\alpha'}(t) + \text{c.c.}$ but in y direction $u_\alpha^*(t)u_{\alpha'}(t) - \text{c.c.}$ The terms in x directions are purely real, while in y direction they are purely imaginary. Multiplied with the factors f_l or g_s , the current is real in both directions, of course.

For the time-dependent $\mathbf{u}(k_i, t)$ one should include another index $\mathbf{u}^j(k_i, t)$, which indicates the occupied band at the start of the laser pulse. For better readability, however, the index of the initial band is dropped in the time-dependent functions $\mathbf{u}(k_i, t)$. Expanding in eigenstates of the unperturbed bulk system,

$$\mathbf{u}(k_i, t) = \sum_{j=1}^4 \tilde{c}_j(k_i, t) \mathbf{u}^j(k_i), \quad (\text{A17})$$

we find

$$u_\alpha^*(k_i, t)u_{\alpha'}(k_i, t) = \sum_{j,j'=1}^4 \tilde{c}_j^*(k_i, t)\tilde{c}_{j'}(k_i, t)u_\alpha^{j*}(k_i)u_{\alpha'}^{j'}(k_i). \quad (\text{A18})$$

Writing

$$u_\alpha^j(k_i) = |u_\alpha^j(k_i)|e^{i\phi_{\alpha,j}(k_i)} \quad (\text{A19})$$

and

$$\tilde{c}_j(k_i, t) = |\tilde{c}_j(k_i, t)|e^{i\varphi_j(k_i, t)}, \quad (\text{A20})$$

the expression under the sum in (A18) becomes

$$\tilde{c}_j^*(k_i, t)\tilde{c}_{j'}(k_i, t)u_\alpha^{j*}(k_i)u_{\alpha'}^{j'}(k_i) = \tilde{C}_{j',j}(k_i, t)U_{\alpha',\alpha}^{j',j}(k_i)e^{i(\Delta\varphi_{j',j}(k_i, t) + \Delta\phi_{\alpha',\alpha}^{j',j}(k_i))}, \quad (\text{A21})$$

with $\tilde{C}_{j',j}(k_i, t) = |\tilde{c}_{j'}(k_i, t)||\tilde{c}_j(k_i, t)|$, $U_{\alpha',\alpha}^{j',j}(k_i) = |u_{\alpha'}^{j'}(k_i)||u_\alpha^j(k_i)|$, $\Delta\varphi_{j',j}(k_i, t) = \varphi_{j'}(k_i, t) - \varphi_j(k_i, t)$, and $\Delta\phi_{\alpha',\alpha}^{j',j}(k_i) = \phi_{\alpha',j'}(k_i) - \phi_{\alpha,j}(k_i)$.

Further, it follows

$$u_\alpha^*(k_i, t)u_{\alpha'}(k_i, t) + u_{\alpha'}^*(k_i, t)u_\alpha(k_i, t) = 2 \sum_{j,j'=1}^4 \tilde{C}_{j',j}(k_i, t)U_{\alpha',\alpha}^{j',j}(k_i) \cos(\Delta\varphi_{j',j}(k_i, t) + \Delta\phi_{\alpha',\alpha}^{j',j}(k_i)) \quad (\text{A22})$$

and

$$u_\alpha^*(k_i, t)u_{\alpha'}(k_i, t) - u_{\alpha'}^*(k_i, t)u_\alpha(k_i, t) = 2i \sum_{j,j'=1}^4 \tilde{C}_{j',j}(k_i, t)U_{\alpha',\alpha}^{j',j}(k_i) \sin(\Delta\varphi_{j',j}(k_i, t) + \Delta\phi_{\alpha',\alpha}^{j',j}(k_i)). \quad (\text{A23})$$

Hence the expression of the current in x direction (A15) contains terms $\sim \cos(\Delta\varphi_{j',j}(k_i, t) + \Delta\phi_{\alpha',\alpha}^{j',j}(k_i))$, whereas terms $\sim \sin(\Delta\varphi_{j',j}(k_i, t) + \Delta\phi_{\alpha',\alpha}^{j',j}(k_i))$ appear in the y component of the current (A16).

As it was shown in the main text, the phase differences $\Delta\phi'_\alpha = \Delta\phi_{\alpha,\alpha}^{3,2}$ change for certain k_i . The helicity of the harmonics changes sign at the corresponding harmonic order. The currents depend on these phase differences, and the dependencies are different for the two directions.

-
- [1] S. Ghimire, A. D. DiChiara, E. Sistrunk, P. Agostini, L. F. DiMauro, and D. A. Reis, Observation of high-order harmonic generation in a bulk crystal, *Nat. Phys.* **7**, 138 (2011).
 [2] O. Schubert, M. Hohenleutner, F. Langer, B. Urbanek, C. Lange, U. Huttner, D. Golde, T. Meier, M. Kira, S. Koch, and R. Huber, Sub-cycle control of terahertz high-harmonic generation by dynamical Bloch oscillations, *Nat. Photon.* **8**, 119 (2014).
 [3] F. Langer, M. Hohenleutner, U. Huttner, S. Koch, M. Kira, and R. Huber, Symmetry-controlled temporal structure of high-

- harmonic carrier fields from a bulk crystal, *Nat. Photon.* **11**, 227 (2017).
 [4] N. Tancogne-Dejean, O. D. Mücke, F. X. Kärtner, and A. Rubio, Impact of the Electronic Band Structure in High-Harmonic Generation Spectra of Solids, *Phys. Rev. Lett.* **118**, 087403 (2017).
 [5] M. Garg, H. Y. Kim, and E. Goulielmakis, Ultimate waveform reproducibility of extreme-ultraviolet pulses by high-harmonic generation in quartz, *Nat. Photon.* **12**, 291 (2018).

- [6] C. Q. Abadie, M. Wu, and M. B. Gaarde, Spatiotemporal filtering of high harmonics in solids, *Opt. Lett.* **43**, 5339 (2018).
- [7] L. Yue and M. B. Gaarde, Structure gauges and laser gauges for the semiconductor Bloch equations in high-order harmonic generation in solids, *Phys. Rev. A* **101**, 053411 (2020).
- [8] G. Ndabashimiye, S. Ghimire, M. Wu, D. A. Browne, K. J. Schafer, M. B. Gaarde, and D. A. Reis, Solid-state harmonics beyond the atomic limit, *Nature (London)* **534**, 520 (2017).
- [9] G. Vampa and T. Brabec, Merge of high harmonic generation from gases and solids and its implications for attosecond science, *J. Phys. B: At. Mol. Opt. Phys.* **50**, 083001 (2017).
- [10] G. Vampa, T. J. Hammond, N. Thiré, B. E. Schmidt, F. Légaré, C. R. McDonald, T. Brabec, D. D. Klug, and P. B. Corkum, All-Optical Reconstruction of Crystal Band Structure, *Phys. Rev. Lett.* **115**, 193603 (2015).
- [11] M. Hohenleutner, F. Langer, O. Schubert, M. Knorr, U. Huttner, S. W. Koch, M. Kira, and R. Huber, Real-time observation of interfering crystal electrons in high-harmonic generation, *Nature (London)* **523**, 572 (2015).
- [12] T. T. Luu, M. Garg, S. Y. Kruchinin, A. Moulet, M. T. Hassan, and E. Goulielmakis, Extreme ultraviolet high-harmonic spectroscopy of solids, *Nature (London)* **521**, 498 (2015).
- [13] M. Baudisch, A. Marini, J. D. Cox, T. Zhu, F. Silva, S. Teichmann, M. Massicotte, F. Koppens, L. S. Levitov, F. J. García de Abajo, and J. Biegert, Ultrafast nonlinear optical response of Dirac fermions in graphene, *Nat. Commun.* **9**, 1018 (2018).
- [14] Y. S. You, Y. Yin, Y. Wu, A. Chew, X. Ren, F. Zhuang, S. Gholam-Mirzaei, M. Chini, Z. Chang, and S. Ghimire, High-harmonic generation in amorphous solids, *Nat. Commun.* **8**, 724 (2017).
- [15] G. P. Zhang, M. S. Si, M. Murakami, Y. H. Bai, and T. F. George, Generating high-order optical and spin harmonics from ferromagnetic monolayers, *Nat. Commun.* **9**, 3031 (2018).
- [16] G. Vampa, T. J. Hammond, M. Taucer, X. Ding, X. Ropagnol, T. Ozaki, S. Delprat, M. Chaker, N. Thiré, B. E. Schmidt, F. Légaré, D. D. Klug, A. Y. Naumov, D. M. Villeneuve, A. Staudte, and P. B. Corkum, Strong-field optoelectronics in solids, *Nat. Photon.* **12**, 465 (2018).
- [17] M. Z. Hasan and C. L. Kane, *Colloquium: Topological insulators*, *Rev. Mod. Phys.* **82**, 3045 (2010).
- [18] *Topological Insulators*, edited by M. Franz and L. Molenkamp, Contemporary Concepts of Condensed Matter Science Vol. 6 (Elsevier, New York, 2013).
- [19] J. Asbóth, L. Oroszlány, and A. Pályi, *A Short Course on Topological Insulators*, Lecture Notes in Physics Vol. 919 (Springer, Berlin, 2016).
- [20] J. Reimann, S. Schlauderer, C. P. Schmid, F. Langer, S. Baierl, K. A. Kokh, O. E. Tereshchenko, A. Kimura, C. Lange, J. Güdde, U. Höfer, and R. Huber, Subcycle observation of lightwave-driven Dirac currents in a topological surface band, *Nature (London)* **562**, 396 (2018).
- [21] H. Koochaki Kelardeh, V. Apalkov, and M. I. Stockman, Graphene superlattices in strong circularly polarized fields: Chirality, Berry phase, and attosecond dynamics, *Phys. Rev. B* **96**, 075409 (2017).
- [22] D. Bauer and K. K. Hansen, High-Harmonic Generation in Solids with and without Topological Edge States, *Phys. Rev. Lett.* **120**, 177401 (2018).
- [23] R. E. F. Silva, Á. Jiménez-Galán, B. Amorim, O. Smirnova, and M. Ivanov, Topological strong-field physics on sub-laser-cycle timescale, *Nat. Photon.* **13**, 849 (2019).
- [24] A. Chacón, W. Zhu, S. P. Kelly, A. Dauphin, E. Pisanty, A. Picón, C. Ticknor, M. F. Ciappina, A. Saxena, and M. Lewenstein, Observing topological phase transitions with high harmonic generation, [arXiv:1807.01616v3](https://arxiv.org/abs/1807.01616v3).
- [25] H. Drüeke and D. Bauer, Robustness of topologically sensitive harmonic generation in laser-driven linear chains, *Phys. Rev. A* **99**, 053402 (2019).
- [26] H. Jürß and D. Bauer, High-harmonic generation in Su-Schrieffer-Heeger chains, *Phys. Rev. B* **99**, 195428 (2019).
- [27] T. T. Luu and H. J. Wörner, Measurement of the Berry curvature of solids using high-harmonic spectroscopy, *Nat. Commun.* **9**, 916 (2018).
- [28] N. Yoshikawa, T. Tamaya, and K. Tanaka, High-harmonic generation in graphene enhanced by elliptically polarized light excitation, *Science* **356**, 736 (2017).
- [29] H. Liu, Y. Li, Y. S. You, S. Ghimire, T. F. Heinz, and D. A. Reis, High-harmonic generation from an atomically thin semiconductor, *Nat. Phys.* **13**, 262 (2017).
- [30] Z. Lou, Y. Zheng, C. Liu, L. Zhang, X. Ge, Y. Li, J. Wang, Z. Zeng, R. Li, and Z. Xu, Ellipticity dependence of nonperturbative harmonic generation in few-layer MoS₂, *Opt. Commun.* **469**, 125769 (2020).
- [31] F. D. M. Haldane, Model for a Quantum Hall Effect without Landau Levels: Condensed-Matter Realization of the “Parity Anomaly,” *Phys. Rev. Lett.* **61**, 2015 (1988).
- [32] G. Jotzu, M. Messer, R. Desbuquois, M. Lebrat, T. Uehlinger, D. Greif, and T. Esslinger, Experimental realization of the topological Haldane model with ultracold fermions, *Nature (London)* **515**, 237 (2014).
- [33] T. Cao, F. Zhao, and S. G. Louie, Topological Phases in Graphene Nanoribbons: Junction States, Spin Centers, and Quantum Spin Chains, *Phys. Rev. Lett.* **119**, 076401 (2017).
- [34] P. A. Pantaleón and Y. Xian, Edge states in a ferromagnetic honeycomb lattice with armchair boundaries, *Phys. B: Condens. Matter* **530**, 191 (2018).
- [35] D. J. Passos, G. B. Ventura, J. M. Viana Parente Lopes, J. M. B. Lopesdos Santos, and N. M. R. Peres, Nonlinear optical responses of crystalline systems: Results from a velocity gauge analysis, *Phys. Rev. B* **97**, 235446 (2018).
- [36] M. Wu, S. Ghimire, D. A. Reis, K. J. Schafer, and M. B. Gaarde, High-harmonic generation from Bloch electrons in solids, *Phys. Rev. A* **91**, 043839 (2015).
- [37] M. Graf and P. Vogl, Electromagnetic fields and dielectric response in empirical tight-binding theory, *Phys. Rev. B* **51**, 4940 (1995).
- [38] R. Peierls, Zur Theorie des Diamagnetismus von Leitungselektronen, *Z. Phys.* **80**, 763 (1933).
- [39] A. L. Kuzemsky, Electronic transport in metallic systems and generalized kinetic equations, *Int. J. Mod. Phys. B* **25**, 3071 (2011).
- [40] A. D. Bandrauk, S. Chelkowski, D. J. Diestler, J. Manz, and K.-J. Yuan, Quantum simulation of high-order harmonic spectra of the hydrogen atom, *Phys. Rev. A* **79**, 023403 (2009).
- [41] J. C. Baggesen and L. B. Madsen, On the dipole, velocity and acceleration forms in high-order harmonic generation from a

- single atom or molecule, *J. Phys. B: At. Mol. Opt. Phys.* **44**, 115601 (2011).
- [42] D. Bauer, H. Bauke, T. Brabec, T. Fennel, C. R. McDonald, D. B. Milošević, S. Pabst, C. Peltz, G. Pöplau, R. Santra, and C. Varin, in *Computational Strong-Field Quantum Dynamics: Intense Light-Matter Interactions*, edited by D. Bauer (De Gruyter, Berlin, 2017).
- [43] D. R. Cooper, B. D’Anjou, N. Ghattamaneni, B. Harack, M. Hilke, A. Horth, N. Majlis, M. Massicotte, L. Vandsburger, E. Whiteway, and V. Yu, Experimental review of graphene, *ISRN Condens. Matter Phys.* **2012**, 501686 (2012).
- [44] I. Floss, C. Lemell, G. Wachter, V. Smejkal, S. A. Sato, X.-M. Tong, K. Yabana, and J. Burgdörfer, *Ab initio* multiscale simulation of high-order harmonic generation in solids, *Phys. Rev. A* **97**, 011401(R) (2018).
- [45] K. K. Hansen, T. Deffge, and D. Bauer, High-order harmonic generation in solid slabs beyond the single-active-electron approximation, *Phys. Rev. A* **96**, 053418 (2017).

5.1.2 Intense-laser-driven electron dynamics and high-order harmonic generation in solids including topological effects

by Daniel Moos, Hannah Jürß, and Dieter Bauer

Physical Review A **102**, 053112 (2020)

DOI: [10.1103/PhysRevA.102.053112](https://doi.org/10.1103/PhysRevA.102.053112)

Reference: [2]

Author Contributions




Daniel Moos	performing the numerical simulations (writing the code and running it), analyzing the results, improving the manuscript
-------------	-------------------------------------------------------------------------------------------------------------------------

Hannah Jürß	analyzing the results, improving the manuscript, supervising the work of the master student Daniel Moos
-------------	---------------------------------------------------------------------------------------------------------

Dieter Bauer	developing the theory, analyzing the results, writing the manuscript, supervision
--------------	-----------------------------------------------------------------------------------

Copyright © of this paper by the American Physical Society.

Intense-laser-driven electron dynamics and high-order harmonic generation in solids including topological effects

Daniel Moos , Hannah Jürß , and Dieter Bauer 

Institut für Physik, Universität Rostock, D-18051 Rostock, Germany



(Received 24 July 2020; revised 30 October 2020; accepted 5 November 2020; published 23 November 2020)

A theory for laser-driven electron dynamics and high-harmonic generation in bulk solids with two lattice sites per unit cell of arbitrary dimension is formulated. In tight-binding approximation, such solids can be described by 2×2 Bloch Hamiltonians. Our theory is able to fully capture topological effects in high-harmonic generation by such systems because no simplifications beyond tight-binding, dipole approximation, and negligible depletion of the valence band are made. An explicit, analytical expression for the electron velocity is given. Exemplarily, the theory is applied to the Su-Schrieffer-Heeger chain and the Haldane model in strong laser fields.

DOI: [10.1103/PhysRevA.102.053112](https://doi.org/10.1103/PhysRevA.102.053112)

I. INTRODUCTION

Topological phase transitions are intimately related to the closing and reopening of band gaps [1–3] as a function of parameters in the Hamiltonian. Above and below such a phase transition, the electron dynamics of the system may qualitatively change drastically, e.g., from clockwise to counterclockwise motion. It is not surprising that such changes affect the radiation emitted by the electrons.

The light emitted by intense-laser-driven electrons may contain high harmonics of the incident laser pulse’s carrier frequency. High-harmonic generation (HHG) by isolated atoms or molecules in the gas phase has been extensively studied over the last decades and is the basis for the synthesis of attosecond pulses, which then can be used to explore ultrafast dynamics directly in the time domain [4]. HHG in solids was observed at modest laser intensities below the destruction threshold [5,6]. It was soon shown that the harmonics contain structural information and thus allows for an all-optical probing of condensed matter [7,8], including the measurement of Berry curvature [9,10]. Very recently, it has been shown that the valence electron density can be probed by HHG [11], complementing the conventional crystallographic methods that probe the ion positions.

A wide area of modern condensed matter physics is concerned with geometrical phases and topology [12–14]. Hence, from the strong-field, attosecond perspective, the natural question arises whether topological effects can be probed using, e.g., HHG, or exploited to affect the strong-field electron dynamics. While predictions are difficult, the ultrafast steering of currents by lasers [15–18], in particular topologically protected edge currents [19], the modification of topological properties via laser dressing [20,21], and ultrafast valleytronics [22] are probably the most promising mergers of modern condensed matter physics and strong-field attosecond science so far.

As topological phase transitions are related to the closing and reopening of band gaps, the simplest but nontrivial systems have two bands. It is further known that topolog-

ically nontrivial phases in the bulk lead to edge states in the corresponding finite system (“bulk-boundary correspondence” [2,14]). However, HHG in finite solids with explicit edge states, while definitely very interesting and with huge topological effects in HHG found numerically [23–25], is hardly accessible analytically. Hence, in this work, we concentrate on the bulk so that a Bloch ansatz can be made, reducing the problem to a 2×2 Bloch Hamiltonian. Prominent examples covered by this approach are, e.g., the Su-Schrieffer-Heeger (SSH) chain [2,26], graphene [27], the Haldane [28], or the Qi-Wu-Zhang [2,29] model. While the electronic structure of these systems and their topological properties are well studied, the investigation of ultrashort, strong-field electron dynamics and HHG in them have started only recently [9,10,22–25,30,31].

In this paper, we aim at providing the theoretical minimum of laser-driven electron dynamics and HHG in solids. Besides restricting ourselves to two bands neither assumptions about, e.g., the dimensionality, are made nor do we approximate transition matrix elements because this may sweep topological effects under the rug. The main result of this paper is an explicit expression for the laser-driven electron velocity as a function of the system-specific three-vector $\mathbf{d}(\mathbf{k})$ (see Eq. (15) below) and the driving laser field. The HHG spectrum can then be calculated from the Fourier transform of the velocity, acceleration, or current [32–34].

The outline of the paper is as follows. In Sec. II, we introduce our theory, including quick reminders about tight-binding, Bloch Hamiltonians, and the coupling of tight-binding Hamiltonians to laser fields. In Sec. II C, we also derive the equations of motion to be solved for the calculation of HHG spectra. The electron velocity is calculated in Sec. II D before, in Sec. II E, the analogies to gas-phase HHG are briefly discussed. In Secs. III A and III B, we use our theory to calculate HHG spectra for the SSH and Haldane model, respectively. The purpose of these results is twofold. First, we had to check that our main result, i.e., the analytical expression for the laser-driven electron velocity, is correct by comparison with the numerical solutions of the equations of

motion in position or \mathbf{k} space. Second, we want to trigger more interest in ‘‘topological HHG’’ by illustrating the counterintuitive electron motion in condensed matter. We conclude in Sec. IV and give some details on the proper choice of the Bloch ansatz and the Haldane model in the Appendix.

II. THEORY

In the following subsections we introduce the theory underlying our calculations of high-harmonic spectra from solids and set the stage notation-wise. Atomic units $\hbar = |e| = m_e = 1$ are used unless indicated otherwise.

A. Tight binding

Starting from a continuous description of a solid, a lattice Hamiltonian is obtained by a tight-binding ansatz [14],

$$\phi_{R\alpha}(\mathbf{r}) = \varphi_{\alpha}(\mathbf{r} - \mathbf{R} - \boldsymbol{\tau}_{\alpha}), \quad \alpha = 1, 2, \dots, M. \quad (1)$$

Here, $\mathbf{R} = \mathbf{R}_{n_1 \dots n_D} = \sum_j n_j \mathbf{a}_j$ is a lattice vector pointing to some unit cell defined by the basis vectors \mathbf{a}_j , $j = 1, 2, \dots, D$, of the D -dimensional system, and the index α labels the M orbitals φ_{α} per unit cell, with $\boldsymbol{\tau}_{\alpha}$ fixing their position within the unit cell. We assume

$$\langle \phi_{R\alpha} | \phi_{R'\beta} \rangle = \delta_{RR'} \delta_{\alpha\beta}, \quad (2)$$

i.e., the orbitals should be orthonormal both within a unit cell and across unit cells. Making use of the discrete translational invariance of \hat{H} one can write the Hamiltonian $\hat{H} = \sum_{R\alpha} |\phi_{R\alpha}\rangle \langle \phi_{R\alpha}| \hat{H} \sum_{R'\beta} |\phi_{R'\beta}\rangle \langle \phi_{R'\beta}|$ in ‘‘hopping form,’’

$$\hat{H} = \sum_{\Delta R} \sum_{\alpha\beta} H_{\alpha\beta}(\Delta R) \sum_{\mathbf{R}} |\phi_{R\alpha}\rangle \langle \phi_{\Delta R + \mathbf{R}, \beta}|, \quad (3)$$

where $\Delta R = R' - R$ and $H_{\alpha\beta}(\Delta R) = \langle \phi_{R\alpha} | \hat{H} | \phi_{R'\beta} \rangle$. The Hamiltonian (3) is a sum over hoppings from cell $\mathbf{R} + \Delta R$ and orbital β to cell \mathbf{R} and orbital α , weighted by the matrix element $H_{\alpha\beta}(\Delta R)$.

With the Bloch ansatz,

$$|\phi_{k\alpha}\rangle = \sum_{\mathbf{R}} e^{i\mathbf{k} \cdot (\mathbf{R} + \boldsymbol{\tau}_{\alpha})} |\phi_{R\alpha}\rangle, \quad (4)$$

i.e.,

$$|\phi_{R\alpha}\rangle = \frac{V_{\text{cell}}}{(2\pi)^D} \int_{\text{BZ}} d^D k e^{-i\mathbf{k} \cdot (\mathbf{R} + \boldsymbol{\tau}_{\alpha})} |\phi_{k\alpha}\rangle, \quad (5)$$

and

$$\langle \phi_{k\alpha} | \phi_{k'\beta} \rangle = \frac{(2\pi)^D}{V_{\text{cell}}} \delta^D(\mathbf{k} - \mathbf{k}') \delta_{\alpha\beta}, \quad (6)$$

where $\int_{\text{BZ}} d^D k$ is the integral over the Brillouin zone and V_{cell} is the volume of the D -dimensional unit cell, follows

$$\hat{H} = \frac{V_{\text{cell}}}{(2\pi)^D} \int_{\text{BZ}} d^D k \sum_{\alpha\beta} H_{\alpha\beta}(\mathbf{k}) |\phi_{k\alpha}\rangle \langle \phi_{k\beta}|, \quad (7)$$

where

$$H_{\alpha\beta}(\mathbf{k}) = \sum_{\Delta R} H_{\alpha\beta}(\Delta R) e^{i\mathbf{k} \cdot (\Delta R + \boldsymbol{\tau}_{\beta} - \boldsymbol{\tau}_{\alpha})} \quad (8)$$

is the tight-binding Bloch Hamiltonian.

The eigenvalues $E_n(\mathbf{k})$ of $H_{\alpha\beta}(\mathbf{k})$ for all \mathbf{k} within the first Brillouin zone will give the band structure consisting, in general, of $n = 1, 2, \dots, M$ bands. We can expand the eigenstates as

$$|\psi_{nk}\rangle = \sum_{\alpha} C_n^{\alpha}(\mathbf{k}) |\phi_{k\alpha}\rangle, \quad (9)$$

where n is the band index. We normalize $\sum_{\alpha} |C_n^{\alpha}(\mathbf{k})|^2 = 1$ so that

$$\langle \psi_{nk'} | \psi_{nk} \rangle = \frac{(2\pi)^D}{V_{\text{cell}}} \delta^D(\mathbf{k} - \mathbf{k}'). \quad (10)$$

Plugging this into the time-independent Schrödinger equation,

$$E_n(\mathbf{k}) |\psi_{nk}\rangle = \hat{H} |\psi_{nk}\rangle, \quad (11)$$

with the Hamiltonian (7), using Eq. (6), and multiplication from the left by $\langle \phi_{k\alpha} |$ leads to

$$E_n(\mathbf{k}) C_n^{\alpha}(\mathbf{k}) = \sum_{\gamma} H_{\alpha\gamma}(\mathbf{k}) C_n^{\gamma}(\mathbf{k}), \quad (12)$$

or, in matrix notation,

$$E_n(\mathbf{k}) \mathbf{C}_n(\mathbf{k}) = \mathbf{H}(\mathbf{k}) \mathbf{C}_n(\mathbf{k}). \quad (13)$$

B. Case of a 2×2 Bloch Hamiltonian

If there are only two orbitals $\alpha = 1, 2$ per unit cell in (1), may they be the two ground states of two atoms at different positions $\boldsymbol{\tau}_{\alpha}$ or the lowest two states in one atom per unit cell, the Bloch-Hamiltonian matrix $\mathbf{H}(\mathbf{k})$ in (13) is 2×2 , leading to two bands. Topological effects arise because of the closing and reopening of a band gap as a function of some parameter in $\mathbf{H}(\mathbf{k})$. Hence, the study of the two bands whose band gap closes and reopens and the corresponding 2×2 Bloch Hamiltonian is usually sufficient. Prime examples for such systems described by 2×2 Bloch Hamiltonians are the SSH chain [2,26] and the Haldane model [28] both of which will be discussed in this work in the context of HHG.

Writing $n = \pm$ instead of $n = 1, 2$ for the two bands, where $+$ denotes the energetically higher conduction band and $-$ the lower valence band, the eigenvalue equation (13) becomes

$$E_{\pm}(\mathbf{k}) \mathbf{C}_{\pm}(\mathbf{k}) = \mathbf{H}(\mathbf{k}) \mathbf{C}_{\pm}(\mathbf{k}). \quad (14)$$

The Hermitian 2×2 Bloch Hamiltonian can be expanded in Pauli matrices,

$$\mathbf{H}(\mathbf{k}) = \mathbf{d}(\mathbf{k}) \cdot \boldsymbol{\sigma}, \quad (15)$$

where $\mathbf{d}(\mathbf{k}) = (d_x(\mathbf{k}), d_y(\mathbf{k}), d_z(\mathbf{k}))^T \in \mathbb{R}^3$ is a three-component vector, and $\boldsymbol{\sigma} = (\sigma_x, \sigma_y, \sigma_z)^T$ is the three-component vector of Pauli matrices,

$$\sigma_x = \begin{pmatrix} 0 & 1 \\ 1 & 0 \end{pmatrix}, \quad \sigma_y = \begin{pmatrix} 0 & -i \\ i & 0 \end{pmatrix}, \quad \sigma_z = \begin{pmatrix} 1 & 0 \\ 0 & -1 \end{pmatrix}. \quad (16)$$

There could be also a term $d_0 \mathbf{1}$ proportional to the 2×2 unity matrix. However, in this work we only discuss systems with $d_0 = 0$. Further, we consider only Hermitian $\mathbf{H}(\mathbf{k})$ in this work so that $\mathbf{d}(\mathbf{k})$ is real.

The tight-binding representation of the system in position space might be of arbitrary dimension D , resulting in D components of the lattice momentum \mathbf{k} . For the SSH model, \mathbf{k} has

just one component k , and for the Haldane model, $\mathbf{k} \in \mathbb{R}^2$. Anyhow, we can write

$$\mathbf{H}(\mathbf{k}) = \begin{pmatrix} d_z(\mathbf{k}) & d_x(\mathbf{k}) - id_y(\mathbf{k}) \\ d_x(\mathbf{k}) + id_y(\mathbf{k}) & -d_z(\mathbf{k}) \end{pmatrix}, \quad (17)$$

with eigenvalues,

$$E_{\pm}(\mathbf{k}) = \pm|\mathbf{d}(\mathbf{k})| = \pm d(\mathbf{k}). \quad (18)$$

We recognize that the specific information about the actual system under consideration lies in the dependence of \mathbf{d} on \mathbf{k} . As long as we are general, we will suppress the \mathbf{k} dependence in the expressions, i.e.,

$$\mathbf{H}(\mathbf{d}) = \begin{pmatrix} d_z & d_x - id_y \\ d_x + id_y & -d_z \end{pmatrix}, \quad (19)$$

with eigenvalues,

$$E_{\pm}(\mathbf{d}) = \pm d. \quad (20)$$

We assume the eigenvectors $\mathbf{C}_{\pm}(\mathbf{k})$ to be normalized, which still leaves the structure-gauge freedom [35] that allows for transformations,

$$\mathbf{C}'_{\pm}(\mathbf{k}) = \exp[i\chi_{\pm}(\mathbf{k})]\mathbf{C}_{\pm}(\mathbf{k}), \quad (21)$$

with some real, differentiable functions $\chi_{\pm}(\mathbf{k})$, without affecting observables such as velocity or current. A possible eigenvector belonging to $E_+(\mathbf{d})$ is

$$\mathbf{C}_+(\mathbf{d}) = \frac{1}{\sqrt{2}} \begin{pmatrix} \sqrt{1+d_z/d} \\ \frac{d_x+id_y}{d_{\perp}} \sqrt{1-d_z/d} \end{pmatrix}, \quad (22)$$

and for $E_-(\mathbf{d})$,

$$\mathbf{C}_-(\mathbf{d}) = \mathbf{C}_+(-\mathbf{d}) = \frac{1}{\sqrt{2}} \begin{pmatrix} \sqrt{1-d_z/d} \\ -\frac{d_x+id_y}{d_{\perp}} \sqrt{1+d_z/d} \end{pmatrix}, \quad (23)$$

where $d_{\perp} = \sqrt{d_x^2 + d_y^2}$. In the literature, the topological properties of the 2×2 Bloch Hamiltonian are conveniently discussed using the Bloch-sphere angles θ, φ , i.e., $\cos \theta = d_z/d$ and $e^{i\varphi} = (d_x + id_y)/(d \sin \theta)$ [2,13]. However, there is no benefit in doing so for our purpose, hence we stick with the Cartesian representation in \mathbf{d} space.

C. Coupling to an external laser field and equations of motion

If an explicitly time-dependent driver, e.g., a laser, is added to the original Hamiltonian \hat{H} the hopping elements in the Hamiltonian $H_{\alpha\beta}(\Delta\mathbf{R})$ in (3) become time dependent, too, and the time-dependent Schrödinger equation reads

$$i\partial_t|\Psi(t)\rangle = \sum_{\Delta\mathbf{R}\alpha\beta} H_{\alpha\beta}(\Delta\mathbf{R}, t) \sum_{\mathbf{R}} |\phi_{\mathbf{R}\alpha}\rangle \langle \phi_{\Delta\mathbf{R}+\mathbf{R},\beta} | \Psi(t)\rangle. \quad (24)$$

$$i \begin{pmatrix} \dot{\alpha}_{k_+}(t) \\ \dot{\alpha}_{k_-}(t) \end{pmatrix} = \begin{pmatrix} E_+(\tilde{\mathbf{d}}) - i\mathbf{C}_+^{\dagger}(\tilde{\mathbf{d}}) \cdot \dot{\mathbf{C}}_+(\tilde{\mathbf{d}}) & -i\mathbf{C}_+^{\dagger}(\tilde{\mathbf{d}}) \cdot \dot{\mathbf{C}}_-(\tilde{\mathbf{d}}) \\ -i\mathbf{C}_-^{\dagger}(\tilde{\mathbf{d}}) \cdot \dot{\mathbf{C}}_+(\tilde{\mathbf{d}}) & E_-(\tilde{\mathbf{d}}) - i\mathbf{C}_-^{\dagger}(\tilde{\mathbf{d}}) \cdot \dot{\mathbf{C}}_-(\tilde{\mathbf{d}}) \end{pmatrix} \begin{pmatrix} \alpha_{k_+}(t) \\ \alpha_{k_-}(t) \end{pmatrix}. \quad (31)$$

Now we could perform a gauge transformation of the eigenvectors $\mathbf{C}_{\pm}(\tilde{\mathbf{d}})$ in (22) and (23) in order to fulfill the

Care has to be exercised to ensure that the tight-binding hopping Hamiltonian leads to gauge-invariant results with respect to the coupling to external fields [36]. The fact that the usual Peierls substitution obeys this gauge invariance of length and velocity gauge for finite SSH chains was shown explicitly in [25].

If the Bloch ansatz is chosen properly, the coupling to a laser field in dipole approximation amounts to the replacement,

$$\mathbf{k} \longrightarrow \mathbf{k}(t) = \mathbf{k} + \mathbf{A}(t), \quad (25)$$

in the Bloch Hamiltonian, where $\mathbf{A}(t)$ is the vector potential. In Appendix A, we show exemplarily for the SSH chain that this does not hold for the “wrong” Bloch ansatz without the τ_{α} in (4) sometimes adopted in the literature. Moreover, the ansatz without the τ_{α} in (4) complicates the calculation of the correct velocity or current responsible for HHG because both are then not simply proportional to the expectation value of $\nabla_{\mathbf{k}}\mathbf{H}(\mathbf{k})$.

Given that we choose the proper Bloch ansatz (4), the time-dependent Schrödinger equation (24) boils down to

$$i\dot{\mathbf{C}}(\mathbf{k}, t) = \mathbf{H}(\tilde{\mathbf{d}})\mathbf{C}(\mathbf{k}, t), \quad \tilde{\mathbf{d}} = \mathbf{d}[\mathbf{k}(t)]. \quad (26)$$

Typically, the propagation for a given \mathbf{k} starts at $t = 0$ with the electron in the valence band, $\mathbf{C}(\mathbf{k}, 0) = \mathbf{C}_-(\mathbf{k})$. The expectation value of the velocity in direction $j = 1, 2, \dots, D$ is given by (see Sec. IID)

$$v_j(\mathbf{k}, t) = \mathbf{C}^{\dagger}(\mathbf{k}, t) \partial_{k_j} \mathbf{H}(\tilde{\mathbf{d}}) \mathbf{C}(\mathbf{k}, t). \quad (27)$$

HHG spectra can then be calculated by Fourier transforming the \mathbf{k} -integrated acceleration $\dot{v}_j(t)$ [32–34], where

$$v_j(t) = \frac{V_{\text{cell}}}{(2\pi)^D} \int_{\text{BZ}} d^D k v_j(\mathbf{k}, t). \quad (28)$$

While Eq. (26) is, from the numerical point of view, most convenient to solve and, in fact, is used to obtain reference results for HHG spectra, it is not yet suited to gain insight into the HHG process, let alone to identify nontrivial topological effects. We therefore proceed and expand in quasistatic states,

$$\mathbf{C}(\mathbf{k}, t) = \alpha_{k_-}(t)\mathbf{C}_-(\tilde{\mathbf{d}}) + \alpha_{k_+}(t)\mathbf{C}_+(\tilde{\mathbf{d}}), \quad (29)$$

where the adiabatic states $\mathbf{C}_{\pm}(\tilde{\mathbf{d}})$ fulfill

$$E_{\pm}(\tilde{\mathbf{d}})\mathbf{C}_{\pm}(\tilde{\mathbf{d}}) = \mathbf{H}(\tilde{\mathbf{d}})\mathbf{C}_{\pm}(\tilde{\mathbf{d}}). \quad (30)$$

The equation of motion for $\alpha_{k_{\pm}}(t)$ follows from (26) and reads

so-called parallel-transport gauge [2,14] condition for the Berry connection, i.e., $i\mathbf{C}_{\pm}^{\dagger}(\tilde{\mathbf{d}}) \cdot \dot{\mathbf{C}}_{\pm}(\tilde{\mathbf{d}}) = 0$. However, this

gauge transformation will affect the cross terms $i\mathbf{C}_{\pm}^{\dagger}(\tilde{\mathbf{d}}) \cdot \dot{\mathbf{C}}_{\mp}(\tilde{\mathbf{d}})$ such that, in the end, the same equations are found for observables such as velocities or currents. Hence we

keep (22) and (23) and do not assume $i\mathbf{C}_{\pm}^{\dagger}(\tilde{\mathbf{d}}) \cdot \dot{\mathbf{C}}_{\pm}(\tilde{\mathbf{d}}) = 0$. The diagonal elements can be transformed away by the substitution,

$$\alpha_{k\pm}(t) = \eta_{k\pm}(t) e^{-i \int^t (E_{\pm}(\tilde{\mathbf{d}}) - i\mathbf{C}_{\pm}^{\dagger}(\tilde{\mathbf{d}}) \cdot \dot{\mathbf{C}}_{\pm}(\tilde{\mathbf{d}})) dt'}, \quad (32)$$

where, under the integral in the exponent, $\tilde{\mathbf{d}} = \mathbf{d}[\mathbf{k}(t')]$, leading to

$$i \begin{pmatrix} \dot{\eta}_{k+}(t) \\ \dot{\eta}_{k-}(t) \end{pmatrix} = \begin{pmatrix} 0 & -\mathcal{A}_{+-}(\tilde{\mathbf{d}}) e^{i \int^t (\Delta E(\tilde{\mathbf{d}}) - \Delta \mathcal{A}(\tilde{\mathbf{d}})) dt'} \\ -\mathcal{A}_{-+}(\tilde{\mathbf{d}}) e^{-i \int^t (\Delta E(\tilde{\mathbf{d}}) - \Delta \mathcal{A}(\tilde{\mathbf{d}})) dt'} & 0 \end{pmatrix} \begin{pmatrix} \eta_{k+}(t) \\ \eta_{k-}(t) \end{pmatrix}. \quad (33)$$

Here,

$$\Delta E(\tilde{\mathbf{d}}) = E_+(\tilde{\mathbf{d}}) - E_-(\tilde{\mathbf{d}}) = 2|\tilde{\mathbf{d}}| = 2\tilde{d} \quad (34)$$

is the energy difference between conduction and valence band,

$$\mathcal{A}_{\pm\pm}(\tilde{\mathbf{d}}) = i\mathbf{C}_{\pm}^{\dagger}(\tilde{\mathbf{d}}) \cdot \dot{\mathbf{C}}_{\pm}(\tilde{\mathbf{d}}) \quad (35)$$

are the intraband Berry connections,

$$\mathcal{A}_{\pm\mp}(\tilde{\mathbf{d}}) = i\mathbf{C}_{\pm}^{\dagger}(\tilde{\mathbf{d}}) \cdot \dot{\mathbf{C}}_{\mp}(\tilde{\mathbf{d}}) \quad (36)$$

are the interband Berry connections, and

$$\Delta \mathcal{A}(\tilde{\mathbf{d}}) = \mathcal{A}_{++}(\tilde{\mathbf{d}}) - \mathcal{A}_{--}(\tilde{\mathbf{d}}). \quad (37)$$

The functions $\eta_{k\pm}(t)$ are invariant under structure-gauge transformations (21). In terms of $\tilde{\mathbf{d}}$, we find for the Berry connections, using $\frac{d}{dt} = \sum_{j=1}^D \dot{k}_j \partial_{k_j}$ and

$$\mathcal{D}_j(a, b) = a \partial_{k_j} b - b \partial_{k_j} a, \quad (38)$$

$$\mathcal{A}_{++}(\tilde{\mathbf{d}}) = -\frac{\sum_j \dot{k}_j \mathcal{D}_j(\tilde{d}_x, \tilde{d}_y)}{2\tilde{d}(\tilde{d} + \tilde{d}_z)}, \quad (39)$$

$$\mathcal{A}_{--}(\tilde{\mathbf{d}}) = -\frac{\sum_j \dot{k}_j \mathcal{D}_j(\tilde{d}_x, \tilde{d}_y)}{2\tilde{d}(\tilde{d} - \tilde{d}_z)} = \mathcal{A}_{++}(-\tilde{\mathbf{d}}), \quad (40)$$

$$\mathcal{A}_{+-}(\tilde{\mathbf{d}}) = \frac{\sum_j \dot{k}_j (\mathcal{D}_j(\tilde{d}_x, \tilde{d}_y) + i\mathcal{D}_j(\tilde{d}_z, \tilde{d}))}{2\tilde{d}\tilde{d}_{\perp}}, \quad (41)$$

$$\mathcal{A}_{-+}(\tilde{\mathbf{d}}) = \mathcal{A}_{+-}^*(\tilde{\mathbf{d}}), \quad (42)$$

$$\Delta \mathcal{A}(\tilde{\mathbf{d}}) = \frac{\tilde{d}_z}{\tilde{d}\tilde{d}_{\perp}^2} \sum_j \dot{k}_j \mathcal{D}_j(\tilde{d}_x, \tilde{d}_y). \quad (43)$$

D. Electron velocity

With the proper Bloch ansatz, the velocity operator for an initial \mathbf{k} and in direction j becomes the 2×2 matrix,

$$\mathbf{v}_j(\tilde{\mathbf{d}}) = \partial_{k_j} \mathbf{H}(\tilde{\mathbf{d}}) = \partial_{k_j} \tilde{\mathbf{d}} \cdot \boldsymbol{\sigma}. \quad (44)$$

Since $\tilde{\mathbf{d}} = \mathbf{d}[\mathbf{k}(t)] = \mathbf{d}[\mathbf{k} + \mathbf{A}(t)]$ we understand that $\partial_{k_j} \mathbf{H}(\tilde{\mathbf{d}}) = \partial_{k_j} \mathbf{H}(\mathbf{k})|_{\mathbf{k}+\mathbf{A}(t)}$. The expectation value for the velocity in direction j of a laser-driven electron starting at lattice momentum \mathbf{k} thus is

$$v_j(\mathbf{k}, t) = \mathbf{C}^{\dagger}(\mathbf{k}, t) \mathbf{v}_j(\tilde{\mathbf{d}}) \mathbf{C}(\mathbf{k}, t) \quad (45)$$

$$= v_j^{-}(\mathbf{k}, t) + v_j^{++}(\mathbf{k}, t) + v_j^{+-}(\mathbf{k}, t) + v_j^{+-}(\mathbf{k}, t), \quad (46)$$

where, using (29) and (32),

$$v_j^{-}(\mathbf{k}, t) = |\eta_{k-}(t)|^2 \mathbf{C}_{-}^{\dagger}(\tilde{\mathbf{d}}) \mathbf{v}_j(\tilde{\mathbf{d}}) \mathbf{C}_{-}(\tilde{\mathbf{d}}), \quad (47)$$

$$v_j^{++}(\mathbf{k}, t) = |\eta_{k+}(t)|^2 \mathbf{C}_{+}^{\dagger}(\tilde{\mathbf{d}}) \mathbf{v}_j(\tilde{\mathbf{d}}) \mathbf{C}_{+}(\tilde{\mathbf{d}}), \quad (48)$$

and

$$v_j^{+-}(\mathbf{k}, t) = \eta_{k-}^*(t) \eta_{k+}(t) e^{-i \int^t (\Delta E(\tilde{\mathbf{d}}) - \Delta \mathcal{A}(\tilde{\mathbf{d}})) dt'} \times \mathbf{C}_{-}^{\dagger}(\tilde{\mathbf{d}}) \mathbf{v}_j(\tilde{\mathbf{d}}) \mathbf{C}_{+}(\tilde{\mathbf{d}}), \quad (49)$$

$$v_j^{+-}(\mathbf{k}, t) = [v_j^{-}(\mathbf{k}, t)]^*. \quad (50)$$

After a cumbersome but straightforward calculation, we obtain

$$v_j^{\pm\pm}(\mathbf{k}, t) = \pm |\eta_{\pm k}(t)|^2 \partial_{k_j} \tilde{d}, \quad (51)$$

$$v_j^{-+}(\mathbf{k}, t) = -\eta_{k-}^*(t) \eta_{k+}(t) e^{-i \int^t [2\tilde{d} - \Delta \mathcal{A}(\tilde{\mathbf{d}})] dt'} \times \frac{1}{\tilde{d}_{\perp}} [\mathcal{D}_j(\tilde{d}_z, \tilde{d}) + i\mathcal{D}_j(\tilde{d}_x, \tilde{d}_y)], \quad (52)$$

$$v_j^{+-}(\mathbf{k}, t) = [v_j^{-+}(\mathbf{k}, t)]^*. \quad (53)$$

The velocity components (51) do not mix $\eta_{+k}(t)$ and $\eta_{-k}(t)$ and hence might be called intraband velocities. We see that these two intraband velocities are in opposite directions because of the symmetry in the dispersion relation $E_{\pm}(\mathbf{k}) = \pm d(\mathbf{k})$. The weighting factors $|\eta_{\pm k}(t)|^2$ account for the populations of the two bands. Berry curvature effects come into play through the velocity contributions (52) and (53) that do mix $\eta_{+k}(t)$ and $\eta_{-k}(t)$, and thus might be called interband velocities. A similar observation has been made in [30,35] for the relation between dipole transition matrix elements and the Berry curvature. The total \mathbf{k} -resolved velocity expectation value in direction j is

$$v_j(\mathbf{k}, t) = (|\eta_{k+}(t)|^2 - |\eta_{k-}(t)|^2) \partial_{k_j} \tilde{d} + 2 \text{Re } v_j^{-+}(\mathbf{k}, t). \quad (54)$$

The first term is the expected group velocity, and the second term is the anomalous velocity, including all topological effects. Integration over the Brillouin zone yields the total velocity in direction j ,

$$v_j(t) = \frac{V_{\text{cell}}}{(2\pi)^D} \int_{\text{BZ}} d^D k v_j(\mathbf{k}, t), \quad (55)$$

which is proportional to the current if the correct Bloch ansatz is chosen.

E. Lewenstein-like model for high-harmonic generation in two-band systems

The intraband velocities have the simple form of the populations $|\eta_{k\pm}(t)|^2$ in the respective band times the corresponding group velocities $[\partial_{k_j} E_{\pm}(\mathbf{k})]_{k+A(t)} = \pm \partial_{k_j} \tilde{d}$.

Harmonic generation by the interband velocity $2 \operatorname{Re} v_j^{-+}(\mathbf{k}, t)$ might be viewed similar to the three-step HHG in atomic gas targets [37]: (i) the electron makes a vertical transition from the valence to the conduction band, (ii) the electron oscillates in the conduction band, and (iii) the electron recombines into the valence band upon emission of a photon whose energy equals the band gap at the \mathbf{k} point where recombination takes place. In that picture, it is assumed that the laser field does not strongly affect the band structure so that harmonics up to the maximum field-free band gap are expected.

Intuitively, one might think that harmonic spectra calculated from the intraband velocity alone do not show a plateau up to the maximum energy gap but only low-order harmonics. However, this is not true, as the energy gap $2d(\mathbf{k})$ enters the expression for $\eta_{k+}(t)$; see Eq. (56).

The initial conditions, describing a fully occupied valence band and an empty conduction band, read $\alpha_{k+}(0) = \eta_{k+}(0) = 0$ and $\alpha_{k-}(0) = \eta_{k-}(0) = 1$. The assumption in the Lewenstein paper on gas HHG [38] that depletion of the population in the electronic ground state is negligible in the parameter regime of interest translates to $\eta_{k-}(t) \simeq 1$. Note that the assumption $\alpha_{k-}(t) \simeq 1$ is not valid because of the complex phase that $\alpha_{k-}(t)$ accumulates (even without laser). With $\eta_{k-}(t) \simeq 1$ at all times we find [39]

$$\eta_{k+}(t) = i \int^t \mathcal{A}_{+-}(\tilde{\mathbf{d}}) e^{i \int' [2\tilde{d} - \Delta A(\tilde{\mathbf{d}})] dt''} dt'. \quad (56)$$

As a consequence, Eq. (54) becomes

$$v_j(\mathbf{k}, t) \simeq (|\eta_{k+}(t)|^2 - 1) \partial_{k_j} \tilde{d} + 2 \operatorname{Re} v_j^{-+}(\mathbf{k}, t), \quad (57)$$

with

$$v_j^{-+}(\mathbf{k}, t) \simeq \tilde{\mathcal{A}}_{-+}^j(\tilde{\mathbf{d}}) \int^t \mathcal{A}_{+-}(\tilde{\mathbf{d}}) e^{-iS(\mathbf{k}, t', t)} dt' \quad (58)$$

where

$$\tilde{\mathcal{A}}_{-+}^j(\tilde{\mathbf{d}}) = \tilde{\mathcal{A}}_{+-}^{j*}(\tilde{\mathbf{d}}) = \frac{1}{\tilde{d}_{\pm}} [\mathcal{D}_j(\tilde{d}_x, \tilde{d}_y) - i \mathcal{D}_j(\tilde{d}_z, \tilde{d})], \quad (59)$$

and the action $S(\mathbf{k}, t', t)$ is

$$S(\mathbf{k}, t', t) = \int_{t'}^t [2\tilde{d} - \Delta A(\tilde{\mathbf{d}})] dt''. \quad (60)$$

The set of equations (56)–(60) for the (\mathbf{k} -resolved) electron velocity is the main result of this work. It provides an explicit expression of the total velocity in terms of $\tilde{\mathbf{d}}(\mathbf{k})$ defining the system under consideration. Topological effects are included via the interband velocity (58). Hence, topologically interesting changes in the chirality of the current (e.g., clockwise or counterclockwise around a certain \mathbf{k} point) can be analyzed. One may also “reverse engineer” a topologically interesting system by defining $\tilde{\mathbf{d}}$ such that the interband current yields the desired (laser-driven) electron dynamics. Of course, a system designed in such a way may correspond to weird hoppings

in position space (an example being the Qi-Wu-Zhang toy model [2,29] with a simple $\tilde{\mathbf{d}}$ but complicated position-space hoppings).

Note that we did neither apply a single-band approximation or semiclassical wave-packet dynamics nor is our result restricted to particular dimensions. As a consequence, the velocity (57) is more general than the commonly employed $\mathbf{v} = \nabla_{\mathbf{k}} E(\mathbf{k}) - \dot{\mathbf{k}} \times \boldsymbol{\Omega}(\mathbf{k})$ [40,41], where $\boldsymbol{\Omega}(\mathbf{k})$ is the Berry curvature.

The \mathbf{k} -integrated interband velocity that will, after Fourier transformation, contribute to interband HHG, reads $2 \operatorname{Re} v_j^{-+}(t)$ with

$$v_j^{-+}(t) \simeq \frac{V_{\text{cell}}}{(2\pi)^D} \int_{\text{BZ}} d^D k \tilde{\mathcal{A}}_{-+}^j(\tilde{\mathbf{d}}) \times \int^t \mathcal{A}_{+-}(\tilde{\mathbf{d}}) e^{-iS(\mathbf{k}, t', t)} dt'. \quad (61)$$

The structure of this expression is the same as for the dipole in the celebrated Lewenstein paper on HHG in gases [38] so that one could embark on transferring all steps outlined there to solids.

The analogy between the three-step model in gas HHG and interband HHG in solids is well known [37]. In [42], a mixed Wannier-Bloch representation is employed for the valence band (Wannier) and conduction band (Bloch), which elucidates the similarity between gas-phase and solid HHG most clearly because Wannier functions are localized in position space (like the ground-state wave function in atomic HHG). In that way one can follow where electrons start and recombine in position space. However, for all practical purposes crucial differences between gas-phase HHG and HHG in solids are the following. First, the action in the gas-phase HHG is simple and reads $S(\mathbf{p}, t', t) = \int_{t'}^t \{[\mathbf{p} + \mathbf{A}(t'')]^2/2 + I_p\} dt''$ where \mathbf{p} is the canonical momentum of the electron and I_p is the ionization potential of the atom. Instead, the functional dependence of the action (60) on \mathbf{k} is rather involved even for the simplest model solids so that the time integral—after insertion of $\mathbf{k}(t)$ —cannot be performed analytically. Second, the dipole transition matrix elements in atomic HHG are rather simple whereas the interband couplings in (33) and the interband velocity (52) expressed explicitly in terms of $\tilde{\mathbf{d}}$ are rather involved. By making approximations to these couplings one may easily sweep topological effects under the carpet, as was also pointed out recently in [35]. The main objective of our paper is to provide explicit, analytical expressions for the velocity, including all topological effects and without any approximations besides tight binding and the restriction to two bands. Further, we note in passing that the \mathbf{k} integration in the solid-state result (61) is performed because all \mathbf{k} states in the valence band are initially populated. Hence, HHG in solids, described by Eq. (61), includes many-electron effects such as the interference of the radiation emitted by “individual” electrons while interaction between the electrons is not taken into account. Instead, the \mathbf{p} integration in gas-phase HHG arises already for a single active electron.

In the Lewenstein paper on gas HHG [38], the integration over the electron’s canonical momentum \mathbf{p} is performed using saddle-point integration. The beauty is that the saddle-point integration there is not just a mathematical trick but allows

for an intuitive interpretation: Only those semiclassical trajectories contribute to HHG that start at the ionization time t' at the origin (where the parent ion is located) and return to the origin at the recombination time t . This makes sense because recombination can only take place at the position of the ion. We may try to proceed analogously to the Lewenstein paper and perform in (61) the integration with respect to \mathbf{k} by searching for stationary $\mathbf{k}_{\text{st}}(t, t')$ that fulfill

$$\nabla_{\mathbf{k}} S(\mathbf{k}, t', t) = \mathbf{0}. \quad (62)$$

If there was not the $\Delta\mathcal{A}(\mathbf{d})$ term in the action (60) we would obtain

$$\mathbf{0} = \nabla_{\mathbf{k}} S(\mathbf{k}, t', t) = 2 \int_{t'}^t \nabla_{\mathbf{k}} \tilde{\mathcal{A}} dt'' = -2 \int_{t'}^t \mathbf{v}^{--}(\mathbf{k}, t'') dt'',$$

from which follows

$$\mathbf{r}(\mathbf{k}, t) - \mathbf{r}(\mathbf{k}, t') = \mathbf{0},$$

where we have defined formally a position,

$$\mathbf{r}(\mathbf{k}, t) = \int_{t'}^t \mathbf{v}^{--}(\mathbf{k}, t'') dt''.$$

Hence, we find formally the same result as for HHG in atoms: The semiclassical electron trajectory returns to its starting point *in position space*. This semiclassical viewpoint also emerged in the studies of HHG in solids based on optical Bloch equations [37]. However, incomplete returns also contribute to HHG in solids [43].

In atomic HHG, the saddle-point equation $\nabla_{\mathbf{p}} S(\mathbf{p}, t', t) = \mathbf{0}$ can be easily evaluated and solved explicitly for the stationary momentum $\mathbf{p}_{\text{st}}(t, t')$. Due to the more involved dispersion relations and the possible presence of the Berry term $\Delta\mathcal{A}(\mathbf{d})$ in the case of solids, it is not possible to find explicit expressions for $\mathbf{k}_{\text{st}}(t, t')$. If the laser field is sufficiently weak such that $A(t)$ is much smaller than the dimensions of the Brillouin zone, one may expand the integrand in $S(\mathbf{k}, t', t)$ up to $A^2(t'')$ and perform the time integral over t'' . In that way it is possible to factorize \mathbf{k} dependence and time dependence in the action. Yet, the result will still have a too complicated dependence on \mathbf{k} to find explicit expressions for $\mathbf{k}_{\text{st}}(t, t')$. However, a graphical or numerical solution would yield, for given excitation and recombination times t', t , the dominating \mathbf{k} , which might be useful for the analysis or interpretation of numerically obtained results. The numerical calculation of entire HHG spectra in this way is not recommended, as it would be much less efficient than simply solving the differential equation (26) numerically.

III. RESULTS

We now test the validity of our theory by applying it to two prime examples of model systems described by 2×2 Bloch Hamiltonians: the SSH chain and the Haldane model.

A. SSH case

In Appendix A, we introduce the position-space representation of the SSH Hamiltonian and derive the Bloch

Hamiltonian,

$$\begin{aligned} \mathbf{H}(\mathbf{k}) &= \begin{pmatrix} 0 & ve^{ik/2} + we^{-ik/2} \\ ve^{-ik/2} + we^{ik/2} & 0 \end{pmatrix} \\ &= (v+w) \cos(k/2) \sigma_x + (w-v) \sin(k/2) \sigma_y, \end{aligned} \quad (63)$$

such that the velocity operator is indeed $\partial_{\mathbf{k}} H(\tilde{\mathbf{d}})$, and the current is proportional to it. We choose real v and w , and a lattice constant $a = 1$. Obviously,

$$\mathbf{d} = \begin{pmatrix} (w+v) \cos(k/2) \\ (w-v) \sin(k/2) \\ 0 \end{pmatrix}, \quad (64)$$

the dispersion relation is

$$E_{\pm}(k) = \pm d = \pm \sqrt{w^2 + v^2 + 2wv \cos k}, \quad (65)$$

and $d = d_{\perp}$. There is only one direction $j = 1$, and the driver A is necessarily parallel to it. Equation (56) becomes in this case,

$$\eta_{k+}(t) = \frac{i(w^2 - v^2)}{4} \int_{t'}^t dt' \frac{\dot{A}(t')}{E_{\pm}^2(k + A(t'))} e^{ij' 2E_{\pm}(k + A(t')) dt''},$$

and Eq. (58) reads

$$\begin{aligned} v^{--}(k, t) &\simeq \frac{(w^2 - v^2)^2}{8E_{\pm}(k + A(t))} \int_{t'}^t dt' \frac{\dot{A}(t')}{E_{\pm}^2(k + A(t'))} \\ &\times e^{-i \int_{t'}^t 2E_{\pm}(k + A(t')) dt''}. \end{aligned} \quad (66)$$

This interband velocity is inserted into (57).

It is known that the topological phase transition of the SSH chain occurs at $w = v$, with $w > v$ giving rise to the nontrivial topological phase, with edge states in finite SSH chains [2]. However, both the intraband velocity $|\eta_{k+}(t)|^2 \partial_{\mathbf{k}} \tilde{\mathbf{d}}$ and the interband velocity (66) are proportional to $(w^2 - v^2)^2$, i.e., completely symmetric under an exchange $w \leftrightarrow v$ so that there is no way to distinguish the trivial and the nontrivial topological phase via HHG in SSH bulk. In fact, for periodic boundary conditions the dangling sites for $w > v$ in a finite chain pair-up, and the velocity expectation value should be invariant under the exchange $v \leftrightarrow w$. In contrast, in finite systems, where the edge states show up explicitly in the topologically nontrivial SSH phase $w > v$, huge differences in the HHG yield between trivial and nontrivial topological phase are observed [23–25].

The k integration required in (61) is performed numerically by sampling the Brillouin zone $[-\pi, \pi]$ with N_k equidistant k values. The result should be the same as that for a calculation in position space with $N = N_k$ unit cells and periodic boundary condition.

Figure 1 shows the HHG spectrum for the SSH chain with $v = -e^{-1.7} \simeq -0.1827$, $w = -e^{-2.3} \simeq -0.1003$ in a laser field of the form,

$$A(t) = A_0 \sin^2 \left(\frac{\omega t}{2n_{\text{cyc}}} \right) \sin \omega t, \quad (67)$$

with $A_0 = 0.1$, $\omega = 0.0075$, $n_{\text{cyc}} = 5$, calculated by Fourier transforming the first time derivative of the velocity expectation value (i.e., the acceleration). We have checked that

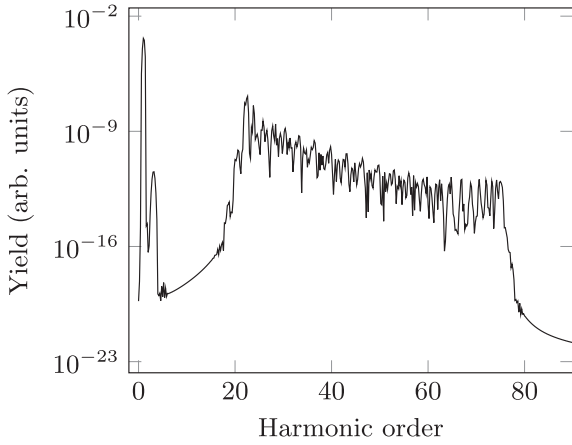


FIG. 1. HHG spectrum for a SSH chain in a laser field with vector potential (67) (SSH and laser parameters are given in the text).

$$\mathbf{H}(\mathbf{k}) = \begin{pmatrix} M + t_2 \sum_n e^{-ik \cdot \mathbf{g}_n} + t_2^* \sum_n e^{ik \cdot \mathbf{g}_n} & t_1 \sum_n e^{ik \cdot \delta_n} \\ t_1 \sum_n e^{-ik \cdot \delta_n} & -M + t_2 \sum_n e^{ik \cdot \mathbf{g}_n} + t_2^* \sum_n e^{-ik \cdot \mathbf{g}_n} \end{pmatrix} \\ = 2\text{Re}(t_2) \sum_n \cos(\mathbf{k} \cdot \mathbf{g}_n) \mathbf{1} + t_1 \sum_n \cos(\mathbf{k} \cdot \delta_n) \sigma_x - t_1 \sum_n \sin(\mathbf{k} \cdot \delta_n) \sigma_y + (M + 2\text{Im}(t_2) \sum_n \sin(\mathbf{k} \cdot \mathbf{g}_n)) \sigma_z. \quad (68)$$

The real part of the next-nearest neighbor hopping amplitude t_2 shifts the energy but does not change the energy difference between both bands. As a consequence, the derivative of the band structure might be influenced, which changes the intraband velocity. However, in this work we choose a purely imaginary t_2 . Further studies might investigate the influence of a nonvanishing real part of t_2 . We obtain for the \mathbf{d} vector in (15),

$$\mathbf{d}(\mathbf{k}) = \begin{pmatrix} t_1 \sum_n \cos(\mathbf{k} \cdot \delta_n) \\ -t_1 \sum_n \sin(\mathbf{k} \cdot \delta_n) \\ M + 2\text{Im}(t_2) \sum_n \sin(\mathbf{k} \cdot \mathbf{g}_n) \end{pmatrix}, \quad (69)$$

and

$$d_{\perp} = \sqrt{|t_1|^2 (3 + 2 \sum_n \cos(\mathbf{k} \cdot \mathbf{g}_n))}, \quad (70)$$

$$d = \sqrt{d_{\perp}^2 + (M + 2\text{Im}(t_2) \sum_n \sin(\mathbf{k} \cdot \mathbf{g}_n))^2}. \quad (71)$$

In the following, we show exemplarily results for HHG due to laser-driven electron dynamics around the K point and the K' point for the topologically trivial and nontrivial phase. Both for the testing of our theory and for a better understanding it is instructive to look at the contributions from specific \mathbf{k} points separately. Afterwards, an integration over the Brillouin zone is performed to obtain measurable HHG spectra.

The Haldane model parameters are $a = 2.683$, $M = 0.026$, $t_1 = -0.1$, and $t_2 = -0.0013i$ (trivial) and $t_2 = -0.0087i$ (nontrivial). The laser pulse is the same as in the SSH example (67) and polarized in the ΓM direction. Figure 2 shows the band structure for the two parameter sets. The values for

the calculations (i) directly in position space for a chain with $N = 50$ unit cells and periodic boundary conditions (see Appendix A), (ii) according to Eqs. (26), (27), and (28) (with the k integral replaced by a discrete sum over $N_k = 50$ equidistant k values in the Brillouin zone), and (iii) according to (57) all give the same spectrum, which shows that, first, the equations of motions are correct, second, that the Bloch ansatz chosen in Appendix A is consistent with the velocity operator $\partial_k \mathbf{H}(\mathbf{d})$, and third, that the assumption of negligible depletion, i.e., $\eta_{k-}(t) \simeq 1$ is valid. The HHG spectrum displays the known features [25] of rapidly dropping low-order harmonics, followed by a plateau of emission in the photon energy interval $[\min(2d), \max(2d)]$.

B. Haldane case

The 2×2 Bloch Hamiltonian for the Haldane model is derived in Appendix B and reads

t_2 were chosen such that the smallest band gap, which is at the K point, is the same below and above the topological phase transition, corresponding to $\simeq 5$ times the laser frequency.

The HHG spectra calculated from the acceleration of the electron initially at the K point are presented in Figs. 3(a) and 3(b). In Fig. 3(a) the HHG spectra in the trivial and nontrivial topological phase (Haldane model parameters as in Fig. 2) calculated from the acceleration parallel to the incoming laser field (\dot{v}_{\parallel}) are shown. We have checked that the calculation (i) according to (26) and (27), (ii) according to (54), and (iii) assuming no depletion (57) give the same spectra. Figure 3(b) shows the corresponding spectra

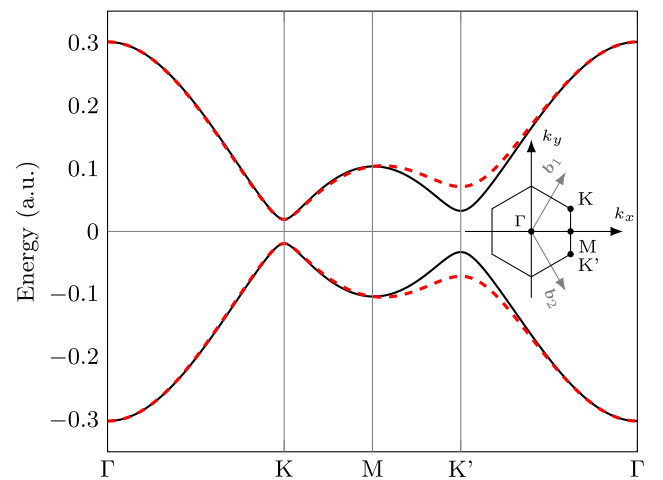


FIG. 2. Band structure of the Haldane model for $a = 2.683$, $M = 0.026$, $t_1 = -0.1$, and $t_2 = -0.0013i$ (trivial, black) and $t_2 = -0.0087i$ (nontrivial, red dashed).

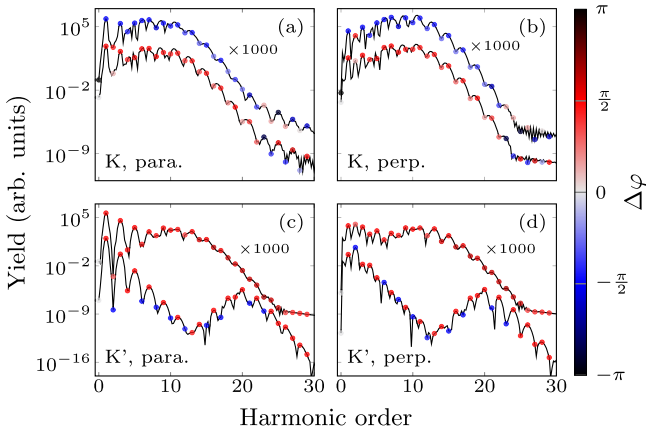


FIG. 3. HHG spectra generated by the electron initially at the K point (a) and (b) and the K' point (c) and (d). (a) and (c) HHG spectra calculated from the acceleration parallel to the polarization direction of the incoming laser field for the trivial phase (upper curve, multiplied by 1000) and the nontrivial topological phase (lower curve). (b) and (d) Respective spectra from the acceleration perpendicular to the polarization direction of the incoming laser field. The phase difference (72) of integer harmonics is color coded in each panel. The Haldane model parameters are the same as in Fig. 2.

calculated from the acceleration perpendicular to the incoming laser field (\dot{v}_\perp). The respective phase difference,

$$\Delta\varphi = \arg(\text{FFT}[\dot{v}_\parallel]) - \arg(\text{FFT}[\dot{v}_\perp]), \quad (72)$$

is color coded in all panels of Fig. 3. It determines the helicity of the emitted light. The phase differences 0 and π (or, equivalently, $-\pi$) mean that the emitted harmonics are linearly polarized. Other phase differences define (together with the magnitudes of the emission polarized along x and y) the ellipticity (or helicity) of the emitted harmonics. It is clearly seen that the phase difference of most of the harmonics flips from $-\pi/2$ in the trivial topological phase to $+\pi/2$ in the nontrivial phase, i.e., the helicity changes. Even the fundamental flips in that way, which seems in contradiction with the findings in [31]. However, note that the polarization axes of the lasers are different in both papers. Even harmonics polarized perpendicular to the incoming laser field appear in Fig. 3(b), with the second behaving anomalously in having a helicity opposite to those of the other harmonics in the trivial phase.

Figures 4(a) and 4(b) show the actual electron trajectories for the electron starting from the K point in the v_x, v_y plane (i.e., v_\parallel, v_\perp plane) in the trivial and nontrivial phase, respectively. The time is color coded. It is clearly seen that the orientation of the trajectory changes from clockwise in the trivial phase to counterclockwise in the nontrivial topological phase. Note that the velocity components v_\parallel, v_\perp at the K point are similar in magnitude despite the linear polarization of the incoming pulse along v_\parallel . This leads to a particularly high ellipticity of the emitted harmonics and even a helicity flip of the fundamental when passing the phase transition.

The corresponding results for the K' point are shown in Figs. 3(c) and 3(d) and 4(c) and 4(d). The HHG spectra in Figs. 3(c) and 3(d) differ more in shape than those for the

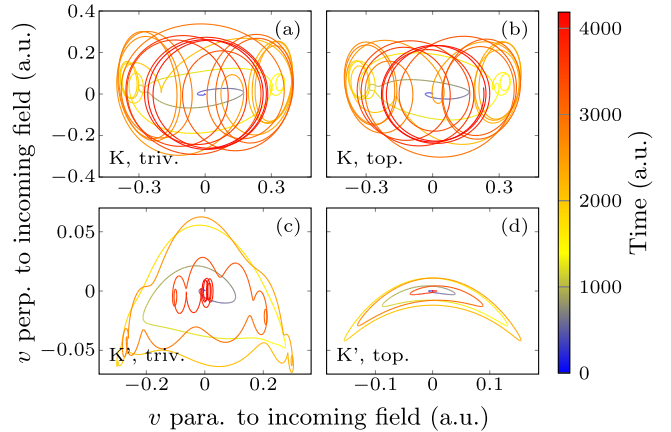


FIG. 4. Electron velocity for the electron initially at the K point (a) and (b), and K' point (c) and (d) in the v_x, v_y (i.e., v_\parallel, v_\perp) plane in the topologically trivial phase (a) and (c) and the nontrivial phase (b) and (d). Haldane model parameters as in Fig. 2. Time is color coded.

K point because the band gaps at the K' point in the trivial and the nontrivial topological phase differ significantly (see Fig. 2). This is why, in the nontrivial topological phase (where the band gap is larger), the characteristic band-gap dip around harmonic order 13 appears. To the left of the dip, the harmonics roll off exponentially, to the right of the dip the harmonics plateau starts to form (at higher laser intensity it would broaden). The helicity flip at the K' point is also very different from the K point. The phase difference of all harmonics is $+\pi/2$ in the trivial phase, and almost every other harmonic flips in the nontrivial topological phase (the fundamental does not flip, the second harmonic does, third, fourth, and fifth do not flip, the sixth does, etc.).

The velocities of the laser-driven electron that starts from the K' point for the trivial and the nontrivial topological phase are shown in Figs. 4(c) and 4(d), respectively. Note that the velocity components in perpendicular direction are much smaller than at the K point. The electron dynamics is very much aligned along the laser polarization direction. There is no switch from clockwise to counterclockwise electron motion below and above the topological phase transition at the K' point. The motion is counterclockwise in both cases. The trajectory looks more regular in the nontrivial topological phase, with the electron returning to zero velocity after the laser pulse. This is because of the larger band gap at the K' point in the nontrivial topological phase for the choice of our Haldane model parameters. For an increased laser intensity the electron dynamics there would also look more “chaotic.”

Figures 5(a) and 5(b) show HHG spectra calculated from the k -integrated electron velocity [Eq. (28)]. For the numerical integration, 1500×1500 k points within the first Brillouin zone were used, which was sufficient to obtain converged results. HHG spectra for the trivial and nontrivial topological phases for polarization directions parallel and perpendicular to the incoming laser field are shown in Figs. 5(a) and 5(b), respectively. The phase difference (72) is again color coded. We find that the helicity flip observed at the K point survives in the k -integrated result.

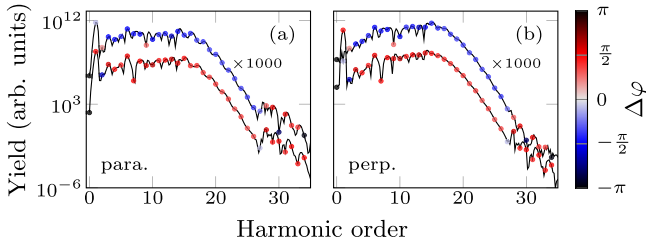


FIG. 5. HHG spectra calculated from the total electron velocity, integrated over the first Brillouin zone. (a) HHG spectra calculated from the acceleration parallel to the polarization direction of the incoming laser field for the trivial phase (upper curve, multiplied by 1000) and the nontrivial topological phase (lower curve). (b) Respective spectra from the acceleration perpendicular to the polarization direction of the incoming laser field. The phase difference (72) of integer harmonics is color coded in each panel. Haldane model parameters as in Fig. 2.

IV. SUMMARY AND CONCLUSIONS

We derived the equation for the velocity of a laser-driven electron in a two-band solid explicitly in terms of the system-specific three-vector $\mathbf{d}(\mathbf{k})$ and the laser field's vector potential $\mathbf{A}(t)$ in dipole approximation. Besides tight binding, dipole approximation, and negligible depletion, we did not make further assumptions such as single-band approximation, semiclassical dynamics, or simplified transition matrix elements (that may break gauge invariance or suppress topological effects). We calculated harmonic spectra by Fourier transforming the acceleration exemplarily for the Su-Schrieffer-Heeger chain and the Haldane model in intense laser fields. While for the Su-Schrieffer-Heeger chain there was no difference in the harmonic spectra above and below the topological phase transition if periodic boundary conditions are used, the helicity of the harmonics may change in the Haldane model driven by a linearly polarized laser field. The helicity changed differently for different harmonics, depending on the initial \mathbf{k} point of the electron. In the overall spectrum a helicity flip for each harmonic is observed. The complex electron dynamics was illustrated by electron trajectories in the velocity plane whose orientation (i.e., chirality) swapped from clockwise to counterclockwise at the K point but did not swap at the K' point. Our analytical formula for the electron velocity allows one to analyze and predict the laser-driven electron dynamics, for instance, whether chirality swaps are expected or not. We carefully checked that our analytical equation for the velocity leads to the same results as those obtained by solving directly the differential equations of motion either in position space or \mathbf{k} space. Although we applied our theory to harmonic generation, other strong-field or few-cycle pulse effects could be studied as well, for instance, laser-driven valleytronics or transient absorption spectroscopy of topologically nontrivial matter.

ACKNOWLEDGMENTS

H.J. acknowledges financial support from the doctoral fellowship program of the University of Rostock.

APPENDIX A: HOW THE CHOICE OF THE BLOCH ANSATZ AFFECTS THE COUPLING TO EXTERNAL FIELDS IN BLOCH HAMILTONIANS AND THE CURRENT OPERATOR IN k SPACE FOR THE SSH CHAIN

The simplest solid-state-like system that displays topological features is the SSH chain [2,26]. The tight-binding Hamiltonian (3) for the SSH chain takes into account two orbitals per unit cell and only intracell ($\Delta\mathbf{R} = 0$) and intercell hoppings ($\Delta\mathbf{R} = \mathbf{a}_1$) with amplitude v and w , respectively,

$$\hat{H} = \sum_m (v|m, 2\rangle\langle m, 1| + w|m+1, 1\rangle\langle m, 2| + \text{H.c.}). \quad (\text{A1})$$

Here, we simplified the notation, i.e., $|\phi_{R\alpha}\rangle \rightarrow |m, \alpha\rangle$ where the cell index m corresponds to $\mathbf{R} \rightarrow m\mathbf{a}_1$ in one dimension, and $\alpha = 1, 2$. Just given a tight-binding Hamiltonian like (A1), we have some freedom to make contact to actual position-space coordinates. The SSH model is usually thought of describing a dimerized chain where, starting from an equidistant atom distribution with a distance $a/2$, the atoms are shifted alternately by a small amount δ to the right and to the left, thus doubling the primitive cell to size a . As long as $\delta \ll a$ we can write $\mathbf{r}_{m2} - \mathbf{r}_{m1} \simeq \mathbf{r}_{m+1,1} - \mathbf{r}_{m2} \simeq a/2$ (where $\mathbf{r}_{m'\alpha} - \mathbf{r}_{m\alpha}$ are the respective distances to hop). The Bloch ansatz (4) then reads

$$|k, \alpha\rangle = \sum_n e^{i(n+(\alpha-1)/2)ak} |n, \alpha\rangle, \quad \alpha = 1, 2, \quad (\text{A2})$$

i.e., the two sites within a unit cell are at positions $\tau_1 = 0$ and $\tau_2 = a/2$. Equation (9) becomes

$$|\pm, k\rangle = \sum_{n\alpha} C_{\pm}^{\alpha}(k) e^{i(n+(\alpha-1)/2)ak} |n, \alpha\rangle, \quad (\text{A3})$$

and insertion into the position-space Hamiltonian (A1) yields

$$E_{\pm}(k)\mathbf{C}_{\pm}(k) = \mathbf{H}(k)\mathbf{C}_{\pm}(k), \quad (\text{A4})$$

where

$$\mathbf{H}(k) = \begin{pmatrix} 0 & s^*(k) \\ s(k) & 0 \end{pmatrix}, \quad (\text{A5})$$

with

$$s(k) = v e^{-iak/2} + w^* e^{iak/2}. \quad (\text{A6})$$

The dispersion relation is

$$E_{\pm}(k) = \pm \sqrt{s(k)s^*(k)}, \quad (\text{A7})$$

and possible normalized eigenvectors are

$$\mathbf{C}_{\pm}(k) = \frac{1}{\sqrt{2}} \begin{pmatrix} 1 \\ \frac{E_{\pm}(k)}{s^*(k)} \end{pmatrix}. \quad (\text{A8})$$

It can be shown [36] that the usual ‘‘minimal substitution’’ $\hat{\mathbf{p}} \rightarrow \hat{\mathbf{p}} + \mathbf{A}(\mathbf{r}, t)$ to couple an electron to an external driver described by a vector potential $\mathbf{A}(\mathbf{r}, t)$ in the continuous case amounts in tight binding to the replacement of the hopping elements,

$$|m', \alpha'\rangle\langle m, \alpha| \rightarrow e^{-i(\mathbf{r}_{m'\alpha'} - \mathbf{r}_{m\alpha})(\mathbf{A}_{m'\alpha'}(t) + \mathbf{A}_{m\alpha}(t))/2} |m', \alpha'\rangle\langle m, \alpha|,$$

where $\mathbf{A}_{m\alpha}(t)$ is the vector potential at position $\mathbf{r}_{m\alpha}$. In dipole approximation, $\mathbf{A}_{m\alpha}(t) = \mathbf{A}(t)$ is independent of space such

that the time-dependent Hamiltonian reads

$$\hat{H}(t) = \sum_m (v(t)|m, 2\rangle\langle m, 1| + w(t)|m+1, 1\rangle\langle m, 2| + \text{H.c.}), \quad (\text{A9})$$

with

$$v(t) = v e^{-iaA(t)/2}, \quad w(t) = w e^{-iaA(t)/2}. \quad (\text{A10})$$

We now try the ansatz (A3) but time dependent,

$$|\Psi(k, t)\rangle = \sum_{n\alpha} C^\alpha(k, t) e^{i(n+(\alpha-1)/2)ak} |n, \alpha\rangle, \quad (\text{A11})$$

for the time-dependent Schrödinger equation,

$$i\partial_t |\Psi(t)\rangle = \hat{H}(t) |\Psi(t)\rangle, \quad (\text{A12})$$

and find, indeed,

$$i\dot{\mathbf{C}}(k, t) = \mathbf{H}(k, t)\mathbf{C}(k, t), \quad (\text{A13})$$

with

$$\mathbf{H}(k, t) = \begin{pmatrix} 0 & s^*(k, t) \\ s(k, t) & 0 \end{pmatrix}, \quad s(k, t) = s[k + A(t)]. \quad (\text{A14})$$

As expected, the laser is coupled by replacing $k \rightarrow k + A(t)$ in the Bloch Hamiltonian. With the initial condition $\mathbf{C}(k, 0) = \mathbf{C}_\pm(k)$ we can follow how a Bloch state $\mathbf{C}_\pm(k)$ evolves in the laser field.

The informed reader may notice that the Bloch Hamiltonian (A5) is not the one usually discussed in the literature when it comes to the topological properties of the SSH model [2,26]. The reason is that a simpler Bloch ansatz is often used, namely

$$|k, \alpha\rangle = \sum_n e^{inak} |n, \alpha\rangle, \quad \alpha = 1, 2, \quad (\text{A15})$$

instead of (A2). This Bloch ansatz leads to the same form of the Bloch Hamiltonian (A5) but with $s(k)$ replaced by

$$\bar{s}(k) = v + e^{iak} w^*, \quad (\text{A16})$$

i.e.,

$$\bar{\mathbf{H}}(k) = \begin{pmatrix} 0 & \bar{s}^*(k) \\ \bar{s}(k) & 0 \end{pmatrix}. \quad (\text{A17})$$

Because

$$s(k) = e^{-iak/2} \bar{s}(k), \quad (\text{A18})$$

the eigenvalues do not change, $E_\pm(k) = \pm\sqrt{s(k)s^*(k)} = \pm\sqrt{\bar{s}(k)\bar{s}^*(k)}$, but the eigenvectors do,

$$\bar{\mathbf{C}}_\pm(k) = \frac{1}{\sqrt{2}} \begin{pmatrix} 1 \\ \frac{E_\pm(k)}{\bar{s}^*(k)} \end{pmatrix}. \quad (\text{A19})$$

In the time-dependent case, (A11) becomes

$$|\overline{\Psi}(k, t)\rangle = \sum_{n\alpha} \bar{C}^\alpha(k, t) e^{inak} |n, \alpha\rangle. \quad (\text{A20})$$

In order to calculate SSH spectra, we need to evaluate the (time derivative of) the current or the velocity expectation value. The current can be derived from the continuity equation using Gauss law and the Heisenberg equation of

motion for the density operator [2]. Because there is only nearest-neighbor hopping and only two sites per unit cell, the intracell current for the SSH chain is simple and reads

$$\hat{j}_m(t) = -i(v^*(t)|m, 1\rangle\langle m, 2| - v(t)|m, 2\rangle\langle m, 1|). \quad (\text{A21})$$

Here, the subscript m indicates that this is the current between sites 1 and 2 within unit cell m . The intercell current through the boundary at $(m+1/2)a$ (i.e., to the right of cell m) reads

$$\hat{j}_{m+1/2}(t) = -i(w^*(t)|m, 2\rangle\langle m+1, 1| - w(t)|m+1, 1\rangle\langle m, 2|). \quad (\text{A22})$$

Note that the current operators are time dependent. With the state (A11) follows for the expectation value of the total current,

$$\langle \hat{j}(t) \rangle(t) = -\frac{2}{a} \mathbf{C}^\dagger(k, t) [\partial_k \mathbf{H}(k)]_{k+A(t)} \mathbf{C}(k, t), \quad (\text{A23})$$

which has the expected form $j = -env$ where n is the particle density (in this case particles per length), $v = \dot{x} = \partial_k H$ is the velocity, and $-e$ is the electron charge ($= -1$ in a.u.).

Instead, with the Bloch ansatz (A15) and (A20) one obtains for the intercell current,

$$\langle \overline{j}_{m+1/2}(t) \rangle(t) = -\frac{1}{a} \bar{\mathbf{C}}^\dagger(k, t) [\partial_k \bar{\mathbf{H}}(k)]_{k+A(t)/2} \bar{\mathbf{C}}(k, t), \quad (\text{A24})$$

and for the intracell current,

$$\langle \overline{j}_m(t) \rangle(t) = \bar{\mathbf{C}}^\dagger(k, t) \bar{\mathbf{J}}_{\text{intracell}}(k, t) \bar{\mathbf{C}}(k, t), \quad (\text{A25})$$

where

$$\bar{\mathbf{J}}_{\text{intracell}}(k, t) = \begin{pmatrix} 0 & -iv^*(t) \\ iv(t) & 0 \end{pmatrix}. \quad (\text{A26})$$

We see that, employing the Bloch ansatz (A15), the intercell current is related to $\partial_k \bar{\mathbf{H}}(k)$. However, the replacement is $k \rightarrow k + A(t)/2$, and the intracell current is not captured by $\partial_k \bar{\mathbf{H}}(k)$. The conclusion thus is that one should use the Bloch ansatz (A2) because only with this ansatz the coupling to an external field is correctly implemented by the replacement $\mathbf{k} \rightarrow \mathbf{k} + \mathbf{A}(t)$ in the field-free Bloch Hamiltonian, and the current calculated using the time-dependent Bloch Hamiltonian agrees with the physically meaningful current derived from the continuity equation in position space.

In the book by Vanderbilt [14], Sec. 2.2.3, the choice for the Bloch ansatz (A2) is referred to as ‘‘convention I’’ while the ansatz (A15) [i.e., the omission of the intracell positions τ_α in (4)] is ‘‘convention II.’’ The choice of the convention not only has consequences for the consistent coupling of the Bloch Hamiltonian to external fields but also for the calculation of topological invariants, as discussed in [14] as well. In the case of the SSH chain, a winding number can be defined that counts how many times the origin in \mathbf{d} space is encircled while k sweeps through the Brillouin zone from $-\pi/a$ to π/a . This picture works well with convention II, because (for $v, w \in \mathbb{R}$) we have $d_x = v + w \cos(ak)$, $d_y = v + w \sin(ak)$, $d_z = 0$ so that $\mathbf{d}(k)$ indeed describes a circle of radius w centered at $\mathbf{d} = (v, 0, 0)$. It is then easy to see that for $w > v$, the origin is encircled once while for $v > w$ the origin lies outside the circle. In finite SSH chains, $w > v$ implies dangling sites at the chain’s edges, leading to edge states. In

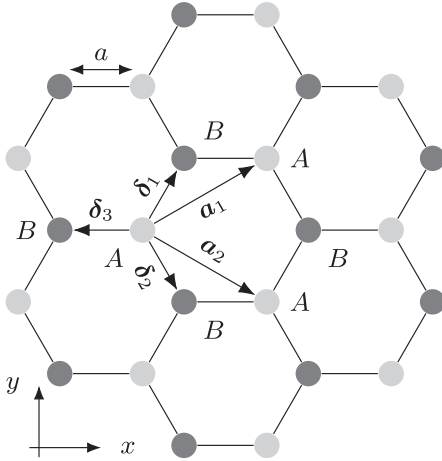


FIG. 6. Geometry of the hexagonal lattice used in the Haldane model. The unit cell consists of two sites A (light gray) and B (dark gray), each contributing one (tight-binding) orbital. The \mathbf{a}_i , $i = 1, 2$, are lattice vectors and connect next-nearest neighbors, the δ_i , $i = 1, 2, 3$, connect nearest neighbors.

that sense, the winding number—defined for the bulk—is a topological invariant, as it “predicts” the presence of edge states in the corresponding finite system. This is an example for the so-called “bulk-boundary correspondence” [14].

Of course, from a pragmatic viewpoint a Bloch ansatz is just a mathematical trick to switch from position space to \mathbf{k} space where the problem simplifies to an (in our case) 2×2 Bloch Hamiltonian (for each \mathbf{k}). One can choose either convention for the Bloch ansatz. While convention II might be more convenient for the discussion of topological properties, convention I is simpler and less error prone for the coupling to external fields and when the calculation of physically meaningful currents $\sim [\nabla_{\mathbf{k}} \mathbf{H}(\mathbf{k})]_{k+A(t)}$ is required.

APPENDIX B: HALDANE MODEL

The Haldane model describes a two-dimensional hexagonal system with broken inversion and broken time-reversal symmetry such that it displays topological effects (without external magnetic field) [28]. The hexagonal lattice with two orbitals A and B per unit cell is shown in Fig. 6. The lattice vectors are

$$\mathbf{a}_1 = \frac{a}{2} \begin{pmatrix} 3 \\ \sqrt{3} \end{pmatrix}, \quad \mathbf{a}_2 = \frac{a}{2} \begin{pmatrix} 3 \\ -\sqrt{3} \end{pmatrix}, \quad (\text{B1})$$

with the lattice constant a . The nearest-neighbor vectors are

$$\delta_1 = \frac{a}{2} \begin{pmatrix} 1 \\ \sqrt{3} \end{pmatrix}, \quad \delta_2 = \frac{a}{2} \begin{pmatrix} 1 \\ -\sqrt{3} \end{pmatrix}, \quad \delta_3 = -a \begin{pmatrix} 1 \\ 0 \end{pmatrix}. \quad (\text{B2})$$

The tight-binding Hamiltonian is

$$\begin{aligned} \hat{H} = & \sum_i M(|i, A\rangle\langle i, A| - |i, B\rangle\langle i, B|) \\ & + \sum_{(i,j)} t_1(|j, A\rangle\langle i, B| + \text{H.c.}) \\ & + \sum_{\langle(i,j)\rangle} \sum_{\alpha \in \{A,B\}} (t_2|j, \alpha\rangle\langle i, \alpha| + \text{H.c.}), \end{aligned} \quad (\text{B3})$$

with an alternating onsite potential M for the orbitals in the first sum (breaking inversion symmetry), nearest-neighbor hopping with the real amplitude t_1 in the second sum, and complex next-nearest neighbor hopping with the amplitude t_2 (breaking time-reversal symmetry) in the third sum. We choose the next-nearest neighbor hopping such that the term with t_2 describes counterclockwise hopping while the term with t_2^* describes clockwise hopping within one hexagon.

As discussed in Appendix A, convention I is simpler for the coupling to external fields and therefore intracell positions should be included in the ansatz,

$$\begin{aligned} |\pm, \mathbf{k}\rangle = & \sum_{mn} e^{i(m\mathbf{a}_1 + n\mathbf{a}_2) \cdot \mathbf{k}} |m, n\rangle \\ & \otimes (C_{\pm}^A(\mathbf{k}) |A\rangle + C_{\pm}^B(\mathbf{k}) e^{i\delta_3 \cdot \mathbf{k}} |B\rangle). \end{aligned} \quad (\text{B4})$$

After a straightforward calculation, and with the vectors,

$$\mathbf{g}_1 = \mathbf{a}_1 - \mathbf{a}_2, \quad \mathbf{g}_2 = -\mathbf{a}_1, \quad \mathbf{g}_3 = \mathbf{a}_2, \quad (\text{B5})$$

the Bloch Hamiltonian (68) is obtained. Introducing

$$\begin{aligned} \tau(\mathbf{k}) &= t_1 \sum_n e^{i\delta_n \cdot \mathbf{k}}, \\ \kappa(\mathbf{k}) &= 2 \operatorname{Re}(t_2) \sum_n \cos(\mathbf{g}_n \cdot \mathbf{k}), \\ \sigma(\mathbf{k}) &= M + 2 \operatorname{Im}(t_2) \sum_n \sin(\mathbf{g}_n \cdot \mathbf{k}), \end{aligned} \quad (\text{B6})$$

the Bloch Hamiltonian can be written as

$$\mathbf{H}(\mathbf{k}) = \begin{pmatrix} \kappa + \sigma & \tau \\ \tau^* & \kappa - \sigma \end{pmatrix}, \quad (\text{B7})$$

and the dispersion relation is

$$E_{\pm}(\mathbf{k}) = \kappa \pm \sqrt{|\tau|^2 + \sigma^2}. \quad (\text{B8})$$

Two possible sets of normalized eigenvectors are

$$\begin{aligned} \mathbf{C}_{+}^{>}(\mathbf{k}) &= \frac{1}{\sqrt{|\mathbf{C}^{>}|^2}} \begin{pmatrix} \sigma + \sqrt{|\tau|^2 + \sigma^2} \\ \tau^* \end{pmatrix}, \\ \mathbf{C}_{-}^{>}(\mathbf{k}) &= \frac{1}{\sqrt{|\mathbf{C}^{>}|^2}} \begin{pmatrix} -\tau \\ \sigma + \sqrt{|\tau|^2 + \sigma^2} \end{pmatrix}, \end{aligned} \quad (\text{B9})$$

and

$$\begin{aligned} \mathbf{C}_{+}^{<}(\mathbf{k}) &= \frac{1}{\sqrt{|\mathbf{C}^{<}|^2}} \begin{pmatrix} \tau \\ -\sigma + \sqrt{|\tau|^2 + \sigma^2} \end{pmatrix}, \\ \mathbf{C}_{-}^{<}(\mathbf{k}) &= \frac{1}{\sqrt{|\mathbf{C}^{<}|^2}} \begin{pmatrix} \sigma - \sqrt{|\tau|^2 + \sigma^2} \\ \tau^* \end{pmatrix}, \end{aligned} \quad (\text{B10})$$

with

$$\begin{aligned} |\mathbf{C}^{>}|^2 &= 2\sqrt{|\tau|^2 + \sigma^2}(\sigma + \sqrt{|\tau|^2 + \sigma^2}), \\ |\mathbf{C}^{<}|^2 &= 2\sqrt{|\tau|^2 + \sigma^2}(-\sigma + \sqrt{|\tau|^2 + \sigma^2}), \end{aligned} \quad (\text{B11})$$

where $\mathbf{C}_{\pm}^{>}$ is used for $\sigma > 0$ and $\mathbf{C}_{\pm}^{<}$ for $\sigma < 0$. This distinction based on the sign of σ is convenient to handle the limit $|\tau| \rightarrow 0$ numerically.

The coupling to an external driver described by a vector potential is performed with the Peierls substitution as in Ap-

pendix A. Using the dipole approximation, the laser is again coupled by replacing $\mathbf{k} \rightarrow \mathbf{k} + \mathbf{A}(t)$ in the Bloch Hamiltonian.

-
- [1] E. Witten, Three lectures on topological phases of matter, *Riv. Nuovo Cimento* **039**, 313 (2016).
- [2] J. Asbóth, L. Oroszlány, and A. Pályi, *A Short Course on Topological Insulators*, Lecture Notes in Physics, Vol. 919 (Springer, Berlin/Heidelberg, 2016).
- [3] M. Z. Hasan and C. L. Kane, Colloquium: Topological insulators, *Rev. Mod. Phys.* **82**, 3045 (2010).
- [4] F. Krausz and M. Ivanov, Attosecond physics, *Rev. Mod. Phys.* **81**, 163 (2009).
- [5] S. Ghimire, A. D. DiChiara, E. Sistrunk, P. Agostini, L. F. DiMauro, and D. A. Reis, Observation of high-order harmonic generation in a bulk crystal, *Nat. Phys.* **7**, 138 (2011).
- [6] G. Ndabashimiye, S. Ghimire, M. Wu, D. A. Browne, K. J. Schafer, M. B. Gaarde, and D. A. Reis, Solid-state harmonics beyond the atomic limit, *Nature (London)* **534**, 520 (2016).
- [7] G. Vampa, T. J. Hammond, N. Thiré, B. E. Schmidt, F. Légaré, C. R. McDonald, T. Brabec, D. D. Klug, and P. B. Corkum, All-Optical Reconstruction of Crystal Band Structure, *Phys. Rev. Lett.* **115**, 193603 (2015).
- [8] F. Langer, M. Hohenleutner, U. Huttner, S. Koch, M. Kira, and R. Huber, Symmetry-controlled temporal structure of high-harmonic carrier fields from a bulk crystal, *Nat. Photon.* **11**, 227 (2017).
- [9] H. Koochaki Kelardeh, V. Apalkov, and M. I. Stockman, Graphene superlattices in strong circularly polarized fields: Chirality, Berry phase, and attosecond dynamics, *Phys. Rev. B* **96**, 075409 (2017).
- [10] T. T. Luu and H. J. Wörner, Measurement of the Berry curvature of solids using high-harmonic spectroscopy, *Nat. Commun.* **9**, 916 (2018).
- [11] H. Lakhota, H. Y. Kim, M. Zhan, S. Hu, S. Meng, and E. Goulielmakis, Laser picroscopy of valence electrons in solids, *Nature (London)* **583**, 55 (2020).
- [12] M. Franz and L. Molenkamp (eds.), *Topological Insulators*, Contemporary Concepts of Condensed Matter Science, Vol. 6 (Elsevier, Amsterdam, 2013).
- [13] B. A. Bernevig, *Topological Insulators and Topological Superconductors* (Princeton University Press, Princeton, 2013).
- [14] D. Vanderbilt, *Berry Phases in Electronic Structure Theory* (Cambridge University Press, Cambridge, 2018).
- [15] M. Schultze, E. M. Bothschafter, A. Sommer, S. Holzner, W. Schweinberger, M. Fiess, M. Hofstetter, R. Kienberger, V. Apalkov, V. S. Yakovlev, M. I. Stockman, and F. Krausz, Controlling dielectrics with the electric field of light, *Nature (London)* **493**, 75 (2013).
- [16] M. Garg, M. Zhan, T. T. Luu, H. Lakhota, T. Klostermann, A. Guggenmos, and E. Goulielmakis, Multi-petahertz electronic metrology, *Nature (London)* **538**, 359 (2016).
- [17] T. Higuchi, C. Heide, K. Ullmann, H. B. Weber, and P. Hommelhoff, Light-field-driven currents in graphene, *Nature (London)* **550**, 224 (2017).
- [18] M. Baudisch, A. Marini, J. D. Cox, T. Zhu, F. Silva, S. Teichmann, M. Massicotte, F. Koppens, L. S. Levitov, F. J. García de Abajo, and J. Biegert, Ultrafast nonlinear optical response of Dirac fermions in graphene, *Nat. Commun.* **9**, 1018 (2018).
- [19] J. Reimann, S. Schlauderer, C. P. Schmid, F. Langer, S. Baierl, K. A. Kokh, O. E. Tereshchenko, A. Kimura, C. Lange, J. Gädde, U. Höfer, and R. Huber, Subcycle observation of lightwave-driven Dirac currents in a topological surface band, *Nature (London)* **562**, 396 (2018).
- [20] H. Hübener, M. A. Sentef, U. De Giovannini, A. F. Kemper, and A. Rubio, Creating stable Floquet–Weyl semimetals by laser-driving of 3D Dirac materials, *Nat. Commun.* **8**, 13940 (2017).
- [21] U. De Giovannini and H. Hübener, Floquet analysis of excitations in materials, *J. Phys. Mater.* **3**, 012001 (2020).
- [22] A. Jimenez-Galan, R. E. F. Silva, O. Smirnova, and M. Ivanov, Lightwave topology for strong-field valleytronics, [arXiv:1910.7398](https://arxiv.org/abs/1910.7398).
- [23] D. Bauer and K. K. Hansen, High-Harmonic Generation in Solids with and without Topological Edge States, *Phys. Rev. Lett.* **120**, 177401 (2018).
- [24] H. Drüeke and D. Bauer, Robustness of topologically sensitive harmonic generation in laser-driven linear chains, *Phys. Rev. A* **99**, 053402 (2019).
- [25] H. Jürß and D. Bauer, High-harmonic generation in Su-Schrieffer-Heeger chains, *Phys. Rev. B* **99**, 195428 (2019).
- [26] W. P. Su, J. R. Schrieffer, and A. J. Heeger, Solitons in Polyacetylene, *Phys. Rev. Lett.* **42**, 1698 (1979).
- [27] A. H. Castro Neto, F. Guinea, N. M. R. Peres, K. S. Novoselov, and A. K. Geim, The electronic properties of graphene, *Rev. Mod. Phys.* **81**, 109 (2009).
- [28] F. D. M. Haldane, Model for a Quantum Hall Effect without Landau Levels: Condensed-Matter Realization of the “Parity Anomaly”, *Phys. Rev. Lett.* **61**, 2015 (1988).
- [29] X.-L. Qi, Y.-S. Wu, and S.-C. Zhang, Topological quantization of the spin Hall effect in two-dimensional paramagnetic semiconductors, *Phys. Rev. B* **74**, 085308 (2006).
- [30] A. Chacón, D. Kim, W. Zhu, S. P. Kelly, A. Dauphin, E. Pisanty, A. S. Maxwell, A. Picón, M. F. Ciappina, D. E. Kim, C. Ticknor, A. Saxena, and M. Lewenstein, Circular dichroism in higher-order harmonic generation: Heralding topological phases and transitions in Chern insulators, *Phys. Rev. B* **102**, 134115 (2020).
- [31] R. E. F. Silva, Á. Jiménez-Galán, B. Amorim, O. Smirnova, and M. Ivanov, Topological strong-field physics on sub-laser-cycle timescale, *Nat. Photon.* **13**, 849 (2019).
- [32] A. D. Bandrauk, S. Chelkowski, D. J. Diestler, J. Manz, and K.-J. Yuan, Quantum simulation of high-order harmonic spectra of the hydrogen atom, *Phys. Rev. A* **79**, 023403 (2009).
- [33] J. C. Baggesen and L. B. Madsen, On the dipole, velocity and acceleration forms in high-order harmonic generation from a single atom or molecule, *J. Phys. B: At., Mol. Opt. Phys.* **44**, 115601 (2011).
- [34] D. Bauer, H. Bauke, T. Brabec, T. Fennel, C. R. McDonald, D. B. Milošević, S. Pabst, C. Peltz, G. Pöplau, R. Santra, and C.

- Varin, in *Computational Strong-Field Quantum Dynamics: Intense Light-Matter Interactions*, edited by D. Bauer, De Gruyter Textbook (De Gruyter, Berlin, 2017).
- [35] L. Yue and M. B. Gaarde, Structure gauges and laser gauges for the semiconductor Bloch equations in high-order harmonic generation in solids, *Phys. Rev. A* **101**, 053411 (2020).
- [36] M. Graf and P. Vogl, Electromagnetic fields and dielectric response in empirical tight-binding theory, *Phys. Rev. B* **51**, 4940 (1995).
- [37] G. Vampa and T. Brabec, Merge of high harmonic generation from gases and solids and its implications for attosecond science, *J. Phys. B: At., Mol. Opt. Phys.* **50**, 083001 (2017).
- [38] M. Lewenstein, P. Balcou, M. Y. Ivanov, A. L'Huillier, and P. B. Corkum, Theory of high-harmonic generation by low-frequency laser fields, *Phys. Rev. A* **49**, 2117 (1994).
- [39] Here, it is again understood that the correct time dependencies have to be employed, i.e., $\mathcal{A}_{+-}(\vec{d}) = \mathcal{A}_{+-}(\vec{d}[\mathbf{k}(t')])$ and, in the exponent, $2\vec{d} - \Delta\mathcal{A}(\vec{d}) = 2d[\mathbf{k}(t'')] - \Delta\mathcal{A}(d[\mathbf{k}(t'')])$.
- [40] G. Sundaram and Q. Niu, Wave-packet dynamics in slowly perturbed crystals: Gradient corrections and Berry-phase effects, *Phys. Rev. B* **59**, 14915 (1999).
- [41] P. Gosselin, F. Ménas, A. Bérard, and H. Mohrbach, Semi-classical dynamics of electrons in magnetic Bloch bands: A Hamiltonian approach, *Europhys. Lett.* **76**, 651 (2006).
- [42] E. N. Osika, A. Chacón, L. Ortmann, N. Suárez, J. A. Pérez-Hernández, B. Szafran, M. F. Ciappina, F. Sols, A. S. Landsman, and M. Lewenstein, Wannier-Bloch Approach to Localization in High-Harmonics Generation in Solids, *Phys. Rev. X* **7**, 021017 (2017).
- [43] L. Yue and M. B. Gaarde, Imperfect Recollisions in High-Harmonic Generation in Solids, *Phys. Rev. Lett.* **124**, 153204 (2020).

5.1.3 High-order harmonic generation in hexagonal nanoribbons

by Hannah Jürß and Dieter Bauer

The European Physical Journal Special Topics **230**:4081–4089 (2021)

DOI: [10.1140/epjs/s11734-021-00106-z](https://doi.org/10.1140/epjs/s11734-021-00106-z)

Reference: [3]

Author Contributions

Hannah Jürß	performing the numerical simulations (deriving the necessary equations for the simulations, writing the code and running it), analyzing the results, writing the manuscript
-------------	-----------------------------------------------------------------------------------------------------------------------------------------------------------------------------

Dieter Bauer	providing critical feedback, supporting the analysis of the results, improving the manuscript, supervision
--------------	------------------------------------------------------------------------------------------------------------



High-order harmonic generation in hexagonal nanoribbons

Hannah Jürß^a and Dieter Bauer^b

Institute of Physics, University of Rostock, 18051 Rostock, Germany

Received 8 January 2021 / Accepted 30 March 2021
© The Author(s) 2021

Abstract The generation of high-order harmonics in finite, hexagonal nanoribbons is simulated. Ribbons with armchair and zig-zag edges are investigated by using a tight-binding approach with only nearest-neighbor hopping. By turning an alternating on-site potential off or on, the system describes for example graphene or hexagonal boron nitride, respectively. The incoming laser pulse is linearly polarized along with the ribbons. The emitted light has a polarization component parallel to the polarization of the incoming field. The presence or absence of a polarization component perpendicular to the polarization of the incoming field can be explained by the symmetry of the ribbons. Characteristic features in the harmonic spectra for the finite ribbons are analyzed with the help of the band structure for the corresponding periodic systems.

1 Introduction

Ultrafast dynamics in condensed matter systems have been studied intensively in recent years [1–8]. In particular, high-order harmonic generation (HHG) has proven to be a powerful tool as it is able to probe static and dynamic properties of the solid target by all-optical means [9–13].

HHG was initially observed for atoms and molecules in the gas phase. For non-perturbative laser intensities and photon energies well below the ionization potential, the energy of the emitted photons can be large multiples of the incident photon's energy, the high-order harmonics.

The mechanisms underlying HHG in solids are similar to those in the gas phase. For instance, the celebrated semi-classical three-step model [14, 15] introduced for isolated atoms, where, in the first step, the electron is excited into the continuum. In the second step, the electron propagates in the presence of the laser-field, and, in the third step, it recombines with the ion upon generating a photon with an energy given by the kinetic energy of the electron at the time of recombination and the ionization potential. A similar model exists for solids [16, 17] where, first, the electron is excited from the valence band to the conduction band, second, the electron in the conduction band and the hole in the valence band propagate in the presence of the laser field, and, third, the electron and hole recombine upon generating a harmonic photon.

If the solid is an insulator or semi-conductor, it has a non-vanishing band gap between the valence and the conduction band. The three-step model of solid-state HHG provides a way to separate two different contributions of harmonic radiation [16]. First, the movement of the electron (and hole) inside the bands create intra-band harmonics. As the electron and hole recombine, a transition between both bands occur. The radiation from this transition is called interband harmonics.

Many studies focus on the bulk of a solid. In reality, solids are finite and have edges. Edge states might cause interesting effects in high-harmonic spectra, in particular when they are topological in nature [18–20]. In this paper, we focus on the high-harmonic spectra from finite systems and compare with the corresponding result for the bulk. We restrict ourselves to the topologically trivial phase in this work.

Graphene is one particularly interesting two-dimensional solid because of its relativistic Dirac cones. In graphene, the atoms form a hexagonal lattice structure. Hexagonal boron nitride (h-BN) is a different example with the same lattice structure. HHG in hexagonal lattice structures has been studied for the bulk and for ribbons for topologically trivial graphene and h-BN [21–25] and the topologically nontrivial Haldane model [26–28].

In this work, we investigate the generation of high-harmonics in hexagonal nanoribbons for two different edge configurations: zig-zag and armchair. Ribbons with and without alternating on-site potentials are investigated in the topologically trivial phase only. The system without alternating on-site potential contains one atomic element (as, e.g., in graphene) whereas

^ae-mail: hannah.juress@uni-rostock.de (corresponding author)

^be-mail: dieter.bauer@uni-rostock.de

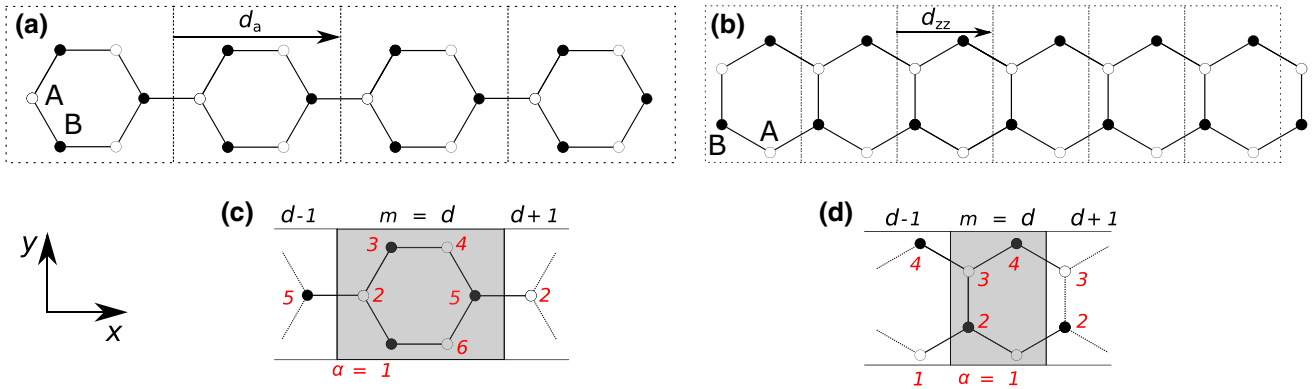


Fig. 1 Sketch of ribbons built from hexagons, for finite (a, b) and infinite (c, d) ribbons. a, c Armchair and b, d zig-zag configuration. The distance between nearest neighbors (indicated by solid lines) is a , the hopping amplitude between them is $t_1 \in \mathbb{R}$. An alternating on-site potential M ($-M$) at sites A (B), indicated by unfilled (filled) circles, is included. The unit cells are marked by dotted rectangles.

two different elements are contained in the case of alternating on-site potential (e.g., h-BN).

The outline of this work is as follows. In Sect. 2, the basic theory is summarized, starting with the finite system without external field in Sect. 2.1. We show the calculation and the results for the band structures for the armchair (Sect. 2.1.1) and the zig-zag (Sect. 2.1.2) ribbon with periodic boundary conditions. In Sect. 2.2 the coupling to an external field is presented. HHG spectra for the finite armchair (Sect. 3.1) and finite zig-zag (Sect. 3.2) ribbons are discussed.

2 Theory

In this work, we investigate hexagonal ribbons in two different configurations, armchair (Fig. 1a) and zig-zag (Fig. 1b). We consider two different types of sites: A and B. The on-site potential is M ($-M$) on lattice sites A (B). In Fig. 1, the lattice sites A and B are indicated by unfilled and filled circles, respectively. The lattice constant for the armchair ribbon is given by $d_a = 3a$, where a is the distance between two neighboring sites. For the zig-zag ribbon, the lattice constant is $d_{zz} = \sqrt{3}a$. Atomic units (a.u.), $\hbar = |e| = m_e = 4\pi\epsilon_0 = 1$, are used if not stated otherwise.

2.1 Static system

The systems have N atomic sites. The atomic orbital at site i is denoted as $|i\rangle$. A general single-electron wavefunction is given by

$$|\psi\rangle = \sum_{i=1}^N g_i |i\rangle. \quad (1)$$

The lattice constant is d_a for the armchair and d_{zz} for the zig-zag ribbon. Here, the finite armchair ribbon contains $N_{\text{hex}} = 4$, the zig-zag $N_{\text{hex}} = 6$ hexagons (unit cells). For the infinite ribbon (c, d), the hoppings inside a unit cell $m = n$ and to neighboring unit cells $m = n \pm 1$ are indicated by solid lines. The lattice sites inside a unit cell are labeled by α (red)

The Hamiltonian in position space and tight-binding approximation reads

$$\hat{H}_0 = t_1 \sum_{\langle i,j \rangle} (|j\rangle\langle i| + \text{h.c.}) + M \left(\sum_{i \in A} |i\rangle\langle i| - \sum_{i \in B} |i\rangle\langle i| \right), \quad (2)$$

where the sum $\sum_{\langle i,j \rangle}$ runs over nearest neighbors i and j and the sums $\sum_{i \in A, B}$ over sites A or B, respectively. The parameter t_1 is the hopping amplitude between adjacent sites. Hopping between next-nearest neighbors is not considered in this work. The eigenstates $|\psi_i\rangle$ fulfill the time-independent Schrödinger equation (TISE)

$$\hat{H}_0 |\psi_i\rangle = E_i |\psi_i\rangle. \quad (3)$$

In the following, we describe the propagation of states $|\psi\rangle$ in position space for ribbons with N_{hex} hexagons (Fig. 1a, b) in time. However, one aim of this work is to relate features in the harmonic spectrum of the finite ribbons with energy differences in the band structure of the corresponding ribbon bulk. Hence, band structures are calculated for the ribbons with periodic boundary conditions in x -direction, see Fig. 1c and d. The resulting Hamiltonian will be given in crystal-momentum space (k -space).

For the distance between adjacent sites we take the value for graphene [29], i.e., $a = 2.68$ a.u. $\simeq 1.42$ Å. For the nearest-neighbor hopping amplitude we use data from simulations without tight-binding approximation [30] with which we want to compare. To that end the energies of an armchair ribbon with four unit cells were calculated, and the nearest-neighbor hopping was adjusted till the band gap was identical for both meth-

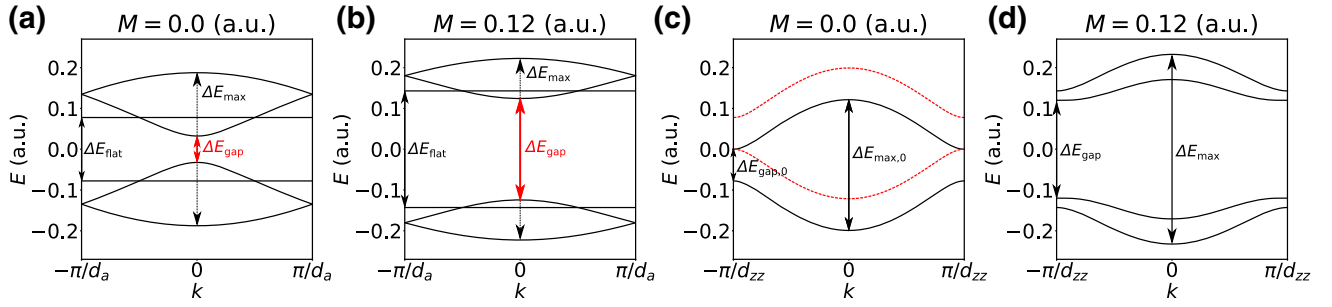


Fig. 2 Band structure for the bulk of the ribbon with armchair (a, b) and zig-zag (c, d) edges for $M = 0$ (a, c) and $M = 0.12$ (b, d) in the first Brillouin zone

ods. As a result we find $t_1 = -0.07776 \approx -2.116$ eV. The negative sign of t_1 is chosen to obey the node rule of quantum mechanics, as in this case the coefficients g_i have all the same sign for the state with the lowest energy.

2.1.1 Armchair ribbon

The calculation leading to the bulk-Hamiltonian for the armchair ribbon is in Appendix A. The unit cell contains six sites, see Fig. 1c. Hence, there are six bands, see Fig. 2a and b. The energies are calculated numerically.

The armchair ribbon has a band gap of $\Delta E_{\text{gap}} = 0.08338$ for a vanishing on-site potential $M = 0$ (Fig. 2a). The band gap ΔE_{gap} increases with the on-site potential M (Fig. 2b). The band structure is symmetric around $E = 0$. Two of the bands are flat, their energy is constant over the whole Brillouin zone. It is given by $E_{\text{flat}} = \pm\sqrt{t_1^2 + M^2}$, see Appendix A.

In the finite ribbon with N_{hex} hexagons, there are also N_{hex} states that have the same energy. Their energy is identical to the energy of the flat bands in the bulk.

2.1.2 Zig-zag ribbon

The bulk-Hamiltonian for the zig-zag ribbon was calculated in [28]. Here, we do not consider hopping between next-nearest neighbors as in [28] (i.e., $t_2 = 0$). The bulk-Hamiltonian reads

$$\hat{H}_{\text{bulk,zz}}(k) = \begin{pmatrix} M & T_1(k) & 0 & 0 \\ T_1(k) & -M & t_1 & 0 \\ 0 & t_1 & M & T_1(k) \\ 0 & 0 & T_1(k) & -M \end{pmatrix}, \quad (4)$$

with $T_1 = 2t_1 \cos(k_i d_{\text{zz}}/2)$. The TISE for the bulk is given by

$$\hat{H}_{\text{bulk,zz}} \mathbf{u}(k) = E(k) \mathbf{u}(k), \quad (5)$$

with the periodic factor $\mathbf{u}(k) = (u_1(k), u_2(k), u_3(k), u_4(k))^T$ in the Bloch-like ansatz.

Other than for the armchair ribbon, the energies of the zig-zag ribbon can be written in a compact, analytical form

$$E(k) = \pm \sqrt{M^2 + t_1^2/4 \left(\sqrt{16 \cos^2(k d_{\text{zz}}/2) + 1} \pm 1 \right)^2}, \quad (6)$$

where both \pm are independent, leading to four bands. Results with and without M are shown in Fig. 2c, and d. For a vanishing on-site potential (c) there is no band gap between the bands with a negative energy (valance bands) and the bands with a positive energy (conduction bands). However, only transitions between the two black, solid or the two red, dashed bands are allowed for a linearly polarized laser field in dipole approximation [31,32]. This creates an effective band gap, $\Delta E_{\text{gap},0}$.

A band gap centered at $E = 0$ appears for non-vanishing on-site potential. It is given by $\Delta E_{\text{gap}} = 2|M|$, an example is shown in Fig. 2d. Transitions between all bands are allowed for $M \neq 0$.

2.2 Coupling to an external field

The coupling of the systems to an external field and the propagation of an electronic wavefunction in time is described in Ref. [28].

The vector potential is linearly polarized along the x -direction (i.e., along the ribbons). For times $0 \leq t \leq 2\pi n_{\text{cyc}}/\omega_0$, the vector potential is given by

$$\mathbf{A}(t) = A_0 \sin^2\left(\frac{\omega_0 t}{2n_{\text{cyc}}}\right) \sin(\omega_0 t) \mathbf{e}_x, \quad (7)$$

and it is zero otherwise. The following laser parameters are used if not stated otherwise: amplitude $A_0 = 0.2$ (intensity $\simeq 7.9 \times 10^{10}$ Wcm $^{-2}$), angular frequency $\omega_0 = 7.5 \cdot 10^{-3}$ (i.e., wavelength $\lambda = 6.1$ μm), and the pulse comprises $n_{\text{cyc}} = 4$ cycles.

The total current is given by

$$\mathbf{J}(t) = \sum_l \langle \Psi^l(t) | \hat{\mathbf{j}}(t) | \Psi^l(t) \rangle, \quad (8)$$

i.e., the sum over all currents arising from the occupied states $|\Psi^l(t)\rangle$, propagated in time. The current operator reads [33]

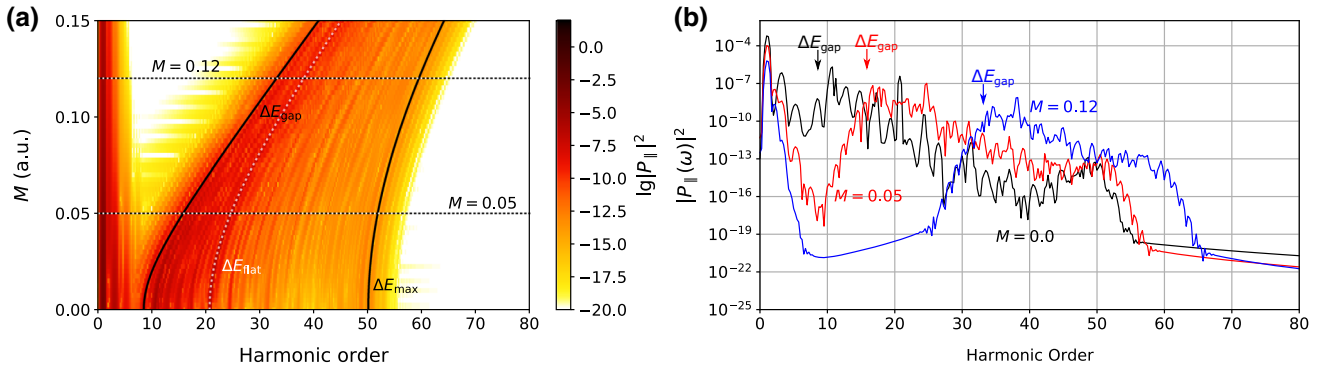


Fig. 3 (a) High-order harmonic spectra for a finite armchair ribbon with $N_{\text{hex}} = 4$ hexagons as function of the on-site potential M . The spectra show the emission polarized parallel to the polarization direction of the incoming laser field. The line representing ΔE_{gap} (ΔE_{max}) indicates

$$\hat{j}(t) = -i \sum_{i,j} (\mathbf{r}_i - \mathbf{r}_j) |i\rangle \langle i| H(t) |j\rangle \langle j|, \quad (9)$$

with $\mathbf{r}_{i,j}$ being the position of the sites i, j with their respective orbitals $|i\rangle$ and $|j\rangle$ and $H(t)$ the time-dependent Hamiltonian (see Ref. [28]). It is assumed that at the beginning of the pulse, all eigenstates with negative energy (i.e., below the Fermi level) are occupied.

The intensity of the emitted light is proportional to

$$|P_{\parallel,\perp}(\omega)|^2 = \left| \text{FFT} \left[j_{x,y}(t) \right] \right|^2. \quad (10)$$

The symbols \parallel and \perp denote the parallel (x -direction) and perpendicular (y -direction) polarization direction with respect to the polarization direction of the linear polarized laser pulse.

3 Results

In this paper, we discuss the high-order harmonic spectra for an armchair ribbon consisting of $N_{\text{hex}} = 4$ hexagons ($N = 24$) and a zig-zag ribbon built of $N_{\text{hex}} = 6$ hexagons ($N = 26$). The results are compared with simulations without the tight-binding approximation for systems of the same size [30]. We briefly discuss the size-dependence of the zig-zag ribbon at the end of this section.

3.1 Ribbon with armchair edges

The high-order harmonic spectra for parallel polarization as function of the on-site potential for the armchair ribbon are shown in Fig. 3a. In addition, the spectra for $M = 0$, $M = 0.05$, and $M = 0.12$ are shown in Fig. 3b. The energy is given in units of the laser frequency $\omega_0 = 0.0075$ (i.e., harmonic order). The laser field is polarized linearly along the ribbon. Light with a

the minimal band gap (maximal energy difference) between the valence and conduction bands of the respective periodic system. The horizontal lines mark the on-site potential of the spectra shown in (b)

polarization direction perpendicular to the field is not emitted. This is due to the symmetry of the system in that direction (i.e., the y -direction) even with a non-vanishing on-site potential (see Fig. 1a). In both plots, the minimal band gaps of the periodic system between valence and conduction band ΔE_{gap} are indicated. The band gap increases with the on-site potential M . The line ΔE_{max} (Fig. 3a) shows the maximal energy difference between valence and conduction band. It also increases with M . The horizontal lines in Fig. 3a mark those M s for which spectra are shown in Fig. 3b.

The band gap of the periodic system with vanishing on-site potential is $E_{\text{gap}} = 0.0644 \approx 8.6 \omega_0$. For the finite system with $N_{\text{hex}} = 4$ one finds a band gap of $0.08338 \approx 11.1 \omega_0$. The band gap of the finite system is larger because there are only 24 eigenstates of the Hamiltonian. Due to the restricted number of states, the sampling of the energy spectrum is not sufficient to capture the minimal band gap of the periodic ribbon. A larger finite chain would resolve it but is not part of this study. We refer to Ref. [34], where the size dependency of a one-dimensional, linear chain was studied. For an on-site potential of $M = 0.12$, the band gap of the finite system is given by $0.245 \approx 33.9 \omega_0$ and that of the periodic system is $E_{\text{gap}} = 0.248 = 33.1 \omega_0$. Here, the band gap of the finite and the band gap of the periodic system are similar.

In the harmonic spectra, one can see that the harmonic yield for small energies drops exponentially. Up to the energy of the band gap, the harmonic yield is relatively low. For energies larger than the band gap, one observes a plateau where the yield is almost constant. An ultimate cut-off is observed at an energy that corresponds to the maximum energy difference between valence and conduction bands ΔE_{max} . Transitions with larger energies are not possible in the tight-binding model. Hence, no harmonics are emitted at larger energies.

The harmonics below the band gap are dominated by movement of electrons inside the bands [35], known as intraband harmonics. Due to the fully occupied valence

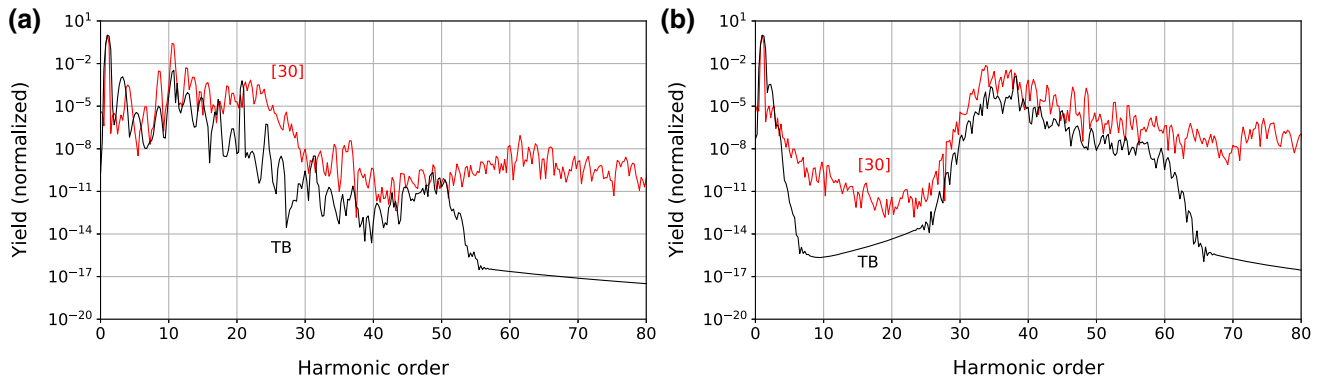


Fig. 4 Comparison of the harmonic yield (normalized to the maximal harmonic yield) of the armchair ribbon for the tight-binding model used in this work (TB) and the calculation without tight-binding approximation from Ref. [30].

For (a) the on-site potential is $M = 0.0$ ($V_{os} = 0.0$) and for (b) it is $M = 0.12$ ($V_{os} = 0.4$). V_{os} is the used parameter of the on-site potential in the reference

bands, there are electrons that move in opposite directions because of opposite band curvature, and therefore the emitted radiation by “individual” electrons destructively interferes, leading to the drop in the harmonic yield [18]. The plateau for larger energies is dominated by transitions between the valence and conduction bands [35], called interband harmonics. The band gap increases with the on-site potential M . As a consequence, the smallest energy of the plateau-region shifts to higher harmonic orders. The ultimate cut-off of the plateau also increases, because the maximal energy difference of the bands also becomes larger with increasing M . The onset and the cut-off of the plateau can be estimated by the periodic system. Its minimal band gap E_{gap} and maximal energy difference E_{max} is plotted in Fig. 3a. The colored-contour plot in Fig. 3a might not be able to show the starting and beginning of the plateau properly. It is better visible in Fig. 3b. The colored vertical arrows indicate the band gap of the respective periodic system. It agrees with the onset of the plateau if the on-site potential M is non-zero. The cut-off of the plateau for $M = 0$ is at around harmonic order 50 and for $M = 0.12$ at around 60 harmonic orders. The maximal energy difference of the periodic system is given by $\Delta E_{max} = 0.375 \approx 50.1 \omega_0$ and $\Delta E_{max} = 0.446 \approx 59.4 \omega_0$ for $M = 0$ and $M = 0.12$, respectively, agreeing with the cut-offs. The plateau is restricted to the region between E_{gap} and E_{max} , as expected.

The flat bands of the band structure (see Fig. 2a, b) are separated by an energy of $\Delta E_{flat} = 2|t_1| = 0.1556 \approx 20.7 \omega_0$ for $M = 0$. The harmonic spectrum shows a peak at this energy. With increasing on-site potential M , the energy difference between those bands increases, indicated by the dotted line ΔE_{flat} in Fig. 3a. There are as many states with the same energy inside the flat bands as there are hexagons in the ribbon. Therefore, many possible transitions have the same transition energy. This large number of transitions with identical energies causes the peak in the spectrum.

The results presented so far are qualitatively the same as the results in Ref. [30], in which no tight-

binding approximation is used. This can be seen from Fig. 4. The system with an on-site potential of $M = 0.12$ has approximately the same band gap as the system with an on-site potential of $V_{os} = 0.4$ in that reference (Fig. 4b). The method without the tight-binding approximation includes states above the conduction bands. Therefore, the spectra in that reference also show harmonics with larger energies than ΔE_{max} . These harmonics are absent when using the tight-binding approximation, here one should include more bands in order to obtain the correct spectra. However, the suppressed harmonic yield below the band gap is visible and also the slope of the plateau is similar. The advantage of the tight-binding approximation is the computational time. The algorithm here is approximately three orders of magnitude faster than the one in Ref. [30].

Note that the hopping parameter t_1 is chosen to fit the band gap of the systems for both methods. However, the maximal energy difference E_{max} is different. One reason for that is the symmetry of the tight-binding bulk Hamiltonian that enforces mirror-symmetric valence and conduction bands about the zero-energy axis. This symmetry is absent in the continuous description of Ref. [30].

3.2 Ribbon with zig-zag edges

Harmonic spectra for the finite zig-zag ribbon with $N_{hex} = 6$ hexagons as function of M are shown in Fig. 5 in parallel (Fig. 5a) and perpendicular (Fig. 5b) polarization direction with respect to the polarization of the incoming laser field. In addition, Fig. 6 shows spectra for three different on-site potentials M (Fig. 6a in parallel and Fig. 6b in perpendicular polarization direction). The corresponding M values are indicated by horizontal lines in Fig. 5. The marked energies ΔE_{gap} and ΔE_{max} indicate the minimal band gap and the maximal energy difference between valence and conduction band of the periodic system, respectively.

In both figures, one can see that without on-site potential, the zig-zag ribbon does not emit light per-

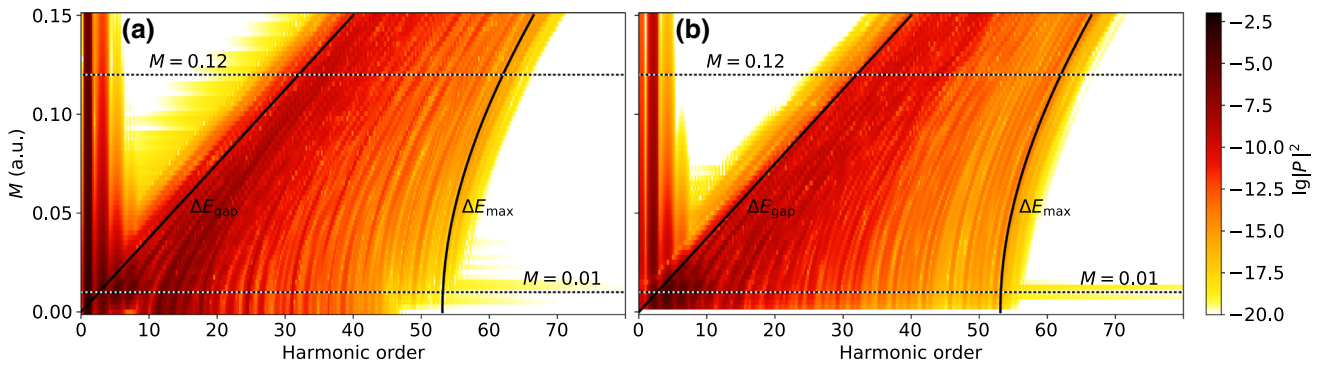


Fig. 5 Harmonic spectra for the finite zig-zag ribbon containing $N_{\text{hex}} = 6$ hexagons as function of the on-site potential M . Spectra in parallel (a) and perpendicular (b) polarization direction to the incoming field are shown. The line

ΔE_{gap} indicates the minimal band gap, the line ΔE_{max} the maximal gap between valence and conduction band as function of M for the periodic system

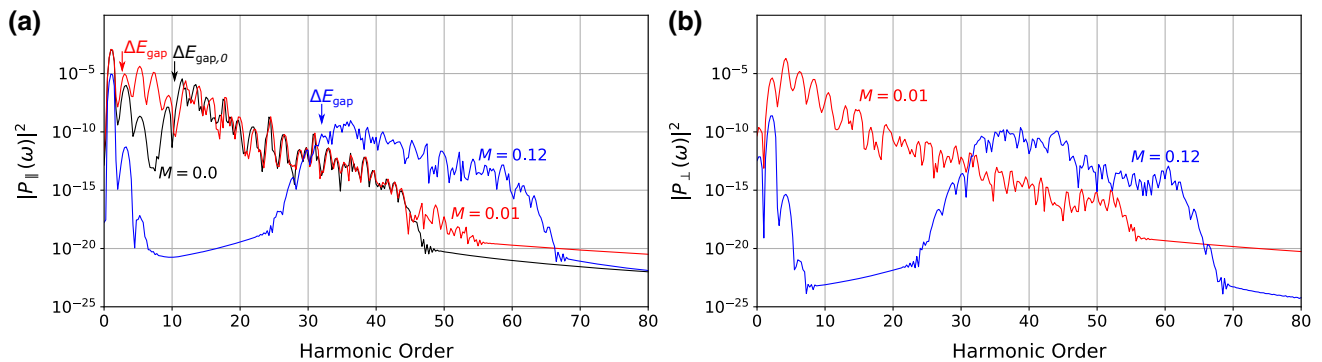


Fig. 6 High-order harmonic spectra of a finite zig-zag ribbon with $N_{\text{hex}} = 6$ hexagons for different on-site potentials M for the parallel (a) and perpendicular (b) polarization

direction to the incoming field. The vertical arrows mark the energy of the band gap for the respective periodic system

perpendicular to the polarization direction of the incoming laser field (i.e., the y -direction). As the on-site potential becomes finite, the symmetry of the system in y -direction is broken. This can be seen in Fig. 1b: the on-site potential at the lowest sites ($\alpha = 1$) is M , on the topmost sites ($\alpha = 4$) it is $-M$. As a consequence, the electrons are attracted more towards the upper sites than to the lower sites. Hence, light polarized in y -direction is now also emitted, i.e., perpendicular to the polarization of the incoming laser field, see Figs. 5b and 6b.

The band gap increases linearly with the on-site potential M and vanishes for $M = 0$. The spectra without on-site potential show an exponential decrease of the harmonic yield. A typical drop similar to the one for the armchair ribbon can be observed below harmonic order 11, best seen in Fig. 6a. This drop of the harmonic yield is explainable by the destructive interference of the intraband emission. One could expect that the interband harmonics should compensate the drop in the yield because of the vanishing band gap. However, as was shown in Refs. [31,32], transitions between certain bands are forbidden in the graphene zig-zag ribbon. This fact was already indicated in Fig. 2c: transitions are only allowed between the lowest valence and the lowest conduction band (black, solid

lines) and between the highest valence and conduction band (red, dashed lines). Therefore, the effective minimal band gap of the periodic system is given by $\Delta E_{\text{gap},0} = |t_1| = 0.07776 \approx 10.4 \omega_0$. This is in good agreement with the onset of the plateau. The maximal energy difference between the bands where transitions are allowed is given by $\Delta E_{\text{max},0} = 0.321 \approx 42.7 \omega_0$, which agrees well with the cut-off.

Further, as the band gap increases, we can see the typical drop of the harmonic yield for energies below ΔE_{gap} . The plateau lies in an energy region between ΔE_{gap} and ΔE_{max} for both polarization directions. This shows that the overall qualitative features in the harmonic spectra of this small zig-zag nanoribbon can be already understood with the help of the band structure of the periodic system. The results are similar to simulations without tight-binding approximation [30]. The only difference is the presence of harmonics above ΔE_{max} without tight-binding approximation due to higher lying states, similar to the armchair ribbon.

As the on-site potential increases, the selection rule for $M = 0$ does not apply anymore due to the broken symmetry in y -direction. However, we observe for the small system with $N_{\text{hex}} = 6$ and a small on-site potential that the spectra still show a drop in the harmonic yield for small energies, indicating the destructive inter-

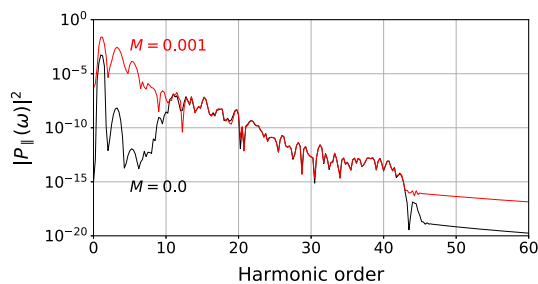


Fig. 7 High-harmonic spectrum in parallel polarization direction to the incoming field for a zig-zag ribbon with $N_{\text{hex}} = 15$ hexagons for on-site potential $M = 0$ and $M = 0.001$. The amplitude of the vector potential is $A_0 = 0.05$

ference of the intraband harmonics and an onset of the interband plateau only at higher harmonic order than expected from ΔE_{gap} . Hence, transitions between the highest valence band and the lowest conduction band are still very unlikely in such a small, finite zig-zag ribbon, otherwise the interband harmonics would fill up the drop of the intraband harmonic yield.

The approximation of a finite system by a periodic system fits better for larger finite systems. In Fig. 7, the harmonic spectrum in parallel polarization direction of a finite chain containing $N_{\text{hex}} = 15$ hexagons is shown. For a vanishing on-site potential $M = 0.0$, the drop in the harmonic yield up to order 11 can be observed.

For a small on-site potential of $M = 0.001$ the harmonic yield below the band gap is increased by several orders. Still, both valence bands are fully occupied, which means that the intraband harmonics interfere destructively as for $M = 0.0$ due to the movement of the electrons inside the bands. Obviously, the interband harmonics compensate the dropping intraband harmonic yield and thus the minimal energy of the interband harmonics must be close to zero. This is only possible if transitions between all bands are allowed, showing that for longer, finite zig-zag ribbons the $M = 0$ selection rule breaks more abruptly for slightly non-vanishing M than for shorter ribbons.

We note that in the calculation for $N_{\text{hex}} = 15$ we chose the amplitude of the vector potential $A_0 = 0.05$ (i.e., intensity $\simeq 7.9 \times 10^{10} \text{ Wcm}^{-2}$). For the same intensity as before ($A_0 = 0.2$) the yield drop for $M = 0$ is not clearly visible. With increasing laser intensity the excursion of the electrons along with the crystal momentum increases, diminishing the destructive interference of the intraband emission. As a result, the drop in the harmonic yield is not as pronounced as for smaller intensities. The fact that in the small ribbon with $N_{\text{hex}} = 6$ the drop is more pronounced might be due to the smaller number of states that do not resemble well continuous bands.

4 Summary and outlook

In this work, we simulated high-harmonic generation in finite hexagonal nanoribbons with armchair and zig-zag

edges. In an intense laser field polarized linearly along the ribbon, the armchair ribbon emits linearly polarized light parallel to the polarization of the incoming field. The zig-zag ribbon emits light parallel and perpendicular to the polarization of the incoming laser pulse if an alternating on-site potential is included. Both ribbons show a suppressed harmonic yield for energies below the band gap. The band gap itself is determined by the on-site potential. The main result of this manuscript is that characteristic features in the harmonic spectra, such as onset and cut-off of the interband-harmonics plateau, can be understood with the help of the band structure for the corresponding periodic systems. The results for the finite ribbons are similar to those from simulations without the tight-binding approximation.

Acknowledgements H.J. acknowledges financial support by the doctoral fellowship program of the University of Rostock.

Funding Information Open Access funding enabled and organized by Projekt DEAL.

Author contribution statement

HJ performed the numerical simulations, analyzed the results, and wrote the manuscript. DB provided critical feedback, supported the analysis of the results, and improved the final version of the manuscript.

Open Access This article is licensed under a Creative Commons Attribution 4.0 International License, which permits use, sharing, adaptation, distribution and reproduction in any medium or format, as long as you give appropriate credit to the original author(s) and the source, provide a link to the Creative Commons licence, and indicate if changes were made. The images or other third party material in this article are included in the article's Creative Commons licence, unless indicated otherwise in a credit line to the material. If material is not included in the article's Creative Commons licence and your intended use is not permitted by statutory regulation or exceeds the permitted use, you will need to obtain permission directly from the copyright holder. To view a copy of this licence, visit <http://creativecommons.org/licenses/by/4.0/>.

A Derivation of armchair bulk-Hamiltonian

For an armchair ribbon with N unit cells and periodic boundary conditions, the Hamiltonian reads

$$\begin{aligned} \hat{H}_0^{\text{arm}} = \sum_{m=1}^N & \left[\sum_{\alpha=1}^6 \left(t_1 |m, \alpha\rangle \langle m, (\alpha+1) \bmod 6| \right. \right. \\ & \left. \left. + (-1)^{\alpha+1} \frac{M}{2} |m, \alpha\rangle \langle m, \alpha| \right) \right. \\ & \left. + t_1 |m, 5\rangle \langle m+1, 2| \right] + \text{h.c.}, \end{aligned} \quad (11)$$

where we now write the state $|i\rangle$ at site i as $|m, \alpha\rangle$ where α indicates the site within unit cell m . In order to obtain the bulk-Hamiltonian, we make a Bloch-like ansatz, taking the relative position within a unit cell into account,

$$|\psi(k)\rangle = \frac{1}{\sqrt{N}} \sum_{m=1}^N e^{imkd_a} |m\rangle \otimes (u_1(k)e^{ikd_a/6}|1\rangle + u_2(k)|2\rangle + u_3(k)e^{ikd_a/6}|3\rangle + u_4(k)e^{ikd_a/2}|4\rangle + u_5(k)e^{2ikd_a/3}|5\rangle + u_6(k)e^{ikd_a/2}|6\rangle). \quad (12)$$

Here, $d_a = 3a$ is the lattice constant for the armchair ribbon. We plug this ansatz into the time-independent Schrödinger equation, $\hat{H}_0|\psi(k)\rangle = E(k)|\psi(k)\rangle$, and multiply by $\sqrt{N}e^{-im'kd_a}\langle m'|$ from the left, leading to

$$\hat{H}_{\text{bulk,arm}} \mathbf{u}(k) = E(k)\mathbf{u}(k), \quad (13)$$

with

$$\hat{H}_{\text{bulk,arm}} = \begin{pmatrix} M & t_1 e^{-ikd_a/6} & 0 & 0 & 0 & t_1 e^{ikd_a/3} \\ t_1 e^{ikd_a/6} & -M & t_1 e^{ikd_a/6} & 0 & t_1 e^{-ikd_a/3} & 0 \\ 0 & t_1 e^{-ikd_a/6} & M & t_1 e^{ikd_a/3} & 0 & 0 \\ 0 & 0 & t_1 e^{-ikd_a/3} & -M & t_1 e^{ikd_a/6} & 0 \\ 0 & t_1 e^{ikd_a/3} & 0 & t_1 e^{-ikd_a/6} & M & t_1 e^{-ikd_a/6} \\ t_1 e^{-ikd_a/3} & 0 & 0 & 0 & t_1 e^{ikd_a/6} & -M \end{pmatrix}, \quad (14)$$

where $\mathbf{u}(k) = (u_1(k), u_2(k), u_3(k), u_4(k), u_5(k), u_6(k))$. For given k , one obtains six eigenstates $\mathbf{u}^j(k)$ and energies $E^j(k)$ ($j = 1, 2, \dots, 6$). Hence, the system has six bands in the tight-binding approximation. We solve the eigenvalue equations numerically for each k . However, we show the calculation of one band analytically. For the periodic part of the Bloch-state we make the ansatz

$$\mathbf{u}_{\text{flat}}(k) = (\beta, 0, -\beta, -\gamma, 0, \gamma)^\top, \quad (15)$$

where the values of β and γ are unknown and k -dependent. Note that this state is zero at the connection points $\alpha = 2$ and 5 to the neighboring hexagons (see Fig. 1(c)). We obtain

$$\hat{H}_{\text{bulk,arm}} \mathbf{u}_{\text{flat}}(k) = \begin{pmatrix} M\beta + t_1 e^{ikd_a/3} \gamma \\ 0 \\ -M\beta - t_1 e^{ikd_a/3} \gamma \\ M\gamma - t_1 e^{-ikd_a/3} \beta \\ 0 \\ -M\gamma + t_1 e^{-ikd_a/3} \beta \end{pmatrix} \stackrel{!}{=} E_{\text{flat}} (\beta, 0, -\beta, -\gamma, 0, \gamma)^\top. \quad (16)$$

This relation holds if

$$M\beta + t_1 e^{ikd_a/3} \gamma = E_{\text{flat}} \beta \quad (17)$$

and

$$M\gamma - t_1 e^{-ikd_a/3} \beta = E_{\text{flat}} \gamma, \quad (18)$$

resulting in the energy

$$E_{\text{flat}} = \pm \sqrt{t_1^2 + M^2}. \quad (19)$$

As this energy is independent of k , the corresponding two bands are flat.

One can also show that the same energies are obtained for a finite armchair ribbon containing N_{hex} hexagons. The ansatz is that the state is zero everywhere except at one hexagon, where it is given by Eq. (15). The same energy (19) is obtained. The degeneracy is given by the number of hexagons in the ribbon N_{hex} .

References

1. S. Ghimire, A.D. DiChiara, E. Sistrunk, P. Agostini, L.F. DiMauro, D.A. Reis, Observation of high-order harmonic generation in a bulk crystal. *Nat. Phys.* **7**, 138–141 (2011)
2. O. Schubert, M. Hohenleutner, F. Langer, B. Urbanek, C. Lange, U. Huttner, D. Golde, T. Meier, M. Kira, S. Koch, R. Huber, Sub-cycle control of terahertz high-harmonic generation by dynamical Bloch oscillations. *Nat. Photon* **8**, 119–123 (2014)
3. G. Ndabashimiye, S. Ghimire, M. Wu, D.A. Browne, K.J. Schafer, M.B. Gaarde, D.A. Reis, Solid-state harmonics beyond the atomic limit. *Nature* **534**, 520–523 (2016)

4. F. Langer, M. Hohenleutner, U. Huttner, S. Koch, M. Kira, R. Huber, Symmetry-controlled temporal structure of high-harmonic carrier fields from a bulk crystal. *Nat. Photonics* **11**, 227–231 (2017)
5. N. Tancogne-Dejean, O.D. Mücke, F.X. Kärtner, A. Rubio, Impact of the electronic band structure in high-harmonic generation spectra of solids. *Phys. Rev. Lett.* **118**, 087403 (2017)
6. G.P. Zhang, M.S. Si, M. Murakami, Y.H. Bai, T.F. George, Generating high-order optical and spin harmonics from ferromagnetic monolayers. *Nat. Commun.* **9**(1), 3031 (2018)
7. G. Vampa, T.J. Hammond, M. Taucer, X. Ding, X. Ropagnol, T. Ozaki, S. Delprat, M. Chaker, N. Thiré, B.E. Schmidt, F. Légaré, D.D. Klug, A.Y. Naumov, D.M. Villeneuve, A. Staudte, P.B. Corkum, Strong-field optoelectronics in solids. *Nat. Photonics* **12**(8), 465–468 (2018)
8. M. Garg, H.Y. Kim, E. Goulielmakis, Ultimate waveform reproducibility of extreme-ultraviolet pulses by high-harmonic generation in quartz. *Nat. Photonics* **12**(5), 291–296 (2018)
9. G. Vampa, T.J. Hammond, N. Thiré, B.E. Schmidt, F. Légaré, C.R. McDonald, T. Brabec, D.D. Klug, P.B. Corkum, All-optical reconstruction of crystal band structure. *Phys. Rev. Lett.* **115**, 193603 (2015)
10. M. Hohenleutner, F. Langer, O. Schubert, M. Knorr, U. Huttner, S.W. Koch, M. Kira, R. Huber, Real-time observation of interfering crystal electrons in high-harmonic generation. *Nature* **523**, 572–575 (2015)
11. T.T. Luu, M. Garg, S.Y. Kruchinin, A. Moulet, M.T. Hassan, E. Goulielmakis, Extreme ultraviolet high-harmonic spectroscopy of solids. *Nature* **521**, 498–502 (2015)
12. Y.S. You, Y. Yin, Y. Wu, A. Chew, X. Ren, F. Zhuang, S. Gholam-Mirzaei, M. Chini, Z. Chang, S. Ghimire, High-harmonic generation in amorphous solids. *Nat. Commun.* **8**(1), 724 (2017)
13. M. Baudisch, A. Marini, J.D. Cox, T. Zhu, F. Silva, S. Teichmann, M. Massicotte, F. Koppens, L.S. Levitov, F.J. García de Abajo, J. Biegert, Ultrafast nonlinear optical response of Dirac fermions in graphene. *Nat. Commun.* **9**(1), 1018 (2018)
14. P.B. Corkum, Plasma perspective on strong field multiphoton ionization. *Phys. Rev. Lett.* **71**(13), 1994–1997 (1993)
15. M. Lewenstein, P. Balcou, M.Y. Ivanov, A. L’Huillier, P.B. Corkum, Theory of high-harmonic generation by low-frequency laser fields. *Phys. Rev. A* **49**, 2117–2132 (1994)
16. G. Vampa, C.R. McDonald, G. Orlando, D.D. Klug, P.B. Corkum, T. Brabec, Theoretical Analysis of High-Harmonic Generation in Solids. *Phys. Rev. Lett.* **113**, 073901 (2014)
17. G. Vampa, T. Brabec, Merge of high harmonic generation from gases and solids and its implications for attosecond science. *J. Phys. B: At. Mol. Opt. Phys.* **50**(8), 083001 (2017)
18. D. Bauer, K.K. Hansen, High-harmonic generation in solids with and without topological edge states. *Phys. Rev. Lett.* **120**, 177401 (2018)
19. H. Driücke, D. Bauer, Robustness of topologically sensitive harmonic generation in laser-driven linear chains. *Phys. Rev. A* **99**, 053402 (2019)
20. H. Jürß, D. Bauer, High-harmonic generation in Su-Schrieffer-Heeger chains. *Phys. Rev. B* **99**, 195428 (2019)
21. D. Dimitrovski, L.B. Madsen, T.G. Pedersen, High-order harmonic generation from gapped graphene: Perturbative response and transition to nonperturbative regime. *Phys. Rev. B* **95**, 035405 (2017)
22. L.A. Chizhova, F. Libisch, J. Burgdörfer, High-harmonic generation in graphene: interband response and the harmonic cutoff. *Phys. Rev. B* **95**, 085436 (2017)
23. N. Yoshikawa, T. Tamaya, K. Tanaka, High-harmonic generation in graphene enhanced by elliptically polarized light excitation. *Science* **356**(6339), 736–738 (2017)
24. H.A. Hafez, S. Kovalev, J.-C. Deinert, Z. Mics, B. Green, N. Awari, M. Chen, S. Germanskiy, U. Lehnert, J. Teichert, Z. Wang, K.-J. Tielrooij, Z. Liu, Z. Chen, A. Narita, K. Müllen, M. Bonn, M. Gensch, D. Turchinovich, Extremely efficient terahertz high-harmonic generation in graphene by hot Dirac fermions. *Nature* **561**, 507–511 (2018)
25. L. Yue, M.B. Gaarde, Structure gauges and laser gauges for the semiconductor Bloch equations in high-order harmonic generation in solids. *Phys. Rev. A* **101**, 053411 (2020)
26. R.E.F. Silva, Á. Jiménez-Galán, B. Amorim, O. Smirnova, M. Ivanov, Topological strong-field physics on sub-laser-cycle timescale. *Nat. Photonics* **13**(12), 849–854 (2019)
27. A. Chacón, D. Kim, W. Zhu, S.P. Kelly, A. Dauphin, E. Pisanty, A.S. Maxwell, A. Picón, M.F. Ciappina, D.E. Kim, C. Ticknor, A. Saxena, M. Lewenstein, Circular dichroism in higher-order harmonic generation: Herald-ing topological phases and transitions in Chern insulators. *Phys. Rev. B* **102**, 134115 (2020)
28. H. Jürß, D. Bauer, Helicity flip of high-order harmonic photons in Haldane nanoribbons. *Phys. Rev. A* **102**, 043105 (2020)
29. D. R. Cooper, B. D’Anjou, N. Ghattamaneni, B. Harack, M. Hilke, A. Horth, N. Majlis, M. Massicotte, L. Vandsburger, E. Whiteway, and V. Yu, Experimental review of Graphene. *ISRN Cond. Matter Phys.* **2012**, Article ID 501686 (2012)
30. H. Driücke and D. Bauer, High-harmonic spectra of hexagonal nanoribbons from real-space time-dependent Schrödinger calculations. (2021). [arXiv:2101.06970](https://arxiv.org/abs/2101.06970) [cond-mat.mes-hall]
31. H. Hsu, L.E. Reichl, Selection rule for the optical absorption of graphene nanoribbons. *Phys. Rev. B* **76**, 045418 (2007)
32. V.A. Saroka, M.V. Shuba, M.E. Portnoi, Optical selection rules of zigzag graphene nanoribbons. *Phys. Rev. B* **95**, 155438 (2017)
33. A.L. Kuzemsky, Electronic transport in metallic systems and generalized kinetic equations. *Int. J. Mod. Phys. B* **25**(23–24), 3071–3183 (2011)
34. K.K. Hansen, D. Bauer, L.B. Madsen, Finite-system effects on high-order harmonic generation: from atoms to solids. *Phys. Rev. A* **97**, 043424 (2018)
35. F. Navarrete, M.F. Ciappina, U. Thumm, Crystal-momentum-resolved contributions to high-order harmonic generation in solids. *Phys. Rev. A* **100**, 033405 (2019)

5.1.4 Edge-state influence on high-order harmonic generation in topological nanoribbons

by Hannah Jürß and Dieter Bauer

The European Physical Journal D **75**:190 (2021)

DOI: [10.1140/epjd/s10053-021-00201-9](https://doi.org/10.1140/epjd/s10053-021-00201-9)

Reference: [4]

Author Contributions

Hannah Jürß	performing the numerical simulations (deriving the necessary equations for the simulations, writing the code and running it), analyzing the results, writing the manuscript
-------------	-----------------------------------------------------------------------------------------------------------------------------------------------------------------------------

Dieter Bauer	providing critical feedback, supporting the analysis of the results, improving the manuscript, supervision
--------------	------------------------------------------------------------------------------------------------------------



Edge-state influence on high-order harmonic generation in topological nanoribbons

Hannah Jürß^{1,a}  and Dieter Bauer^{1,b}¹ Institute of Physics, University of Rostock, 18051 Rostock, GermanyReceived 26 March 2021 / Accepted 14 June 2021 / Published online 29 June 2021
© The Author(s) 2021

Abstract. The high-order harmonic generation in finite topological nanoribbons is investigated using a tight-binding approximation. The narrow, two-dimensional ribbons consist of hexagonal structures. A topological phase transition is defined by a sudden change of the topological invariant. In the bulk, this kind of phase transition might occur if an existing band gap closes and reopens again. Through the bulk-boundary correspondence, this is related to the emergence of topologically protected edge states in the respective finite systems. For the finite ribbons studied in this work, the variation of the tight-binding parameters leads to the emergence of two edge states after the closing of the band gap. The energies of those edge states as functions of the tight-binding parameters display crossings and avoided crossings, which influence the high-harmonic spectra.

1 Introduction

Topological insulators are a special kind of solid-state material that is an electrical insulator in its bulk but conducting on its edges or surfaces. The edge or surface states are protected against perturbations [1]. The first realization of a topological insulator in the experiment was reported by König et al. in 2007 [2] using HgTe quantum wells. Topological insulators might play a big role in the development of quantum computers [1, 3].

Recent studies show that the topological phase of a solid can have a huge influence on the generation of high-order harmonic radiation. In fact, the topological phase might affect the harmonic yield by several orders of magnitude [4–6], flip the helicity of the emitted photons [7–9] or introduce circular dichroism [10]. In three-dimensional topological insulators, the harmonic yield of bulk and surface states show a different dependency on the ellipticity of the laser field [11].

It is known that the high-harmonic generation (HHG) in solids in general carries information about the static and dynamic properties of the solid [12–17]. In this work, we investigate two-dimensional, hexagonal nanoribbons that are narrow, i.e., the ribbons are much longer in one of the two dimensions. The systems are described using a tight-binding approximation where hopping between nearest neighbors are allowed, thus describing graphene ribbons. The HHG in graphene was studied previously, for example in Refs. [18–21]. Adding an alternating on-site potential because of different

atomic elements such as in hexagonal boron nitride (h-BN), for instance, the sublattice symmetry is broken. HHG in h-BN has been studied as well, e.g., in Refs. [22–24]. The dependence of HHG on the on-site potential for hexagonal ribbons was studied in [25, 26].

With a broken time-reversal symmetry, the system might become topologically non-trivial. This can be achieved by including a complex hopping between next-nearest neighbors as in the Haldane-model [27]. The Haldane-model in the context of HHG was studied in Refs. [7, 8, 10].

In this paper, we examine how the edge states of Haldane nanoribbons influence the emission of high-order harmonics. Topological nanoribbons were studied without an external field in Ref. [28]. Although edge states are only present in finite systems, the bulk-boundary correspondence [29] tells that a non-vanishing difference between the topological invariants of the bands for the bulk imply the presence of edge states in the respective finite system. The question then is which topological effects in HHG spectra are due to bulk already and which require the explicit presence of edge states. An example system where the explicit presence of edge states is necessary to see any topological effect in HHG spectra is the one-dimensional Su-Schrieffer-Heeger chain [9]. In 2D systems such as the Haldane model, on the other hand, one can observe helicity flips already for bulk only [7, 9].

The outline of the paper is as follows. In Sec. 2, we summarize the theoretical methods used in this work. In Sec. 3.1, the properties of the static system are explained, with a focus on the edge states. The HHG of Haldane nanoribbons is discussed in Sec. 3.2. If not

^a e-mail: hannah.juerss@uni-rostock.de (corresponding author)

^b e-mail: dieter.bauer@uni-rostock.de

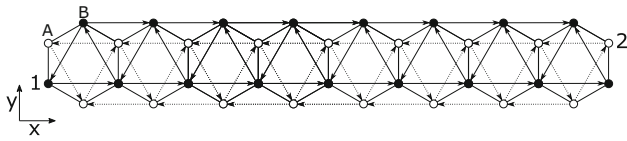


Fig. 1 Sketch of a nanoribbon with zigzag edges comprising eight hexagons. The circles indicate the atomic sites. The on-site potential on sites with an unfilled circle is given by M (sublattice A), and for the filled circles, it is given by $-M$ (sublattice site B). Lines (without arrow) indicate the hopping between nearest neighbors (amplitude t_1). The arrows indicate the next-nearest neighbor hopping with amplitude it_2 in the direction of the arrow (and $-it_2$ in the opposite direction). We label the lower left edge site ‘1’ and the upper right edge site ‘2’

stated otherwise, atomic units (a.u., $\hbar = |e| = m_e = 4\pi\epsilon_0 = 1$) are used throughout this paper.

2 Theory

The systems that are investigated in this work are hexagonal ribbons with zigzag edges as shown in Fig. 1. The simulated ribbons consist of 30 hexagons though (not only eight, as shown in Fig. 1). A tight-binding approximation is used. The circles in Fig. 1 indicate the sites with an on-site potential M ($-M$) for the unfilled (filled) circles, corresponding to the two sublattice sites A (unfilled) and B (filled). Lines without arrows indicate hopping between the nearest neighboring sites with an amplitude $t_1 \in \mathbb{R}$. The arrows indicate a complex next-nearest neighbor hopping with amplitude it_2 (with $t_2 \in \mathbb{R}$) along the arrows (and $-it_2$ in the opposite direction). The complex next-nearest neighbor hopping breaks the time-reversal symmetry, making the system topologically nontrivial for sufficiently large t_2 [27]. In this work, we will vary t_2 .

Note, the hopping parameter t_2 cannot be influenced in a solid and is given by the system itself. However, the topological phase might be controlled by the complex phase of the hopping amplitude (here fixed to $e^{i\varphi_{t_2}} = i$) or by the sub-cycle structure of non-resonant external fields [30]. Topological phase transitions are easier to control on synthetic platforms like waveguides [31] or cold atoms [32] but there is no HHG in these topological systems.

2.1 Static system

The theoretical description of the topological ribbons is almost the same as in Ref. [8], with the difference that periodic boundary conditions were assumed there. As a consequence, the hopping elements from the left to the right edge of the ribbon are missing in the present work.

The Hamiltonian describing the electrons on the ribbon reads in tight-binding approximation

$$\hat{H}_0 = t_1 \sum_{\langle i,j \rangle} (|j\rangle \langle i| + \text{h.c.}) + it_2 \sum_{\ll i,j \gg} (|j\rangle \langle i| - \text{h.c.}) + M \left(\sum_{i \in A} |i\rangle \langle i| - \sum_{i \in B} |i\rangle \langle i| \right) \quad (1)$$

where the sums $\sum_{\langle i,j \rangle}$ and $\sum_{\ll i,j \gg}$ run over all nearest and next-nearest neighboring sites i, j , respectively. The sum $\sum_{i \in A}$ ($\sum_{i \in B}$) include all sites on sublattice site A (B). The state $|i\rangle$ denotes the atomic orbital at site i . A general state reads

$$|\psi\rangle = \sum_{i=1}^N g_i |i\rangle, \quad (2)$$

where N is the number of sites in the system.

The time-independent Schrödinger equation

$$\hat{H}_0 |\psi_l\rangle = E_l |\psi_l\rangle \quad (3)$$

is solved to obtain the eigenstates $|\psi_l\rangle$ with their respective energies E_l . The number of eigenstates is given by the number of sites N , i.e., $l = 0, 1, 2, \dots, N - 1$. The labeling is such that the energies of the states increase with l , i.e., $E_0 \leq E_1 \leq E_2 \leq \dots \leq E_{N-1}$. Equation (3) is solved numerically by diagonalization of the Hamiltonian (1).

The distance between nearest neighbors is set to $a = 2.68 \text{ a.u.} \simeq 1.42 \text{ \AA}$ and the hopping between them to $t_1 = -0.1 \text{ a.u.} \simeq -2.7 \text{ eV}$, the parameters for graphene [33]. The on-site potential M and the next-nearest neighbor hopping amplitude t_2 are varied in this work.

2.2 Coupling to an external field

The ribbons are coupled to an external field via velocity gauge, which translates to the Peierls substitution [34] in tight-binding approximation. The gauge-invariant coupling of general tight-binding systems to external fields was derived in Ref. [35].

The laser pulses are described by a vector potential of the form

$$\mathbf{A}(t) = A_0 \sin^2 \left(\frac{\omega_0 t}{2n_0} \right) \sin(\omega_0 t) \mathbf{e}_x, \quad (4)$$

for times $0 \leq t \leq 2\pi n_0 / \omega_0$ (and zero otherwise). It is linearly polarized along the ribbon, that is, in x -direction. The number of cycles in the laser pulse is chosen $n_0 = 5$, the amplitude of the vector potential $A_0 = 0.05$ (intensity $\simeq 5 \times 10^9 \text{ Wcm}^{-2}$), and the angular frequency is $\omega_0 = 7.5 \cdot 10^{-3}$ (i.e., wavelength $\lambda_0 = 6.1 \mu\text{m}$).

We assume that all states with an energy smaller than $E = 0$ are occupied. Due to the symmetry of the energy spectrum, these are half of the states. Hence, $|\Psi_l(t)\rangle$ with $l = 0, 1, 2, \dots, N/2 - 1$ are propagated in time, starting from $|\Psi_l(t = 0)\rangle = |\psi_l\rangle$.

The total current is given by

$$\mathbf{J}(t) = \sum_{l=0}^{N/2-1} \langle \Psi^l(t) | \hat{\mathbf{j}}(t) | \Psi^l(t) \rangle, \quad (5)$$

where the current operator is given by [36]

$$\hat{\mathbf{j}}(t) = -i \sum_{i,j} (\mathbf{r}_i - \mathbf{r}_j) |i\rangle \langle i| \hat{H}(t) |j\rangle \langle j|, \quad (6)$$

with the positions $\mathbf{r}_{i,j}$ of sites i, j . The time-dependent Hamiltonian reads

$$\langle i | \hat{H}(t) | j \rangle = \langle i | \hat{H}_0 | j \rangle e^{-i(\mathbf{r}_i - \mathbf{r}_j) \cdot \mathbf{A}(t)}. \quad (7)$$

Harmonic spectra are calculated from the two components of the current (5) via a Fourier transformation,

$$P_{\parallel,\perp}(\omega) = \int_{-\infty}^{+\infty} \mathbf{j}_{x,y}(t) e^{-i\omega t} dt. \quad (8)$$

Here, \parallel and \perp denote the polarization direction of the emitted light with respect to the incoming field: parallel (x -direction) and perpendicular (y -direction), respectively. In the code, the Fourier transformation is approximated by the fast Fourier transformation. The functions $|P_{\parallel,\perp}(\omega)|^2$ are proportional to the intensity of the emitted light [37–39] polarized in the respective direction. The phase difference

$$\Delta\phi = \arg(P_{\parallel}(\omega)P_{\perp}^*(\omega)) \quad (9)$$

indicates the helicity of the emitted photons.

3 Results

3.1 Static system

The number of atoms and eigenstates for the 30-hexagon long ribbons is $N = 122$. In Fig. 2, the energies of all states as function of the next-nearest neighbor hopping amplitude t_2 are shown for $M = 0$ (Fig. 2a) and $M = 0.01$ (Fig. 2b). For $M = 0$ (Fig. 2a), a band gap opens as t_2 increases so that the fully occupied valence band with $E < 0$ and the empty conduction band with $E > 0$ become well-separated. In the middle of the gap, two states appear around an energy of $E = 0$. One of this state is occupied, the other one not. For the system with an on-site potential of $M = 0.01$ (Fig. 2b), there is already a band gap for $t_2 = 0$ but without states in the middle. First, this band gap closes

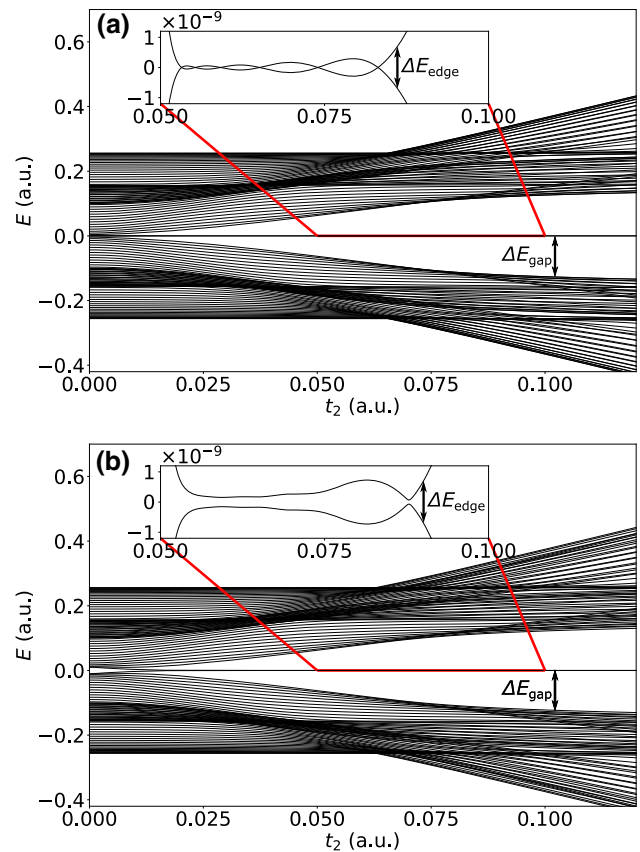


Fig. 2 Energies of the system for **a** $M = 0$ and **b** $M = 0.01$ as function of t_2 . The insets show the evolution of the two states in a tiny energy interval around $E = 0$

with increasing t_2 before it opens up again for larger values. This band gap closure is an indication for a topological phase transition. In fact, in the middle of the band gap two states appear when the band gap opens up again. We will call those two states edge states because their probability density is located on the edges of the chain, as shown in Fig. 4. We define the energy difference ΔE_{gap} as the energy difference between the valence band and the lowest edge state energy.

The insets in Figs. 2a,b are magnifications and show the tiny energies of both edge states between $0.05 \leq t_2 \leq 0.10$. Their difference is defined as ΔE_{edge} . Surprisingly, the energies of these states do not just monotonically converge to $E = 0$. For $M = 0$, they cross six times in the interval shown before their energies separate for larger t_2 . For the finite on-site potential in Fig. 2b, the crossings turn into avoided crossings.

In Fig. 3, the energy difference between the edge states ΔE_{edge} is shown for different M as function of t_2 . It shows the crossings for $M = 0$ and that these crossings become avoided crossings for larger M . As the on-site potential increases further, the avoided crossings tend to smooth out. For $M = 0.01$ and $M = 0.02$, there are mainly two local minima. The energy difference ΔE_{edge} decreases with t_2 up to a local minimum at around $t_2 = 0.059$ for $M = 0.01$. The slope of ΔE_{edge}

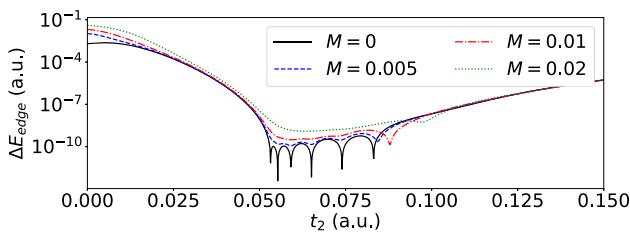


Fig. 3 Energy difference between the edge states as function of t_2 on a logarithmic scale for different on-site potentials M

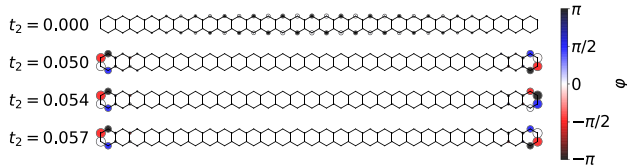


Fig. 4 Wave function of the highest occupied state (lowest state of the two edge states) for $M = 0$ and different t_2 . The size of the circles indicates the probability density. The phase of the wave function is indicated by the color of the circles

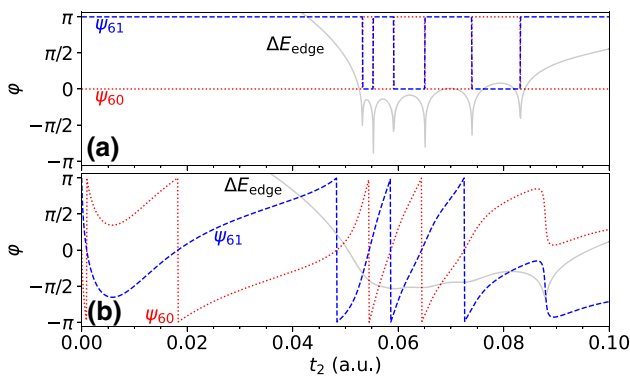


Fig. 5 Phase of the wave function of the initially highest occupied state (ψ_{60}) and the lowest unoccupied state (ψ_{61}) on site 2 (see Fig. 1) of the ribbon as function of t_2 for an on-site potential $M = 0$ (a) and $M = 0.01$ (b). The differences of the energies of both states ΔE_{edge} on a logarithmic scale from Fig. 3 are included in gray to show that phase jumps occur at (avoided) crossings

following this local minimum is quite shallow, rendering it a flat local minimum. A much more localized minimum occurs at $t_2 = 0.088$. Both minima are shifted toward larger t_2 as M increases. The other crossings cannot be observed anymore as the on-site potential becomes larger.

In Fig. 4, the wave function ψ_{60} of the state within the band gap with the smaller energy is shown. This is the highest, initially occupied state. The size of the sketched circles at the lattice site scales with the probability density there. The phase of the wave function is indicated by the color of the circles. For ease of comparison, we use a phase convention for the initial states for which the phase at site 1 is zero (see Fig. 1). The

wave functions are given for different t_2 but fixed on-site potential $M = 0$. For $t_2 = 0$ the probability density is equally located on the upper and lower edge. With increasing t_2 , the electron probability moves toward the left and right edges. The same happens for the lowest unoccupied state ψ_{61} , whose phase is different but probability density is the same (not shown). Because of the dominant location of the electron at the edges, we call these two states edge states. Clearly, for a system periodic in x -direction, these kind of states are absent due to the absence of left and right edges.

Crossings of the energies between both edge states occur at $t_2 = 0.053$ and $t_2 = 0.055$. For $t_2 = 0.05$, one can see a certain symmetry of the highest occupied state in Fig. 4. The phases of the wave function at the four leftmost sites, reading from top to bottom, is identical to the phases at the four rightmost sites but reading from bottom to top. The electron is mainly located on those eight sites. The wave function is symmetric under rotation by 180° about an axis perpendicular to the xy -plane of the ribbon and through its center. For $t_2 = 0.054$, the energies of both edge states have crossed so that the occupied state should now have the properties of the (for lower t_2) unoccupied one, and the other way around. Indeed, the phases of the wave function on the right edge of state ψ_{60} are now different. The state is not symmetric anymore under rotations by 180° . The phases at the four rightmost sites reading, from bottom to top, is identical to the phase at the four leftmost sites, read from top to bottom, plus π . This is indeed the symmetry of the other edge state. The next crossing appears at $t_2 = 0.055$. The symmetry of the highest occupied state for $t_2 = 0.057$ is now identical to the state for $t_2 = 0.05$, indicating that another crossing occurred.

In order to identify the exchange of the edge states, it is sufficient to look at the phases at, e.g., site 2 (see Fig. 1). In Fig. 5, the phase at this site for both edge states ψ_{60} and ψ_{61} is shown as function of t_2 . In Fig. 5a, the phases for $M = 0$ are shown. The phases are constant for small t_2 . For the highest occupied state ψ_{60} , the phase is $\varphi = 0$ and $\varphi = \pi$ for the lowest unoccupied state ψ_{61} . At each crossing, the phases of both states change to the value of the other state, indicating that the properties of both states are exchanged each time their energies cross. In order to remind for which t_2 crossings occur, the energy difference ΔE_{edge} from Fig. 3 is sketched in gray. In Fig. 5b, the same is plotted for an on-site potential of $M = 0.01$. From a local minimum at $t_2 = 0.0058$, both phases increase up to $t_2 = 0.088$ where ΔE_{edge} assumes a minimum. (Note that we plot phases modulo 2π within the interval $[-\pi, \pi)$ so that phases exceeding π reenter at $-\pi$.) In a narrow neighborhood around this value of t_2 , both phases change by about π in a continuous manner, which is characteristic of an avoided crossing. The properties of the two edge states also exchange in this case so that the previously highest occupied state becomes the previously lowest unoccupied state and the other way around.

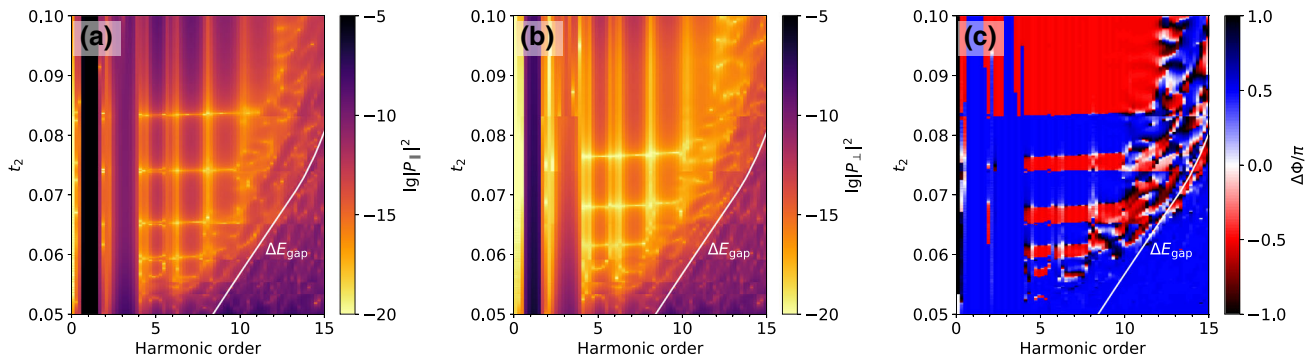


Fig. 6 High-order harmonic spectrum in **a** parallel and **b** perpendicular direction to the polarization of the external field, and **c** the corresponding phase difference between both components as a contour plot as function of t_2 . The on-site potential is $M = 0.0$. The white line ΔE_{gap} is the gap between the valence band and the lowest edge state

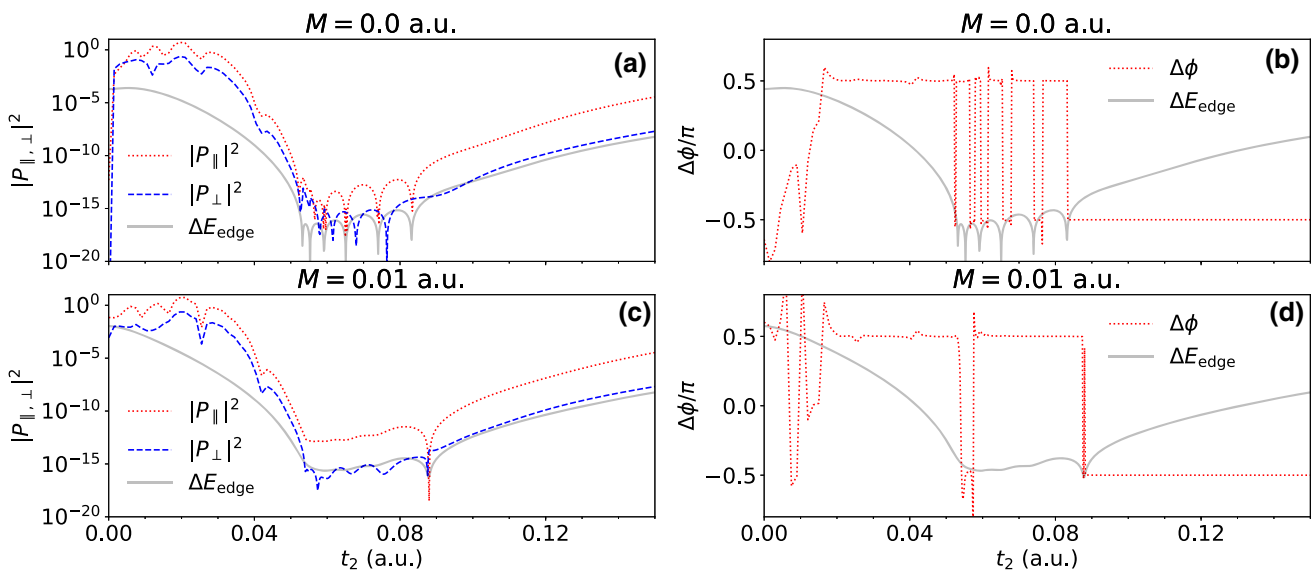


Fig. 7 Harmonic yield for both polarization directions **a**, **c**) and phase difference **b**, **d**) for harmonic order 5 as function of t_2 . For **a**, **b**, the on-site potential is $M = 0$, for **c**, **d** $M = 0.01$. The energy difference ΔE_{edge} is included in gray to ease the interpretation of the results (extra y -axis for ΔE_{edge} suppressed)

3.2 High-harmonic generation

Figure 6 shows harmonic spectra in parallel (Fig. 6a) and perpendicular (Fig. 6b) polarization direction to the polarization of the incoming field for $M = 0$ as function of t_2 . In Fig. 6c, the phase difference (9) between both components is shown. Just to avoid confusion, in the previous sections, we discussed phases of electronic edge states φ , and now we examine the phases of the emitted harmonic radiation $\Delta\phi$. The goal is to understand how both are related.

We only show the spectra for the parameter space where the properties of the edge states matter. For more details at other parameters, in particular higher harmonic orders, we refer to Ref. [8]. The harmonics of interest are below energy ΔE_{gap} , which is defined by the highest state of the valence band and the lowest edge state (see Fig.2). The harmonic yield in this region decreases exponentially with harmonic order due

to the destructive interference of intraband harmonics [4]. However, odd harmonics can still be observed up to order 9 or 11, depending on t_2 . At certain t_2 , the harmonic yield drops drastically for harmonics 5 till 9. This can be seen as a yellow horizontal traces in Figs. 6a,b. In the phase plot, several flips of the phase from blue to red color (flip by $\pm\pi$) can be observed. For a fixed harmonic order (5 till 9), the phase difference flips several times as t_2 increases.

In Fig. 7, the harmonic yield in both polarization directions for harmonic order 5 is shown for $M = 0$ (Fig. 7a) and $M = 0.01$ (Fig. 7c) as function of t_2 . The respective phase differences (9) are shown in Fig. 7b ($M = 0$) and Fig. 7d ($M = 0.01$). The energy difference of the edge states ΔE_{edge} is included (with an extra y -axis suppressed, as only the behavior as function of t_2 is relevant).

In Fig. 7a, one can see a decreased harmonic yield in parallel polarization direction that occurs exactly at the

points where ΔE_{edge} is minimal (crossing of the edge states). There is an exception for the first two local minima of ΔE_{edge} where no significant decrease in the harmonic yield is observed. The minima of the yield in the perpendicular direction are located between two crossings (again with an exception between the first two crossings). In the phase difference (Fig. 7b), a phase flip from $\Delta\phi = \pi/2$ to $\Delta\phi = -\pi/2$ can be observed for the last four crossings. The phase flips back to $\Delta\phi = \pi/2$ between two crossing points. The back-flip of the phase is located at about the local minima of the yield in perpendicular polarization direction. Interestingly, the phase difference is $\Delta\phi = \pi/2$ before the first crossing and becomes $\Delta\phi = -\pi/2$ after the last crossing point. Further, we note that the harmonic yield in parallel polarization direction is related to ΔE_{edge} for sufficiently large t_2 ($t_2 > 0.055$).

In Figs. 7c and 7d, the harmonic yield and the phase difference is shown for $M = 0.01$. The harmonic yield in parallel polarization direction drops again drastically at the local minimum of ΔE_{edge} at $t_2 = 0.088$. This is the point where the energies of the edge states have an avoided crossing. The harmonic yield in perpendicular direction drops at the same value but not as much as the yield in parallel direction. Before the first local minimum of ΔE_{edge} , the phase difference is fluctuating around values $\Delta\phi = \pi/2$. At the first local minimum at $t_2 = 0.059$, a phase flip to $\Delta\phi = -\pi/2$ can be observed but the phase flips back to $\Delta\phi = \pi/2$ for a slightly larger t_2 . At the point of the avoided crossing at $t_2 = 0.088$, the phase flips permanently to $\Delta\phi = -\pi/2$.

The two graphs of the phase difference Figs. 7b,d show that the (avoided) crossings of the edge state energies cause a phase flip by π . Between two crossings, the phase flips back slightly after the first of the two crossings. Comparing the phases for small and large t_2 , the phase changes from $\Delta\phi = \pi/2$ (small t_2) to $\Delta\phi = -\pi/2$ (large t_2).

The phase flips at the crossing points can be understood by the edge states. The properties of the initially occupied and unoccupied edge state exchange at each crossing point (and the avoided crossing at $t_2 = 0.088$ for $M = 0.01$). Therefore, the occupied edge state suddenly has the symmetry of the unoccupied state and the other way around. This affects the yield and the helicity of the emitted harmonics, as just demonstrated.

In the parameter regime where the phase flips occur, the harmonic yield for both polarization directions differs several orders of magnitude for fixed t_2 . This means that despite $\Delta\phi = \pm\pi/2$, the ellipticity of the emitted harmonics is close to zero, i.e., the harmonics are almost linearly polarized. Nevertheless, the helicity flips discussed in this work should be measurable experimentally by interferometric means.

4 Summary and outlook

The edge states in the simulated finite, topological nanoribbons show a specific behavior as the tight-

binding parameters are varied. The two edge states do not converge to the same energy but show crossings and avoided crossings. These crossings have a significant influence on the harmonic generation process. The phase difference between the two polarization components of the emitted light for certain harmonic orders change where the edge state energies cross (or have an avoided crossing). We find that the yield of low-order harmonics polarized parallel to the polarization of the incoming field is related to the energy difference of the edge states.

Certainly, our model studies presented in this work are highly idealized and simplified, as is the original Haldane model for the corresponding bulk. However, tailorable anomalous Hall systems are available (see, e.g., [40] and references therein), and a more realistic theoretical description of HHG in such systems is worthwhile to pursue in future work.

Acknowledgements H.J. acknowledges financial support by the doctoral fellowship program of the University of Rostock.

Author contributions

H.J. performed the numerical simulations, analyzed the results, and wrote the manuscript. D.B. provided critical feedback, supported the analysis of the results, and improved the final version of the manuscript.

Funding Open Access funding enabled and organized by Projekt DEAL.

Data availability This manuscript has no associated data or the data will not be deposited. [Authors' comment: The data that support the findings of this study are available on request from the author H.J.]

Open Access This article is licensed under a Creative Commons Attribution 4.0 International License, which permits use, sharing, adaptation, distribution and reproduction in any medium or format, as long as you give appropriate credit to the original author(s) and the source, provide a link to the Creative Commons licence, and indicate if changes were made. The images or other third party material in this article are included in the article's Creative Commons licence, unless indicated otherwise in a credit line to the material. If material is not included in the article's Creative Commons licence and your intended use is not permitted by statutory regulation or exceeds the permitted use, you will need to obtain permission directly from the copyright holder. To view a copy of this licence, visit <http://creativecommons.org/licenses/by/4.0/>.

References

1. M.Z. Hasan, C.L. Kane, Colloquium: Topological insulators. *Rev. Mod. Phys.* **82**, 3045–3067 (2010)

2. M. König, S. Wiedmann, C. Brüne, A. Roth, H. Buhmann, L.W. Molenkamp, X.-L. Qi, S.-C. Zhang, Quantum Spin Hall Insulator State in HgTe Quantum Wells. *Science* **318**(5851), 766–770 (2007)
3. J.E. Moore, The birth of topological insulators. *Nature* **464**, 194–198 (2010)
4. D. Bauer, K.K. Hansen, High-harmonic generation in solids with and without topological edge states. *Phys. Rev. Lett.* **120**, 177401 (2018)
5. H. Drüeke, D. Bauer, Robustness of topologically sensitive harmonic generation in laser-driven linear chains. *Phys. Rev. A* **99**, 053402 (2019)
6. H. Jürß, D. Bauer, High-harmonic generation in Su-Schrieffer-Heeger chains. *Phys. Rev. B* **99**, 195428 (2019)
7. R.E.F. Silva, Á. Jiménez-Galán, B. Amorim, O. Smirnova, M. Ivanov, Topological strong-field physics on sub-laser-cycle timescale. *Nat. Photonics* **13**, 849–854 (2019)
8. H. Jürß, D. Bauer, Helicity flip of high-order harmonic photons in Haldane nanoribbons. *Phys. Rev. A* **102**, 043105 (2020)
9. D. Moos, H. Jürß, D. Bauer, Intense-laser-driven electron dynamics and high-order harmonic generation in solids including topological effects. *Phys. Rev. A* **102**, 053112 (2020)
10. A. Chacón, D. Kim, W. Zhu, S.P. Kelly, A. Dauphin, E. Pisanty, A.S. Maxwell, A. Picón, M.F. Ciappina, D.E. Kim, C. Ticknor, A. Saxena, M. Lewenstein, Circular dichroism in higher-order harmonic generation: Heralding topological phases and transitions in Chern insulators. *Phys. Rev. B* **102**, 134115 (2020)
11. D. Baykuseva, A. Chacón, D. Kim, D.E. Kim, D.A. Reis, S. Ghimire, Strong-field physics in three-dimensional topological insulators. *Phys. Rev. A* **103**, 023101 (2021)
12. G. Vampa, T.J. Hammond, N. Thiré, B.E. Schmidt, F. Légaré, C.R. McDonald, T. Brabec, D.D. Klug, P.B. Corkum, All-optical reconstruction of crystal band structure. *Phys. Rev. Lett.* **115**, 193603 (2015)
13. M. Hohenleutner, F. Langer, O. Schubert, M. Knorr, U. Huttner, S.W. Koch, M. Kira, R. Huber, Real-time observation of interfering crystal electrons in high-harmonic generation. *Nature* **523**, 572–575 (2015)
14. T.T. Luu, M. Garg, S.Y. Kruchinin, A. Moulet, M.T. Hassan, E. Goulielmakis, Extreme ultraviolet high-harmonic spectroscopy of solids. *Nature* **521**, 498–502 (2015)
15. G. Vampa, T. Brabec, Merge of high harmonic generation from gases and solids and its implications for attosecond science. *J. Phys. B: At. Mol. Opt. Phys.* **50**, 083001 (2017)
16. Y.S. You, Y. Yin, Y. Wu, A. Chew, X. Ren, F. Zhuang, S. Gholam-Mirzaei, M. Chini, Z. Chang, S. Ghimire, High-harmonic generation in amorphous solids. *Nat. Commun.* **8**, 724 (2017)
17. M. Baudisch, A. Marini, J.D. Cox, T. Zhu, F. Silva, S. Teichmann, M. Massicotte, F. Koppens, L.S. Levitov, F.J. García de Abajo, J. Biegert, Ultrafast nonlinear optical response of Dirac fermions in graphene. *Nat. Commun.* **9**, 1018 (2018)
18. D. Dimitrovski, L.B. Madsen, T.G. Pedersen, High-order harmonic generation from gapped graphene: Perturbative response and transition to nonperturbative regime. *Phys. Rev. B* **95**, 035405 (2017)
19. L.A. Chizhova, F. Libisch, J. Burgdörfer, High-harmonic generation in graphene: Interband response and the harmonic cutoff. *Phys. Rev. B* **95**, 085436 (2017)
20. N. Yoshikawa, T. Tamaya, K. Tanaka, High-harmonic generation in graphene enhanced by elliptically polarized light excitation. *Science* **356**, 736–738 (2017)
21. H.A. Hafez, S. Kovalev, J.-C. Deinert, Z. Mics, B. Green, N. Awari, M. Chen, S. Germanskiy, U. Lehnert, J. Teichert, Z. Wang, K.-J. Tielrooij, Z. Liu, Z. Chen, A. Narita, K. Müllen, M. Bonn, M. Gensch, D. Turchinovich, Extremely efficient terahertz high-harmonic generation in graphene by hot Dirac fermions. *Nature* **561**, 507–511 (2018)
22. N. Tancogne-Dejean and A. Rubio, “Atomic-like high-harmonic generation from two-dimensional materials,” *Science Advances*, vol. 4, Feb 2018
23. G. Le Breton, A. Rubio, N. Tancogne-Dejean, High-harmonic generation from few-layer hexagonal boron nitride: Evolution from monolayer to bulk response. *Phys. Rev. B* **98**, 165308 (2018)
24. L. Yue, M.B. Gaarde, Structure gauges and laser gauges for the semiconductor Bloch equations in high-order harmonic generation in solids. *Phys. Rev. A* **101**, 053411 (2020)
25. H. Jürß and D. Bauer, “High-order harmonic generation in hexagonal nanoribbons,” *The European Physical Journal Special Topics*, Apr 2021
26. H. Drüeke, D. Bauer, “High-harmonic spectra of hexagonal nanoribbons from real-space time-dependent Schrödinger calculations,” *Eur. Phys. J. Spec. Top.* (2021). <https://doi.org/10.1140/epjs/s11734-021-00188-9>
27. F.D.M. Haldane, Model for a Quantum Hall Effect without Landau Levels: Condensed-Matter Realization of the “Parity Anomaly“. *Phys. Rev. Lett.* **61**, 2015–2018 (1988)
28. N. Hao, P. Zhang, Z. Wang, W. Zhang, Y. Wang, Topological edge states and quantum Hall effect in the Haldane model. *Phys. Rev. B* **78**, 075438 (2008)
29. J. Asbóth, L. Oroszlány, and A. Pályi, *A Short Course on Topological Insulators*, vol. 919 of *Lecture Notes in Physics*. Springer, 2016
30. Á. Jiménez-Galán, R.E.F. Silva, O. Smirnova, M. Ivanov, Lightwave control of topological properties in 2D materials for sub-cycle and non-resonant valley manipulation. *Nat. Photonics* **14**, 728–732 (2020)
31. M. C. Rechtsman, J. M. Zeuner, Y. Plotnik, Y. Lumer, D. Podolsky, F. Dreisow, S. Nolte, M. Segev, and A. Szameit, “Photonic Floquet topological insulators,” *Nature*, vol. 496, pp. 196 EP –, Apr 2013
32. N. Goldman, J. Dalibard, A. Dauphin, F. Gerbier, M. Lewenstein, P. Zoller, I.B. Spielman, Direct imaging of topological edge states in cold-atom systems. *Proc. Natl. Acad. Sci.* **110**(17), 6736–6741 (2013)
33. D. R. Cooper, B. D’Anjou, N. Ghattamaneni, B. Harack, M. Hilke, A. Horth, N. Majlis, M. Massicotte, L. Vandsburger, E. Whiteway, and V. Yu, “Experimental Review of Graphene,” *ISRN Condensed Matter Physics*, vol. 2012, Apr 2012. Article ID 501686

34. R. Peierls, Zur Theorie des Diamagnetismus von Leitungselektronen. *Zeitschrift für Physik* **80**, 763–791 (1933)
35. M. Graf, P. Vogl, Electromagnetic fields and dielectric response in empirical tight-binding theory. *Phys. Rev. B* **51**, 4940–4949 (1995)
36. A. L. Kuzemsky, “Electronic transport in metallic systems and generalized kinetic equations,” *International Journal of Modern Physics B*, vol. 25, no. 23n24, pp. 3071–3183, 2011
37. A.D. Bandrauk, S. Chelkowski, D.J. Diestler, J. Manz, K.-J. Yuan, Quantum simulation of high-order harmonic spectra of the hydrogen atom. *Phys. Rev. A* **79**, 023403 (2009)
38. J.C. Baggesen, L.B. Madsen, On the dipole, velocity and acceleration forms in high-order harmonic generation from a single atom or molecule. *J. Phys. B: At. Mol. Opt. Phys.* **44**, 115601 (2011)
39. D. Bauer, H. Bauke, T. Brabec, T. Fennel, C. R. McDonald, D. B. Milošević, S. Pabst, C. Peltz, G. Pöplau, R. Santra, and C. Varin, *Computational Strong-Field Quantum Dynamics: Intense Light-Matter Interactions*. De Gruyter Textbook, De Gruyter
40. C.-Z. Chen, Y.-M. Xie, J. Liu, P.A. Lee, K.T. Law, Quasi-one-dimensional quantum anomalous hall systems as new platforms for scalable topological quantum computation. *Phys. Rev. B* **97**, 104504 (2018)

5.1.5 Topological edge-state contributions to high-order harmonic generation in finite flakes

by Hannah Jürß and Dieter Bauer

Physical Review B **106**, 054303 (2022)

DOI: [10.1103/PhysRevB.106.054303](https://doi.org/10.1103/PhysRevB.106.054303)

Reference: [5]



Author Contributions

Hannah Jürß	performing the numerical simulations (deriving the necessary equations for the simulations, writing the code and running it), analyzing the results, writing the manuscript
-------------	-----------------------------------------------------------------------------------------------------------------------------------------------------------------------------

Dieter Bauer	providing critical feedback, supporting the analysis of the results, improving the manuscript, supervision
--------------	------------------------------------------------------------------------------------------------------------

Copyright © of this paper by the American Physical Society.

Topological edge-state contributions to high-order harmonic generation in finite flakes

Hannah Jürß  and Dieter Bauer *Institute of Physics, University of Rostock, 18051 Rostock, Germany*

(Received 27 May 2022; accepted 29 July 2022; published 5 August 2022)

Edge states play a major role in the electron dynamics of topological insulators as they are the only conducting part in such materials. In this work we consider the Haldane model for a two-dimensional topological insulator, subjected to an intense laser field. We compare the numerically simulated high-harmonic generation (HHG) in the bulk of the Haldane model to HHG in corresponding finite flakes with edge states present, and explain the differences. In particular, peaks for energies below the bulk band gap appear in the spectra for the finite flakes. The positions of these peaks show a strong dependence on the size of the flakes, which can be explained using the dispersion relation for the edge states.

DOI: [10.1103/PhysRevB.106.054303](https://doi.org/10.1103/PhysRevB.106.054303)

I. INTRODUCTION

In recent years, high-order harmonic generation (HHG) in condensed matter attracted more and more interest in the ultrafast, strong field physics community. The seminal paper reporting the observation of HHG in a bulk crystal appeared in 2011 [1]. The process of HHG can be used to image the static properties [2–4] and dynamical processes [5–8] inside condensed matter and opens paths towards new light sources [9–11]. For the generation of high harmonics, the target is illuminated by an intense laser pulse. In a solid, the laser excites electrons from the valence into the conduction band. The hole in the valence band and the electron in the conduction band propagate and eventually recombine upon the emission of a photon (interband harmonics). This simple three-step model for high-order harmonic generation in solids [12] is similar to the one in the gas phase [13,14]. It was shown though [15] that the collision of the electron with the hole can be imperfect and still generate harmonic radiation. Light can also be emitted by the movement of the electron and hole in bands, so called intraband harmonics, and by the time-dependent populations and transitions [16]. The theory of HHG in solids is summarized in the tutorial [17]. The review [18] also focuses on the experimental progress in this field.

Often, HHG is discussed in terms of the bulk properties of the system. However, the edges may have a significant influence on the emission of light as well [19–24]. In particular, topological insulators might be of interest, which are insulating in their interior (i.e., their bulk) but allow for current flow along the edges (in two-dimensional materials) or surfaces (in three dimensions). These edge currents are topologically protected against various kinds of perturbations [25].

The paradigmatic example for a topological insulator in two dimensions (2D) is the Haldane model [26], which is formulated in tight-binding approximation and was originally introduced as a toy model for a topological insulator without external magnetic field. Later it turned out that the hoppings Haldane introduced in his model are similarly realized in real

materials through spin-orbit coupling [27]. Moreover, the Haldane model can be experimentally realized using cold atoms [28] or photonic platforms [29]. In the following, we refer to this hypothetical material obeying the Haldane model as Haldanite. Haldanite has a honeycomb structure like graphene. Finite honeycomb lattices may have zigzag or armchair edges both allowing for edge states [30,31]. In this work we investigate a finite flake with the shape of a hexagon, as shown in Fig. 1. All edges of that flake are of zigzag type.

In order to transform topologically trivial graphene into topologically nontrivial Haldanite, an alternating on-site potential is added to break the sublattice symmetry and to open a band gap. The model is now describing materials like hexagonal boron nitride, which have a honeycomb structure too but consist of two different elements. Yet, in order to render the system topological, a complex hopping between next-nearest neighbors is introduced that breaks time-reversal symmetry.

Harmonic generation in Haldanite has been studied for the bulk [32,33] and finite ribbons [24,34]. Further studies were devoted to HHG in three-dimensional (3D) topological insulators. In an experiment on HHG in Bi_2Te_3 , harmonics attributed to topological surface states were found to depend on the carrier envelope phase, leading to noninteger harmonics [23]. In Bi_2Se_3 [35,36] and BiSbTeSe_2 [22], the dependence of the surface and bulk harmonic spectra on the polarization and orientation of the laser pulse was investigated. In our current work, the focus lies on finite Haldanite flakes and a comparison of the HHG spectra with those from the bulk. Edge states exist in the finite flakes considered. Energetically, the edge states lie in the band gap between the valence and the conduction band of the bulk and are expected to strongly modify HHG as compared to HHG from the bulk alone.

Indeed, our results show additional peaks for the finite flakes that are absent in the spectrum of the bulk system. In particular, two peaks are observed that shift in energy as the size of the system is changed. A direct connection between the edge states and those peaks is found.

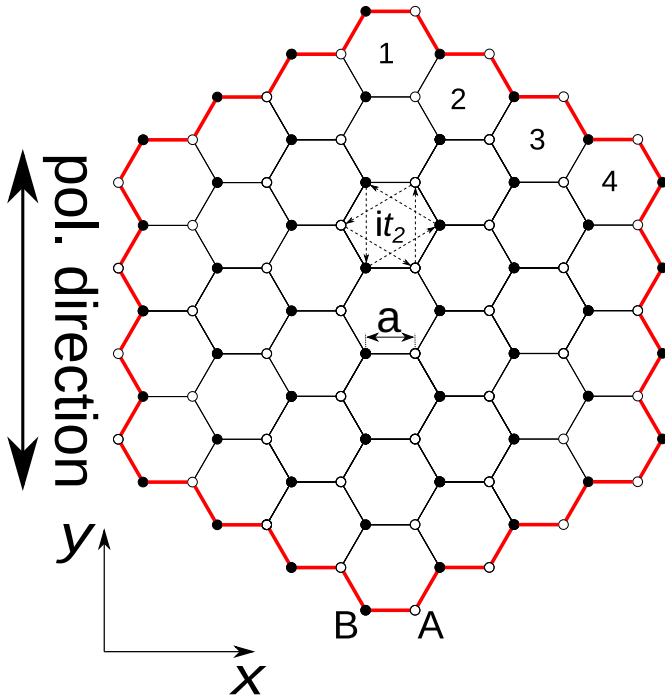


FIG. 1. Sketch of a finite Haldanite flake of size $N = 4$ (number of hexagons on each edge). There are two sublattice sites: A (open circles) and B (filled circles). The hopping between nearest neighbors (amplitude $t_1 \in \mathbb{R}$) is indicated by solid lines connecting the sites, the distance between two sites being a . The next-nearest neighbor hopping is only highlighted for one example hexagon by the dotted arrows. The hopping amplitude along the arrows is it_2 and $-it_2$ in the opposite direction ($t_2 \in \mathbb{R}$). The polarization direction of the laser field is indicated by the double-headed arrow. The edge of the flake is marked by the red line. Its length, the circumference, is denoted $s(N)$ in the text.

The paper is structured as follows: in Sec. II the methods to describe the system theoretically are presented. The results for the static system are discussed in Sec. III before the emission spectra are analyzed in Sec. IV. First, the spectra for the finite flakes are compared to the spectrum for the bulk in Sec. IV A. Second, the dependence of the spectra on the flake size is investigated in Sec. IV B, and third, the main features in the spectra are analyzed in Sec. IV C by filtering them out and investigating the corresponding currents that lead to these features. The main result on the currents along the edges that lead to the observed spectral features for different system sizes is discussed in Sec. V before the paper is summarized in Sec. VI. Atomic units (a.u.; $\hbar = |e| = m_e = 4\pi\epsilon_0 = 1$) are used throughout this paper unless stated otherwise.

II. METHODS

The theoretical description of the system is similar to our previous works [24,34,37]. In particular, the method to calculate high-harmonic spectra is the same.

A. Finite system without external field

Figure 1 shows the type of hexagonal Haldanite flakes considered. This kind of flakes has only zigzag edges. Each

edge of the flake is formed by N small hexagons, e.g., $N = 4$ in the example in Fig. 1. The circumference of the flake is given by

$$s(N) = 6a(2N - 1). \quad (1)$$

The hopping parameters between nearest and next-nearest neighbors are t_1 and $\pm it_2$, respectively. In addition, an alternating on-site potential M ($-M$) is assigned to sublattice site A (B).

The Hamiltonian reads

$$\hat{H}_0 = M \left(\sum_{i \in A} |i\rangle \langle i| - \sum_{i \in B} |i\rangle \langle i| \right) + t_1 \sum_{\langle i, j \rangle} (|i\rangle \langle j| + |j\rangle \langle i|) + \sum_{\langle\langle i, j \rangle\rangle} (t_2^{ij} |i\rangle \langle j| + (t_2^{ij})^* |j\rangle \langle i|). \quad (2)$$

The sum over $i \in A$ ($i \in B$) in the first term includes all sites on sublattice A (B). As usual, $\langle i, j \rangle$ indicates nearest-neighbor pairs and $\langle\langle i, j \rangle\rangle$ next-nearest neighbor pairs. For the next-nearest neighbors the hopping amplitude depends on the direction. The element t_2^{ij} indicates the hopping from site j towards site i (complex conjugate in the opposite direction) and is given by

$$t_2^{ij} = \begin{cases} it_2 & \text{for hopping along the arrows,} \\ -it_2 & \text{for hopping against the arrows,} \end{cases} \quad (3)$$

where the arrows are indicated in Fig. 1.

The time-independent Schrödinger equation

$$\hat{H}_0 |\psi_i\rangle = E_i |\psi_i\rangle \quad (4)$$

is solved numerically. The eigenenergies E_i of the respective eigenstates $|\psi_i\rangle$ are sorted in an ascending order, $E_0 \leq E_1 \leq E_2 \leq \dots$.

B. Coupling to an external field

The matrix elements of the corresponding time-dependent Hamiltonian in velocity gauge are given by [38]

$$\langle i | \hat{H}(t) | j \rangle = \langle i | \hat{H}_0 | j \rangle e^{-i(\mathbf{r}_i - \mathbf{r}_j) \cdot \mathbf{A}(t)}, \quad (5)$$

where \mathbf{r}_i (\mathbf{r}_j) are the coordinates of the sites i, j in position space, and $\mathbf{A}(t)$ is the vector potential (in dipole approximation).

States $|\psi_i\rangle$ with an energy smaller than the Fermi energy zero ($E_i < 0$) are initially occupied. The time evolution of a state $|\Psi_i(t)\rangle$ follows the time-dependent Schrödinger equation

$$i \partial_t |\Psi_i(t)\rangle = \hat{H}(t) |\Psi_i(t)\rangle, \quad (6)$$

which is solved with a fifth-order Dormand-Prince method with adaptive step size control [39]. The initial states are the eigenstates of the unperturbed system, $|\Psi_i(t=0)\rangle = |\psi_i\rangle$.

C. Calculation of HHG spectra

To obtain the emitted harmonic spectrum, the derivative of the electric current is used. The operator to calculate the current between two sites i and j is given by

$$\hat{\mathbf{J}}_{i,j}(t) = -i(\mathbf{r}_i - \mathbf{r}_j) \times [|i\rangle \langle i| \hat{H}(t) |j\rangle \langle j| - |j\rangle \langle j| \hat{H}(t) |i\rangle \langle i|]. \quad (7)$$

The contribution of one electron to the total current operator is [40]

$$\begin{aligned}\hat{\mathbf{j}}(t) &= -i \sum_{i,j} \hat{\mathbf{j}}_{i,j}(t) \\ &= -i \sum_{i,j} (\mathbf{r}_i - \mathbf{r}_j) |i\rangle \langle i| \hat{H}(t) |j\rangle \langle j|.\end{aligned}\quad (8)$$

For the total current, the currents $\mathbf{j}_l(t)$ due to the electrons in all occupied states $|\Psi_l(t)\rangle$ are summed up,

$$\mathbf{J}(t) = \sum_l \mathbf{j}_l(t) = \sum_l \langle \Psi_l(t) | \hat{\mathbf{j}}(t) | \Psi_l(t) \rangle. \quad (9)$$

Fourier transforming both components of the current, parallel (\parallel , y direction), and perpendicular (\perp , x direction) to the external field, leads to

$$P_{\parallel,\perp}(\omega) = |P_{\parallel,\perp}(\omega)| e^{i\varphi_{\parallel,\perp}(\omega)} = \int_{-\infty}^{+\infty} \mathbf{j}_{\parallel,\perp}(t) e^{-i\omega t} dt. \quad (10)$$

The intensity of the emitted light (yield) is proportional to $|P_{\parallel,\perp}(\omega)|^2$, and its helicity is encoded in the phase difference

$$\Delta\varphi(\omega) = \varphi_{\parallel}(\omega) - \varphi_{\perp}(\omega). \quad (11)$$

Numerically, the Fourier transformation is approximated by a fast Fourier transformation (FFT). A Hann window is applied before computing the FFT.

D. Bulk system

The results for HHG in finite flakes are compared to the corresponding simulation results for Haldanite bulk. How HHG in Haldanite bulk can be calculated is explained in detail in Ref. [41]. The important equations for this work are listed in this section.

As usual, a periodic lattice is assumed, which can in this case be broken down to a 2×2 Hamiltonian by making a Bloch ansatz. Assuming that the next-nearest neighbor hopping it_2 is completely imaginary, one finds

$$\mathbf{H}(\mathbf{k}) = \begin{pmatrix} \sigma & \tau \\ \tau^* & -\sigma \end{pmatrix}, \quad (12)$$

with

$$\begin{aligned}\tau(\mathbf{k}) &= t_1 \sum_{n=1}^3 e^{i\delta_n \cdot \mathbf{k}}, \\ \sigma(\mathbf{k}) &= M + 2t_2 \sum_{n=1}^3 \sin(\mathbf{g}_n \cdot \mathbf{k}),\end{aligned}\quad (13)$$

and δ_n and \mathbf{g}_n are vectors between nearest and next-nearest neighbors, respectively. The time-independent Schrödinger equation

$$\mathbf{H}(\mathbf{k})\mathbf{C}_{\pm}(\mathbf{k}) = E_{\pm}(\mathbf{k})\mathbf{C}_{\pm}(\mathbf{k}) \quad (14)$$

has two solutions for each \mathbf{k} , one for the valence band $[E_-(\mathbf{k}), \mathbf{C}_-(\mathbf{k})]$ and one for the conduction band $[E_+(\mathbf{k}), \mathbf{C}_+(\mathbf{k})]$.

By coupling the system to an external field $\mathbf{A}(t)$, the lattice momentum \mathbf{k} becomes time dependent

$$\mathbf{k}(t) = \mathbf{k} + \mathbf{A}(t) \quad (15)$$

and the time-dependent Schrödinger equation becomes

$$i\dot{\mathbf{C}}(\mathbf{k}, t) = \mathbf{H}[\mathbf{k}(t)]\mathbf{C}(\mathbf{k}, t). \quad (16)$$

The initial condition is $\mathbf{C}(\mathbf{k}, t=0) = \mathbf{C}_-(\mathbf{k})$.

To obtain the harmonic spectra, the current

$$v_j(\mathbf{k}, t) = \mathbf{C}^\dagger(\mathbf{k}, t) \partial_{k_j} \mathbf{H}[\mathbf{k}(t)] \mathbf{C}(\mathbf{k}, t) \quad (17)$$

is calculated. Here j stands for the coordinate, it is either $j = x$ or $j = y$.

This is calculated for different \mathbf{k} values within the first Brillouin zone. The total current v_j is obtained by integration over \mathbf{k} . The harmonic spectrum is given by the Fourier transform of the acceleration \dot{v}_j , similar to the finite flakes.

E. Parameters

A value of $t_2 = 0.03$ is chosen for the next-nearest neighbor hopping amplitude. The on-site potential is set to $M = 0.01$. Furthermore, the parameters of graphene are used for the distance between nearest neighbors $a = 2.68$ a.u. $\simeq 1.42$ Å and for the hopping amplitude between them $t_1 = -0.1$ a.u. $\simeq -2.7$ eV [42]. With these values used throughout the paper, the system is in the topological phase [26].

The linearly polarized laser pulse with a \sin^2 envelope is described by the vector potential in dipole approximation

$$\mathbf{A}(t) = A_0 \sin^2\left(\frac{\omega_0 t}{2n_0}\right) \sin(\omega_0 t) \mathbf{e}_y, \quad (18)$$

for times $0 \leq t \leq 2\pi n_0/\omega_0$ and zero otherwise. The number of cycles is set to $n_0 = 10$, the amplitude of the field is $A_0 = 0.05$ (corresponding to an intensity of $\simeq 5 \times 10^9$ W cm $^{-2}$), and the angular frequency is $\omega_0 = 7.5 \times 10^{-3}$ (wavelength of $\lambda_0 = 6.1$ μm).

III. UNPERTURBED HEXAGONAL FLAKES

The energies E_i of the respective eigenstates $|\psi_i\rangle$ of the unperturbed, finite system ($N = 10$) are plotted against the index i in Fig. 2(a). The highest occupied state has an energy $E_{299} = -0.00621$. The electron density of this state is mainly located along the edge of the flake, as shown in Fig. 2(c). There are several such edge states. We call a state an edge state if at least 90% of the probability density is located at the edge of the flake. In Fig. 2(a) the edge states (ES) are indicated in red.

To transform the edge states from position space to momentum space, we Fourier transform the part of the state that is localized along the edge. The edge is indicated by a red line in Fig. 1, i.e., it is one dimensional, so the obtained k is also one dimensional. Each of the transformed states are plotted color coded in red shades on a linear scale at their energy against momentum k . The result for $N = 10$ is depicted in Fig. 2(b). The maxima of the absolute value of the Fourier-transformed edge states follow an almost linear dispersion relation in momentum space. The slope of the dispersion relation determines the group velocity v_g . To approximate the slope only the two edge states around $E = 0$ are used, i.e., the highest occupied state $|\psi_{\text{HO}}\rangle$ (for $N = 10$ this is $|\psi_{299}\rangle$) and the lowest unoccupied state $|\psi_{\text{LU}}\rangle$ (for $N = 10$ this is $|\psi_{300}\rangle$).

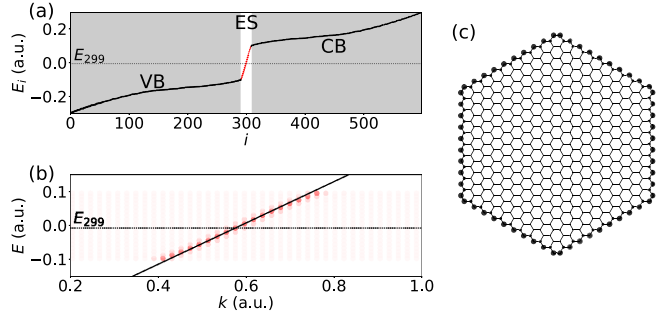


FIG. 2. (a) Energies of a finite flake ($N = 10$) plotted in ascending order. The edge states (ES) are highlighted in red and without a shaded background. The states of the valence band (VB) and conduction band (CB) are indicated by a shaded background. The dotted, horizontal line indicates the energy of the highest occupied state (E_{299}). (b) Color-coded Fourier transform of the edge states. The slope of the solid line is determined by the maxima for the highest occupied ($i = 299$) and lowest unoccupied ($i = 300$) state. (c) Probability density of the highest occupied state (E_{299}). The radii of the circles centered at the lattice sites are proportional to the probability density. The localization very close to the edge sites is clearly visible.

The group velocity is

$$v_g = \frac{\partial E}{\partial k} \approx \frac{E_{LU} - E_{HO}}{k_{LU} - k_{HO}} =: \frac{\Delta E_{\text{edge}}}{\Delta k_{\text{edge}}}. \quad (19)$$

Here k_{HO} (k_{LU}) is the k value where the absolute value of the Fourier-transformed state $|\psi_{HO}\rangle$ ($|\psi_{LU}\rangle$) has its maximum.

The group velocity v_g defined in this way is calculated for flakes of sizes $N = 1, 2, 3, \dots, 20$ and plotted in Fig. 3. For very small flakes the interpretation as a group velocity does not make much sense. Nevertheless, we can formally evaluate (19) and obtain for $v_g(N = 1) = 0.3312$ (not shown in Fig. 3). The group velocities for $N = 2$ and $N = 3$ are still far off from the values for larger flakes. The resolution in k space increases with increasing flake size. The further increase of v_g for $N = 4, 5, \dots, 20$ is smaller. For the largest considered flake we find $v_g(N = 20) = 0.6107$.

IV. EMISSION SPECTRA

A. Comparison between finite flakes and the bulk system

In Fig. 4 the emitted spectra for the finite system ($N = 7$) and the bulk (with a sampling of 50×50 points in the first

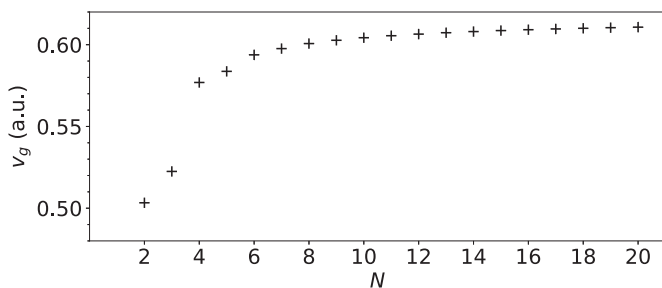


FIG. 3. Group velocity v_g calculated with (19) as a function of the flake size N .

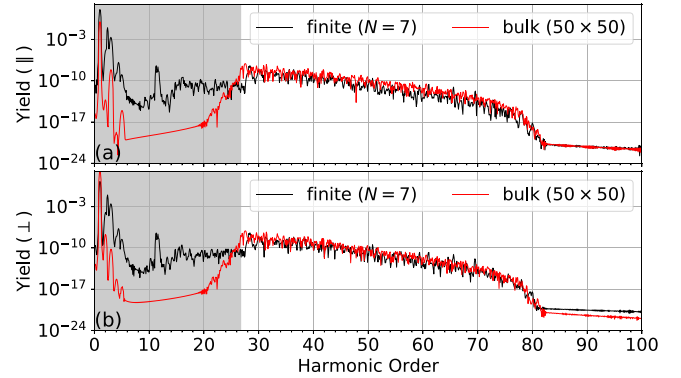


FIG. 4. Comparison between the spectra for the finite ($N = 7$) and the bulk (50×50 points in k space) system in (a) parallel and (b) perpendicular polarization direction to the external laser field. The shaded areas indicate energies below the band gap of the bulk system. The spectrum of the bulk is shifted in yield such that the fundamental harmonic in parallel direction to the external field has a yield equal to 1. The spectrum of the finite flake is shifted in yield such that the plateaus (nonshaded area) from both systems have a comparable yield in parallel polarization direction.

Brillouin zone) are shown. Figure 4(a) shows the spectra parallel (y direction) and Fig. 4(b) the spectra perpendicular (x direction) to the polarization direction of the external field. For energies above the band gap, the spectra for the finite flake and the bulk are similar.

For energies below the band gap, the bulk system shows peaks only at integer harmonic orders up to harmonic 5. However, the yield of even harmonics is more enhanced in the perpendicular direction compared to their yield in parallel direction. This originates from the broken symmetry of the flake in x direction (compare sublattice sites on the left and right edge of the flake in Fig. 1). For the finite system, more peaks are observed in that energy region. Due to the presence of edge states in the finite system and the absence of those in the bulk, we expect that at least some of these peaks are related to edge states. Furthermore, the harmonic yield at small energies is for almost every energy smaller in the bulk than in the finite flake (relative to the above band-gap harmonics). This indicates a contribution from the edges of finite flakes to small order harmonics.

The intraband harmonics for a fully occupied band usually interfere destructively. This leads to a suppressed harmonic yield for energies below the band gap [19]. This phenomenon can be observed for the bulk as the harmonics below the band gap are suppressed compared to the harmonics above the band gap. For harmonics above the band gap, the interband harmonics start to contribute significantly to the overall spectrum. With edge states present within the band gap, the gap between occupied and unoccupied states effectively decreases. The edge states act as an additional band within the band gap, allowing for emission at photon energies that are not possible for bulk. It was already shown in previous works that edge states can enhance the harmonic yield for energies below the band gap [19–21]. A similar effect was found for states within the band gap due to impurities [43,44].

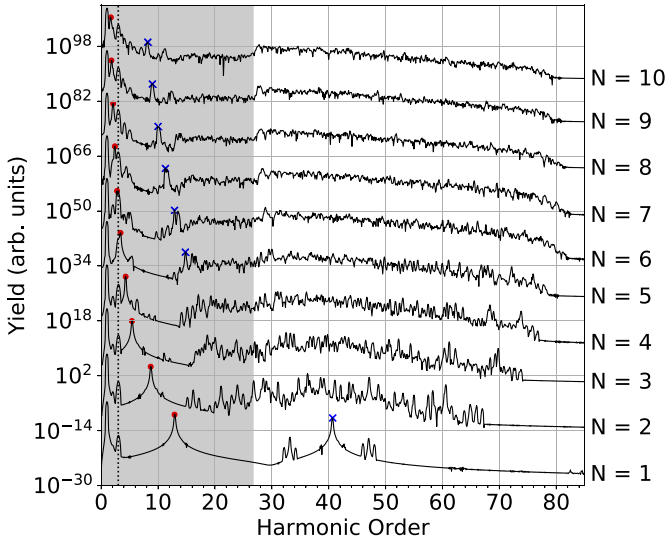


FIG. 5. Harmonic spectra in parallel polarization direction for different flake sizes N . The red bullets (blue crosses) indicate the first (second) peak that shifts continuously to smaller harmonic orders as the flake size increases. For $N = [2, 3, 4]$ the second peak could not be unambiguously identified. The spectra are multiplied by a factor of $10^{12(N-1)}$ for better visibility. The dotted, vertical line indicates harmonic order three.

B. Dependence on the flake size

In Fig. 5 the spectra for different flake sizes ($1 \leq N \leq 10$) are plotted. For energies larger than the band gap, the spectra are almost the same for flakes $N \geq 6$. For the harmonics in the sub-band-gap regime of the bulk (gray shaded area) the spectra depend on the size of the flakes. In particular, there are two peaks, indicated by a red bullet and a blue cross, that can be clearly observed in most of the spectra. These peaks shift towards smaller harmonic orders as the size of the flakes increases. A peak shift related to the carrier envelope phase was observed in Ref. [23]. However, the peaks and their shifts that we observe in this work originate from a different effect, as will be discussed in the following.

Let us denote the position of the first peak (red bullet) by $\omega_1(N)$, the second one (blue cross) by $\omega_2(N)$. Furthermore, the dotted, vertical line indicates harmonic order three in order to see that this common harmonic peak is independent on the flake size N .

C. Filtered current

For this consideration we use a flake of size $N = 7$, Fig. 6(a). Each edge of the flake (between two corners) is divided into segments consisting of three lattice sites each. This is indicated in Fig. 6(b). The total current between the sites within one segment is calculated using (7). The corners of the flake are left out because the used segments cannot be placed around those in a consistent way.

To investigate the origin of the peaks, we apply a frequency filter of the form

$$f_m(\omega) = e^{-(\omega - \omega_m)^2 / (2\sigma^2)} \quad (20)$$

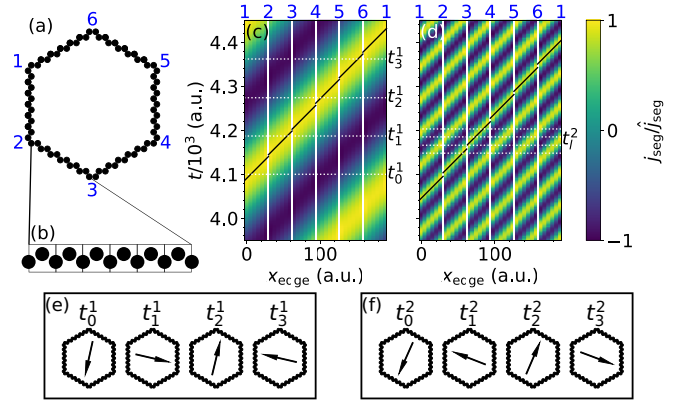


FIG. 6. (a) Hexagonal flake ($N = 7$) with indicated corners (blue numbers). (b) Zoom into one edge (between two corners) with indication of segments containing three sites each. (c) and (d) Frequency-filtered current, spatially and temporally resolved, for (c) $\omega_1 = 2.4\omega_0$ and (d) $\omega_2 = 11.3\omega_0$. The white vertical lines in (c) and (d) indicate the positions of the corners of the flake. The diagonal black line segments correspond to a velocity $v = 0.5976$, i.e., the group velocity determined by the band structure for $N = 7$. These line segments are plotted for each edge between two corners separately. The horizontal lines in (c) and (d) depict different times t_l^i (with $i = 1$ for the first peak, $i = 2$ for the second one, $l = 0, 1, 2, 3$) which are sorted in an ascending order $t_0^i < t_1^i < t_2^i < t_3^i$. (e) and (f) Direction of the spatially integrated current (frequency filtered) over the whole edge of the flake depicted as arrow for the first $i = 1$ (e) and second $i = 2$ (f) peak and for different times t_l^i .

to the Fourier-transformed currents of each segment. We chose $\sigma = 0.001$.

By dividing the edge into segments, a spatial resolution of the current is achieved. Note, however, that an electron may follow different pathways within one segment. It can either go directly from one edge site of a segment to the opposite edge site by next-nearest neighbor hopping (hopping distance $\sqrt{3}a$) or sequentially by nearest-neighbor hopping (total hopping distance $2a$). The latter option has as a larger hopping amplitude so that we use it for the following analysis. It was also used to calculate the approximate dispersion relation for the edge states shown in Fig. 1. Ignoring the corners, the position of segment n is given by

$$x_{\text{edge}}(n) = 2an. \quad (21)$$

Figures 6(c) and 6(d) show the results for the filtered current, resolved in time and space. The vertical white lines indicate the position of the corners. The numbers of the corners are indicated at the top of the panels. Their respective positions on the flake are indicated in Fig. 6(a). The current is positive if it points in an anticlockwise direction along the edge of the flake and it is negative if it points in the opposite direction. Because the current around the corners are not captured, the current appears discontinuous at those corner points. Figures 6(e) and 6(f) indicate the direction of the total current of the filtered peak, summed up over the whole edge. The times at which these are plotted, are indicated by the dotted, horizontal lines in Figs. 6(c) and 6(d).

Figure 6(c) shows the filtered current for $\omega_1 = 2.4 \omega_0$ (first peak) and in Fig. 6(d) for $\omega_2 = 11.3 \omega_0$. The diagonal black lines indicate the positions of particles moving with a velocity of $v = 0.5976$. This velocity is the previously determined group velocity v_g for $N = 7$, calculated from the slope of the edge-state dispersion relation. The black line segments are only plotted between two corners because of the discontinuities at the corners.

For the first peak [Fig. 6(c)] the current has one local maximum and one local minimum along the edge of the chain at all times. The local maximum and minimum are located on the opposite side of the flake for all times. The sign of the current indicates whether the current points in clockwise (negative sign) or anticlockwise (positive sign) direction along the edge. Hence, the total current is not zero, as shown by the arrow in Fig. 6(e). Over time, the total current for this peak rotates in an anticlockwise direction. The velocity of this rotation is determined by the group velocity v_g , which is indicated by the diagonal black lines in Fig. 6(c). The change of the total current over times causes the emission of photons.

The current filtered around the second peak [Fig. 6(d)] shows a five-times higher symmetry. There are five local maxima and minima each. Again, these local maxima and minima move along the edge of the flake with a constant velocity close to v_g (diagonal black lines). The total current for this peak is again finite. Its direction is shown for different times in Fig. 6(f). The higher symmetry causes a faster rotation of the total current, and hence photons with a higher energy are emitted.

Note that the rotation of the total current for both peaks is opposite. For the first peak, the total (edge) current rotates in anticlockwise direction [Fig. 6(e)] and for the second peak in clockwise direction [Fig. 6(f)]. Comparing the helicities [Eq. (11)] of the emitted light from both peaks (for all flake sizes) shows that the first peak always emits photons with an opposite helicity compared to the second peak. The values are $-\pi/2$ for the first peak and $\pi/2$ for the second.

In the Supplemental Material [45] a similar calculation for the trivial phase is performed showing that the observed effects are caused by the presence of the topological edge states.

V. CONNECTION BETWEEN SUB-BAND-GAP HARMONIC SPECTRA AND EDGE-STATE DISPERSION RELATION

It was shown in the previous section that the current corresponding to the sub-band-gap peaks rotates with a constant velocity that is very close to the group velocity determined by the edge-state dispersion relation. In this section we generalize this investigation and include various flake sizes.

First, we focus on the ω_1 peak at the smaller harmonic order (indicated with red bullets in Fig. 5). The circumference $s(N)$ of the flakes depends linearly on N , see (1). In Fig. 7 the red circles indicate the inverse of the peak position $1/\omega_1$ as a function of N , showing a linear dependence. This behavior is expected because the group velocity v_g is almost constant for (sufficiently big) flake sizes (see Fig. 3),

$$v = \frac{s(N)}{T_1(N)} = \frac{s(N)\omega_1^{\text{th}}(N)}{2\pi} = \text{const.}, \quad (22)$$

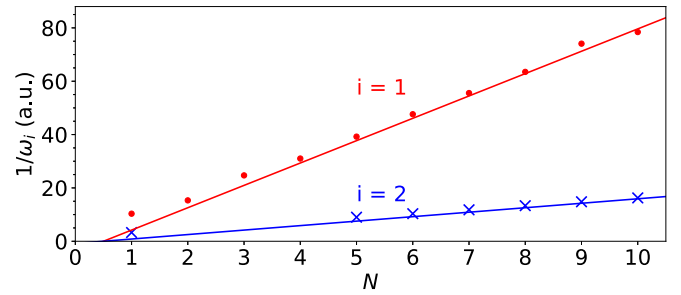


FIG. 7. Data points for the inverse peak positions $1/\omega_i$ for the first ($i = 1$) and second ($i = 2$) peak as a function of the flake size N . The red solid line ($i = 1$) corresponds to the theoretical angular frequency ω_1^{th} determined from the group velocity of the edge states. The solid blue line ($i = 2$) corresponds to five times that group velocity.

where T_1 is the time the electrons need to encircle the flake and ω_1^{th} is the respective theoretical angular frequency. With

$$\frac{1}{\omega_1^{\text{th}}(N)} = \frac{s(N)}{2\pi v} = \frac{6a(2N-1)}{2\pi v} \quad (23)$$

then follows the linear dependence between $1/\omega_1^{\text{th}}(N)$ and N , as seen from the simulations. As the edge-state group velocity v_g (19) determines the velocity of the movement along the edges we replace v by v_g and obtain

$$\frac{1}{\omega_1^{\text{th}}(N)} = \frac{s(N)}{2\pi v_g} = \frac{s(N)\Delta k_{\text{edge}}}{2\pi \Delta E_{\text{edge}}}. \quad (24)$$

Due to the finite numerical resolution $\Delta k = 2\pi/s$ for the edge states in k space, $\Delta k_{\text{edge}} = n\Delta k$ where $n = 1, 2, 3, \dots$, and thus

$$\frac{1}{\omega_1^{\text{th}}(N)} = \frac{s(N)\Delta k_{\text{edge}}}{2\pi \Delta E_{\text{edge}}} = \frac{n}{\Delta E_{\text{edge}}}. \quad (25)$$

As expected, we found that $\Delta k_{\text{edge}} = \Delta k$ (i.e., $n = 1$). This means that the highest occupied and lowest unoccupied edge state are separated in k space by the given resolution Δk . Hence, the peak position should be similar to the energy difference between the lowest unoccupied and highest occupied edge state, which was confirmed by our data (not shown).

The red line in Fig. 7 was calculated according to (23) with the velocity v set to the group velocity of a large flake $v_g(N = 20) = 0.6107$, see Fig. 3. The data points agree with the linear function predicted from our theory. The deviation of the data points from the linear function can be explained by the small differences of the numerically determined group velocity for different flake sizes.

As seen in the previous section, this indicates that the peaks in the spectra (Fig. 5) marked by the red dots originate from a movement of the current along the edge. The group velocity v_g is similar for sufficiently large flake sizes. Hence, the time for the current to move along the edge of the flake increases with the flake size, and the corresponding frequency decreases.

The blue crosses in Fig. 7 are the data points for the second peak in the spectra at $\omega_2(N)$. Similar to $\omega_1(N)$, a linear dependence between $1/\omega_2$ and N can be observed but with a smaller slope. It was shown in the previous section that the edge current corresponding to this peak has a five-times

higher symmetry. This leads to a five-times faster oscillation and thus to a peak position ω_2 at a frequency approximately five-times higher than ω_1 . The factor between both peaks is not exactly five because of discrete values in our model system (discrete energy spectrum of the unperturbed system, discrete resolution in frequency). The blue line ($i = 2$) is a plot of the linear function

$$\frac{1}{\omega_2^{\text{th}}(N)} = \frac{s(N)}{2\pi 5 v_g} = \frac{6a(2N-1)}{2\pi 5 v_g}. \quad (26)$$

It agrees very well with the data points.

The observed effect is not restricted to this kind of hexagonal flakes. We observed similar peaks for triangular flakes. However, the factor between both peaks in the spectra was close to two instead of five in this case.

VI. SUMMARY

Harmonic spectra for Haldanite bulk and finite, hexagonal Haldanite flakes were compared. Differences occur mainly for harmonic orders below the bulk band gap. Two strong

peaks in the spectra could be identified that depend on the size of the flake. These peaks shift continuously towards smaller harmonic orders as the flake size increases. We could explain the positions of these peaks by nonuniform currents along the edges. The spatial and temporal change in the current causes the emission of light whose frequency is determined by the dispersion relation of the static system. The lower-energy peak corresponds to one round trip of the current's maximum and also to the energy difference between lowest unoccupied and highest occupied edge state. The higher-energy peak corresponds to a fifth of a round trip because the envelope of the current has a five-times higher symmetry, which leads to a five-times faster oscillation in the total, spatially integrated current.

ACKNOWLEDGMENTS

Funding by the German Research Foundation - SFB 1477 "Light-Matter Interactions at Interfaces," Project No. 441234705, is gratefully acknowledged. H.J. acknowledges financial support by the doctoral fellowship program of the University of Rostock.

-
- [1] S. Ghimire, A. D. DiChiara, E. Sistrunk, P. Agostini, L. F. DiMauro, and D. A. Reis, Observation of high-order harmonic generation in a bulk crystal, *Nat. Phys.* **7**, 138 (2011).
 - [2] G. Vampa, T. J. Hammond, N. Thiré, B. E. Schmidt, F. Légaré, C. R. McDonald, T. Brabec, D. D. Klug, and P. B. Corkum, All-Optical Reconstruction of Crystal Band Structure, *Phys. Rev. Lett.* **115**, 193603 (2015).
 - [3] N. Tancogne-Dejean, O. D. Mücke, F. X. Kärtner, and A. Rubio, Impact of the Electronic Band Structure in High-Harmonic Generation Spectra of Solids, *Phys. Rev. Lett.* **118**, 087403 (2017).
 - [4] H. Lakhota, H. Y. Kim, M. Zhan, S. Hu, S. Meng, and E. Goulielmakis, Laser picoscopy of valence electrons in solids, *Nature (London)* **583**, 55 (2020).
 - [5] O. Schubert, M. Hohenleutner, F. Langer, B. Urbanek, C. Lange, U. Huttner, D. Golde, T. Meier, M. Kira, S. Koch, and R. Huber, Sub-cycle control of terahertz high-harmonic generation by dynamical Bloch oscillations, *Nat. Photonics* **8**, 119 (2014).
 - [6] M. Hohenleutner, F. Langer, O. Schubert, M. Knorr, U. Huttner, S. W. Koch, M. Kira, and R. Huber, Real-time observation of interfering crystal electrons in high-harmonic generation, *Nature (London)* **523**, 572 (2015).
 - [7] Y. S. You, Y. Yin, Y. Wu, A. Chew, X. Ren, F. Zhuang, S. Gholam-Mirzaei, M. Chini, Z. Chang, and S. Ghimire, High-harmonic generation in amorphous solids, *Nat. Commun.* **8**, 724 (2017).
 - [8] M. Baudisch, A. Marini, J. D. Cox, T. Zhu, F. Silva, S. Teichmann, M. Massicotte, F. Koppens, L. S. Levitov, F. J. García de Abajo, and J. Biegert, Ultrafast nonlinear optical response of Dirac fermions in graphene, *Nat. Commun.* **9**, 1018 (2018).
 - [9] T. T. Luu, M. Garg, S. Y. Kruchinin, A. Moulet, M. T. Hassan, and E. Goulielmakis, Extreme ultraviolet high-harmonic spectroscopy of solids, *Nature (London)* **521**, 498 (2015).
 - [10] G. Ndabashimiye, S. Ghimire, M. Wu, D. A. Browne, K. J. Schafer, M. B. Gaarde, and D. A. Reis, Solid-state harmonics beyond the atomic limit, *Nature (London)* **534**, 520 (2016).
 - [11] F. Langer, M. Hohenleutner, U. Huttner, S. Koch, M. Kira, and R. Huber, Symmetry-controlled temporal structure of high-harmonic carrier fields from a bulk crystal, *Nat. Photonics* **11**, 227 (2017).
 - [12] G. Vampa and T. Brabec, Merge of high harmonic generation from gases and solids and its implications for attosecond science, *J. Phys. B: At., Mol. Opt. Phys.* **50**, 083001 (2017).
 - [13] P. B. Corkum, Plasma perspective on strong field multiphoton ionization, *Phys. Rev. Lett.* **71**, 1994 (1993).
 - [14] M. Lewenstein, P. Balcou, M. Y. Ivanov, A. L'Huillier, and P. B. Corkum, Theory of high-harmonic generation by low-frequency laser fields, *Phys. Rev. A* **49**, 2117 (1994).
 - [15] L. Yue and M. B. Gaarde, Expanded view of electron-hole recollisions in solid-state high-order harmonic generation: Full-Brillouin-zone tunneling and imperfect recollisions, *Phys. Rev. A* **103**, 063105 (2021).
 - [16] P. Jürgens, B. Liewehr, B. Kruse, C. Peltz, D. Engel, A. Husakou, T. Witting, M. Ivanov, M. J. J. Vrakking, T. Fennel, and A. Mermillod-Blondin, Origin of strong-field-induced low-order harmonic generation in amorphous quartz, *Nat. Phys.* **16**, 1035 (2020).
 - [17] L. Yue and M. B. Gaarde, Introduction to theory of high-harmonic generation in solids: tutorial, *J. Opt. Soc. Am. B* **39**, 535 (2022).
 - [18] E. Goulielmakis and T. Brabec, High harmonic generation in condensed matter, *Nat. Photonics* **16**, 411 (2022).
 - [19] D. Bauer and K. K. Hansen, High-Harmonic Generation in Solids with and without Topological Edge States, *Phys. Rev. Lett.* **120**, 177401 (2018).

- [20] H. Drüeke and D. Bauer, Robustness of topologically sensitive harmonic generation in laser-driven linear chains, *Phys. Rev. A* **99**, 053402 (2019).
- [21] H. Jürß and D. Bauer, High-harmonic generation in Su-Schrieffer-Heeger chains, *Phys. Rev. B* **99**, 195428 (2019).
- [22] Y. Bai, F. Fei, S. Wang, N. Li, X. Li, F. Song, R. Li, Z. Xu, and P. Liu, High-harmonic generation from topological surface states, *Nat. Phys.* **17**, 311 (2021).
- [23] C. P. Schmid, L. Weigl, P. Grössing, V. Junk, C. Gorini, S. Schlauderer, S. Ito, M. Meierhofer, N. Hofmann, D. Afanasiev, J. Crewse, K. A. Kokh, O. E. Tereshchenko, J. Gütde, F. Evers, J. Wilhelm, K. Richter, U. Höfer, and R. Huber, Tunable non-integer high-harmonic generation in a topological insulator, *Nature (London)* **593**, 385 (2021).
- [24] H. Jürß and D. Bauer, Edge-state influence on high-order harmonic generation in topological nanoribbons, *Eur. Phys. J. D* **75**, 190 (2021).
- [25] M. Z. Hasan and C. L. Kane, Colloquium: Topological insulators, *Rev. Mod. Phys.* **82**, 3045 (2010).
- [26] F. D. M. Haldane, Model for a Quantum Hall Effect without Landau Levels: Condensed-Matter Realization of the “Parity Anomaly”, *Phys. Rev. Lett.* **61**, 2015 (1988).
- [27] C. L. Kane and E. J. Mele, Quantum Spin Hall Effect in Graphene, *Phys. Rev. Lett.* **95**, 226801 (2005).
- [28] G. Jotzu, M. Messer, R. Desbuquois, M. Lebrat, T. Uehlinger, D. Greif, and T. Esslinger, Experimental realization of the topological Haldane model with ultracold fermions, *Nature (London)* **515**, 237 (2014).
- [29] M. C. Rechtsman, J. M. Zeuner, Y. Plotnik, Y. Lumer, D. Podolsky, F. Dreisow, S. Nolte, M. Segev, and A. Szameit, Photonic Floquet topological insulators, *Nature (London)* **496**, 196 (2013).
- [30] N. Hao, P. Zhang, Z. Wang, W. Zhang, and Y. Wang, Topological edge states and quantum Hall effect in the Haldane model, *Phys. Rev. B* **78**, 075438 (2008).
- [31] W. Yao, S. A. Yang, and Q. Niu, Edge States in Graphene: From Gapped Flat-Band to Gapless Chiral Modes, *Phys. Rev. Lett.* **102**, 096801 (2009).
- [32] R. E. F. Silva, Á. Jiménez-Galán, B. Amorim, O. Smirnova, and M. Ivanov, Topological strong-field physics on sub-laser-cycle timescale, *Nat. Photonics* **13**, 849 (2019).
- [33] A. Chacón, D. Kim, W. Zhu, S. P. Kelly, A. Dauphin, E. Pisanty, A. S. Maxwell, A. Picón, M. F. Ciappina, D. E. Kim, C. Ticknor, A. Saxena, and M. Lewenstein, Circular dichroism in higher-order harmonic generation: Heralding topological phases and transitions in Chern insulators, *Phys. Rev. B* **102**, 134115 (2020).
- [34] H. Jürß and D. Bauer, Helicity flip of high-order harmonic photons in Haldane nanoribbons, *Phys. Rev. A* **102**, 043105 (2020).
- [35] D. Baykusheva, A. Chacón, D. Kim, D. E. Kim, D. A. Reis, and S. Ghimire, Strong-field physics in three-dimensional topological insulators, *Phys. Rev. A* **103**, 023101 (2021).
- [36] D. Baykusheva, A. Chacón, J. Lu, T. P. Bailey, J. A. Sobota, H. Soifer, P. S. Kirchmann, C. Rotundu, C. Uher, T. F. Heinz, D. A. Reis, and S. Ghimire, All-optical probe of three-dimensional topological insulators based on high-harmonic generation by circularly polarized laser fields, *Nano Lett.* **21**, 8970 (2021).
- [37] H. Jürß and D. Bauer, High-order harmonic generation in hexagonal nanoribbons, *Eur. Phys. J.: Spec. Top.* **230**, 4081 (2021).
- [38] M. Graf and P. Vogl, Electromagnetic fields and dielectric response in empirical tight-binding theory, *Phys. Rev. B* **51**, 4940 (1995).
- [39] W. Press, S. Teukolsky, W. Vetterling, and B. Flannery, *Numerical Recipes 3rd Edition: The Art of Scientific Computing* (Cambridge University Press, Cambridge, 2007).
- [40] A. L. Kuzemsky, Electronic transport in metallic systems and generalized kinetic equations, *Int. J. Mod. Phys. B* **25**, 3071 (2011).
- [41] D. Moos, H. Jürß, and D. Bauer, Intense-laser-driven electron dynamics and high-order harmonic generation in solids including topological effects, *Phys. Rev. A* **102**, 053112 (2020).
- [42] D. R. Cooper, B. D’Anjou, N. Ghattamaneni, B. Harack, M. Hilke, A. Horth, N. Majlis, M. Massicotte, L. Vandsburger, E. Whiteway, and V. Yu, Experimental review of graphene, *ISRN Condens. Matter Phys.* **2012**, 501686 (2012).
- [43] C. Yu, K. K. Hansen, and L. B. Madsen, Enhanced high-order harmonic generation in donor-doped band-gap materials, *Phys. Rev. A* **99**, 013435 (2019).
- [44] V. E. Nefedova, S. Fröhlich, F. Navarrete, N. Tancogne-Dejean, D. Franz, A. Hamdou, S. Kaassamani, D. Gauthier, R. Nicolas, G. Jargot, M. Hanna, P. Georges, M. F. Ciappina, U. Thumm, W. Boutu, and H. Merdji, Enhanced extreme ultraviolet high-harmonic generation from chromium-doped magnesium oxide, *Appl. Phys. Lett.* **118**, 201103 (2021).
- [45] See Supplemental Material at <http://link.aps.org/supplemental/10.1103/PhysRevB.106.054303> for a short comparison between the results of the topological and trivial systems.

Supplemental material: Topological edge-state contributions to high-order harmonic generation in finite flakes

Hannah Jürß and Dieter Bauer
Institute of Physics, University of Rostock, 18051 Rostock, Germany

I. SIZE DEPENDENCE FOR A TOPOLOGICAL TRIVIAL SYSTEM

The findings in our manuscript are now compared to the same system in the topological trivial phase to show that the topology plays a role for the effect described in the manuscript. The parameters are $M = 0.15$ and $t_2 = 0.01$ and all the other parameters are the same as previously. This leads to a minimal band gap for the bulk system of $E_{\text{gap}} = 26.14\omega_0$, which is comparable to the band gap of the topological non-trivial system ($E_{\text{gap}} = 26.8\omega_0$).

In Fig. 1, the harmonic spectra for different flake sizes are plotted. Similar to the size-dependent peaks for the topological phase (discussed in the manuscript), we identify one peak that appears to be dependent on the size of the flake. This peak for different flake sizes is indicated by the red bullets up to flake size $N = 5$. For larger flakes it vanishes into the other emitted light and is not clearly visible anymore. Different to the topological phase, this peak seems to converge to the minimal band gap energy of the bulk (gray shaded area) instead of zero as it was observed for the topological system. That means, this peak is restricted to interband harmonics whereas the

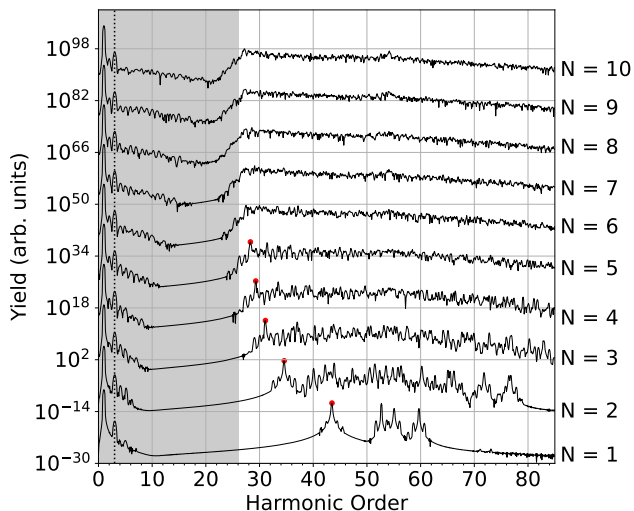


FIG. 1. Harmonic spectra in parallel polarization direction for different flake sizes N in the trivial phase. The red bullets for the spectra up to $N = 5$ indicates a peak, which shifts to smaller energies as the system size increases. The spectra are multiplied by a factor of $10^{12(N-1)}$ for better visibility. The dotted, vertical line indicates harmonic order three.

peaks in the topological system were observed in the intraband energy region, in which the edge states are located.

II. SPATIAL RESOLVED CURRENT

Similar to results in the manuscript, a frequency filter is applied to the spatially resolved current along the edge. In addition, a straight path from the bottom, through the center, to top of the flake is divided into segments containing three sites each. The total current between all three sites of one segment is summed up to get a spatially resolved current along this path. In Fig. 2a only certain sites of a flake ($N = 5$) are indicated. The black dots indicate the path along the edge and the red dots the path through the center of the flake.

Fig. 2b,c show the filtered currents ($\omega = 28.3\omega_0$) in time and position for the trivial flake. Subplot (b) shows the current as function of x_{edge} , the position at the edge (black dots in Fig. 2a). The vertical lines indicate the different corners. The current is positive if it points in a clockwise direction along the edge of the flake. In (c) the filtered current along the path through the flake is indicated. The position is denoted as x_{center} . The current is positive if it points in positive y -direction, i.e., upwards. The currents in both subplots are normalized to the same value. Note that the current is resolved for segments containing three sites each. The segments at the bottom and top of the path through the bulk are differently oriented than the segments along the edge. So the current at the boundaries in Fig. 2c are different to the values in (b).

Fig. 2d,e show the same plot, but now for the topological phase, filtered at harmonic $\omega = 3.4\omega_0$. Note that for better comparison, the size of the flake is $N = 5$. In the manuscript the results for $N = 7$ are shown.

There are main differences between the filtered peak for the topological and trivial case. However, both peaks have in common that the current along the edge has one maximum and one minimum at each time. The extreme points move along the edge in an anti-clockwise direction. However, the frequency of this movement is much higher for the trivial case, because the peak energy is larger as well ($\omega = 28.3\omega_0$ for the trivial case, $\omega = 3.4\omega_0$ for the topological case). The current along the edge of the trivial system is weaker compared to the currents at the center (by a factor larger than 4).

For the topological phase however, the current at the edges are much larger than the one at the center (two

orders of magnitude). The current at the center is now almost non-existing.

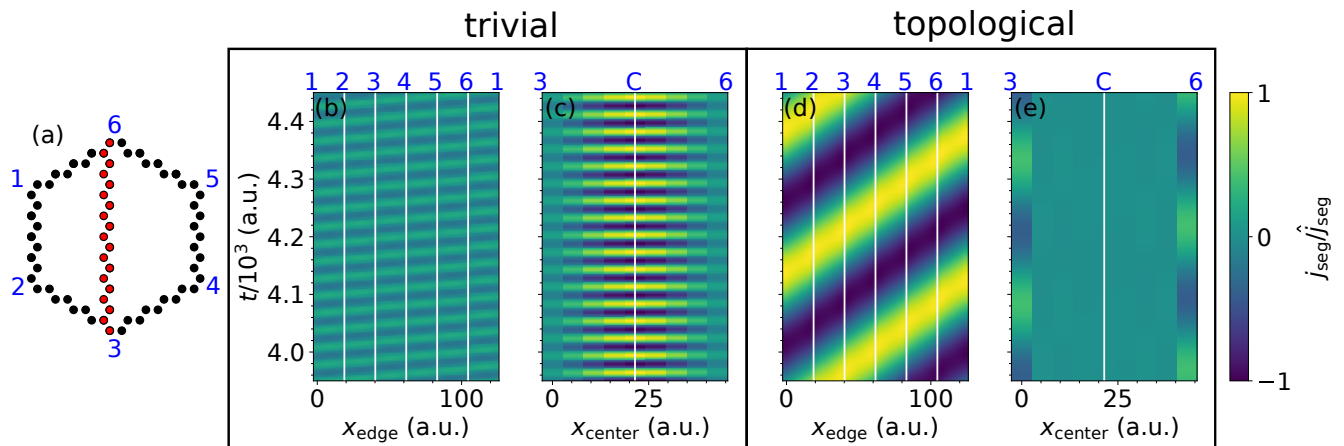


FIG. 2. (a) Hexagonal flake ($N = 5$) in which only the edge sites (black dots) and the sides along a path through the bulk of the flake (red dots) are indicated. The (blue) numbers numerate the corners, the letter C indicates the center of the flake. (b,c) Spatially resolved current, filtered at $\omega = 28.3 \omega_0$ for the trivial system. Normalized to the maximum of both plots. (d,e) Spatially resolved current, filtered at $\omega = 3.4 \omega_0$ for the topological system. Normalized to the maximum of both plots. (b,d) Filtered current along the edge, the corners are indicated by vertical lines. (c,e) Filtered currents along a path through the center of the flake, the center is indicated by a vertical line.

5.2 Additional publication during my Ph.D. studies

This publication was published during my Ph.D. studies but is not part of this cumulative thesis because a different model (the SSH model) was investigated:

- [48]: L. Bielke, H. Jürß, V. Burgtorf, and D. Bauer: *Formation of the solid-state high-order harmonic generation plateau through destructive interference*, Phys. Rev. A **107**, 033111 (2023), DOI: [10.1103/PhysRevA.107.033111](https://doi.org/10.1103/PhysRevA.107.033111)

5.3 List of conference contributions

- H. Jürß and D. Bauer: **High harmonic generation in graphene-like systems** (Poster), 55th Symposium on Theoretical Chemistry, Rostock, September 22-26, 2019
- H. Jürß: **High-harmonic generation in topological graphene nanoribbons** (Poster), International Workshop on Atomic Physics, MPI-PKS Dresden, November 19 - 22, 2019
- H. Jürß, D. Moos, and D. Bauer: **High-Harmonic Generation in Topological Condensed Matter** (Talk), APS Virtual DAMOP Meeting, June 1-5, 2020
- H. Jürß, D. Moos, and D. Bauer: **Helicity flip of harmonics from finite and infinite topological nanoribbons** (Talk), CMD2020GEFES online, August 31 - September 4, 2020
- H. Jürß, D. Moos, D. Bauer: **Comparison of high-order harmonic generation in finite and bulk honeycomb lattices** (Talk) APS March Meeting 2021 (virtual), March 15-19, 2021
- H. Jürß and D. Bauer: **Edge state contributions to high-order harmonic generation in topological condensed matter** (Talk): DAMOP 2021 (virtual), May 31–June 4, 2021
- H. Jürß and D. Bauer: **Edge state contributions in high-order harmonic generation of topological insulators** (Poster), ViCPEAC (virtual ICPEAC) 2021, July 20-23, 2021
- H. Jürß and D. Bauer: **High-harmonic generation in finite Haldanite flakes** (Talk), DPG Spring Meeting of the Atomic, Molecular, Quantum Optics and Photonics Section (virtual), March 14-18, 2022
- H. Jürß: **Edge state contributions to high-order harmonic generation in topological insulators** (Talk), Atto-FEL 2022, University College London, June 27-30, 2022
- H. Jürß, L. Bielke, and D. Bauer: **Size and sampling effects of the high-order harmonic generation in Su-Schrieffer-Heeger chains** (Poster), International Workshop on Atomic Physics, MPI-PKS Dresden, November 28 - December 2, 2022
- H. Jürß and D. Bauer: **Dephasing effects in high-order harmonic generation from finite Su-Schrieffer-Heeger chains** (Talk), DPG Spring Meeting of the Atomic, Molecular, Quantum Optics and Photonics Section 2023, Hanover, March 5-10, 2023

6 Bibliography

- [1] H. Jürß and D. Bauer, “Helicity flip of high-order harmonic photons in Haldane nanoribbons”, *Phys. Rev. A* **102**, 043105 (2020).
- [2] D. Moos, H. Jürß, and D. Bauer, “Intense-laser-driven electron dynamics and high-order harmonic generation in solids including topological effects”, *Phys. Rev. A* **102**, 053112 (2020).
- [3] H. Jürß and D. Bauer, “High-order harmonic generation in hexagonal nanoribbons”, *The European Physical Journal Special Topics* **230**, 4081–4089 (2021).
- [4] H. Jürß and D. Bauer, “Edge-state influence on high-order harmonic generation in topological nanoribbons”, *The European Physical Journal D* **75**, 190 (2021).
- [5] H. Jürß and D. Bauer, “Topological edge-state contributions to high-order harmonic generation in finite flakes”, *Phys. Rev. B* **106**, 054303 (2022).
- [6] T. H. Maiman, “Stimulated Optical Radiation in Ruby”, *Nature* **187**, 493–494 (1960).
- [7] A. McPherson, G. Gibson, H. Jara, U. Johann, T. S. Luk, I. A. McIntyre, K. Boyer, and C. K. Rhodes, “Studies of multiphoton production of vacuum-ultraviolet radiation in the rare gases”, *J. Opt. Soc. Am. B* **4**, 595–601 (1987).
- [8] M. Ferray, A. L’Huillier, X. F. Li, L. A. Lompre, G. Mainfray, and C. Manus, “Multiple-harmonic conversion of 1064 nm radiation in rare gases”, *Journal of Physics B: Atomic, Molecular and Optical Physics* **21**, L31 (1988).
- [9] P. Mulser and D. Bauer, *High power laser-matter interaction*, Springer tracts in modern physics 238 (Springer, Heidelberg ; New York, 2010), ISBN: 978-3-540-50669-0.
- [10] J. J. Macklin, J. D. Kmetec, and C. L. Gordon, “High-order harmonic generation using intense femtosecond pulses”, *Phys. Rev. Lett.* **70**, 766–769 (1993).
- [11] A. L’Huillier and P. Balcou, “High-order harmonic generation in rare gases with a 1-ps 1053-nm laser”, *Phys. Rev. Lett.* **70**, 774–777 (1993).
- [12] Z. Chang, A. Rundquist, H. Wang, M. M. Murnane, and H. C. Kapteyn, “Generation of Coherent Soft X Rays at 2.7 nm Using High Harmonics”, *Phys. Rev. Lett.* **79**, 2967–2970 (1997).
- [13] T. T. Luu, Z. Yin, A. Jain, T. Gaumnitz, Y. Pertot, J. Ma, and H. J. Wörner, “Extreme-ultraviolet high-harmonic generation in liquids”, *Nature Communications* **9**, 3723 (2018).
- [14] S. Ghimire, A. D. DiChiara, E. Sistrunk, P. Agostini, L. F. DiMauro, and D. A. Reis, “Observation of high-order harmonic generation in a bulk crystal”, *Nature Physics* **7**, 138–141 (2011).
- [15] O. Schubert, M. Hohenleutner, F. Langer, B. Urbanek, C. Lange, U. Huttner, D. Golde, T. Meier, M. Kira, S. W. Koch, and R. Huber, “Sub-cycle control of terahertz high-harmonic generation by dynamical Bloch oscillations”, *Nature Photonics* **8**, 119–123 (2014).

- [16] S. Ghimire, G. Ndabashimiye, A. D. DiChiara, E. Sistrunk, M. I. Stockman, P. Agostini, L. F. DiMauro, and D. A. Reis, “Strong-field and attosecond physics in solids”, *Journal of Physics B: Atomic, Molecular and Optical Physics* **47**, 204030 (2014).
- [17] R. E. F. Silva, Á. Jiménez-Galán, B. Amorim, O. Smirnova, and M. Ivanov, “Topological strong-field physics on sub-laser-cycle timescale”, *Nature Photonics* **13**, 849–854 (2019).
- [18] A. Chacón, D. Kim, W. Zhu, S. P. Kelly, A. Dauphin, E. Pisanty, A. S. Maxwell, A. Picón, M. F. Ciappina, D. E. Kim, C. Ticknor, A. Saxena, and M. Lewenstein, “Circular dichroism in higher-order harmonic generation: Heralding topological phases and transitions in Chern insulators”, *Phys. Rev. B* **102**, 134115 (2020).
- [19] D. Bauer and K. K. Hansen, “High-Harmonic Generation in Solids with and without Topological Edge States”, *Phys. Rev. Lett.* **120**, 177401 (2018).
- [20] H. Drüeke and D. Bauer, “Robustness of topologically sensitive harmonic generation in laser-driven linear chains”, *Phys. Rev. A* **99**, 053402 (2019).
- [21] H. Jürß and D. Bauer, “High-harmonic generation in Su-Schrieffer-Heeger chains”, *Physical Review B* **99**, 195428 (2019).
- [22] C. P. Schmid, L. Weigl, P. Grössing, V. Junk, C. Gorini, S. Schlauderer, S. Ito, M. Meierhofer, N. Hofmann, D. Afanasiev, J. Crewse, K. A. Kokh, O. E. Tereshchenko, J. Gädde, F. Evers, J. Wilhelm, K. Richter, U. Höfer, and R. Huber, “Tunable non-integer high-harmonic generation in a topological insulator”, *Nature* **593**, 385–390 (2021).
- [23] Y. Bai, F. Fei, S. Wang, N. Li, X. Li, F. Song, R. Li, Z. Xu, and P. Liu, “High-harmonic generation from topological surface states”, *Nature Physics* **17**, 311–315 (2021).
- [24] D. Baykusheva, A. Chacón, D. Kim, D. E. Kim, D. A. Reis, and S. Ghimire, “Strong-field physics in three-dimensional topological insulators”, *Phys. Rev. A* **103**, 023101 (2021).
- [25] D. Baykusheva, A. Chacón, J. Lu, T. P. Bailey, J. A. Sobota, H. Soifer, P. S. Kirchmann, C. Rotundu, C. Uher, T. F. Heinz, D. A. Reis, and S. Ghimire, “All-Optical Probe of Three-Dimensional Topological Insulators Based on High-Harmonic Generation by Circularly Polarized Laser Fields”, *Nano Letters* **21**, 8970–8978 (2021).
- [26] C. Heide, Y. Kobayashi, D. R. Baykusheva, D. Jain, J. A. Sobota, M. Hashimoto, P. S. Kirchmann, S. Oh, T. F. Heinz, D. A. Reis, and S. Ghimire, “Probing topological phase transitions using high-harmonic generation”, *Nature Photonics* **16**, 620–624 (2022).
- [27] F. D. M. Haldane, “Model for a Quantum Hall Effect without Landau Levels: Condensed-Matter Realization of the ”Parity Anomaly””, *Phys. Rev. Lett.* **61**, 2015–2018 (1988).
- [28] P. A. Franken, A. E. Hill, C. W. Peters, and G. Weinreich, “Generation of Optical Harmonics”, *Phys. Rev. Lett.* **7**, 118–119 (1961).
- [29] P. B. Corkum, “Plasma perspective on strong field multiphoton ionization”, *Phys. Rev. Lett.* **71**, 1994–1997 (1993).
- [30] N. Ben-Tal, N. Moiseyev, R. Kosloff, and C. Cerjan, “Harmonic generation in ionizing systems by the time-dependent complex coordinate Floquet method”, *Journal of Physics B: Atomic, Molecular and Optical Physics* **26**, 1445 (1993).

- [31] O. E. Alon, V. Averbukh, and N. Moiseyev, “Selection Rules for the High Harmonic Generation Spectra”, *Phys. Rev. Lett.* **80**, 3743–3746 (1998).
- [32] H. Eichmann, A. Egbert, S. Nolte, C. Momma, B. Wellegehausen, W. Becker, S. Long, and J. K. McIver, “Polarization-dependent high-order two-color mixing”, *Phys. Rev. A* **51**, R3414–R3417 (1995).
- [33] D. B. Milošević, W. Becker, and R. Kopold, “Generation of circularly polarized high-order harmonics by two-color coplanar field mixing”, *Phys. Rev. A* **61**, 063403 (2000).
- [34] F. Ceccherini, D. Bauer, and F. Cornolti, “Dynamical symmetries and harmonic generation”, *Journal of Physics B: Atomic, Molecular and Optical Physics* **34**, 5017 (2001).
- [35] R. Baer, D. Neuhauser, P. R. Ždánská, and N. Moiseyev, “Ionization and high-order harmonic generation in aligned benzene by a short intense circularly polarized laser pulse”, *Phys. Rev. A* **68**, 043406 (2003).
- [36] X. Liu, X. Zhu, L. Li, Y. Li, Q. Zhang, P. Lan, and P. Lu, “Selection rules of high-order-harmonic generation: Symmetries of molecules and laser fields”, *Phys. Rev. A* **94**, 033410 (2016).
- [37] H. K. Avetissian, S. Sukiasyan, H. H. Matevosyan, and G. F. Mkrtchian, “Disorder-induced effects in high-harmonic generation process in fullerene molecules”, *arXiv:2304.04208* (2023).
- [38] T. Hansen and L. B. Madsen, “Effects of lattice imperfections on high-harmonic generation from correlated systems”, *arXiv:2306.08379* (2023).
- [39] M. Lewenstein, P. Balcou, M. Y. Ivanov, A. L’Huillier, and P. B. Corkum, “Theory of high-harmonic generation by low-frequency laser fields”, *Phys. Rev. A* **49**, 2117–2132 (1994).
- [40] G. Ndabashimiye, S. Ghimire, M. Wu, D. A. Browne, K. J. Schafer, M. B. Gaarde, and D. A. Reis, “Solid-state harmonics beyond the atomic limit”, *Nature* **534**, 520–523 (2016).
- [41] M. Wu, D. A. Browne, K. J. Schafer, and M. B. Gaarde, “Multilevel perspective on high-order harmonic generation in solids”, *Phys. Rev. A* **94**, 063403 (2016).
- [42] G. Vampa and T. Brabec, “Merge of high harmonic generation from gases and solids and its implications for attosecond science”, *Journal of Physics B: Atomic, Molecular and Optical Physics* **50**, 083001 (2017).
- [43] F. Navarrete, M. F. Ciappina, and U. Thumm, “Crystal-momentum-resolved contributions to high-order harmonic generation in solids”, *Phys. Rev. A* **100**, 033405 (2019).
- [44] L. Yue and M. B. Gaarde, “Expanded view of electron-hole recollisions in solid-state high-order harmonic generation: Full-Brillouin-zone tunneling and imperfect recollisions”, *Phys. Rev. A* **103**, 063105 (2021).
- [45] G. Vampa, C. R. McDonald, G. Orlando, P. B. Corkum, and T. Brabec, “Semiclassical analysis of high harmonic generation in bulk crystals”, *Phys. Rev. B* **91**, 064302 (2015).
- [46] M. Wu, S. Ghimire, D. A. Reis, K. J. Schafer, and M. B. Gaarde, “High-harmonic generation from Bloch electrons in solids”, *Phys. Rev. A* **91**, 043839 (2015).
- [47] E. N. Osika, A. Chacón, L. Ortmann, N. Suárez, J. A. Pérez-Hernández, B. Szafran, M. F. Ciappina, F. Sols, A. S. Landsman, and M. Lewenstein, “Wannier-Bloch Approach to Localization in High-Harmonics Generation in Solids”, *Phys. Rev. X* **7**, 021017 (2017).

- [48] L. Bielke, H. Jürß, V. Burgtorf, and D. Bauer, “Formation of the solid-state high-order harmonic generation plateau through destructive interference”, *Phys. Rev. A* **107**, 033111 (2023).
- [49] H. Haug and S. W. Koch, *Quantum Theory of the Optical and Electronic Properties of Semiconductors*, 5th ed. (WORLD SCIENTIFIC, Singapore, 2009), ISBN: 978-981-283-883-4.
- [50] G. Vampa, C. R. McDonald, G. Orlando, D. D. Klug, P. B. Corkum, and T. Brabec, “Theoretical Analysis of High-Harmonic Generation in Solids”, *Phys. Rev. Lett.* **113**, 073901 (2014).
- [51] G. G. Brown, Á. Jiménez-Galán, R. E. F. Silva, and M. Ivanov, “A Real-Space Perspective on Dephasing in Solid-State High Harmonic Generation”, *arXiv:2210.16889* (2022).
- [52] C. Q. Abadie, M. Wu, and M. B. Gaarde, “Spatiotemporal filtering of high harmonics in solids”, *Opt. Lett.* **43**, 5339–5342 (2018).
- [53] E. Goulielmakis and T. Brabec, “High harmonic generation in condensed matter”, *Nature Photonics* **16**, 411–421 (2022).
- [54] L. Yue and M. B. Gaarde, “Introduction to theory of high-harmonic generation in solids: tutorial”, *J. Opt. Soc. Am. B* **39**, 535–555 (2022).
- [55] *The Nobel Prize in Physics 2016*. *NobelPrize.org*. *Nobel Prize Outreach AB 2023*. *Wed. 13 Sep 2023*, <https://www.nobelprize.org/prizes/physics/2016/summary/>.
- [56] M. Z. Hasan and C. L. Kane, “Colloquium: Topological insulators”, *Reviews of Modern Physics* **82**, 3045–3067 (2010).
- [57] J. K. Asbóth, L. Oroszlány, and A. Pályi, *A Short Course on Topological Insulators*, Vol. 919, *Lecture Notes in Physics* (Springer International Publishing, Cham, 2016), ISBN: 978-3-319-25607-8.
- [58] K. von Klitzing, G. Dorda, and M. Pepper, “New Method for High-Accuracy Determination of the Fine-Structure Constant Based on Quantized Hall Resistance”, *Phys. Rev. Lett.* **45**, 494–497 (1980).
- [59] C. L. Kane and E. J. Mele, “Quantum Spin Hall Effect in Graphene”, *Phys. Rev. Lett.* **95**, 226801 (2005).
- [60] S.-Q. Shen, *Topological Insulators: Dirac Equation in Condensed Matters*, 2nd, *Springer Series in Solid-State Sciences*, volume 187 (Springer, Berlin, Heidelberg, 2017), ISBN: 978-981-10-4606-3.
- [61] G. Sundaram and Q. Niu, “Wave-packet dynamics in slowly perturbed crystals: Gradient corrections and Berry-phase effects”, *Phys. Rev. B* **59**, 14915–14925 (1999).
- [62] P. Gosselin, F. Ménas, A. Bérard, and H. Mohrbach, “Semiclassical dynamics of electrons in magnetic Bloch bands: A Hamiltonian approach”, *Europhysics Letters* **76**, 651–656 (2006).
- [63] T. T. Luu and H. J. Wörner, “Measurement of the Berry curvature of solids using high-harmonic spectroscopy”, *Nature Communications* **9**, 916 (2018).

- [64] G. Jotzu, M. Messer, R. Desbuquois, M. Lebrat, T. Uehlinger, D. Greif, and T. Esslinger, “Experimental realization of the topological Haldane model with ultracold fermions”, *Nature* **515**, 237–240 (2014).
- [65] F. D. M. Haldane and S. Raghu, “Possible Realization of Directional Optical Waveguides in Photonic Crystals with Broken Time-Reversal Symmetry”, *Phys. Rev. Lett.* **100**, 013904 (2008).
- [66] A. B. Khanikaev, S. Hossein Mousavi, W.-K. Tse, M. Kargarian, A. H. MacDonald, and G. Shvets, “Photonic topological insulators”, *Nature Materials* **12**, 233–239 (2013).
- [67] M. C. Rechtsman, J. M. Zeuner, Y. Plotnik, Y. Lumer, D. Podolsky, F. Dreisow, S. Nolte, M. Segev, and A. Szameit, “Photonic Floquet topological insulators”, *Nature* **496**, 196–200 (2013).
- [68] M. C. Rechtsman, Y. Plotnik, J. M. Zeuner, D. Song, Z. Chen, A. Szameit, and M. Segev, “Topological Creation and Destruction of Edge States in Photonic Graphene”, *Phys. Rev. Lett.* **111**, 103901 (2013).
- [69] Á. Jiménez-Galán, R. E. F. Silva, O. Smirnova, and M. Ivanov, “Lightwave control of topological properties in 2D materials for sub-cycle and non-resonant valley manipulation”, *Nature Photonics* **14**, 728–732 (2020).
- [70] J. Liu, B.-W. Li, Y.-Z. Tan, A. Giannakopoulos, C. Sanchez-Sanchez, D. Beljonne, P. Ruffieux, R. Fasel, X. Feng, and K. Müllen, “Toward Cove-Edged Low Band Gap Graphene Nanoribbons”, *J. Am. Chem. Soc.* **137**, 6097–6103 (2015).
- [71] T. Cao, F. Zhao, and S. G. Louie, “Topological Phases in Graphene Nanoribbons: Junction States, Spin Centers, and Quantum Spin Chains”, *Phys. Rev. Lett.* **119**, 076401 (2017).
- [72] D. J. Rizzo, G. Veber, T. Cao, C. Bronner, T. Chen, F. Zhao, H. Rodriguez, S. G. Louie, M. F. Crommie, and F. R. Fischer, “Topological band engineering of graphene nanoribbons”, *Nature* **560**, 204–208 (2018).
- [73] H. Hsu and L. E. Reichl, “Selection rule for the optical absorption of graphene nanoribbons”, *Phys. Rev. B* **76**, 045418 (2007).
- [74] V. A. Saroka, M. V. Shuba, and M. E. Portnoi, “Optical selection rules of zigzag graphene nanoribbons”, *Phys. Rev. B* **95**, 155438 (2017).
- [75] W. P. Su, J. R. Schrieffer, and A. J. Heeger, “Solitons in Polyacetylene”, *Phys. Rev. Lett.* **42**, 1698–1701 (1979).
- [76] M. L. Bera, J. O. de Almeida, M. Dziurawiec, M. Płodzień, M. M. Maśka, M. Lewenstein, T. Grass, and U. Bhattacharya, “Topological phase detection through high-harmonic spectroscopy in extended Su-Schrieffer-Heeger chains”, [arXiv:2305.02025](https://arxiv.org/abs/2305.02025) (2023).
- [77] C. Ma, X.-B. Bian, and T.-Y. Du, “Role of symmetry breaking in high-order harmonic generation from Su-Schrieffer-Heeger systems”, *Phys. Rev. B* **106**, 125117 (2022).
- [78] L. A. Chizhova, F. Libisch, and J. Burgdörfer, “High-harmonic generation in graphene: Interband response and the harmonic cutoff”, *Phys. Rev. B* **95**, 085436 (2017).

- [79] G. Le Breton, A. Rubio, and N. Tancogne-Dejean, “High-harmonic generation from few-layer hexagonal boron nitride: Evolution from monolayer to bulk response”, *Phys. Rev. B* **98**, 165308 (2018).
- [80] H. Drüeke and D. Bauer, “High-harmonic spectra of hexagonal nanoribbons from real-space time-dependent Schrödinger calculations”, *The European Physical Journal Special Topics* **230**, 4065–4070 (2021).
- [81] N. Rana, M. S. Mrudul, and G. Dixit, “Generation of Circularly Polarized High Harmonics with Identical Helicity in Two-Dimensional Materials”, *Phys. Rev. Appl.* **18**, 064049 (2022).
- [82] T. Wu, G. Yuan, X. Zhang, Z. Wang, Z. Yi, C. Yu, and R. Lu, “Effect of stacking configuration on high harmonic generation from bilayer hexagonal boron nitride”, *Optics Express* **31**, 9817–9826 (2023).
- [83] Z. Peng, Y. Lang, Y. Zhu, J. Zhao, D. Zhang, Z. Zhao, and J. Yuan, “Crystal-Momentum-Resolved Contributions to Harmonics in Laser-Driven Graphene”, *Chinese Physics Letters* **40**, 054203 (2023).
- [84] W. Mao, A. Rubio, and S. A. Sato, “Enhancement of high-order harmonic generation in graphene by mid-infrared and terahertz fields”, *arXiv:2306.17346* (2023).
- [85] N. Yoshikawa, T. Tamaya, and K. Tanaka, “High-harmonic generation in graphene enhanced by elliptically polarized light excitation”, *Science* **356**, 736–738 (2017).
- [86] M. Baudisch, A. Marini, J. D. Cox, T. Zhu, F. Silva, S. Teichmann, M. Massicotte, F. Koppens, L. S. Levitov, F. J. García de Abajo, and J. Biegert, “Ultrafast nonlinear optical response of Dirac fermions in graphene”, *Nature Communications* **9**, 1018 (2018).
- [87] H. A. Hafez, S. Kovalev, J.-C. Deinert, Z. Mics, B. Green, N. Awari, M. Chen, S. Germanskiy, U. Lehnert, J. Teichert, Z. Wang, K.-J. Tielrooij, Z. Liu, Z. Chen, A. Narita, K. Müllen, M. Bonn, M. Gensch, and D. Turchinovich, “Extremely efficient terahertz high-harmonic generation in graphene by hot Dirac fermions”, *Nature* **561**, 507–511 (2018).
- [88] O. Neufeld, N. Tancogne-Dejean, H. Hübener, U. De Giovannini, and A. Rubio, “Are There Universal Signatures of Topological Phases in High-Harmonic Generation? Probably Not.”, *Phys. Rev. X* **13**, 031011 (2023).
- [89] M. Graf and P. Vogl, “Electromagnetic fields and dielectric response in empirical tight-binding theory”, *Phys. Rev. B* **51**, 4940–4949 (1995).
- [90] L. Yue and M. B. Gaarde, “Structure gauges and laser gauges for the semiconductor Bloch equations in high-order harmonic generation in solids”, *Phys. Rev. A* **101**, 053411 (2020).
- [91] R. Peierls, “Zur Theorie des Diamagnetismus von Leitungselektronen”, *Zeitschrift für Physik* **80**, 763–791 (1933).
- [92] A. L. Kuzemsky, “Electronic transport in metallic systems and generalized kinetic equations”, *International Journal of Modern Physics B* **25**, 3071–3183 (2011).
- [93] A. D. Bandrauk, S. Chelkowski, D. J. Diestler, J. Manz, and K.-J. Yuan, “Quantum simulation of high-order harmonic spectra of the hydrogen atom”, *Physical Review A* **79**, 023403 (2009).

- [94] J. C. Baggesen and L. B. Madsen, “On the dipole, velocity and acceleration forms in high-order harmonic generation from a single atom or molecule”, *Journal of Physics B: Atomic, Molecular and Optical Physics* **44**, 115601 (2011).
- [95] D. Bauer, ed., *Computational strong-field quantum dynamics: intense light-matter interactions*, De Gruyter graduate (Walter de Gruyter GmbH, Berlin ; Boston, 2017), ISBN: 978-3-11-041725-8.

Danksagung

An dieser Stelle möchte ich mich bei allen Leuten bedanken, ohne deren Unterstützung und Zusammenarbeit diese Arbeit nicht zustande gekommen wäre.

Besonders bedanken möchte ich mich bei meinem Betreuer Prof. Dieter Bauer, ohne ihm wäre diese Arbeit nicht möglich gewesen. Vor etwa fünf Jahren bin ich seiner Arbeitsgruppe beigetreten, um meine Masterarbeit unter seiner Betreuung anzufertigen. Ein Jahr später hat er mir eine Promotionsstelle angeboten, die es mir ermöglichte meine Forschung fortzusetzen und zu intensivieren. Er hat sich immer Zeit für mich genommen, um mir Probleme und Zusammenhänge zu erklären, sowie meine Fragen zu beantworten. Ich bedanke mich sehr für seine Unterstützung und für sein Vertrauen in mich.

An dieser Stelle möchte ich mich auch für die finanzielle Förderung meiner Promotion im Rahmen des Promotionsstipendienprogramms der Universität Rostock bedanken.

Des Weiteren bedanke ich mich bei allen aktuellen und ehemaligen Mitgliedern der Arbeitsgruppe Quantentheorie & Vielteilchensysteme. Ich habe viel während meiner Zeit in der Arbeitsgruppe lernen dürfen und stets Unterstützung und Hilfe erhalten. Insbesondere möchte ich mich diesbezüglich bei meiner Büronachbarin Helena und unserem Postdoc Francisco bedanken. Innerhalb der gesamten Arbeitsgruppe herrschte stets eine angenehme Arbeitsatmosphäre. Ich bedanke mich für die Zeit, die ich in der Arbeitsgruppe verbringen durfte. Besonders möchte ich mich auch bei Frau Hertzfeldt bedanken, die mir geholfen hat, mich im Bürokratie-Dschungel zurechtzufinden. Bei Fragen und Problemen hatte sie stets ein offenes Ohr für mich.

Ein besonderer Dank gilt auch meinem persönlichen Umfeld, Familie und Freund*innen für ihre Unterstützung, auch in schwierigen Zeiten.

Eidesstattliche Versicherung

Ich versichere hiermit an Eides statt, dass ich die vorliegende Arbeit selbstständig angefertigt und ohne fremde Hilfe verfasst habe. Dazu habe ich keine außer den von mir angegebenen Hilfsmitteln und Quellen verwendet und die den benutzten Werken inhaltlich und wörtlich entnommenen Stellen habe ich als solche kenntlich gemacht.

Rostock

(Abgabedatum)

(Unterschrift)